Advanced measurement techniques to improve predictive modelling of cutting processes by using inverse simulation

Mechanics and Industrial Production Department

Mondragon Unibertsitatea
Goi Eskola Politeknikoa
Faculty of Engineering

To obtain the title of

DOCTOR IN APPLIED ENGINEERING

Presented by

ANDRÉS SELA BARRIAL

Supervised by

DR. PEDRO J. ARRAZOLA,
DR. DANIEL SOLER AND DR. GUÉNAËL GERMAIN

In ARRASATE in 2021

DECLARATION OF ORIGINALITY

Hereby I, Andrés Sela Barrial, declare, that this paper is my original authorial work, which I have worked out by my own. All sources, references and literature used or excerpted during elaboration of this work are properly cited and listed in complete reference to the due source.

Yo, Andrés Sela Barrial declaro que esta tesis doctoral es original, fruto de mi trabajo personal, y que no ha sido previamente presentado para obtener otro título o calificación profesional. Las ideas, formulaciones, imágenes, ilustraciones tomadas de fuentes ajenas han sido debidamente citadas y referenciadas.

Arrasate, 2021

ABSTRACT

Machining is one of the most widely employed manufacturing operations, contributing from 3 to 10% of GDP in developed countries. Despite this prevalence, tools and cutting conditions are often chosen on a trial-and-error basis which is costly and time consuming. In recent years, predictive models have emerged as one of the most promising approaches to address this issue. To function correctly however, predictive models require accurate data related to appropriate material properties (e.g., constitutive models, damage law).

Thermomechanical tests are usually not representative of the extreme conditions found in machining processes and thus, the material laws obtained through these approaches might not accurately reflect real industrial processes. Inverse identification has the potential to address this problem, characterizing the material under real industrial conditions. However, acquiring information about workpiece temperature, strain or strain rate, remains a challenge.

The present study, therefore, presents improved techniques to measure temperature, plastic strain and strain rate to be used as input in an inverse approach. These techniques were applied to the thermomechanical characterization and orthogonal machining of a Ti6Al4V alloy. This alloy is widely used because of its good mechanical properties and its ability to maintain them at elevated temperatures. However, it is also classified as a difficult-to-cut material, mainly due to the low thermal conductivity, its chemical reactivity and its hardness at high temperatures.

As a first approach, thermomechanical tests were carried out to acquire a more in-depth knowledge of the material behaviour and to set-up a methodology to measure (i) temperature with infrared filming, and (ii) plastic strain with Digital Image Correlation. In addition, a methodology to measure the adiabatic self-heating based on a thermodynamic analysis of a 3D volume was developed.

Additionally, chip segmentation frequency was then used as an input in an inverse approach to optimize ductile failure law from orthogonal cutting tests. The prediction error was reduced from more than 100% to less than 10% in chip segmentation frequency predictions, while maintaining the accuracy in the other outcomes. Thermal measurements were carried out together with cutting forces, validating the ductile failure law proving that both workpiece temperature and cutting forces were in counter-phase.

A novel grid distortion based methodology able to measure plastic strain in the shear zone under plane strain conditions was also developed and validated. This grid method can have significant application in industry, as it proved to be an appropriate technique to measure subsurface damage, providing accurate results and reducing measurement subjectivity. The method was applied to analyze the effect of inputs such as workpiece initial microstructure, tool radius, and tool coating.

LABURPENA

Mekanizatua oso prozesu garrantzitsua da, horrek herrialde garatuetan barne produktu gordinaren %3-tik %10-era bitarteko tasak erakusten duenez. Hala ere, prozesuko ebaketa-baldintza eta mekanizazio-erremintak ez dira sistematikoki aukeratzen, eta honek denboran eta kostuan galerak sortzen du.

Karakterizazio termomekanikoen saiakuntzetan mekanizatuan bezalako muturreko baldintzak lortzen ez direnez, lortutako isurpen legeak ez dira mekanizatu prozesuen adierazgarri. Alderantzizko simulazioa irtenbide posible bat izan liteke baina tenperatura, deformazioa eta deformazio abiaduraren neurketak burutzea erronka izaten jarraitzen ditu.

Tesi honetan tenperatura, deformazio eta deformazio abiaduraren neurketak egiteko metodo berriak aurkezten dira, alderantzizko simulazioetan sarrera parametro gisa erabiltzeko. Azaltzen diren metodoak karakterizazio termomekaniko eta Ti6Al4V aleazioen ebaketa ortogonalean aplikatu ziren. Material hori oso erabilia da dituen ezaugarri mekanikoengatik -erresistentzia espezifiko altua, zurruntasuna, gogortasuna eta neke eta korrosioarekiko duen erresistentziagatik- eta gainera ezaugarri horiek tenperatura altuetan mantentzen dituelako. Hala ere, mekanizatzeko aleazio zaila da, txirbil segmentatua sortzen duelako.

Mekanizatzen hasi aurretik, karakterizazio termomekanikoa burutu zen, materialaren portaeraren ezagutza handiagoa izateko eta neurketa metodologiak baieztatzeko. Tenperatura neurtzeko filmazio infragorria erabili zen, eta deformazioa irudi digitalen korrelazioarekin. Gainera, barne-beroketa adiabatikoa (*adiabatic self-heating*) neurtzeko 3Dn egindako analisi termodinamikoan oinarritutako metodologia bat aurkezten da.

Mekanizatuan, ebaketa ortogonalen baldintzetan tenperatura neurketak egin ziren. Horiekin harikortasun irizpidea egiaztatu zen. Alderantzizko simulazioaren bidez txirbilaren segmentazio maiztasuna sarrera moduan erabili zen aipatutako irizpidea optimizatzeko. Txirbilaren segmentazio maiztasunaren iragarpenean errorea murriztu zen, %100 baino handiagoa izatetik %10 baino txikiagoa izatera igaroz, gainerako irteera aldagaien zehaztasuna mantenduz.

Ebaketa eremuan deformazio plastikoak neurtzeko sare mekanizatuen distortsioan oinarritutako metodo berri bat garatu da. Metodo horrek aplikazio garrantzitsua izan dezake industrian, gainazal azpiko kaltea neurtzeko baliagarria zela frogatu baitzen, lortutako balioak zehatzak zirelako subjektibotasuna murriztuz. Metodo hori piezaren hasierako mikroegitura, erremintaren erradio eta estaldura efektuaren analisia egiteko erabili zen.

RESUMEN

El mecanizado es uno de los procesos de fabricación más empleados, representando entre un 3 y un 10% del PIB en los países desarrollados. Sin embargo, las herramientas y las condiciones de corte son generalmente escogidas por prueba y error conllevando a un derroche de tiempo y dinero. Es por ello que el desarrollo de modelos predictivos ha aparecido como una opción interesante. Estos modelos necesitan parámetros precisos de entrada.

Hay ocasiones en las que los ensayos de caracterización no representan las condiciones extremas alcanzadas en el mecanizado. Esto implica que las leyes de fluencia del material no reflejen los procesos reales con precisión. La simulación inversa surge así como una posible solución. Sin embargo, la medición de la temperatura de la pieza, la deformación o la velocidad de deformación sigue siendo un reto.

Este estudio muestra técnicas mejoradas de medición de temperatura, deformación plástica y velocidad de deformación, para incluirlas como variables de entrada en la simulación inversa. Estos métodos fueron aplicados tanto en ensayos de caracterización termomecánica como en corte ortogonal de la aleación Ti6Al4V. Este material es ampliamente usado debido a sus buenas propiedades mecánicas así como su resistencia a la corrosión y fatiga, manteniéndolas a temperaturas elevadas. Sin embargo, esta aleación se conoce como un material difícil de mecanizar por su baja conductividad térmica, reactividad y su dureza a altas temperaturas.

En primer lugar, se realizó una caracterización termomecánica para adquirir un mayor conocimiento del comportamiento del material, así como para desarrollar una metodología de medición tanto de temperatura mediante filmación infrarroja como de deformación plástica a través de correlación digital de imágenes. Se presenta además una metodología para medir el *adiabatic self-heating* basándose en un análisis termodinámico en 3D.

Asimismo, se utilizó la frecuencia de segmentación para optimizar la ley de fallo dúctil mediante simulación inversa a partir de ensayos de corte ortogonal. El error se redujo desde más de un 100% hasta menos de un 10%, manteniendo la precisión en el resto de variables. Se realizaron medidas térmicas junto con fuerzas de corte, validando la ley de fallo dúctil, mostrando como las fuerzas y la temperatura estaban en contra-fase.

Además, se ha desarrollado una novedosa técnica basada en la distorsión de una malla capaz de medir deformaciones plásticas en la zona de corte bajo condiciones de deformación plana. Este método puede tener una aplicación significativa en la industria, ya que permite medir daño subsuperficial reduciendo la subjetividad. Este método se aplicó para analizar el efecto de variables de entrada como la microestructura, el radio y el recubrimiento de la herramienta.

"No hay nada repartido de modo más equitativo en el mundo que la razón: todo el mundo está convencido de tener suficiente"

— Descartes

A ti, Andrea, mi amor, mi apoyo incondicional
que mejor que Roma para resumir nuestra historia.

ACKNOWLEDGMENTS

Llegamos a este mundo con las manos vacías, por lo que cada logro alcanzando merece un “gracias”.

Nel ámbitu más personal, mención especial pal mio pá y la mio ma, Domi y Ascen, pela oportunidá de venir equí, allá pel añu 2015 y por tol apoyu prestáu (non solo económicu) y prestosu. Tamién, a la mio familia política, Germán y María José, y a la mio hermana Lucía, porque sé perbién qu’aguantanos mutuamente nun ye pa nada cenciello.

A tola familia en xeneral, porque somos munchos y ye imposible ponevos a toos. Eso sí, nun me prestaría escaeceme de los mios cuatro güelos. Por tol sofitu dende siempres y por tol sofitu que vos merecéis vosotres agora.

También, a los doctorandos por estar ahí tanto en los momentos difíciles (que no son pocos, ya me entendéis) como en los momentos de desconexión. Caben destacar los cafés (unos cuantos, a eso siempre puntuales) tanto para llorar como para reír. He de agradecer, en especial, a aquellos con los que más tiempo he compartido como Gorka, Lazkano, Harry, Duo, David o Asier. También a los ya no doctorandos como Buru, Mikel, Iñaki o Badiola, y a Denis, porque si no a ver cómo saldrían los ensayos. Pero en general, a todos... Espero que si alguno no está mencionado no se lo tome como algo personal.

Desde que llegué a la Universidad tenía claro que me gustaría dedicarme al mundo de la investigación y ser profesor, por lo que, llegados a este punto tengo mucho que agradecer a mis directores. Pedro, por acogerme en primero de máster y luego de nuevo de vuelta, Eskerrik asko! y Dani, por toda la ayuda de todo tipo (y los viajes a Angers, de eso no te puedes quejar) Moltes gràcies! También a Guénaël (y Linamaría), por acogerme en Angers. Merci beaucoup!

No me quiero olvidar del profesor de la Universidad de Oviedo gracias al cual estoy aquí. También, a los profesores del máster de MU y al servicio de secretaría, que buena chapa le hemos dado (Miren Murgiondo y Patricia, sobre todo).

Por último, pero lo más importante, a ti, Andrea. Anda que no hemos vivido cosas... pandemia incluida. Poco se puede decir ya que no sepas, aunque ya sabes que no me cansaré de decírtelo. Espero seguir cumpliendo etapas a tu lado, gracias, siempre!

CONTENTS

LIST OF FIGURES

LIST OF TABLES

ACRONYMS

DIC	Digital Image Correlation
JC	Johnson and Cook law
FEM	Finite Element Model
ROI	Region of Interest
WEDM	Wire Electro Discharge Machining
IR	Infrared Radiation
RT	Room Temperature
PIV	Particle Image Velocimetry
SHPB	Split Hopkinson Pressure Bar

NOMENCLATURE

Symbol	Description	Unit
α	Clearance angle of the tool	$^\circ$
γ	Rake angle of the tool	$^\circ$
r_e	Edge radius of the tool	µm
v_c	Cutting speed	m min^{-1}
F_c	Cutting force	N
F_f	Feed force	N
R	Resultant force	N
f	Feed	mm
h	Uncut chip thickness	mm
h_c	Chip thickness	mm
w	Width of cut	mm
ϕ	Shear angle	$^\circ$
T	Temperature	°C
ε_{eq}	Equivalent plastic strain	-
ε	Plastic strain	-
$\dot{\varepsilon}_{eq}$	Equivalent plastic strain rate	s^{-1}
ε_{em}	Emissivity of the object	-
σ_{SB}	Stefan-Boltzmann's constant	W/m^{2}K^4
β	Adiabatic self-heating parameter	-
β_1	Adiabatic self-heating parameter (definition 1)	-
β_2	Adiabatic self-heating parameter (definition 2)	-
A	Johnson and Cook law constant	MPa
B	Johnson and Cook law constant	MPa
C	Johnson and Cook law constant	-
m	Johnson and Cook law constant	-
n	Johnson and Cook law constant	-
$\dot{\varepsilon}_0$	Reference strain rate	s^{-1}
T_{sz}	Temperature in the shear zone	°C

l_c	Tool-chip contact length	mm
T_{ch}	Chip temperature	°C
T_{tool}	Tool temperature	°C
t_{sz}	Thickness of the shear zone	mm
R_a	Average roughness value	µm
R_t	Peak value of the roughness	µm
R_v	Valley value of the roughness	µm
R_z	Distance between the peak and the valley value	µm
T_{melt}	Melting point of the material	°C
D	Damage	-
η	Stress triaxiality	-
$(\varepsilon_{f,0})_T$	Strain to failure under shear conditions	-
c	Stress triaxiality constant	-
a	Temperature sensitivity of the strain to failure	K^{-1}
T_{crit}	Critical temperature	°C
T_U	Upper limit (temperature) of the ductile failure law	°C
T_L	Lower limit (temperature) of the ductile failure law	°C
γ_{theo}	Theoretical shear strain in a shear model	-
Δl	Displacement measured by the Gleeble	mm
w_s	Thickness of the shear zone	mm
ε_{comp}	Compression strain component	-
V_{comp}	Compression velocity	m min^{-1}
t	Time	min
F_{comp}	Compressive action of the applied load	N
F_s	Shear action of the applied load	N
W_p	Plastic work done	W
$Q_{\Delta T}$	Heat associated with the temperature rise measure	W
F	Compression load	N
L	Displacement	mm
ρ	Density of the material	kg m^3
c_p	Specific heat capacity	J kg^{-1} K^{-1}
V	Volume of the shear zone	m^3
ΔT_{IR}	Temperature rise measure with the infrared camera	K
Q_{cond}	Conduction heat loss	W

d_α	Thermal diffussivity of the material	$m^2\ s^{-1}$
k	Heat conduction	$W\ m^{-1}\ K^{-1}$
Q_{conv}	Convection heat loss	W
Q_{rad}	Radiation heat loss	W
A_{loss}	Section of losses	m^2
h	Heat convection coefficient of the air	$W\ m^{-2}\ K^{-1}$
T_{surf}	Average temperature of the sample	K
T_{air}	Temperature of the surroundings	K
Q_{mt}	Heat loss due to mass flux	W
ΔT_{sz}	Average temperature oscillation	°C
ΔF_c	Force oscillation	$N\ mm^{-1}$
Δh_c	Chip thickness oscillation	mm
q	Non-uniform power law distribution of velocity	-
P_e	Peclet number	-
χ	Proportion of the shearing flux	-
K	Analytical parameter	-
τ	Shear stress	MPa
T_0	Room temperature	°C
a_e	Width of the path	µm
a_v	Distance between two straight paths	µm
a_p	Depth of cut	µm
r	Radius of the ball	µm
L_{CD}	Length of the deformed segment	µm
L_{AB}	Length of the undeformed segment	µm
V_{CD}	Speed of the deformed segment	$m\ min^{-1}$
V_{AB}	Speed of the undeformed segment	$m\ min^{-1}$
$\dot{\varepsilon}_{xx}$	Strain rate in horizontal direction	s^{-1}
$\dot{\varepsilon}_{yy}$	Strain rate in vertical direction	s^{-1}
$\dot{\gamma}_{xy}$	Shear strain rate	s^{-1}
$\dot{\varepsilon}_{eq}$	Equivalent strain rate	s^{-1}
u_{L_0}	Standard uncertainty	µm
σ_x	Standard deviation in horizontal direction	µm
σ_y	Standard deviation in vertical direction	µm
$T_{surface}$	Surface temperature measured	°C

u_T	Uncertainty on the temperature measurement	°C
σ	Flow stress of the material	MPa
σ_D	Damaged flow stress of the material	MPa

1

INTRODUCTION

Machining is a widely employed industrial process because it provides good dimensional tolerances and good surface finishing in quite complex features. It is estimated that around 15% of all mechanical components are obtained from machining operations, contributing from 3 to 10% of GDP in developed countries (Arrazola et al., 2013).

Considering this scale of usage, the proper selection of tools (coating, material) and cutting conditions is of great interest, both for cost reduction and improved machining performance. In fact, it is estimated that savings of up to 20% could be made by selecting the proper tool and cutting conditions (Ezugwu, 2005). Nevertheless, many parameters of the process are still chosen through trial and error, based on empirical databases or the technical experience of the operator or CAD/CAM programmer. This, in addition to the unwanted impact on the bottom line, does not always provide the optimum solution. Furthermore, the validity of the created databases is limited to the range of conditions tested, and is rendered useless when a new tool or workpiece material appears.

Thus, an alternative method is needed to predict not only fundamental variables (forces, chip thickness, tool chip contact length, temperatures, strain, strain rate), but also critical industrial outcomes such as surface integrity, stability, tool wear or burrs. Predictive modelling has emerged as a promising approach, aiming to increase productivity without affecting the finished quality of the manufactured part. Predictive models can take many forms including empirical models, Finite Element Models (FEM), analytical modelling, or hybrid approaches, among others. Figure 1.1 shows some examples of the use of predictive models to predict scientific variables or industrial outcomes.

Machining processes however, are among the most complex to model and simulate due to the severe plastic deformation suffered by the metal being cut and the extreme tribological conditions reached between the tool and the workpiece (Melkote et al., 2017). For instance, Arrazola et al., 2004 showed through finite element simulations that under widely used conditions for cutting steel C45 (cutting speed of 300 m/min and feed of 0.2 mm) the process reached strain rates of up to 10^5 s^{-1} and equivalent plastic strains of up to 4. Moreover, the heat rate was around 10^5 K/s, reaching temperatures close to the melting point of the material. This all takes place in a volume lower than 1 mm^3 and in a very low lapse of time (milliseconds) (Trent and Wright, 2000). Similarly, Harzallah et al., 2020 proved that, at cutting speeds representative of the broaching process (up to 15 m/min), Ti6Al4V subjected to the orthogonal cutting process reached equivalent plastic strains close to 2, strain rates higher than 5000 s^{-1} and temperatures close to 550°C in the primary shear zone.

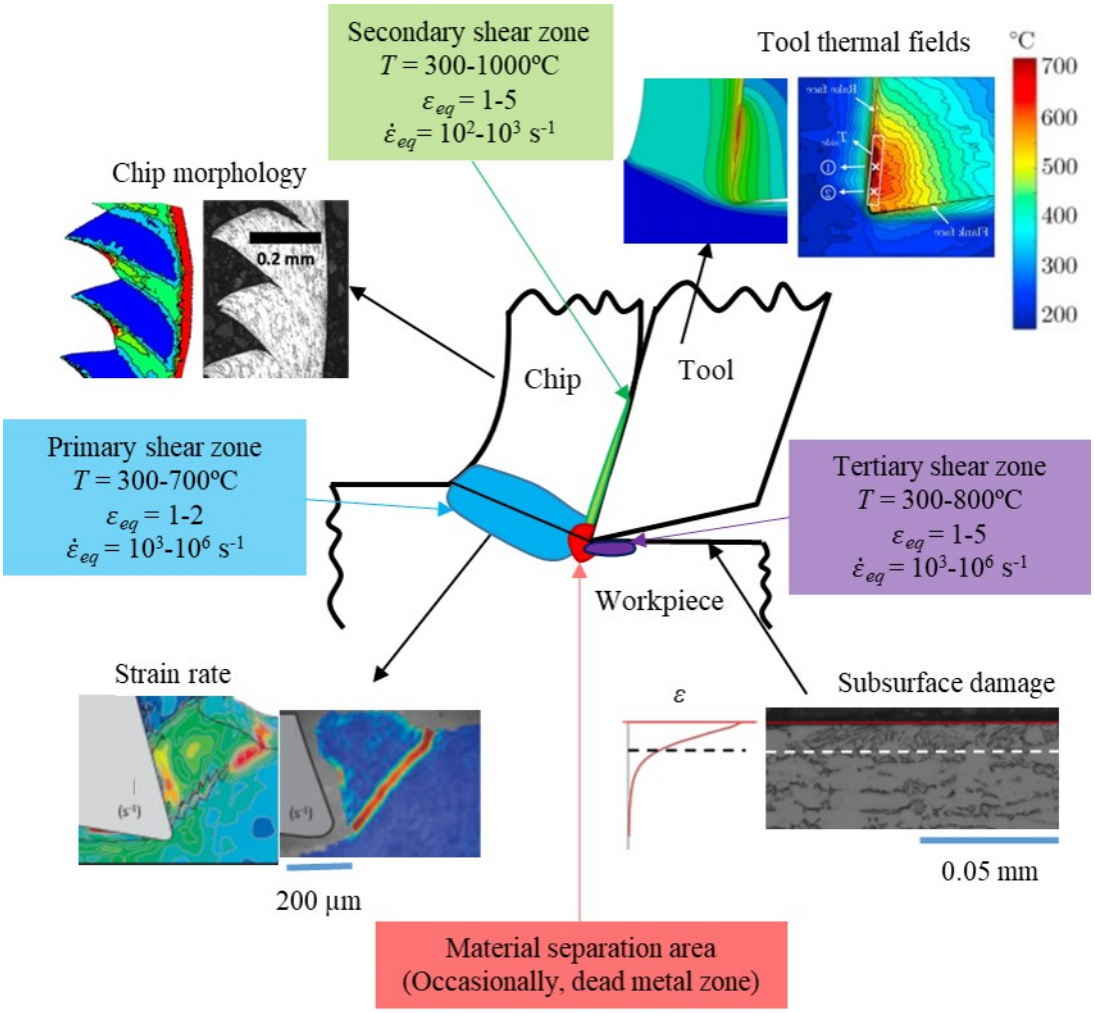

Figure 1.1: Examples of the use of predictive models to predict different scientific and industrial outcomes in machining and the conditions reached during the machining process are given. Predictive results are located to the left, and experimental results to the right. Chip geometry, adapted from Childs et al., 2018. Thermal fields, adapted from Saez de Buruaga et al., 2018. Strain rate fields, adapted from Harzallah et al., 2020. Subsurface damage (surface integrity), adapted from Ortiz de Zarate et al., 2018

These two examples clearly represent the extreme conditions undergone during the machining process, making it difficult to accurately model. It is also almost impossible to develop thermomechanical characterization set-ups able to reproduce the cutting conditions commonly found in real industrial processes. The conditions reached in the main cutting zones are summarized in Figure 1.1.

This research work focuses on the thermomechanical characterization and orthogonal cutting of the titanium alloy Ti6Al4V. These alloys are widely used in the aeronautical, automotive, and medical sectors due to their high relative strength and corrosion resistance, and their ability to maintain these properties at elevated temperatures. They are defined as difficult-to-cut materials mainly due to their low thermal conductivity, their chemical reactivity and the high strength at elevated temperatures. In addition, their low thermal conductivity leads to the generation of segmented chips, hampering the reproduction of the conditions undergone during machining.

It is important to note that the accuracy of predictive modelling is strongly dependent on the reliability of the input parameters, being especially relevant flow stress or damage law. Materials are usually characterized by carrying out thermomechanical tests in Gleeble thermomechanical simulators or using Split Hopkinson Pressure Bars (SHPB).

However, the conditions under which the material is characterized are still far different from those of the machining process. Therefore, the use of constitutive models to reproduce machining conditions needs extrapolation to higher strain and strain rates, which could influence the accuracy of the predicted results.

One further input to be taken into consideration is the friction model. New research into friction characterization under machining conditions has shown that friction could be governed by the shear stress of the material (Ortiz de Zarate et al., 2021) thus indicating the importance of material identification.

Inverse simulation appears thus as a possible promising option to carry out material identification under these realistic machining conditions. The idea is to optimize the initial thermomechanical characterization by using machining outcomes obtained under real machining conditions. This procedure is summarized in Figure 1.2.

In general, predictive models are validated considering fundamental variables such as cutting forces or chip thickness and morphology, as these are relatively easy to measure. The use of dynamometers to measure cutting forces has been widely used for many years. Tool temperature can be determined with thermocouples or infrared techniques; and chip geometry is easily measured with optical measurements. However, other significant variables such as equivalent plastic strain, strain rate or workpiece temperature fields are not usually taken into account in the analysis as techniques to obtain their measurements are still being under development.

The present study, therefore, presents improved techniques to measure workpiece temperature, plastic strain and strain rate, with the aim of reporting valuable inputs to be used in an inverse simulation analysis. These techniques were applied to the

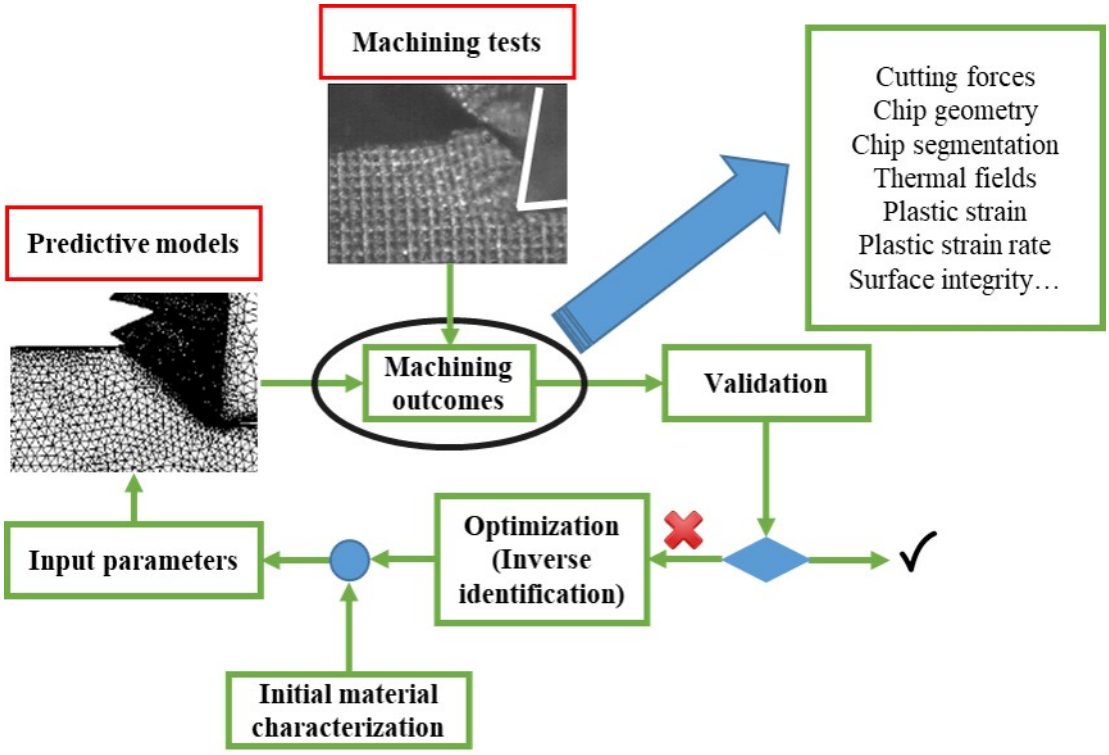

Figure 1.2: Flow chart of the procedure followed to validate predictive models (FEM in the example)

thermomechanical characterization and orthogonal machining of a Ti6Al4V alloy to obtain its value in the primary shear zone, and on the machined surface.

Objectives

The main goal of this research project is therefore defined as:

Development of advanced techniques to measure key scientific variables and industrial outcomes such as workpiece temperature, equivalent plastic strain and strain rate, and surface integrity, to provide a more in depth knowledge of the cutting process and to generate reliable experimental data to validate and optimize predictive models by using inverse simulation.

To attain this goal, the following research objectives are proposed:

1. Development of a methodology to characterize material behaviour under shear and compression load modes. This involves the establishment of equivalent plastic strain, strain rate and temperature measurement techniques to improve the quality

of the experimental data obtained through thermomechanical tests, including the characterization of adiabatic self-heating.

2. Development of a methodology to measure the temperature in the primary shear zone during orthogonal cutting to understand in greater depth material behaviour under real machining conditions.

3. Establishment of an inverse simulation methodology which optimizes material ductile failure law.

4. Development of a procedure to measure in-process strain and strain rate under orthogonal cutting conditions for Ti6Al4V. This procedure should overcome the technical limitations associated with traditional techniques, by carrying out the measurements under plane strain conditions representative of the orthogonal cutting process.

5. Establishment of a methodology to measure post process surface integrity which considers subsurface damage as an indicator of the surface state of a workpiece, thereby reducing the subjectivity related with microstructural and microhardness-based measurements.

Structure of the document

This document is organized as follows:

- *Chapter 2: Literature review*

  A summary and critical analysis of the main works related to the topic is set out, including the discussion of these references and the identification of the research opportunities. These research opportunities define the objectives shown above.

- *Chapter 3: Thermomechanical characterization of the workpiece material*

  The material behaviour subjected to different load modes was analysed based on a new sample design. Temperatures, plastic strain, and strain rates were measured in order to provide a more in-depth knowledge of the material behaviour. In addition, the adiabatic self-heating was characterized through a new proposed methodology. The measurements were used to validate the finite element model.

- *Chapter 4: Temperature measurements*

  This chapter focuses on orthogonal cutting. The effect of machining conditions on workpiece temperature is analysed and compared to numerical and analytical results. Workpiece temperature in the shear zone is measured using infrared filming. Accurate temperature measurement in the shear zone is critical and few attempts could be found in literature. Thermal measurements allow the segmentation frequency to be

measured and compared with that based on cutting force measurements, in order to validate the ductile failure law and to carry out the inverse analysis.

- *Chapter 5: Strain and strain rate measurements*

  Techniques to measure equivalent plastic strain and strain rate in-process under real machining conditions when cutting Ti6Al4V were tested. These include the speckle pattern technique employed in the thermomechanical analysis and a mechanical pattern created through micromilling. A novel method was then developed to measure equivalent plastic strain using a self-designed customized set-up to achieve plane strain conditions representative of the orthogonal cutting process.

- *Chapter 6: Subsurface damage measurements*

  The subsurface damage of the sample subjected to a wide range of machining conditions was analysed employing different measurement techniques such as metallographic etching, microhardness measurements and grid distortion analysis. The grid distortion technique was employed to analyse the effect of different machining inputs such as workpiece material, tool coating and edge radius.

- *Chapter 7: Conclusions and future lines*

  The conclusions of this study are summarized in this chapter, together with future lines.

- *Chapter 8: Contributions*

  The scientific contributions (journal papers and conferences) resulting from the work developed are summarized in this chapter.

The document structure is summarized in Figure 1.3.

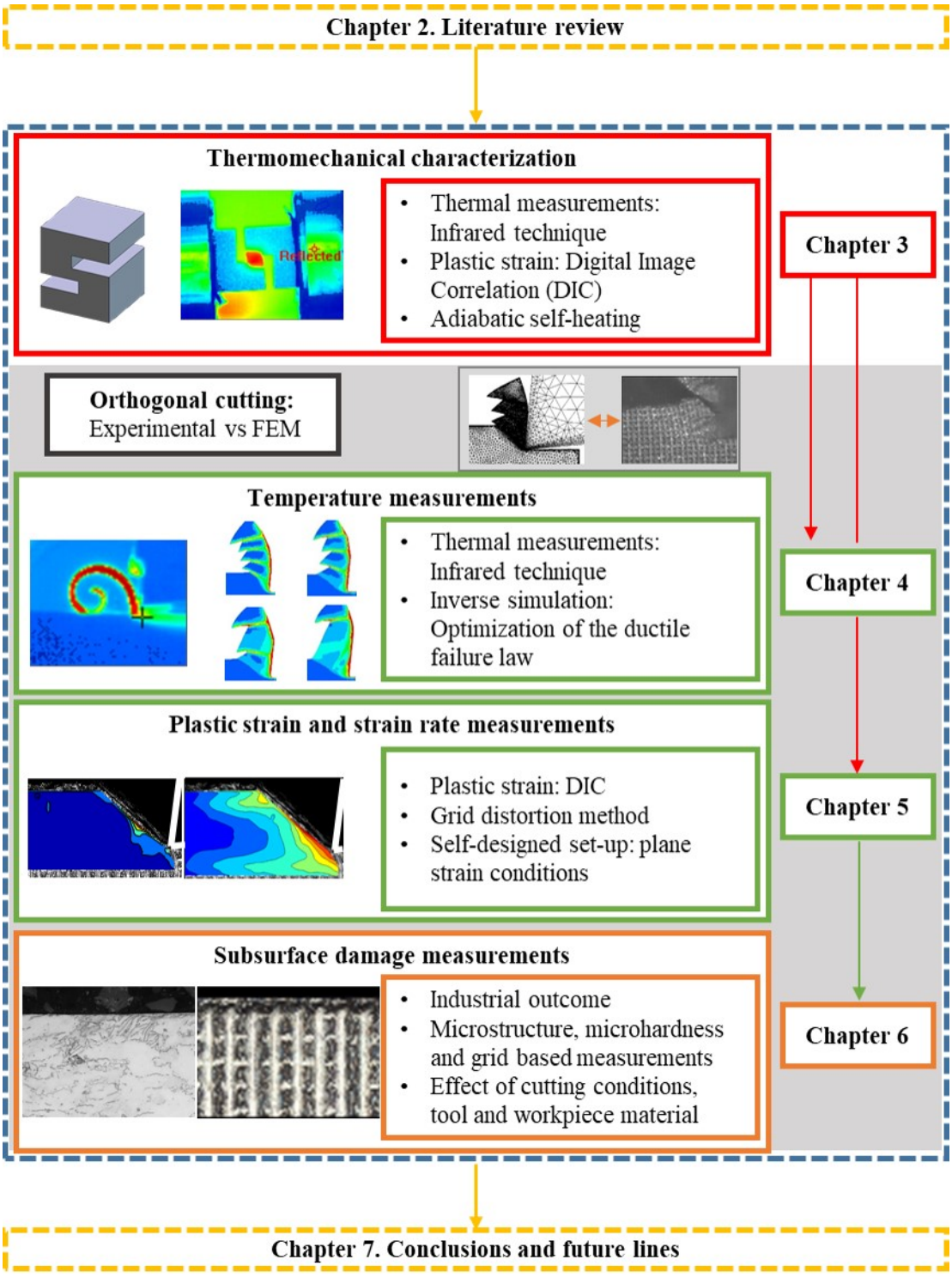

Figure 1.3: Dissertation structure

2

LITERATURE REVIEW

Machining is a complex process and constant efforts are being made in order to improve productivity and part quality. Many research works are focused on difficult-to-cut materials as they represent a relevant issue for machining industry. The increasing use of this kind of alloys has led to scientific community to study the physics under the chip formation mechanisms of these materials.

Earlier, these research works used to be focused on analysing a posteriori of the workpiece state (surface) or the chip morphology, as it was difficult to take experimental data directly from the shear zone. In parallel, analytical modelling was the only one available to analyse the cutting process, with the early models presented by Merchant, 1945 or Oxley, 1989. In fortune, this has changed and now different predictive model approaches are able to accurately reproduce chip formation providing interesting results about local phenomena such as heat or strain concentrations. This precision is difficult to be achieved with an analytical approach.

However, the accuracy of these models depends on the reliability of the input parameters. This has opened new research opportunities as traditional material characterization is out of the range of conditions typically employed in machining. In order to generate more robust models, efforts are being made focusing on in-situ measurements during the cutting process, mainly focused on strain and thermal fields. These results would be useful to understand the physics under the machining process more in depth. In addition, they could be used as input to validate or optimize the numerical models.

Therefore, within this chapter, first, the fundamentals of machining were analysed, with a special focus on the machining of titanium alloys, as one of the most widely used difficult-to-cut alloys. Then, a brief analysis of the most commonly employed techniques to carry out constitutive material characterization was given, pointing out their major drawbacks. Following, the measurement techniques available in literature to measure plastic strain and temperature were deeply analysed. Finally, surface integrity was analysed taking into consideration subsurface damage as a relevant industrial outcome.

2.1 MACHINING FUNDAMENTALS

Machining process removes material from a workpiece generating the chip and a new surface. Although all machining operations have three-dimensional nature, the orthogonal cutting process is widely employed to study relevant aspects with regard to chip formation mechanisms as it allows the process to be studied in two dimensions. In orthogonal configuration, the tool has a clearance and rake angle (α and γ, respectively) with a

finite edge radius (r_e). There is a relative movement between the tool and the workpiece, with a constant cutting speed (v_c). The edge has to be normal to the cutting and feed directions in order to fulfill orthogonal cutting conditions. The resultant force (R) can be decomposed in two main cutting forces, the cutting force (F_c), parallel to the cutting speed and the feed force, F_f, normal to the cutting motion (see Figure 2.1).

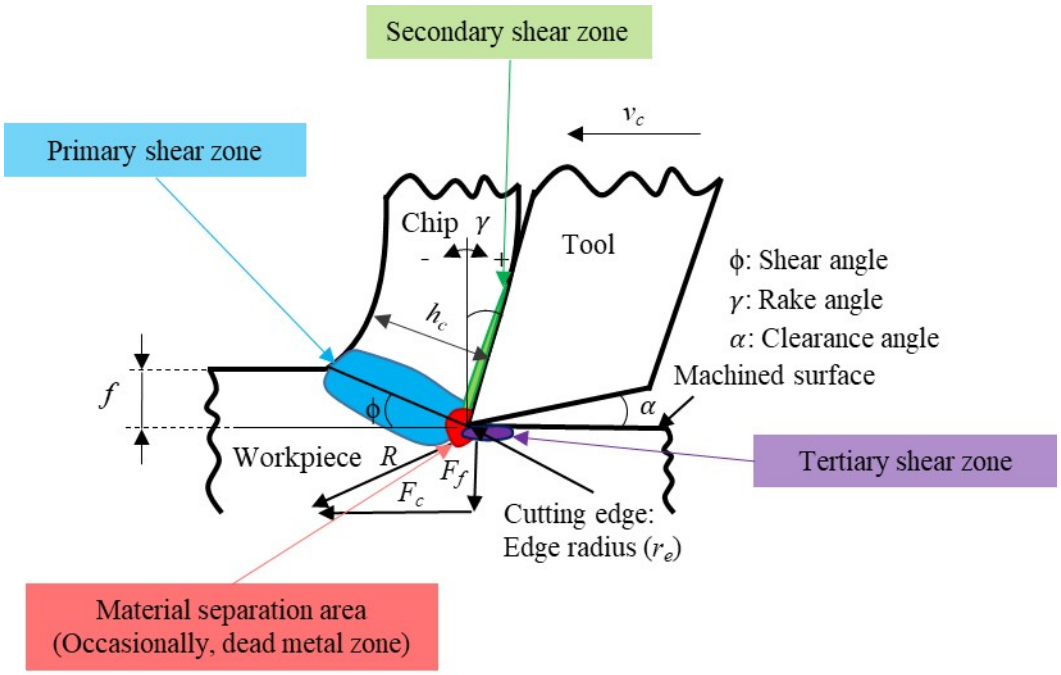

Figure 2.1: Representation of the orthogonal cutting process

Orthogonal cutting allows the chip formation mechanisms to be analysed enabling three different cutting regions to be distinguished, together with the dead metal zone, close to the tool. This dead metal zone becomes higher for higher edge radii because of the increasing on the ploughing action. The three regions are: (i) the shear zone (primary shear zone), (ii) the chip-tool interface (secondary shear zone) and (iii) the tool-workpiece interface (tertiary shear zone). During the cutting process, the heat is generated due to plastic deformation in the primary shear zone and friction along the tool-chip and the tool-workpiece interface. In addition, other portion of heat is generated along the machined surface because of the rubbing action (Kishawy and Hosseini, 2019). It is assumed that almost all the energy required for cutting is turned into heat in the cutting domain and the maximum temperature takes place at the tool-chip interface (Dogu et al., 2006).

In the primary shear zone the direction of the material flow changes which leads to high strain rates and thermal gradients. Because of these extreme conditions it is generally assumed that the model could be approximated to an adiabatic behaviour (Harzallah, 2018). The determination of the temperature and the plastic strain within

this zone is still a challenge nowadays. Below the shear zone, the material is undeformed while above this zone the created chip flows up at a different speed. The separation is usually defined as a shear plane according to the shear angle (ϕ). These are represented by the uncut chip thickness (h), which in orthogonal cutting is equal to the feed (f), and the deformed chip thickness (h_c), as shown in Figure 2.1.

The secondary shear zone is located in the contact between the rake face of the tool and the chip and is characterized by an intense friction action. In addition, the workpiece is subjected to elevated plastic strains and high temperatures which could lead to local melting of the material. The highest strain is reached in the secondary zone, whose value could vary between 1 to more than 5 depending on the workpiece material and the cutting conditions.

Finally, the tertiary shear zone could be defined based on the contact between the tool flank face and the workpiece surface. The rubbing action is a relevant source of heat, causing a notable temperature rise along the machined surface. This zone would define the surface integrity of the final part and would become more relevant when tool wear appears.

Orthogonal cutting configuration could be experimentally reproduced with different cutting set-ups, being the most widely used the turning of a tube or a disk or linear cutting devices. Many examples can be found in literature, see, for instance Saez de Buruaga et al., 2018, Harzallah et al., 2017 or Zhang et al., 2019, among others. These configurations can be seen in Figure 2.2.

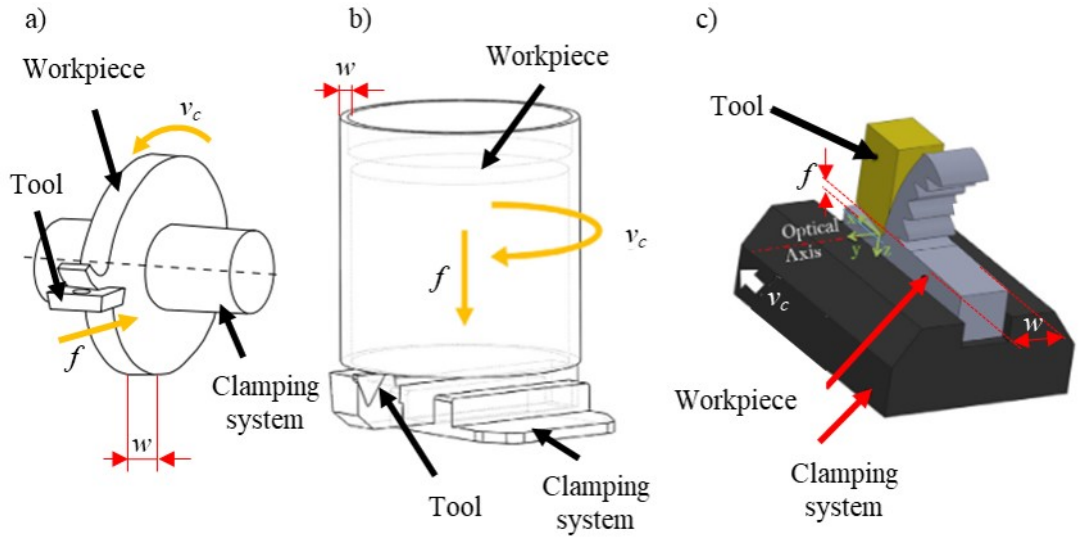

Figure 2.2: Orthogonal cutting devices. a) Turning of a disk (adapted from Harzallah, 2018); b) Turning of a tube (adapted from Saez de Buruaga et al., 2018); c) Linear cutting device (adapted from Harzallah et al., 2017)

However, it is worth mentioning that the cutting speed in the turning of a tube would not be constant along the width of cut, as it increases with the radius of the tube for a constant angular velocity. Also the cutting speed when turning a disk depends on the radius of the disk and the feed. Therefore, among all the configurations available, linear cutting devices seem to be the ones which better fulfill the orthogonal configuration as it facilitates the stability of the cutting process. Furthermore, it allows the process to be filmed through high speed and infrared devices, to determine relevant aspects about the chip formation process. Nevertheless, the main limitation of this configuration lies in the maximum cutting speed achievable, which is often limited to values lower than 200 m/min (Zhang et al., 2019; Thimm et al., 2019).

All the configurations shown above present the same drawback. The deformations reached during the orthogonal cutting process have to be purely two-dimensional along the cutting plane without out of plane displacements. In general, it is assumed that the ratio of the cutting width to the uncut chip thickness, w/f, should be higher than 10 (Ghadbeigi et al., 2008). Nevertheless, the application of this criterion does not avoid out of plane displacements and pure plane strain configuration is not achieved.

This issue is not widely analysed in literature and may not be relevant when some outcomes such as cutting forces, chip morphology, cutting temperature or surface integrity are studied. However, these displacements could influence the plastic strain and strain rates reached within the shear zone. In addition, the values experimentally obtained could not be directly compared with orthogonal 2D simulations. Few attempts can be found in literature aiming to overcome this issue. For instance, Lee et al., 2006, Guo et al., 2015 or Zhang et al., 2017 employed glass to constrain both sides, maintaining the possibility of filming the process, whereas Ghadbeigi et al., 2008 constrained the face to be analysed between two halves in order to analyse the shear zone after a quick stop test. Both configurations, which can be seen in Figure 2.3, reduced as much as possible out of plane displacement.

Among all the materials, titanium alloys present relevant properties such as high strength-to-weight ratio, great stiffness and toughness, and fatigue and corrosion resistance, keeping these properties at elevated temperatures (Kishawy and Hosseini, 2019). These properties make these materials interesting to applications such as aerospace industry, defense, steam turbine blades, automotive and biomedical industry, due to their biocompatibility. However, these good properties are also coupled with a very low thermal conductivity or high chemical reactivity at high temperatures, which could have a negative impact during the machining of these alloys.

For instance, during machining of titanium alloys, the tool becomes quickly worn due to the high temperatures reached close to the tool and the elevated abrasion during the cutting process (Li et al., 2016). This poor machinability could be directly related to the thermomechanical properties of titanium alloys and lead titanium alloys to be defined as difficult-to-cut materials.

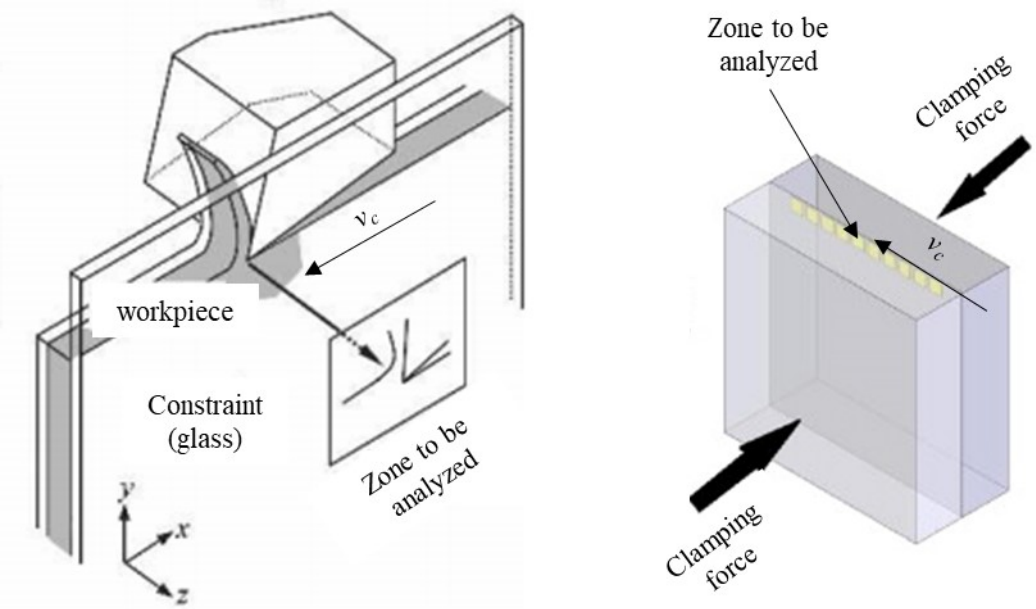

Figure 2.3: Different set-ups employed in literature to avoid side flow (out of plane displacements). Left side: glass constraint, adapted from Lecompte et al., 2006. Right side: zone to be analysed constrained between two workpieces, adapted from Ghadbeigi et al., 2008

During the cutting process, the heat generated because of plastic work and friction is essentially dissipated in four dissimilar ways (by the cutting tool, the chip, the workpiece and into the environment). However, because of the low thermal conductivity of titanium alloys (for instance, the thermal conductivity of Ti6Al4V is around 7 W/mK whereas nickel alloys and steels could have conductivities close to 100), there is no effective heat dissipation by the workpiece. In addition, it has been demonstrated that titanium generates thinner chips than other alloys, leading to a lower contact area also reducing the amount of heat dissipated by the chip, causing higher stresses on the cutting tool (Narutaki et al., 1983). Therefore, it is estimated that the tool absorbs more than the 80% of the heat generated, reducing tool life (Ezugwu and Wang, 1997; Kishawy and Hosseini, 2019).

In addition, when these alloys reach temperatures higher than 500°C they become very reactive. Unfortunately, these temperatures are typically reached during machining processes, as stated by Harzallah et al., 2020, even at low cutting speeds. Under these conditions, titanium could react, for instance, with the coating layer, removing this coating and causing premature tool failure (Rahman et al., 2003). Another factor to be taken into account is the hardening effect. This hardening occurs due to plastic deformation and diffusion. At the aforementioned temperatures, molecules of oxygen and nitrogen could harden the surface layer because of diffusion, hampering the machining process (Kishawy and Hosseini, 2019).

Apart from all the aspects previously mentioned, another relevant issue which explains the poor machinability of titanium alloys lies in their mechanics of chip formation. During machining of Ti6Al4V, as a typical example of titanium alloy, chip segmentation was proved to occur over a wide range of cutting speeds by Childs et al., 2018, for instance. Chip segmentation is a key aspect in machining as it could influence tool life because of the periodic stresses generated (Kishawy and Hosseini, 2019). Chip segmentation in titanium is assumed to be due to two different physical phenomena depending on the working regime. At high cutting speeds, the low thermal conductivity of the material causes heat concentration in the shear zone and high temperatures within this zone, leading to a thermal softening effect and adiabatic shearing (Ye et al., 2018; Childs et al., 2018). However, at low cutting speeds, chip segmentation is assumed to be due to the lack of ductility (Elbestawi et al., 1996; Ortiz de Zarate et al., 2019).

Therefore, although there is a wide number of studies focused on machining of Ti6Al4V, further research is needed in order to understand more in depth how it behaves under different cutting conditions so as to increase the productivity of the machining of these alloys.

2.2 MATERIAL CHARACTERIZATION

Knowing the material behaviour (flow stress, damage law or friction properties) is a relevant issue in order to develop accurate predictive models. Among all the input parameters, material characterization is of wide relevance as it has been stated by Arrazola et al., 2013 or Melkote et al., 2017, for instance.

Material laws are usually obtained through thermomechanical tests, which have to be done under conditions close the real ones reached during the process to be modelled. However, this is extremely difficult in the machining case because of the extreme conditions reached: equivalent plastic strain up to 5, strain rate higher than 10^6 s^{-1}, high temperatures (close to the melting point in some cases) and high heat rates concentrated in a low portion of material and in a very short period of time. In addition, the tensional state reached in machining is quite complex, combining different load modes such as tension, compression or shear, depending on the cutting conditions (Wang and Liu, 2016; Childs et al., 2018).

Some mechanical tests can be carried out to characterize the mechanical behaviour of the material under close to these extreme conditions. The uniaxial tensile test is one of the most commonly used due to its simplicity. However, this test does not reproduce the strain and strain rates reached during machining because of the necking phenomenon which causes strain concentration, resulting in a local reduction of the deformed area leading to fracture at relative low strains. In addition, the tensional state of the machining process is not reproduced with a tensile test.

In order to reach higher strains, Gleeble machines can be used, but the strain rates are still lower than the ones reached in the machining process (Hosford, 2010), especially for cutting operations carried out at high cutting speeds.

Although typical cylindrical samples as the ones used by Germain et al., 2013 are not able to reproduced these machining conditions, some specific samples are being developed aiming to overcome this in Gleeble machines through shear samples (Tarigopula et al., 2008; Hor et al., 2013b; Harzallah et al., 2017). These samples are able to reach strain rates close to 1000 s^{-1}, which could be comparable with the typical strain rate of the broaching process. An example of a hat sample, employed by Harzallah et al., 2017 is shown in Figure 2.4. The strain concentrates in the zone highlighted in red, simulating a shear mode.

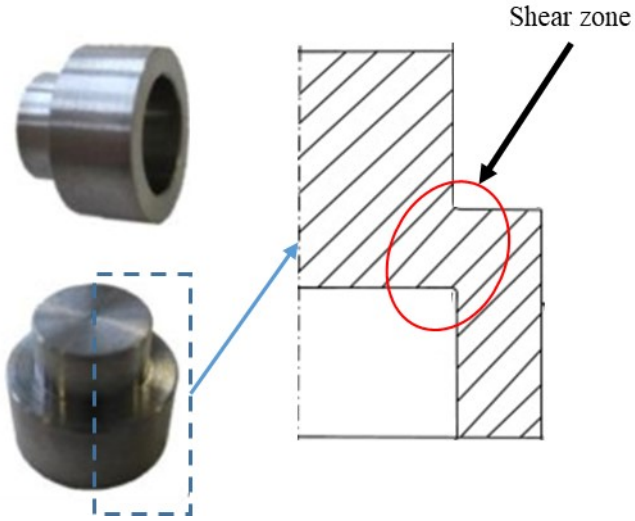

Figure 2.4: Example of a hat sample employed to reproduce shear mode. Adapted from Harzallah et al., 2017

To reach higher strain rates, dynamic tests could be carried out. The most widely employed one is Split Hopkinson Pressure Bar (SHPB), reaching strain rates up to 10^4 s^{-1} (Kolsky, 1949). However, depending on the material, the strains reached are lower than one. Higher strain rates could be reached with multiaxial impact tests ($10^6 - 10^8$ s^{-1}) or ballistic configurations (Field et al., 2004).

The typical strain rates reached with different thermomechanical simulators compared to machining conditions are shown in Figure 2.5.

Same problems appear to characterize the damage or friction law. Nevertheless, some research works haven been carried out studying fracture based on triaxiality (Bao, 2003). This knowledge is of wide relevance to reproduce chip segmentation, typical of titanium alloys (Childs et al., 2018).

In addition, there are many techniques to characterize friction (as it is summarized in Melkote et al., 2017) but no one of these methods is able to reproduce the phe-

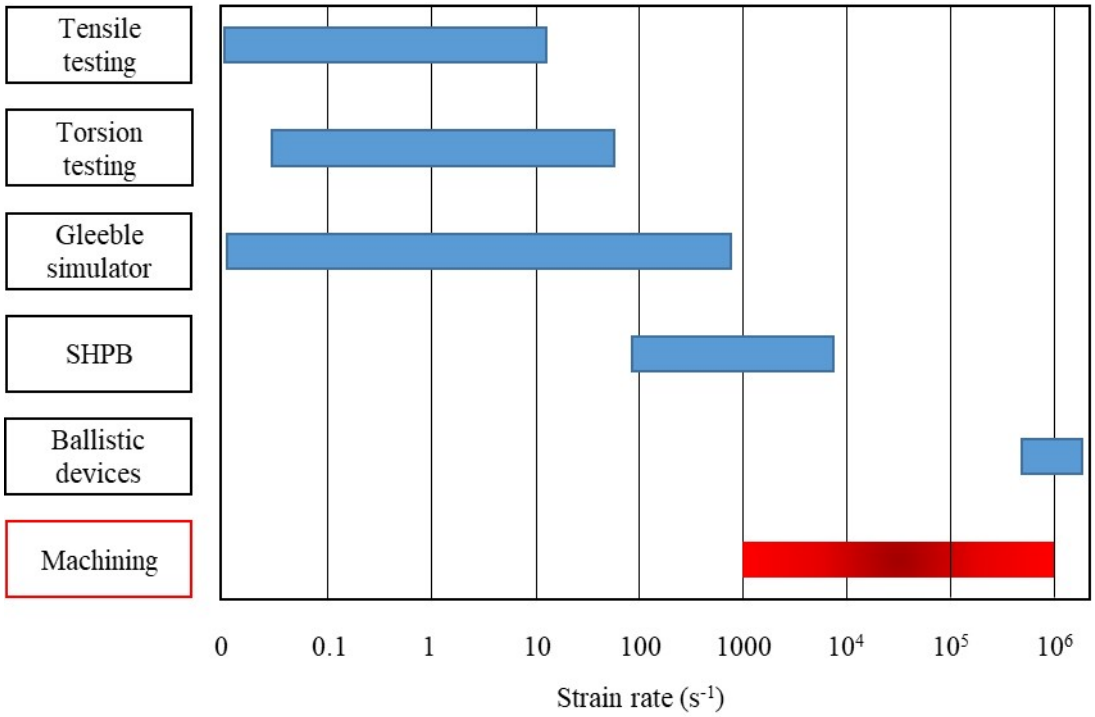

Figure 2.5: Comparison between the strain rates reached during a typical machining operation in the primary shear zone with the main thermomechanical simulators available in literature

nomenon of sticking and sliding between the chip and the tool properly. New efforts on friction characterization are relating the shear stress of the material with the friction in the chip-workpiece interface (Ortiz de Zarate et al., 2021), thus making the material characterization more important.

Therefore, a proper methodology to reproduce these extreme conditions is needed to be developed in order to obtain accurate material laws to reproduce machining conditions.

2.2.1 *Temperature measurement*

During thermomechanical characterization, a proper temperature control is essential. However, in practice, it is quite impossible to reach pure isothermal conditions due to heat conduction along the sample, conduction between anvils and sample and possible losses with the surroundings (convection and conduction) (Xiao et al., 2021).

Taking Gleeble thermo-mechanical simulators as example, they are a good option as they enable to have high heating rate and accurate thermomechanical loading, the heating being controlled through Joule effect. Bennett et al., 2010 demonstrated that the stress measurements could differ more than 20% due to inhomogeneous temperature

along the sample. This could lead to mispredictions on the material properties (Evans and Scharning, 2001). In addition, this thermal gradient could influence sample microstructure (Quan et al., 2016).

Temperature is usually measured through thermocouples. Basically, thermocouples produce an output voltage which depends on the temperature difference between the junctions of two metal wires. The main advantage is the relative availability of the thermocouples which are less expensive than other techniques. For instance, Xiao et al., 2021 carried out a comprehensive study to show the relevance of thermal gradients during material characterization. However, in this work, the thermal gradient was measured based on two thermocouples distributed along the sample, which could not reflect the thermal field properly. Similarly, Kardoulaki et al., 2014 or Semiatin et al., 2017 studied the effect of thermal gradients because of resistance heating in Gleeble characterization by welding three thermocouples along the sample. Shao et al., 2018 determined the heat flux along the sample during tensile testing by six thermocouples evenly distributed, which notably hampers the data treatment.

Thermocouples, however, influence the heat flow, they have limited transient response and they only allow a single point to be measured making the acquisition of thermal fields difficult (Hoyne et al., 2013; Kröning et al., 2016). In addition, the spatial resolution of thermocouples is notably limited, making them an unsuitable option when high temperature gradients are expected (Rooyen and Becker, 2018).

To address these issues, higher spatial resolutions could be obtained through infrared thermography. In infrared techniques, the surface temperature of the body is measured based on its emitted thermal energy. This technique can be used to measure also temperature fields (Dinc et al., 2008). In comparison with thermocouples, this technique presents many advantages such as being a non-intrusive technique with a very fast response. However, the main disadvantage lies in the fact that sources of error such as emissivity, reflections, absorption and obstructions need to be controlled. These difficulties lead to a common opinion that temperatures obtained by IR techniques are good enough for a comparative analysis but it is not appropriated for reporting quantitative values (Soler et al., 2015).

Physically, this technique is based on Stefan-Boltzman law, equation (1), which established the relationship between the radiated energy, q_r, and the absolute temperature of a body, T.

$$q_r = \varepsilon_{em}\sigma_{SB}T^4 \tag{1}$$

where ε_{em} is the emissivity of the object and σ_{SB} is Boltzman's constant.

In an early study by Dewes et al., 1999 it was shown that IR techniques reported lower temperatures than thermocouples. As a possible explanation, heat losses and bad estimation of the emissivity or the sources of error mentioned above could be relevant

issues. Nevertheless, Rooyen and Becker, 2018 showed that for high-strain-temperature process this technique is more useful than thermocouples.

2.2.1.1 *Adiabatic self-heating*

Together with a proper thermal control of the test, it is worth mentioning that during plastic deformation the part being deformed is self-heated because of this high deformation. The majority of the work employed in the deformation is transformed into heat (phenomenon known as adiabatic self-heating) whereas a small amount is employed as stored energy (Knysh and Korkolis, 2015). This part of the energy is stored in lattice, while the rest contributes to the development of dislocation structures (Zubelewicz, 2019).

Within this context, different definitions could be found in literature representing this phenomenon which, in this work, have been distinguished as β_1 and β_2. Therefore, the adiabatic self-heating could be defined as the ratio between the heat spent to heat the sample to the plastic work done during deformation, β_1, and is usually taken as 0.9-0.95 (Dumoulin et al., 2010; Knysh and Korkolis, 2015; Bonk et al., 2016). This has been studied for years and the first attempt was made by Taylor and Quinney (Taylor and Quinney, 1934). This approach is widely accepted and many commercially available FEM software such as Deform, AdvantEdge or Forge NXT use it.

Nevertheless, other researchers defined the adiabatic self-heating as the ratio between the heat experimentally observed via thermal variations to the total plastic work (Rittel et al., 2017; Härtel et al., 2018), β_2. Under pure adiabatic conditions, these definitions lead to the same result, however, when heat losses play an important role (at low strain rates or at high temperatures) the values reported by each definition could differ notably.

The temperature rise directly influences the performance of the thermomechanical test as it affects the flow curve of the material (Chrysochoos et al., 1989). In addition, the adiabatic temperature rise may not only affect the mechanical properties of the material but also the material microstructure during the tests, as stated by Feng et al., 2014.

Therefore, the control and knowledge of this temperature rise (caused by the adiabatic self-heating) is a key aspect on the performance of the thermomechanical characterization and to develop any accurate FEM model.

Several attempts were found in literature aiming to measure adiabatic self-heating. According to Zhao, 1993, the temperature variation during a compression test is a result from the combination between the heat generated by plastic deformation, the heat produced due to friction and the heat loss through conduction between the sample and the dies. This approach was tested at 300°C in a wide range of strain rates. It was stated that the heat generated by friction is negligible. In the study, heat losses due to radiation and convection were assumed to be negligible, which, at high temperatures, could lead to a bad estimation of the temperature.

Rittel et al., 2017 characterized the adiabatic self-heating for different materials, strain rates and load modes at room temperature. In spite of the comprehensive study carried out, heat losses such as conduction were not included in the analysis, which

could explain the low values of adiabatic self-heating obtained at these elevated strain rates. The adiabatic self-heating was directly determined according to the temperature measurements, that is, β_2.

Kapoor and Nemat-Nasser, 1998 employed infrared images to determine the adiabatic heating taking into account also conduction heat losses in a one dimensional analysis. In addition, they measured that the amount of stored energy was not higher than 5% and most of the applied energy was transformed into heat, as expected, especially at high strain rates. The tests were done at room temperature, so the effect of temperature on adiabatic self-heating was not analysed.

Bonk et al., 2016 performed tensile tests in a vacuum chamber to avoid convection losses, and, therefore, they only needed to take into account conduction and radiation. The temperature was measured through different K-thermocouples distributed along the region of interest. Similar approach was taken by Knysh and Korkolis, 2015 avoiding the necessity of controlling what was happening outside the region of interest. The temperature was measured with an infrared camera whereas Digital Image Correlation was used to determine possible heat losses due to mass flux. The method is based on the uniaxial tension test of a long, slender rod applying a one dimensional approach. However, both approaches were carried out at low strain rates, typical from tensile tests but far different from industrial conditions. In addition, it was demonstrated that neglecting heat losses such as conduction and radiation during the process leads to an underestimation of the adiabatic self-heating, as the temperature gradually increases during deformation process.

One of the main aspects with regard to adiabatic heating is the strain rate. When this strain rate is low, usually lower than 0.001 s^{-1}, the process could be assumed as isothermal as there is enough time to dissipate the heat. Contrary, at higher strain rates, higher than 10 s^{-1}, the process can be assumed nearly adiabatic. In the intermediate regime, the process is neither adiabatic nor isothermal, being necessary the characterization of this phenomenon (Mataya and Sackschewsky, 1994; Knysh and Korkolis, 2015).

Also, the temperature is an aspect to be taken into consideration (Oh et al., 1992; Goetz and Semiatin, 2001) as higher temperatures imply higher heat losses, directly influencing adiabatic self-heating. Therefore, a proper way to characterize it in this regime would be needed.

Likewise, Rittel et al., 2017 demonstrated the dependence of this parameter on the loading mode and the material. It was also stated that even at strain rates higher than 1000 s^{-1}, β_2, could be far different from 1.

Although both definitions of adiabatic self-heating are acceptable, it is necessary to establish a proper way to characterize it. In literature, both definitions are used indistinctly, which could lead to misunderstandings and totally different values. For this reason, very different values could be found in literature with regard to this parameter as Table 2.1 shows, focused on Ti6Al4V.

Table 2.1: Different values of adiabatic self-heating found in literature for Ti6Al4V under different conditions. Tests carried out at room temperature

Load mode	Strain rate (s^{-1})	Def.	β	Reference
Shear	460	β_2	0.2-0.7	Macdougall and Harding, 1998
Compression	3000	β_2	0.5-1.0	Mason et al., 1994
Compression	3000	β_2	0.4	Rittel and Wang, 2008
Compression	2000	β_2	0.4-0.5	Rittel et al., 2017
Tension	1500-3400	β_2	0.3-0.4	Rittel et al., 2017
Shear	2800-7000	β_2	0.4-0.5	Rittel et al., 2017
Tension	500-7000	β_2	0.5-0.6	Smith et al., 2019
Tension	0.001-0.01	β_1	0.6-0.9	Knysh and Korkolis, 2015
Compression	1-50	β_1	0.9-0.98	Bruschi et al., 2004

Summarizing, although adiabatic self-heating was experimentally measured by different researchers, no agreement was found between them. In addition, the majority of the tests were made at room (or low) temperatures although it was demonstrated that it can notably vary with temperature due to the increase on heat losses (Goetz and Semiatin, 2001). Regarding the techniques employed on the adiabatic self-heating characterization, thermal imaging or thermocouple measurements are the most widely used. However, as it was explained above, thermocouples embedded to the specimen may change the heat flux and they only allow single point measurements to be done. Thus, infrared imaging seems to be the best option. In addition, heat losses play an important role when the material is subjected to high thermomechanical loads so they should be included in the analysis.

2.2.2 *Strain and strain rate measurements*

Knowledge of strain and strain rate during thermomechanical tests is of great interest mainly by two reasons. First, strain and strain rate are important variables in order to understand the material behaviour subjected to different load modes and, second, these outcomes are valuable inputs so as to be used to validate and optimize the numerical models.

For thermomechanical characterization, equivalent plastic strain (often defined according to Von Mises criterion) is usually determined according to different analytical equations which are commonly limited by a high amount of assumptions. For instance, typical cylindrical samples, although they are the most widely used samples for material characterization, are known to suffer barreling because of the deformation process, causing the equivalent plastic strain calculated to be not accurate, at least in the external face. Similarly, Drozd et al., 2011 applied analytical equations assuming pure plane strain

conditions for a flat specimen tested on a Gleeble simulator. However, plane strain condition is only applicable into the part and not in the non constrained faces. Hor et al., 2013a determined the plastic strain of a shear sample assuming pure shear but the accuracy of this assumption was not tested.

Traditional methodologies for thermomechanical tests involving high-temperature-strain processes usually determine the strain from strain gauges and extensometers. However, these techniques suffered from spatial resolution problems and thermally induced errors (Rooyen and Becker, 2018). Also, they can be equipped with dilatometers, but they are not able to properly reproduce the plastic strain reached during the test, as it should be placed in the point where the plastic strain tends to be higher and more concentrated (Shao et al., 2018).

Therefore, it is worth considering full-field measurements as they could be helpful in further improvements of the specimen design and results and model validation. Amongst all the techniques, it is of particular interest for thermomechanical characterization the use of DIC (Tarigopula et al., 2008).

DIC is a non-contact method which allows the plastic strain to be determined by correlating two images of the same sample where a random speckle pattern was created, one deformed and the other undeformed (Khoo et al., 2016). As a principal drawback, the quality of the pattern is often inconsistent as it is highly dependent on the human operator (Lecompte et al., 2006; Bossuyt, 2013).

In Figure 2.6 the variability is shown for different patterns created by spray painting. With regard to this technique, Haddadi and Belhabib, 2008 studied, qualitatively, the errors on the measurement depending on the pattern quality. Some coarse conclusions can be drawn: (i) the addition of particles randomly spread along the previous pattern increases the accuracy of the strain measurement, (ii) a bad speckle pattern makes the correlation impossible and (iii) the use of an optimized pattern which can be printed directly could be an appropriate solution to avoid these problems.

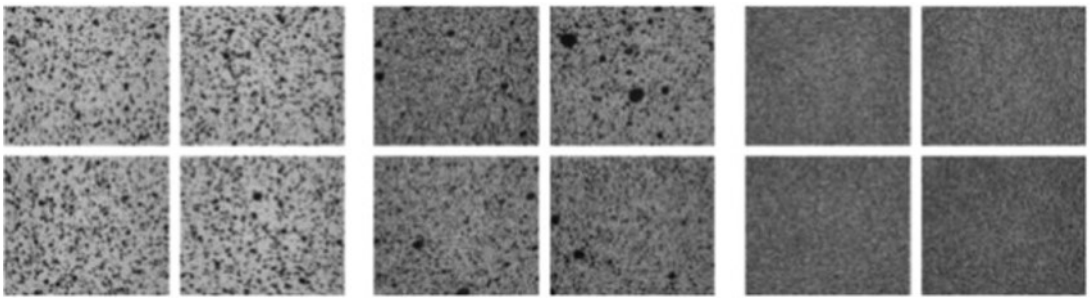

Figure 2.6: Variability of speckle patterns created by spray painting. Adapted from Bossuyt, 2013

Another aspect apart from speckle quality is the pattern size (Lecompte et al., 2006; Pottier et al., 2014). Lecompte et al., 2006 concluded that the lower the subset (or facet, that is, a portion of the pattern which is selected for tracking), the better the results were. However, the subset size should be higher enough to reproduce the expected strains.

With regard to speckle size, it is not always needed to obtain the smallest speckles as an evenly distributed speckle pattern could be enough.

To create these patterns speckle painting is a widely used technique. However, as surface painting is a very random process, different ways to create patterns appear in literature. For instance, Shi et al., 2018 presented a technique in which the graphite powder was sprayed with an airbrush and attached to the surface of specimen by means of electrostatic adsorption. To ensure a good quality of the pattern, the pressure of the airbrush, the spray angle and distance should be controlled. The main advantage of this kind of patterns is the capability of obtaining patterns with low sizes in comparison to traditional paints. Nevertheless, the pattern is very easy to be damaged, in special when it contacts other surface or a fluid.

DIC technique has been successfully employed by different researchers in thermomechanical tests. Martínez-Donaire et al., 2014 and Güler and Efe, 2018 measured strain fields for aluminum and steel alloys at room temperature by using acrylic painting to generate the pattern. However, few attempts have been found at high temperatures, due to oxidation of the sample, burning and peeling off of the painting or surface radiation which can lead to image saturation or decorrelation (Rooyen and Becker, 2018; Zhang et al., 2020).

Nevertheless, some authors have overcome these problems. For instance, Shao et al. (Shao et al., 2016; Shao et al., 2018) measured strain fields in aluminum up to 500°C by using a high temperature painting. In addition, ceramic coatings and cobalt oxide painting were employed to measure strain fields up to 1200°C in nickel alloys (Novak and Zok, 2011). Sakanashi et al., 2017 employed a commercially available heat-resistant paint to carry out measurements up to 500°C in stainless steel. Koohbor et al., 2016 developed a 3D-DIC methodology to characterize stainless steel properties up to 1200°C based on flat specimens.

Therefore, a proper technique to measure equivalent plastic strain is necessary so as to provide reliable experimental data to carry out the material characterization and the model validation. In addition, strain measurements at high temperatures is still a challenge and more investigation is needed in this field.

2.2.3 *Examples of inverse simulation in machining*

Although the obtained material laws obtained based on thermomechanical tests could not be representative enough of the material behaviour under real machining conditions, they could be employed as a valuable input in an inverse simulation approach. This technique optimizes the material parameters based on the experimental values obtained from real machining tests according to a predefined objective function.

Several attempts can be found within the machining field employing inverse simulation trying to optimize material laws. Pujana et al., 2007 or Shrot and Bäker, 2010 aimed to characterize the flow behaviour of the material based on machining tests and simulations.

They carried out a sensitivity analysis varying different parameters in Johnson and Cook (JC) and Zerili-Armstrong laws. For instance, Shrot and Bäker, 2010 analysed the effect of JC constants on cutting force predictions. Cutting force was proved to be accurately predicted regardless of the set of JC parameters used. This can be seen in Figure 2.7.

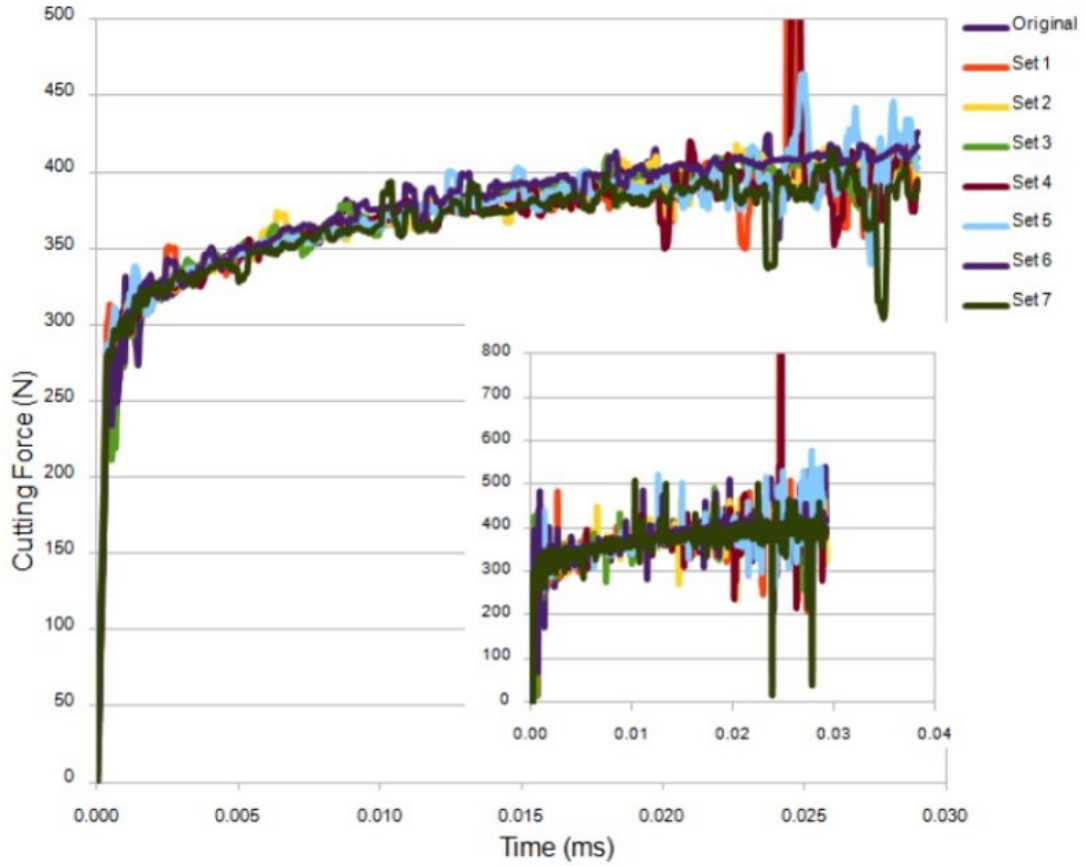

Figure 2.7: Cutting force prediction with different values of JC parameters. Adapted from Shrot and Bäker, 2010

Based on this analysis, it can be stated that a high degree of accuracy on cutting force predictions could not be used as unique input to validate the material characterization. Furthermore, it was demonstrated the difficulty of characterizing the material behaviour based only on inverse analysis and machining simulations as this analysis could lead to non-realistic physical values of the material parameters. To ensure the results, more variables should be taken into consideration in the analysis. Also Hardt et al., 2021 carried out an inverse analysis in AISI 1045, demonstrating the non-uniqueness of the machining process and the necessity of proper lower and upper limits in order to keep the physics of the process in the analysis.

In spite of this statement, Shrot and Bäker (Shrot and Bäker, 2011; Shrot and Bäker, 2012) proposed an inverse method aiming to optimize the flow stress parameters according to JC law. Apart from cutting force, they also took into account chip morphology in the inverse procedure.

Sartkulvanich et al., 2004 carried out an inverse simulation approach based on Oxley predictive model (Oxley, 1989). Oxley theory was employed to predict cutting forces, average temperatures and other machining outcomes such as chip thickness, shear plane length or the thickness of the secondary shear zone. For the characterization, different flow stress models were applied, which are modifications of the JC law for each specific material. After the optimization, they saw that feed force was not predicted, with prediction errors higher than 40%. Therefore, optimizing only the flow stress law may not be optimum solution.

Daoud et al. (Daoud et al., 2015a; Daoud et al., 2015b) proposed a flow stress law dependent on the rake angle for different aluminum alloys. As it is known, the rake angle is one of the most influential parameters in machining, causing notable changes in cutting forces, strain fields or temperatures (Daoud et al., 2015b; Harzallah et al., 2020). Nevertheless, although the obtained law could report accurate values of different machining outcomes such as cutting forces or chip geometry, it is neglecting the physical meaning as material parameters could not be dependent on the tool employed.

A similar approach was employed by Malakizadi et al., 2016 for different materials (Inconel 718, AISI 1080, Al6082-T6) to enhance flow stress law parameters based on Oxley theory, taking into consideration cutting forces, chip thickness and tool-chip contact length. It was shown that the JC material parameters obtained through traditional thermomechanical testing devices could lead to poor predictions.

Klocke et al., 2013 used inverse identification with AISI 1045 and Inconel 718. They assumed a material behaviour according to JC law, and, in order to simplify the analysis, they established that the constants A, B and n (material flow stress parameters of the JC law) could be assumed to be accurate enough as they were obtained through quasi-static thermomechanical tests. Moreover, to reproduce chip segmentation, the Cockcroft and Latham damage criterion was also included in the inverse analysis. The optimization was based on cutting force and chip geometry. The approach systematically compares cutting results from machining tests with simulation results and interpolates the material parameters to fit these results, always taking into account the physical sense of the optimized parameters. The results were in agreement with the experiments as can be seen in Figure 2.8. However, more segmentation was observed in the model than in the experimental test, showing the relevance of having a proper characterization of the damage law.

Franchi et al., 2017 proposed an inverse method to determine not only the flow stress parameters but also the fiction coefficient according to the Coulomb law. Apart from cutting forces, they employed the cutting temperature in the shear zone as an input in the optimization. This variable is a very important outcome of the machining process which

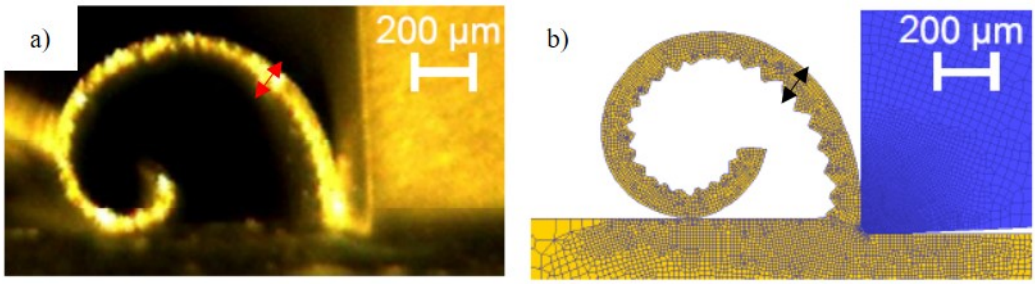

Figure 2.8: Chip morphology obtained during an orthogonal test of Inconel 718. a) Experimental chip morphology (high speed video image). b) Predicted chip morphology after inverse simulation. Adapted from Klocke et al., 2013

is usually not taken into consideration in this kind of analysis as its correct measurement is still a challenge (Cotterell et al., 2013) as it will be discussed in the following section.

Zhang et al., 2018 or Thimm et al., 2019 linked the use of the DIC technique with inverse identification for orthogonal cutting. Zhang et al., 2018 employed low cutting speeds in order to reduce as much as possible thermal effects on flow stress, simplifying thus the amount of parameters to optimize. The quantities used for the inverse analysis were the cutting forces, shear angle and the velocity field.

To sum up, Table 2.2 summarizes the materials commonly used in the analysis and the aim of the inverse approach: flow stress law, damage law or friction behaviour.

Table 2.2: Main materials employed for inverse simulation in orthogonal machining and the optimized law: FS = Flow stress law; D = Damage law; Fric. = Friction law

Ref.	Material	FS	D	Fric.
Shrot and Bäker, 2012	AISI 52100	✓	✗	✗
Agmell et al., 2014	AISI 4140	✓	✗	✗
Pujana et al., 2007	42CrMo4, 20NiCrMo	✓	✗	✗
Sartkulvanich et al., 2004	AISI H13, AISI 1045, AISI P20	✓	✗	✗
Daoud et al., 2015a	Al2024-T3, Al6061-T6, Al7075-T6	✓	✗	✗
Malakizadi et al., 2016	Inconel 718, AISI 1080, Al6082-T6	✓	✗	✗
Klocke et al., 2013	Inconel 718, AISI 1045	✓	✓	✗
Hardt et al., 2021	AISI 1045	✓	✗	✗
Franchi et al., 2017	SAF 2507, AISI 316	✓	✗	✓
Zhang et al., 2018	Al6061-T4	✓	✗	✗
Zhang et al., 2019	NAB Alloy	✓	✗	✗
Razanica et al., 2020	Inconel 718	✓	✓	✗
Thimm et al., 2019	AISI 1045	✓	✗	✗

As can be seen, the majority of the works presented above are usually focused on optimizing the flow stress law, not taking into account other relevant aspects such as friction or damage law, widely important in case of segmented chips. Only Klocke et al., 2013, or, recently, Razanica et al., 2020 took into account the damage law in the analysis and Franchi et al., 2017 the friction coefficient.

Ortiz de Zarate et al., 2019 proved that, for orthogonal cutting of Ti6Al4V, regardless of the flow stress law chosen, the predictions where only accurate when the flow stress law was properly coupled with a damage law. Furthermore, Ortiz de Zarate et al., 2020 or Yaich et al., 2020 carried out a comprehensive sensitivity analysis showing the relevance of a proper ductile failure characterization to carry out accurate machining predictions. Nevertheless few studies were found aiming to optimize the material characterization behaviour by using inverse simulation in Ti6Al4V, see, for instance, Ulutan and Özel, 2013 which was not included in Table 2.2 as it was based on face turning.

Moreover, the research works mentioned above are usually based on machining outcomes such as cutting forces, chip morphology, shear angle or tool-chip contact length. Other important outcomes are often not taking into consideration such as temperature in the shear zone, plastic strain or strain rate (the main variables employed are summarized in Table 2.3). In addition, these variables could vary depending on the position.

Table 2.3: Main variables employed for inverse simulation in machining: F_c-F_f = Cutting and feed force; T_{sz} = Temperature in the shear zone; h_c = Chip thickness; ϕ = Shear angle; l_c = Tool-chip contact length; ε_{eq} = Equivalent plastic strain in the shear zone, usually taken as an average value along the shear plane; T_{ch} = Chip temperature; T_{tool} = Tool temperature; t_{sz} = Thickness of the shear zone

Ref.	F_c-F_f	T_{sz}	h_c	ϕ	l_c	ε_{eq}	Other
Shrot and Bäker, 2012	✓	✗	✓	✗	✗	✗	✗
Agmell et al., 2014	✓	✗	✓	✗	✗	✗	✗
Pujana et al., 2007	✓	✗	✓	✓	✓	✗	T_{tool}
Sartkulvanich et al., 2004	✓	✗	✗	✗	✗	✗	t_{sz}
Daoud et al., 2015a	✓	✗	✓	✗	✗	✗	✗
Malakizadi et al., 2016	✓	✗	✓	✗	✓	✗	✗
Klocke et al., 2013	✓	✗	✓	✗	✗	✗	✗
Hardt et al., 2021	✓	✗	✓	✗	✗	✗	T_{tool}
Franchi et al., 2017	✓	✓	✗	✗	✗	✗	✗
Zhang et al., 2018	✓	✗	✗	✓	✓	✗	✗
Zhang et al., 2019	✓	✗	✗	✗	✗	✓	✗
Razanica et al., 2020	✓	✗	✓	✗	✓	✗	✗
Thimm et al., 2019	✓	✗	✗	✗	✗	✓	✗

Summarizing, the experimental knowledge of these outcomes would be relevant to improve the optimization algorithms, but, nowadays, temperature in the shear zone, strain and strain rate measurements during machining are still a challenge. Therefore a proper way to measure these outcomes is necessary in order to generate robust experimental data to validate and optimize the material laws.

2.3 TEMPERATURE MEASUREMENT IN MACHINING

Temperature measurement is a great challenge in machining because of the difficulties on measuring temperatures close to the cutting edge or along the shear zone. In addition, heat generation during metal cutting is an important factor to be known as it directly affects machining performance in terms of wear, reducing tool life or surface integrity (Komanduri and Hou, 2001; Cotterell et al., 2013), especially when cutting low thermal conductivity materials such as titanium alloys.

Temperature in the primary shear zone affects mechanical properties of workpiece material whereas the elevated temperatures reached in the secondary shear zone result in higher tool wear. However, the experimental data available is notably low, although several attempts have been made, due to different aspects such as, (i) limited access to the measuring region, (ii) the heat is concentrated in a low portion of the workpiece and the tool, (iii) the measuring point is a moving area and (iv) the thermal gradient is high (Al Huda et al., 2002).

To attain this goal, some solutions have been tested in literature, being the most commonly employed thermocouples and infrared measurements (thermal cameras and pyrometry).

In the review presented by Davies et al., 2007 it is stated that thermocouples, because of their complexity and the difficulties in reducing the uncertainties, could be a good tool when a qualitative study is needed. However, thermocouples can not be employed to measure workpiece temperature in the shear zone during cutting although they could be useful to estimate the heat flow between tool and workpiece.

This technique was employed by some authors such as Hong and Ding, 2001, who integrated a thermocouple flush in the insert rake face in order to validate the model and to investigate the effect of the cryogenic cooling.

O'sullivan and Cotterell, 2001 measured the temperature during orthogonal turning of Al6082-T6 by welding two thermocouples to the workpiece being cut. However, the thermocouples should be far enough from the insert so as not to be expelled from the workpiece, reporting temperatures notably lower than the ones actually reached in the shear zone.

In short, tool-work thermocouples are widely employed to measure the cutting temperatures in the interface between the tool and the chip. While this technique is easy to apply, it only enables the determination of the average temperature over all contact

area. However, as was previously mentioned in Section 2.2, thermocouple technique is an intrusive method which could influence the heat flow.

With regard to infrared imaging, Dinc et al., 2008 used infrared thermography demonstrating its capability of measuring tool thermal fields by validating the analytical approach proposed in the research work. Soler et al., 2015 proved that the uncertainty associated with this way of measuring temperatures could be reduced to 15%, especially at low temperatures, near 500°C and about 8% for temperatures close to 1000°C. Thermal fields in the tool were also measured by Saez de Buruaga et al., 2018 for orthogonal turning of different steels. An example is shown in Figure 2.9.

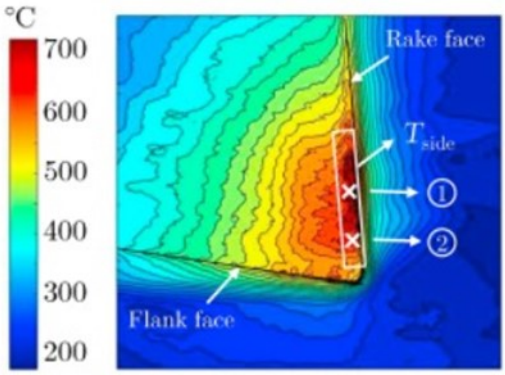

Figure 2.9: Tool thermal fields during orthogonal cutting. Adapted from Saez de Buruaga et al., 2018

Although infrared technique is widely employed to measure tool temperature, few attempts could be mentioned aiming to measure workpiece temperature in the shear zone. Franchi et al., 2017 employed infrared technique to measure maximum workpiece temperature in the shear zone. However, the measurements were carried out with the objective located far from this shear zone, being difficult to establish whether the maximum temperature reported represents tool, chip or workpiece, as can be seen in Figure 2.10. In addition, the methodology employed to calibrate the emissivity, based on a sample progressively heated without deformation could not be representative of the real emissivity reached during the process, as the extreme strain and strain rates reached could influence the emissivity.

It is worth highlighting that, recently, Harzallah et al., 2020 published an interesting work in which thermal fields in the shear zone during orthogonal cutting of Ti6Al4V were reported. They showed the temperature variations and the effect of relevant input parameters such as cutting speed or rake angle, but few more attempts could be found in literature.

To sum up, infrared imaging shows the main advantage in the fact that it is a non-intrusive technique and allows thermal fields to be measured. However, the emissivity of the body and chip-obstruction could be the main drawbacks. In addition, few attempts

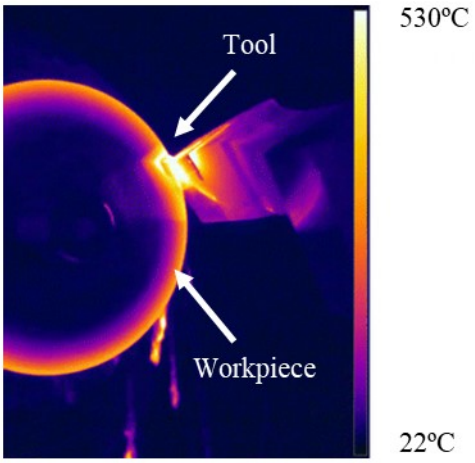

Figure 2.10: Example of workpiece temperature measurement during orthogonal cutting of AISI 316. Adapted from Franchi et al., 2017

were found aiming to measure temperature in the shear zone, because of the extreme conditions reached in the machining process, which hampers the measurement.

Double wavelength fiber optic pyrometers are other widely used technique for measuring temperatures. The technique uses the ratio of optical powers at different spectral bands to implement a self-referencing technique, avoiding emissivity problems (Komanduri and Hou, 2001; Tapetado et al., 2016). The use of optical fibers enables the measurement of the temperatures in very localized areas with a spatial resolution limited by the numerical aperture and the dimensions of the fiber. The measured temperature does not depend on the distance between the fiber end and the target. In addition, pyrometers employ low-loss optical components designed for telecommunications purposes in order to reduce the temperature errors. However, like thermocouples, thermal fields can not be measured with this technique.

Other earlier attempts can be found in the literature trying to measure temperatures during cutting (da Silva and Wallbank, 1999; Longbottom and Lanham, 2005). For instance, Dearnley, 1986 proposed a metallographic technique. It is widely known that microstructure analysis of machining parts reveal a heat affected zone. A clear relationship between microstructure and temperature measurements was shown by Medina-Clavijo et al., 2018. The boundary of the heat affected zone could be taken as an isotherm that could be employed for temperature estimation during cutting.

Similarly, the temperature distribution could be estimated based on hardness measurement variation with workpiece depth (Smart and Trent, 1975; da Silva and Wallbank, 1999). However, it is necessary to previously calibrate the dependence between the temperature and the hardness. It is assumed that the accuracy of the predictions, according to da Silva and Wallbank, 1999, would be around $\pm$ 25°C.

Kato and Fujii, 1996 proposed the use of thermosensitive painting. The idea lies in the fact that, at an specific temperature, the paint suffers a chemical reaction and these changes could be employed to estimate the temperature. In addition, low melting point PVD particles could be also spread along the surface to be measured. After cutting, the boundaries between the melted and un-melted materials act as a qualitative indicator of the temperature (Longbottom and Lanham, 2005).

Other possible techniques are also reported in the review presented by Longbottom and Lanham, 2005. One of the earliest approaches was the calorific method. The idea is to submerge the piece to be measured into water so as to measure the water temperature rise. However, because of the high temperatures reached during cutting, the piece would cool before being submerged.

2.4 STRAIN AND STRAIN RATE MEASUREMENTS IN MACHINING

Knowledge of the plastic strain reached during the machining would be of great interest to understand more in depth the material behaviour under machining conditions and as input to validate the numerical models. However, the measurement of strain and strain rate during a real machining process is still a challenge Zhang et al., 2019.

Different researchers aimed to measure strain and strain rate under real machining conditions based on the DIC methodology, explained in Section 2.2. Baizeau et al., 2017 studied different ways of creating the pattern, comparing etched or blasted specimens with different pressures, the specimens subjected to dissimilar preparation procedures did not show differences concerning correlation. However, the blasted surface at 1 bar reported the most accurate results.

To avoid size problems, image correlation employing microstructural based patterns could be a solution (Ghadbeigi et al., 2010). This analysis needs a surface treatment to reveal the microstructure (polishing and etching), and it is employed, in general, at very low scales. Recently, Harzallah et al., 2020 employed material microstructure as a random speckle pattern for Ti6Al4V, avoiding decorrelation problems up to 15 m/min. As an example, Figure 2.11 shows the evolution of the strain rate field during orthogonal cutting of Ti6Al4V at 15 m/min.

Pottier et al., 2014 used DIC technique to study chip segmentation process when machining Ti6Al4V. The tool rake angle was fixed to zero degrees, whereas the width of cut and the feed were 3 and 0.25 mm, respectively. This selection is based on the necessity of a large shear zone, trying also to reduce as much as possible out of plane displacements keeping the width to feed ratio higher than 10 (see Section 2.1). The cutting speed was set to 6 m/min, ensuring serrated chips representative of machining of titanium alloys.

Zhang et al., 2017 proposed a new methodology based on DIC to obtain the cutting stress field based on strain measurements. The workpiece material for the tests was Al 7075-T651 whose surface was grounded to remove the oxide layers. For the observations, the side surface was polished using grit SiC paper followed by sandblasting in order to

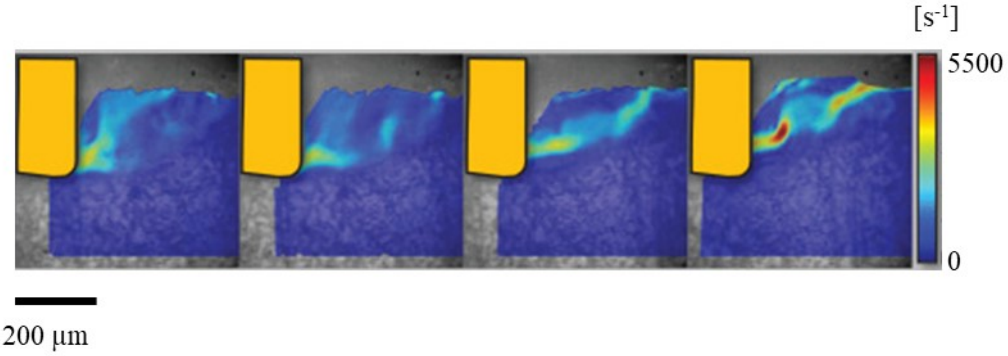

Figure 2.11: Strain rate field at different cutting times in orthogonal cutting of Ti6Al4V at 15 m/min and $f = 0.25$ mm. Adapted from Harzallah et al., 2020

generate random irregularities. Finally, regarding cutting conditions, the rake angle was set to 20 degrees. In addition, the cutting speed was lower than 0.5 m/min to facilitate the filming and to reduce as much as possible thermal effects.

Although the materials used are close to industrial environment, the conditions analysed are often far different from the industrial ones.

However, Zhang et al., 2019 proposed the use of a mechanical pattern, generated by grinding, and they proved the capability of DIC technique of measuring strain at industrial cutting speeds when cutting NAB alloy as shown in Figure 2.12. Thimm et al., 2019 also used digital image correlation to carry out inverse simulation at high cutting speeds (up to 160 m/min). Both employed continuous chip materials.

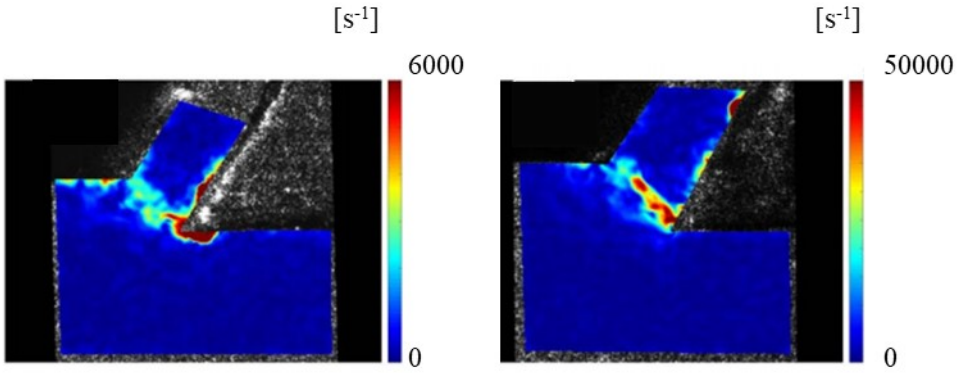

Figure 2.12: Strain rate field under different cutting conditions during orthogonal cutting of NAB alloy. Left: $v_c = 30$ m/min and $f = 0.1$ mm; right: $v_c = 150$ m/min and $f = 0.15$ mm. Adapted from Zhang et al., 2019

Apart from DIC techniques, other options appear in literature aiming to measure plastic strain fields during a machining process. The Particle Image Velocimetry (PIV) is

a technique which computes the velocity field by tracking the motion of different particles to determine strain and strain rates as shown in Figure 2.13.

This technique needs a very high density seeding with almost no gap between adjacent particles (Gnanamanickam et al., 2009). Nevertheless, it is worth mentioning that when the density of asperities is low, they could be individually tracked to determine their displacement field. For the specific case of machining, the particles to be tracked are asperities created on the surface. However, this technique is still limited to very low cutting speeds, usually lower than 1 m/min.

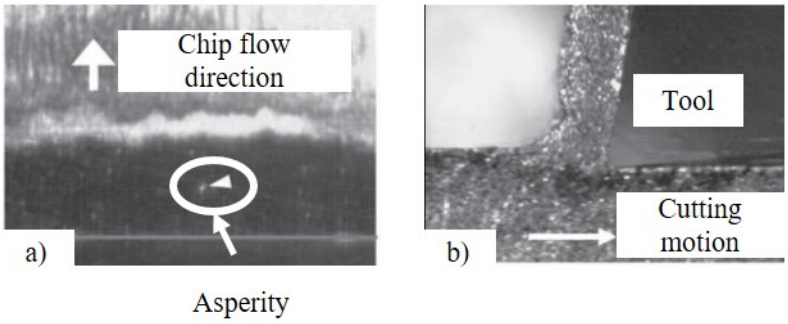

Figure 2.13: Example of density of asperities for a machining cases: a) Low density of asperities. b) High density of asperities. Adapted from Lee et al., 2006

Asperities in the workpiece can scatter light significantly different than the surrounding regions, causing traditional DIC algorithms to fail. However, they can be tracked to estimate the strain field. These asperities are created by roughening the workpiece with grit silicon carbide abrasive paper, for example, similar to the method explained in Zhang et al., 2019. This roughening generates a high density of asperities that are easily discernible in sequences of images (Lee et al., 2006).

Guo et al., 2011 used and improved the PIV technique to study the deformation process on machining. They studied the influence of process parameters on the state of the machined surfaces. For this reason, the trajectories of different particles were tracked and this enabled the deformation histories of the chip and machined surface to be characterized.

Out of plane displacements could cause the loss of focus and decorrelation problems and continuous chips are also preferable to carry out the measurements properly. That is why, 70Cu-30Zn brass, commercially pure copper and commercially pure titanium were used with a rake angle of 20 degrees. An example for the brass case is shown in Figure 2.14.

PIV technique was also used by Guo et al., 2015 to analyse flow dynamics and strain fields in cutting. This analysis allowed the effect of different parameters like cutting speed or rake angle on chip formation and chip geometry to be determined.

The research works presented above are focused on easy to cut materials and cutting conditions far different from the real ones reached in the industry. The cutting speed

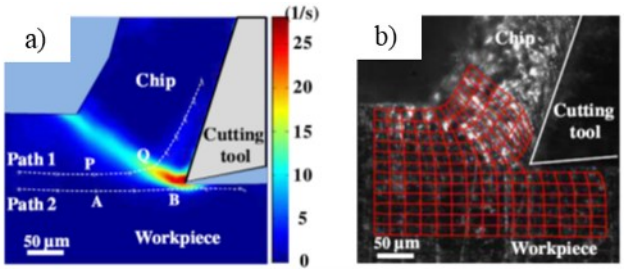

Figure 2.14: a) Strain rate field for brass machining with PIV measurements. b) Equivalent grid distortion. Adapted from Guo et al., 2011

is always kept too low in order to avoid thermal effects and to facilitate the filming. In addition, the materials analysed are usually known for their ductility, generating continuous chips which do not represent industrial purposes.

The limitations of DIC/PIV techniques usually to low cutting speeds and, especially, continuous chips (conditions mostly tested in literature) are due to technical limitations rather than the technique itself. In general, higher cutting speeds imply no enough illumination, no enough spatial resolution and decorrelation problems. In order to record the process at higher cutting speeds, higher frame rates are needed (which means lower fields of view).

The strain of a surface can be also obtained by measuring the distortion suffered by a grid (Jeelani and Ramakrishnan, 1982), usually comparing two images of the undeformed and the deformed grid, similar to the measurement protocol followed for DIC measurements. The accuracy of the method is highly conditioned by grid spatial resolution.

The use of grids is not new and it is widely accepted for measuring strain in mechanical processes. For instance, one of the earliest attempts was carried out by Stevenson and Oxley, 1969. This technique, in general, has some advantages as:

- The grid is an integral part of the surface and with mechanical grids decorrelation problems are avoided.
- The grid reproduces the plastic deformation of the surface faithfully.
- High strains can be analysed reducing the size of the grid. Nevertheless, the grid size should be higher enough to be able to reproduce the expected strains.
- As the plastic strain is much higher than elastic one, the grid can be used to measure permanent displacement fields.

The grid can be generated on the surface by different ways such as mechanical method, microgrid deposition, photo-resist method or electron-lithographic technique.

- Electron-lithographic technique: the process is as follows (Karimi, 1984; Ghadbeigi et al., 2008):

1. An electro-sensitive resin is deposited on the surface. Then, the coated sample is heated to promote the adhesion of the resin.
2. The resin is irradiated with an electron beam from the Scanning Electron Microscope (SEM), following the pattern required.
3. The lines of irradiated resin are removed using a special solvent.
4. The exposed metal is electro-etched to create the lines along the irradiation paths.
5. The remaining resin is removed with a chemical agent.

All these steps are summarized in Figure 2.15.

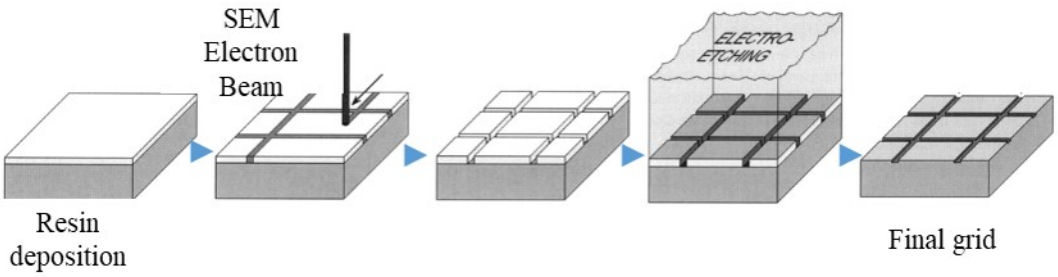

Figure 2.15: Steps followed to create a microgrid via electron-lithographic technique. Adapted from Karimi, 1984

The importance of this grid technique in comparison to others lies on its capability of being applied at high temperature. In addition, micro-scale deformations could be determined by generating the proper high dense grid.

Figure 2.16 shows the final state of a grid using this technique for an aluminum alloy Al5182, with a 10x10 μm microgrid and a cutting speed of 40 mm/s.

- Photo-resist method (Lee, 1984; Schnur and Lee, 1984): The surface of the workpiece is exposed to ultraviolet light through a photographic negative of the grid pattern. Although electron-litographic technique can be used at high temperatures, photo-resist methods are commonly used for cutting applications where strain may be highly localized as happens in machining process. This is especially used when only a qualitative study is needed as it is not possible to generate high dense grids. Examples of different grid states after the machining process with grid created by photo-resist method are shown in Figure 2.17.

- Mechanical methods: there are some mechanical methods which can be used to develop a grid pattern on the workpiece surface. For instance, Jeelani and Ramakrishnan, 1982 used a rotatory microtome. The technique consists of an indenter which reciprocates vertically the pattern. The edge of the indenter is kept perpendicular

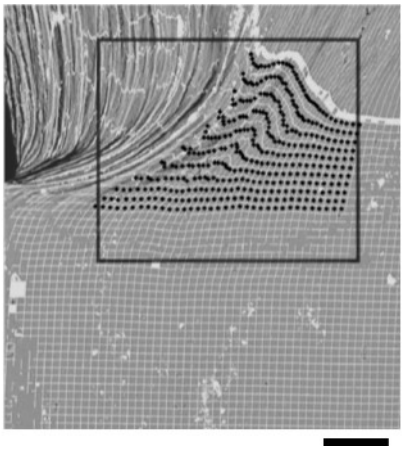

Figure 2.16: Grid state after orthogonal cutting of Al5182 with a microgrid in the workpiece. Two specimens were clamped together to ensure plane strain and to freeze the cutting process. Scale bar: 80 µm. Adapted from Ghadbeigi et al., 2008

to the forward motion of the tool holder. Other possible option is the use of laser printing, as stated by Pujana et al., 2008. One of the main advantages of the mechanical methods lies in the fact that the grid is a properly part of the surface, avoiding possible decohesion problems.

These methods do not need any special equipment as the measurements could be made after the machining test in a quick stop test. Therefore, it could be a good method to measure the final strain state (not the strain history). A proper method to generate the grid would be needed, easier than the ones reported in the literature. In addition, the necessity of ensuring plane strain conditions leads to the needed of designing a set-up able to reproduce these conditions in order to be comparable with numerical 2D models of orthogonal cutting.

To sum up, Table 2.4 summarizes the main research works found aiming to measure plastic strain during orthogonal machining.

Summarizing, the majority of the studies related to plastic strain measurements are focused on easy to cut materials which tend to create continuous chips whereas segmented chips are barely analysed. In addition, plane strain conditions representative of the orthogonal cutting process are not always ensured, strain measurements being influenced by out of plane displacements. Therefore, the development of a proper technique to determine plastic strain under plane strain conditions of materials which tend to create segmented chip such as Ti6Al4V would be of great interest in order to understand more in depth the material behaviour under real machining conditions.

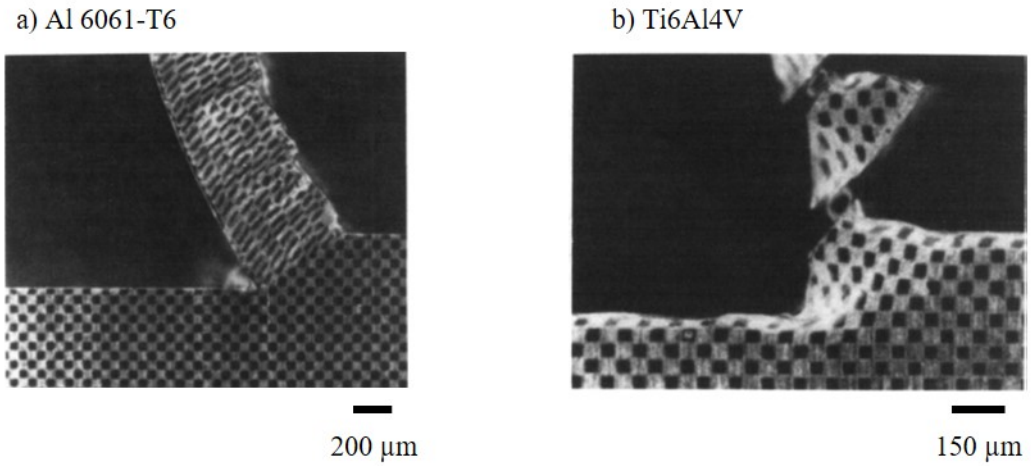

Figure 2.17: Examples of grids created by photoresist method. a) Al 6061-T6. b) Ti6Al4V. Adapted from Schnur and Lee, 1984

2.5 SURFACE INTEGRITY

Knowing the final state of the generated surface (surface integrity) is of considerable relevance to properly understand the differences on material behaviour under dissimilar conditions. Therefore, throughout this section, a brief overview of surface integrity is first given, then the analysis is focused on subsurface damage, taking into consideration the different ways of measuring it and the effects that different machining inputs (cutting conditions, workpiece and tool material) could have on it.

Surface integrity condition directly influences the part life and it is especially associated with fatigue life and corrosion problems, inducing the initiation of surface cracks and residual stresses (Ulutan and Ozel, 2011). The scheme of a machined surface is shown in Figure 2.18. Surface integrity can be characterized according to their topographical or metallurgical aspects and its mechanical state. Therefore, surface integrity can be mainly divided in (i) surface roughness, (ii) residual stresses and (iii) material surface damage.

1. Surface roughness is one of the most commonly used parameters to characterize the machined surface of any manufactured part (Novovic et al., 2004). This parameter is usually defined as the average value (R_a) or the peak value (R_t), and it is very variable depending on the machining process (Davim et al., 2009). Another significant parameters are the valley (R_v) or the distance between the peak and the valley (R_z) (Tekçe et al., 2018). A schematic representation of the main parameters defining the surface roughness is shown in Figure 2.19.

2. Residual stresses are the stresses that still are in the material once the workpiece has been liberated from the thermomechanical load applied during machining. These

Table 2.4: Research works related to strain and strain rate measurements with their characteristics. Segm. = Segmented chip; Cont. = Continuous chip. The v_c column represents the maximum cutting speed reported in the research work

Ref.	Tech.	Material	v_c (m/min)	Chip	Plane strain
Pottier et al., 2014	DIC	Ti6Al4V	6	Segm.	✗
Harzallah et al., 2020	DIC	Ti6Al4V	15	Segm.	✗
Baizeau et al., 2017	DIC	Al7020-T6	90	Cont.	✗
Zhang et al., 2017	DIC	Al7075-T6	0.5	Cont.	✗
Thimm et al., 2019	DIC	AISI 1045	160	Cont.	✗
Zhang et al., 2019	DIC	NAB Alloy	180	Cont.	✗
Gnanamanickam et al., 2009	PIV	Al6061-T6	0.6	Cont.	✓
Lee et al., 2006	PIV	Cu, lead	0.6	Cont.	✓
Lee et al., 2006	PIV	Al6061-T6	0.6	Cont.	✓
Guo et al., 2011	PIV	Cu, TI	3	Cont.	✓
Guo et al., 2011	PIV	Brass	3	Cont.	✓
Guo et al., 2015	PIV	Brass	0.6	Cont./Segm.	✗
Ghadbeigi et al., 2008	Grid	Al5182	2.5	Cont.	✓
Schnur and Lee, 1984	Grid	Al6061-T6	0.05	Cont.	✗
Schnur and Lee, 1984	Grid	Ti6Al4V	0.05	Segm.	✗
Pujana et al., 2008	Grid	42CrMo4	300	Cont.	✗

stresses are supposed to be due to remanent plastic strain along the surface of the workpiece and thermal effects (Ulutan and Ozel, 2011). Residual stresses depend on the processing and machining history of the workpiece and they are a potential risk in terms of crack initiation and propagation (Brinksmeier et al., 1982).

3. Material surface damage: the material suffers high thermomechanical loads during the process which result in high temperatures and quick cooling, high stresses and strains and high chemical energies which can cause surface defects on the workpiece. These defects can be classified into two groups. On the one hand, the material damage on the surface (or pick-ups), which include metal debris, smeared material/redeposited layer, pluckings or side flow. On the other hand, subsurface damage includes surface drag (plastic strain), white layers or cracks (Ulutan and Ozel, 2011; Yang and Liu, 2015) (the possible causes and examples of the defects are shown in Figure 2.20).

   These defects lead to a worse surface integrity condition and, thus, a worse fatigue life (Pawade et al., 2008; Zhou et al., 2012).

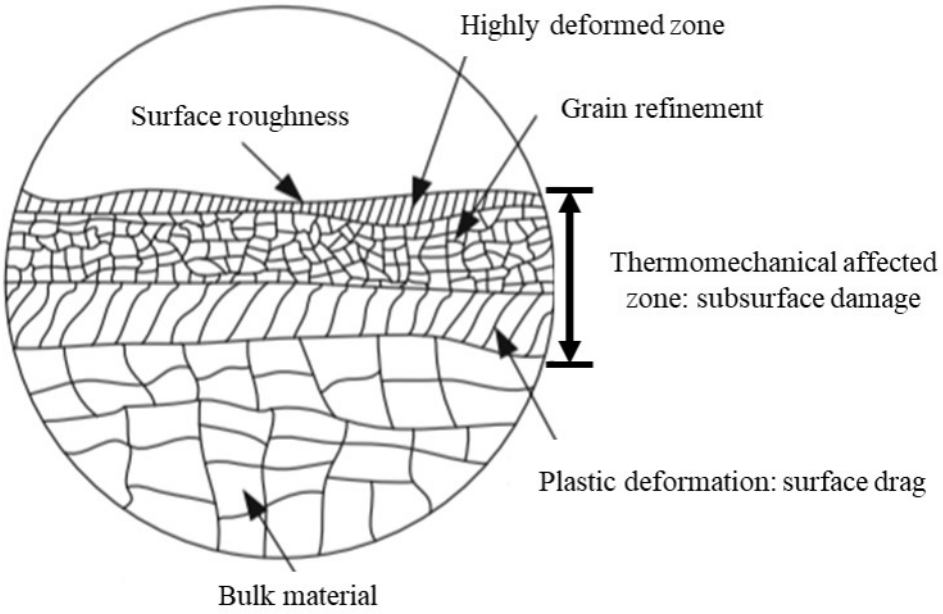

Figure 2.18: Representation of a machined surface. Adapted from Liang and Liu, 2017

2.5.1 *Subsurface damage measurements*

As mentioned above, during the machining operations, the workpiece is exposed to elevated thermomechanical loads and high chemical energies. This leads to microstructural alterations to a shallow depth from the surface that may have different thermomechanical behaviour compared to the bulk material. Such alterations could result in reducing service life (Ulutan and Ozel, 2011; Touazine et al., 2019). However, there are in literature different ways to quantify the depth of the machining affected zone, all of them reporting different results.

One of the most widely employed techniques is based on metallographic observations. One possible way is the optical measurement based on etched specimens. It is assumed that the distortions generated due to the machining operation causes changes in the workpiece which could be observed through microstructural observations. For instance, metallographic etching technique was employed by Shyha et al., 2018 to determine the machining affected zone, showing the existence of two different layers when Ti6Al4V was subjected to milling process: a highly deformed region and a moderated one. Joshi et al., 2015 carried out this analysis to study the effect of different cooling approaches on the surface integrity after orthogonal machining. Ortiz de Zarate et al., 2018 and Childs et al., 2018 used this methodology to determine the machining performance and to validate the numerical model for Ti6Al4V under broaching conditions.

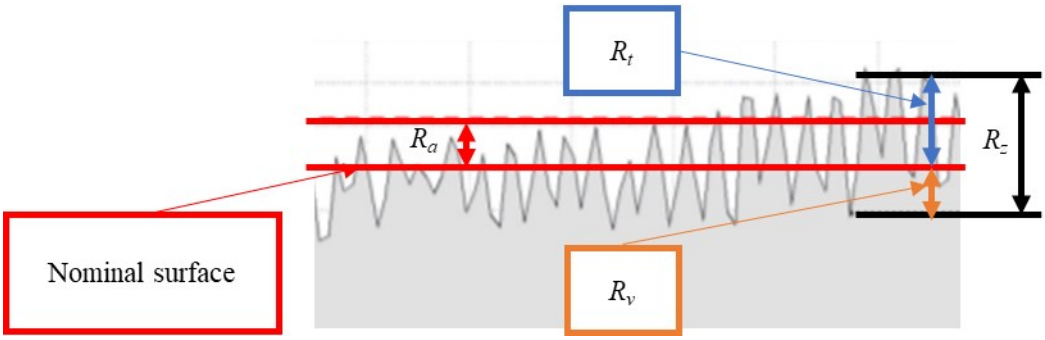

Figure 2.19: Representation of the surface roughness parameters. Adapted from Tekçe et al., 2018

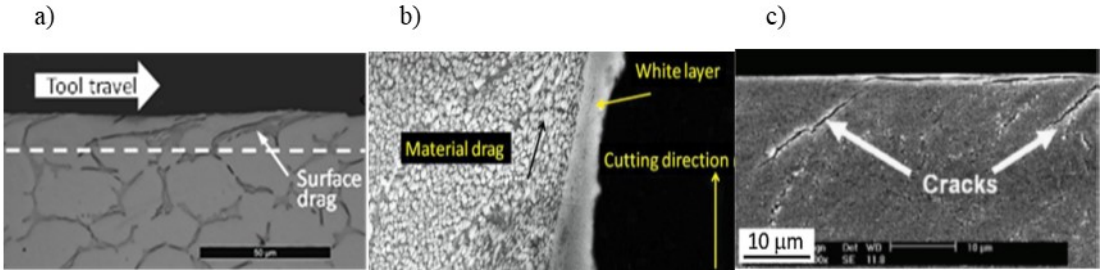

Figure 2.20: Different types of subsurface material damage. a) Subsurface damage (surface drag or plastic strain). b) White layer (diffusion). c) Cracks (excessive mechanical stresses). Adapted from Childs et al., 2018, Herbert et al., 2012 and M'Saoubi et al., 2015

These are only few examples of the application of this technique as it has been widely employed and more examples can be found in the reviews about the topic (Ulutan and Ozel, 2011; Liang et al., 2019). However, in spite of its notable acceptance, the main drawback of this technique lies in the fact that it is not possible to wholly measure the defects leading to some subjectivity in the measurements.

Apart from metallographic etching, the same principle could be followed by measuring it using a Scanning Electron Microscope (SEM), which permits higher magnification and resolution. Some examples can be found, for instance, in Ortiz de Zarate et al., 2018 or Shyha et al., 2018 for Ti6Al4V and in M'Saoubi et al., 2012 for Inconel 718.

In order to address this main drawback, average intragrain misorientation parameter, determined after a EBSD analysis, would be a possible option to quantify the subsurface damage (Liang et al., 2019). This was employed by M'Saoubi et al. (M'Saoubi et al., 2012; M'Saoubi et al., 2014), for different difficult-to-cut alloys. This technique avoids the subjectivity although it is expensive and very time consuming. The values reported through this technique are higher than the ones measured through metallographic etching, as shown in Figure 2.21.

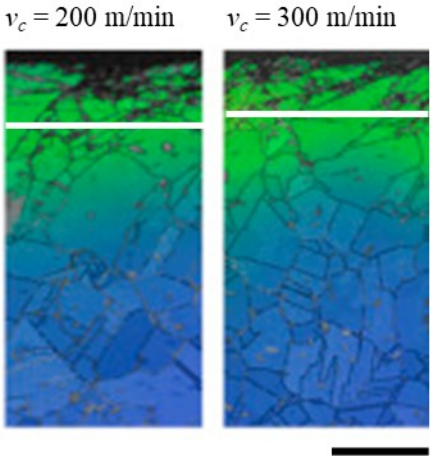

Figure 2.21: Qualitative comparison between the subsurface damage measured through metallographic etching (white line) and EBSD under the same cutting conditions (f = 0.15 mm). Scale bar: 20 µm. Adapted from M'Saoubi et al., 2012

Microhardness measurements revealed that the materials tends to be harder on the surface than on the bulk (Ulutan and Ozel, 2011). This could be an indicator of the subsurface damage. For instance, Liang and Liu, 2017, analyzing the effect of tool wear on surface integrity, showed that the values obtained through microhardness measurements were higher than with commonly used metallographic etching technique (see Figure 2.22). Touazine et al., 2019 demonstrated that this kind of measurement could be also far different from the values reported through EBSD method. It is worth noting that this technique is expected to properly reflect the mechanical alterations along the workpiece surface, however a certain degree of subjectivity remains as the applied load could report different values causing notable oscillations on the measurements.

In addition, studies of strain measurements in machining have shown that techniques such as DIC (Outeiro et al., 2015; Baizeau et al., 2016; Meurer et al., 2020), PIV (Guo et al., 2011; Jawahir et al., 2011) or grid distortion (Bailey and Jeelani, 1976; Ghadbeigi et al., 2008) could be also used to determine the subsurface damage. All these techniques are able to reduce the subjectivity associated with the techniques mentioned above. Moreover, they allow, in some cases, not only the depth of the machining affected zone but also the magnitude of the equivalent plastic strain along this line to be measured.

Outeiro et al., 2015 and Baizeau et al., 2016 were able to measure and validate residual strains by using DIC (see Figure 2.23), using high rake angles (30°), which facilitates continuous chips, high cutting speed (90 m/min) and high width of cut, in order to be as close as possible to plane strain conditions.

Nevertheless, due to border constraints, they were able to measure the plastic strain into the bulk material but not close to the machined surface, where the plastic strain would be higher. Outeiro et al., 2015 reported similar subsurface damages employing DIC

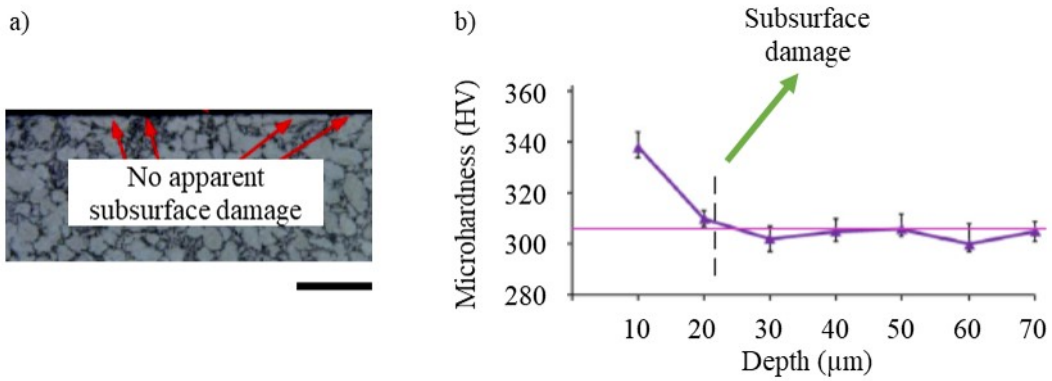

Figure 2.22: Subsurface damage measured through a) metallographic etching and b) microhardness measurements under the same cutting conditions (v_c = 60 m/min and f = 0.1 mm). Scale bar: 50 μm. Adapted from Liang and Liu, 2017

and microhardness techniques. Meurer et al., 2020 took a similar approach, reporting a methodology to carry out this kind of measurements.

PIV technique was employed in a similar way, for instance by Calistes et al., 2009, for ductile and easy to cut materials. However, these techniques are usually limited as side flow could cause the algorithm to fail because of the loss of focus. With regard to grid technique, the commonly reported grids (Bailey and Jeelani, 1976; Ghadbeigi et al., 2008) are, in general, difficult to be created. In addition grids created by metal deposition could be peeled off during the process.

Therefore, a proper technique to quantitative estimate the amount of subsurface damage is needed, avoiding the subjectivity associated with traditional techniques, easy to be implemented and without typical border and decorrelation problems associated with DIC/PIV techniques.

2.5.2 *Subsurface damage: effect of machining parameters*

The knowledge of how machining parameters (cutting conditions, workpiece material and cutting tool) have influence on subsurface damage would be of great interest in order to increase the productivity without negatively affecting surface integrity. Concerning the cutting conditions, the analysis was focused on cutting speed and feed effects on subsurface damage, parameters which define the productivity of the process. Then, the effect of tool radius and coating was studied and, finally, the relevance of workpiece microstructure. In general, the study was focused on Ti6Al4V as one of the most widely employed alloys.

It is widely accepted that the amount of subsurface damage increases with the feed (Wang et al., 2014; Hou et al., 2018), regardless of the cutting speed applied. It is worth

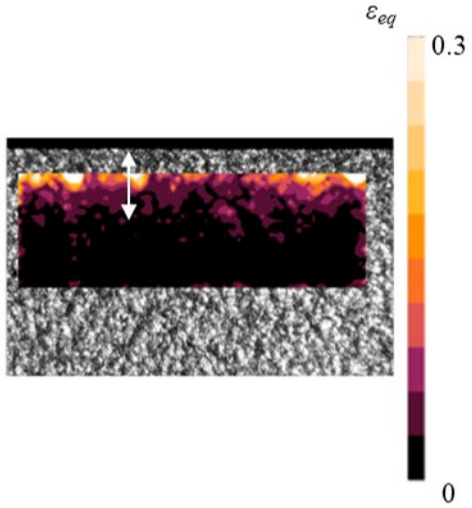

Figure 2.23: Subsurface damage measured by using DIC after orthogonal cutting of OFHC copper. Subsurface damage around 0.25 mm. Adapted from Outeiro et al., 2015

mentioning that feed effect is more remarkable at high feeds whereas the increase is less noticeable at low feeds (Islam, 2012), phenomenon which could be related to edge radius effects.

However, the effect of cutting speed is not clearly reported in literature. Wang et al., 2014 reported no variation on subsurface damage under dry milling of Ti6Al4V at high cutting speeds between 100 and 400 m/min. The depth, measured based on microhardness, was around 20 µm. Something similar was reported by Hou et al., 2018 for a multistep dry turning operation at lower cutting speeds measured based on SEM images, In this case, the cutting speed was varied between 30 and 70 m/min. This can be seen in Figure 2.24 and the results at 70 m/min were not included. Also, Yang and Liu, 2018 and Liu et al., 2019 found this behaviour for peripheral milling based on etched measurements.

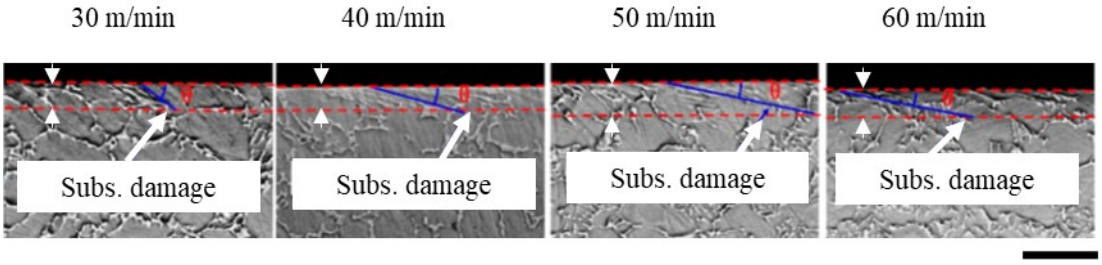

Figure 2.24: Subsurface damage measured through SEM measurements under different cutting conditions. $f = 0.25$ mm. Workpiece material Ti6Al4V. Scale bar: 20 µm. Adapted from Hou et al., 2018

On the contrary, other authors reported a decreasing trend with cutting speed, especially during no dry cutting based on metallographic measurements (Edkins et al., 2014; Joshi et al., 2015). This was also found by Rotella et al., 2014 based on microhardness measurements also for orthogonal dry turning and Oyelola et al., 2018 also reported a decreasing trend in the range between 50 and 150 m/min under dry cutting.

Nevertheless, others reported the opposite trend. For instance, Rotella et al., 2018, during dry turning of additive manufactured Ti6Al4V parts, found a slight increase in the depth of the affected layer using both microhardness and etched measurements with the cutting speed, in the range between 50 and 110 m/min. Similar results were reported by Islam, 2012 during orthogonal dry cutting from 15 to 65 m/min. At low cutting speeds, up to 7.5 m/min, the same trend was obtained by Ortiz de Zarate et al., 2018 using both etched and SEM analysis. However, it is worth noting that the variations mentioned above with cutting speed seems lower in the range of cutting speeds tested.

Other authors such as Puerta Velásquez et al., 2010 and Safari et al., 2015, however, found a remarkable influence of the cutting speed during dry milling at high cutting speeds, reporting a notable increase with the subsurface damage with the cutting speed. All these behaviours are summarized in Figure 2.25.

Therefore, all the results presented showed the necessity of having an experimental technique able to measure the subsurface damage avoiding the subjectivity associated with microstructural based measurements as no agreement was found between researchers concerning the effect of cutting conditions. In addition, the studies are mainly focused on high cutting speeds (higher than 30 m/min) whereas a clear lack of knowledge was found in the low cutting speed regime, which could be representative of the broaching process.

Concerning the cutting tool, it is widely accepted that sharp tools are preferable in order to obtain a good surface finish as the force in feed direction is expected to be reduced. However, no many studies focused on analysing its effect on subsurface damage when cutting Ti6Al4V were found.

Chen et al., 2019 briefly analysed the effect of cutting edge radius in orthogonal cutting of Ti6Al4V at 100 m/min. Based on microhardness measurements, they reported a higher affected layer with the lower radius, contrary to what expected. On the contrary, based on etched measurements, the deformed layer was higher with the higher radius. Wyen et al., 2013 carried out a comprehensive covering a wide range of cutting edge radii (from 6 to 50 µm) during dry milling of Ti6Al4V at 70 m/min. Notable increase was found on the subsurface damage especially when varying the radius between 6 and 30 µm. Above this value, the subsurface damage seems to be constant regardless of the value of the edge radius. These results were reported based on etched measurements. Nespor et al., 2015 analysed the surface integrity after ball end milling compared to orthogonal cutting. The study was focused on residual stresses but they reported an increasing deformed layer with the edge radius at 15 m/min as Figure 2.26 shows based on metallographic measurements.

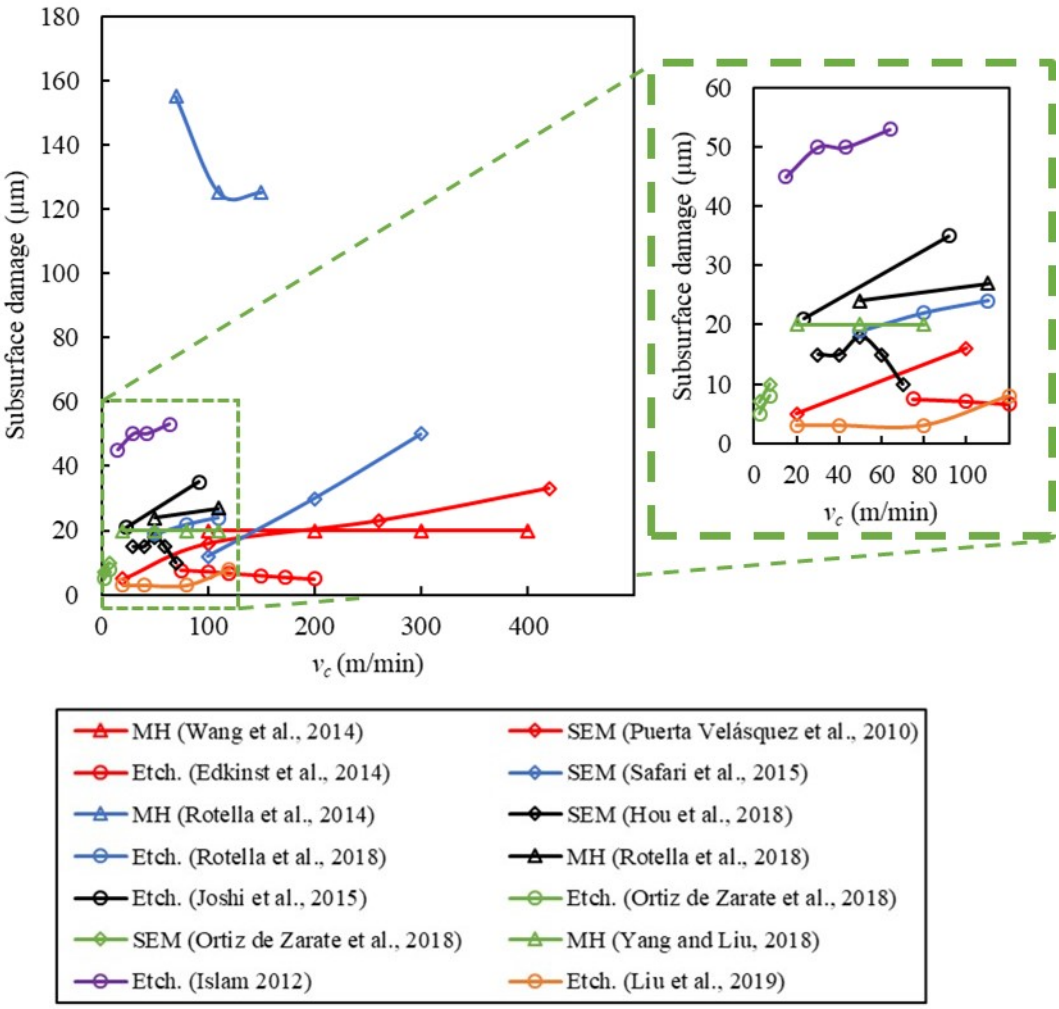

Figure 2.25: A review of subsurface damage measurements reported in literature for cutting of Ti6Al4V (effect of cutting speed). In the legend: MH means microhardness and Etch. means etched based measurements. Focus at low cutting speeds (broaching regime)

Therefore, in spite of the few references shown above, the effect of tool edge radius on subsurface damage is briefly analysed in literature. Furthermore, the majority of the studies were focused on high cutting speeds.

Another important aspect is the tool coating. The effect of tool coating on surface integrity of Ti6Al4V is not widely spread in literature. Wang and Liu, 2018 published a comprehensive review analyzing the relevance of tool material on surface integrity of different difficult-to-cut superalloys but the majority of the studies were focused on nickel based alloys as Inconel 718.

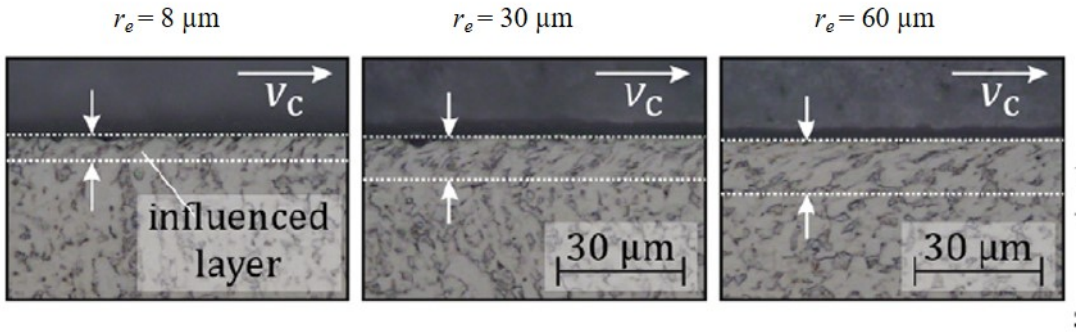

Figure 2.26: Subsurface damage with different cutting edge radii in orthogonal cutting of Ti6Al4V. Adapted from Nespor et al., 2015

According to Ginting and Nouari, 2009 the effect of tool coating, with different wear states, seems to be negligible at high cutting speeds based on microhardness measurements. Something similar was reported by Arulkirubakaran and Senthilkumar, 2017 although lower surface roughness were obtained with coated tools, so coating could have a slight effect on surface integrity.

Nevertheless, a comprehensive study is needed to characterize the tool coating effect under different cutting conditions in order to choose the best tool material to increase the productivity.

Finally, the microstructure of the material being cut is another aspect to take into account. The majority of the studies when machining Ti alloys and, specifically, Ti6Al4V, are mainly focused on shear band formation or subsurface microstructure without analyzing the effect of material microstructure itself in machining outcomes such as machinability or surface integrity (Telrandhe et al., 2017).

Bertolini et al., 2019 studied the different machining behaviours found when cutting wrought and additive manufactured Ti6Al4V parts. These two different processes lead to dissimilar microstructural issues. With regard to surface integrity, no significant differences were found in terms of surface roughness but differences on subsurface defects were found. A similar analysis, done by Bordin et al., 2014, reported lower surface roughness when cutting the wrought material whereas the subsurface damage, based on etched and microhardness measurements, remained almost constant. Remarkable differences on subsurface damage depending on the microstructure of the additive part were found, however, by Rotella et al., 2018. Also remarkable differences were observed by Oyelola et al., 2018 analyzing additive manufactured Ti6Al4V workpieces with different microstructures at high cutting speeds. The effect of microstructure anisotropy after turning additive workpieces was analysed by Lizzul et al. (Lizzul et al., 2020a; Lizzul et al., 2020b) and slight differences on subsurface damage were observed depending on microstructure orientation as shown in Figure 2.27.

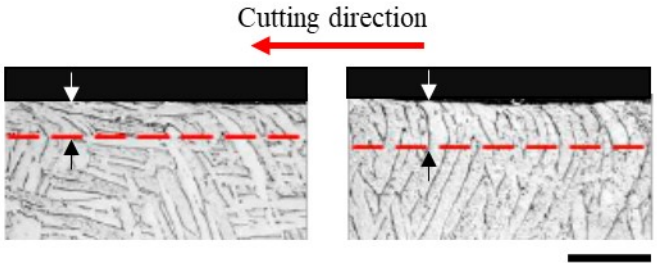

Figure 2.27: Subsurface damage with different microstructural orientations. Adapted from Lizzul et al., 2020a. Cutting conditions: $v_c = 80$ m/min and $f = 0.2$ mm. Scale bar: 20 µm

Table 2.5 summarizes the main effects of machining inputs on subsurface damage according to the literature analysed.

Table 2.5: Summary of the effects of machining inputs on subsurface damage

Type of input	Input	Effect
Cutting conditions	f	↑
Cutting conditions	v_c	?
Tool geometry	r_e	↑
Tool material	Coating	?
Workpiece material	Microstructural orientation	?

The majority of the studies analyzing microstructural aspects are focused on studying the performance of additive manufactured specimens. However, the effect of the initial microstructure on surface integrity is not clear and it is a relevant aspect to be taken into consideration.

2.6 CRITICAL ANALYSIS AND RESEARCH OPPORTUNITIES

Based on the analysis of the literature, the following research opportunities, addressed during this research work, can be summarized:

- Material characterization carried out through thermomechanical testing needs to be enhanced so as to reproduce the machining conditions properly. The experimental set-up commonly used to characterize the material are usually far from these machining conditions, therefore new designs are needed aiming to reproduce, at least, the stress state (shear and compression) and the strain reached during the machining process. In addition, plastic strain and temperature control is essential to carry out the material characterization properly.

- The plastic work employed to deform the material is converted into heat which results in a temperature rise in the region of interest. This phenomenon is known as adiabatic self-heating and two different definitions could be found in the literature for this parameter. The knowledge of this phenomenon would be helpful to improve material characterization and numerical validation.

- Material characterization needs to be optimized to reproduce chip segmentation behaviour properly. Among all the studies found in literature focused on inverse simulation, few of them were found aiming to optimize the ductile failure law. However, it is known that, especially at low cutting speeds, the effect of ductile failure law on machining predictions is high. Therefore, an inverse methodology should be developed in order to optimize ductile failure law for Ti6Al4V based on machining outcomes.

- Concerning strain analysis, in spite of the progress made on the field, strain and strain rate measurements under real machining conditions are still a challenge. The attempts found in the literature are usually focused on non difficult-to-cut materials (ductile materials with continuous chips) and, in general, at low cutting speeds. In addition, the majority of the studies are not able to measure under plane strain conditions, typical of the orthogonal cutting process. Thus, a proper methodology to measure these variables is needed to understand more in depth the machining of Ti6Al4V alloys and to validate the numerical models.

- Surface integrity is a key aspect in machining. Among all the possibilities to characterize surface integrity, the depth of the machining affected zone (subsurface damage) is one of the most widely used indicators. However, these measurements are usually based on microstructural measurements which could be influenced by the subjectivity, making impossible to wholly measure the defects. Therefore, a methodology to measure it reducing this subjectivity would be very helpful for machining research.

- The effect of cutting conditions, especially cutting speed, on subsurface damage is not clearly reported in the literature. In addition, the effect of edge radius and tool coating on subsurface damage is not widely analysed. Finally, the microstructure of the workpiece material could play a relevant role on workpiece surface integrity and its effect has not been extensively studied.

3

THERMOMECHANICAL CHARACTERIZATION OF THE WORKPIECE MATERIAL

It has been stated that reliable models are needed to reduce the cost associated with the selection of tools and cutting conditions in machining. First, to generate reliable models a proper material characterization is needed, which could be used as a valuable input in an inverse analysis under machining conditions. This material characterization is usually made through thermomechanical tests in order to know the material flow and ductile failure. In addition, the knowledge of the microstructural state after a mechanical process is of great interest as it gives some insights into the material behaviour in terms of fracture and ductility.

An appropriate temperature control is essential during thermomechanical characterization. In practice, pure isothermal conditions are impossible to obtain due to the heat losses into the surroundings. Therefore, it is important to quantify all possible temperature variations during the test. In spite of this relevance, temperature is usually measured through thermocouples which limit the amount of data acquired and, more importantly, influence the heat flow. For this reason, infrared thermography could be a good choice to obtain a full field measurement of the thermal fields during the test as well as being a non-intrusive method. One of the major drawbacks of infrared thermography is the determination of the emissivity of the sample, as this depends on factors such as temperature, chemical composition, surface roughness and surface oxidation (Cao et al., 2011; Zhang et al., 2015).

These models need to be validated over a wide range of conditions. Hence, plastic strain and strain rate measurements are gaining importance nowadays. The knowledge of plastic strain and strain rate is not only useful to validate numerical models, but also to carry out thermomechanical characterization properly, as they define the material flow behaviour.

In addition, the material being deformed is self heated during the test because of plastic work. Knowledge of adiabatic self-heating is of wide relevance as it determines the real temperature at which the part has been deformed. Often this parameter is taken around 0.95 according to the earlier definition given by Taylor and Quinney, 1934. This approach is useful when adiabatic conditions can be assumed. However, in general, especially at relatively low strain rates, this assumption may not be accurate enough as thermal losses (conduction, convection or radiation) could play a relevant role and 2D finite element software usually neglects them in order to carry out the calculus. Thus, a proper characterization of this phenomenon is needed to develop material characterization properly and to generate accurate and reliable numerical models. Furthermore, two

different definitions of the adiabatic self-heating were found, which are used indistinctly. This could lead to misunderstandings, as the values reported for the adiabatic self-heating parameter could differ substantially as shown in Table 2.1.

Therefore, this chapter is organized as follows. First, the experimental set-up and the numerical model analysis were explained. Then, the thermomechanical behaviour of the material was analysed taking into consideration force measurements and microstructural analysis through etched samples. Next, a thermal analysis was carried out in order to prove the relevance of a proper temperature control. After that, the strain measurement protocol was explained and validated. Experimental results were compared with numerical simulations. Finally, the methodology to determine the adiabatic self-heating was explained.

3.1 EXPERIMENTAL AND FE-BASED MODELLING PROCEDURES

It has been demonstrated that the stress state reached during orthogonal cutting of Ti6Al4V could be quite complex, combining tension, compression and shear modes depending on the cutting conditions (Wang and Liu, 2016; Childs et al., 2018). In addition, at low cutting speeds, the tensional state becomes mainly governed by compression and shear. These modes could be distinguished thanks to the triaxiality parameter, which is the ratio between the hydrostatic pressure and the equivalent stress. However, the majority of the studies are focused on compression. For this reason, different samples were designed aiming to reproduce shear and shear/compression modes representative of the orthogonal cutting process.

3.1.1 *Experimental set-up*

Uniaxial compression loading of the specimens was carried out using a Gleeble 3500 thermo-mechanical testing machine. The specimens were located between two tungsten carbide anvils. The friction between the anvils and the specimen was negligible thanks to the use of graphite sheets. The vacuum chamber was opened so the process could be filmed. Therefore, vacuum was not created. This could lead to heat losses due to convection and oxidation of the samples.

The machine heats the specimen based on the Joule effect with a heating rate of 10°C/s up to the desired temperature. The testing temperature was held constant for 30 s to ensure the homogeneity along the sample. The temperature was controlled through a K-thermocouple welded to the specimen (see Figure 3.1b). In the present case, these temperatures were room temperature (RT), 600 and 900°C. The Gleeble machine records the force and the displacement during the process, in order to analytically determine the plastic strain.

The testing specimens were designed to reach tensional states representative of the orthogonal cutting process. Through numerical simulations, it was stated that triaxialities

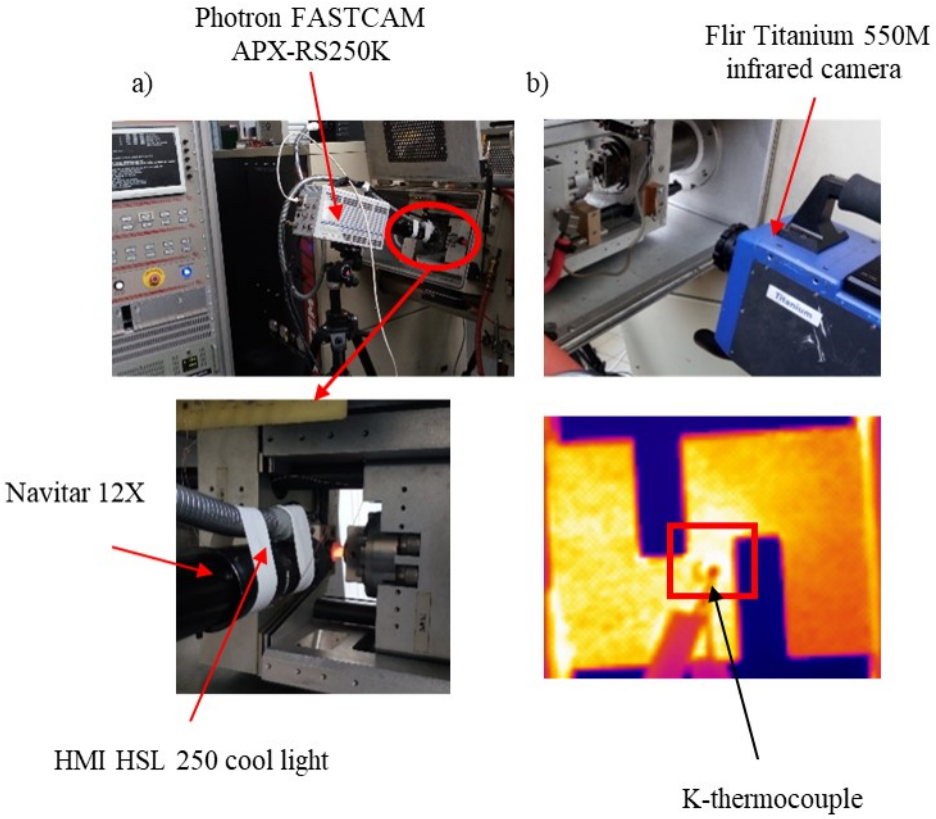

Figure 3.1: Experimental set-up of thermomechanical compression tests: a) Photron FASTCAM APX-RS250K with HMI HSL 250 cool light; b) FLIR Titanium 550M with focus on the shear zone (infrared image) and the K-thermocouple

during the process would be between 0 (pure shear) and 0.3 (compression), typical values found during orthogonal cutting of Ti6Al4V (Wang and Liu, 2016; Childs et al., 2018). Based on numerical analysis, the testing specimens a and b (see Figure 3.2) consisted of a shear sample with a theoretical shear thickness of 1 and 0.1 mm, similar to the ones proposed by (Hor et al., 2013a). Sample c represented a combination of shear and compression. They were named according to the dimension highlighted in Figure 3.2 and fabricated through wire electro discharge machining (WEDM). The length of the shear zone was 2 mm whereas the width was 10 mm for each sample. It is worth mentioning that the specimens were designed with flat faces so the process could be filmed.

The compressed distance was 2 mm and the speed was kept constant and set to 1.9 mm/s to keep the strain rate constant during the experimental test.

All the tests were filmed with a frame rate of 9000 frames per second using a Photron FASTCAM APX-RS250K from the surface. The objective used was a Navitar 12X. The sample was lit with HMI HSL 250 cool light (see Figure 3.1a).

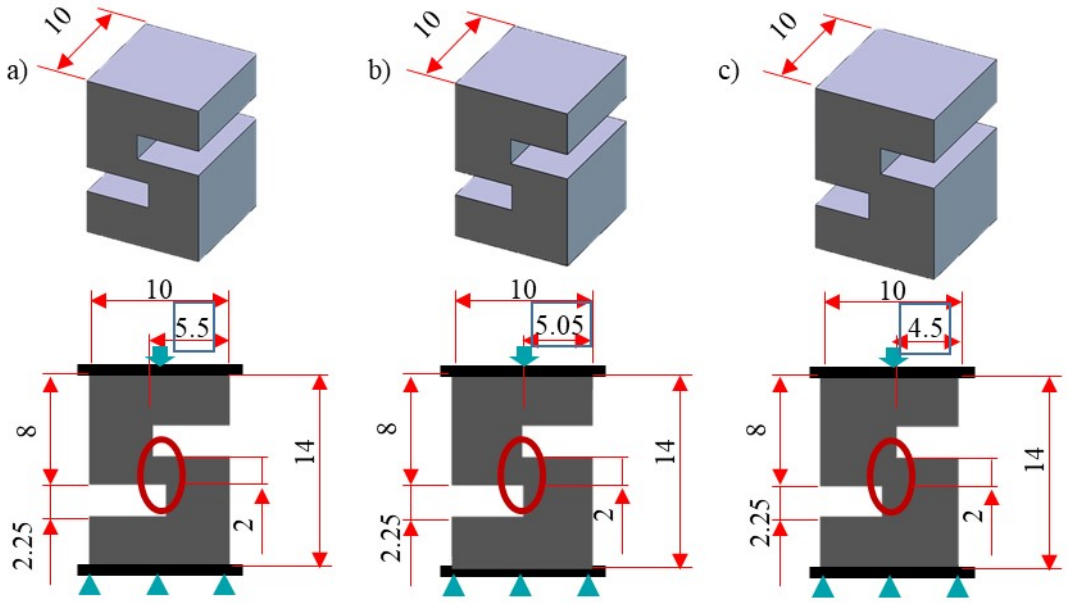

Figure 3.2: Designed specimens to reproduce different conditions (strain rate and load mode) with slight variations in the sample design. Specified modes based on the triaxiality analysis given in Section 3.2: a) Shear sample S55; b) Shear sample S505; c) Shear+Compression sample S45. Names given according to the dimension highlighted in blue

To carry out DIC measurements from this surface, a speckle pattern was created. Different painting methods were tested to ensure good adhesion under the tested conditions (see Section 3.4.1.1), with enough resolution and no decorrelation problems. The aim of these measurements was to properly determine the shear zone and to obtain the strain and strain rate fields. DIC analysis was done using GOM Correlate software. The noise error on plastic stain measurements was quantified by analysing the equivalent plastic strain obtained between 100 frames without movement.

Infrared images of the sample being deformed were taken using the FLIR Titanium 550M with 1000 Hz of sampling frequency. The emissivity was characterized thanks to the thermocouple welded to the surface as Figure 3.1b shows. At high temperatures (600 and 900°C), the effect of reflected temperature was totally negligible and the emissivity could be directly determined by comparing infrared and thermocouple measurements. However, at room temperature the effect of reflected temperature must be properly characterized. In this case, the diffuser reflector method was employed (Usamentiaga et al., 2014). The self heating of the material was used as the heating source and the anvil reflection was employed to estimate the reflected temperature. For this specific case, the reflected temperature was 32°C. Further details were included in Section 3.3.

Finally, material microstructure was analysed so as to study the existence of some changes in the microstructure due to the deformation process. The deformed samples

were mounted in a resin and polished up to mirror finishing. Then, they were etched with Kroll's reagent to reveal the microstructure. For each sample geometry, the undeformed microstructure was compared with the sample after being deformed at each temperature.

The material employed was the widely used aeronautical alloy Ti6Al4V. The material was provided as a solid hot rolled bar with a diameter of 80 mm, delivered in the annealed condition. The initial microstructure of the sample was revealed with Kroll's reagent and shows a microstructure with primary α grains and $\alpha + \beta$ colonies, see Figure 3.3. The material as received had a grain size of 10.5 ASTM and the measured microhardness was $350\text{HV}_{0.05}$.

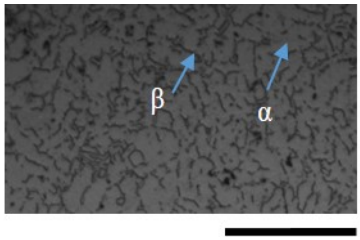

Figure 3.3: Initial microstructure of the Ti6Al4V employed. Scale bar: 50 μm

According to material data-sheet, the density was 4430 kg/m^3 and the chemical composition is summarized in Table 3.1.

Table 3.1: Chemical composition of the Ti6Al4V

Element	V	Al	Fe	C	O	N	Ti
Weight percent	4.05	6.36	0.16	0.015	0.019	0.006	Bal.

3.1.2 *Finite Element Model with AdvantEdge*

The aim of the numerical analysis was to provide knowledge of the physics of the compression process (in terms of triaxiality and damage) and reliable outputs to be compared with the experimental results.

AdvantEdge employs elastoplastic Lagrangian code with continuous remeshing and adaptive meshing. Remeshing technique ensures minimum element sizes in the region of interest as severe strain, strain rate and temperatures are expected. The minimum element size was set to 20 μm in the shear zone to achieve accurate results, comparable to the mesh size employed in DIC measurements. The mesh employed is shown in Figure 3.4.

AdvantEdge is a commercial finite element software which provides more flexibility than other generic software such as Abaqus to model the machining process. Although the software is mainly designed to carry out machining simulations, it was used to reproduce

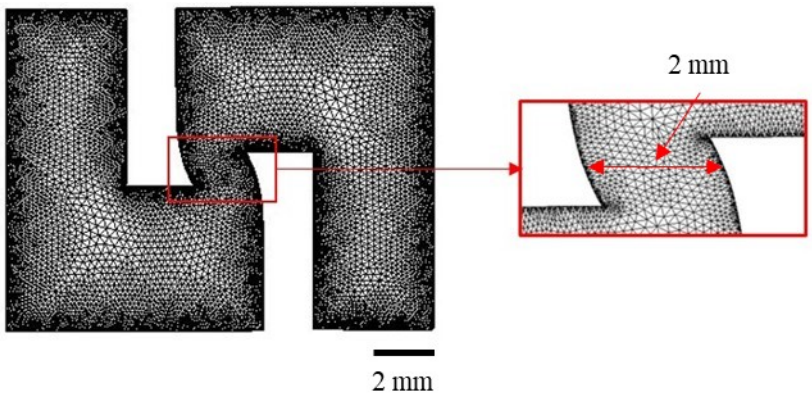

Figure 3.4: Deformed mesh with special focus on the region of interest (ROI)

2D compression tests. The anvil was simulated as a rigid body (tool in the software) and the feed was set to 12 mm in order to be higher than the height of the sample (10 mm). The movement was imposed to the elastoplastic sample, setting the loading speed to 1.9 mm/s. Convection losses were taken into account in the simulation and any contact between tool and sample was modelled as a thermomechanical contact.

To obtain reliable outputs, an appropriate selection of input parameters is a key aspect. Among all the flow stress laws presented in the literature, a comprehensive study was carried out by Ortiz de Zarate et al., 2019. They compared different machining outcomes using different flow stress laws coupled with a ductile failure law, concluding that the Johnson and Cook model was accurate in reproducing the machining behaviour. The model considers isotropic hardening, strain rate hardening and thermal softening as three independent phenomena and avoid couplings, simplifying the simulations. The material constants are summarized in Table 3.2 and they were taken from (Childs et al., 2018).

Table 3.2: Johnson and Cook model parameters taken from Childs et al., 2018

A (MPa)	B (MPa)	C	n	$\dot{\varepsilon}_0$ (s^{-1})	T_{melt} (°C)	m
1130	530	0.0165	0.39	1	1650	0.61

To reproduce the damage suffered by the Ti6Al4V under compression it is necessary to introduce a ductile failure model (Childs et al., 2018). The ductile failure model was introduced as two-staged and physical-based. The Mohr-Coulomb law represents failure initiation leading to a flow stress reduction and it is based on the accumulation of damage (D) along a streamline. This damage could be modelled as a function of stress triaxiality (η) and different failure coefficients ($(\varepsilon_{f,0})_T$ and c) as shown in equation (2). It was assumed that failure starts when the damage reaches a value of 1.

$$\begin{aligned} D &= \int_0^{\bar{\varepsilon}_f} \frac{d\bar{\varepsilon}}{\bar{\varepsilon}_f} \\ \bar{\varepsilon}_f &= (\varepsilon_{f,0})_T \exp(c\eta) \end{aligned} \tag{2}$$

The effect of the temperature on the damage was introduced based on equation (3). Thus, the strain to failure ($\bar{\varepsilon}_f$) is also a function of the failure strain under shear/torsion conditions ($(\varepsilon_{f,0})_T$), the stress triaxiality (η), the stress triaxiality constant (c) and the temperature sensitivity a.

$$\begin{aligned} (\varepsilon_{f,0})_T &= \varepsilon_{f,0}(1+aT), \quad && T < T_{crit} \\ (\varepsilon_{f,0})_T &= \infty, && T > T_{crit} \end{aligned} \tag{3}$$

Therefore, if the accumulated damage value does not reach 1, the plastic behaviour of the material is only modelled by the Johnson and Cook model, whereas if this value is 1, damage evolution governs flow stress reduction. Both, flow and ductile failure laws were implemented by user define subroutines.

The damaged flow stress, σ_D, depends on the reduction function, caused by the damage, and the flow stress without damage, see equation (4). In addition, because of the healing effect, the damage will not affect the flow stress at temperatures higher than a critical one, defined as T_U. Below this critical temperature, the flow stress reduction is temperature dependent as shown in equation (5).

$$\sigma_D = f(\eta, T)\sigma \tag{4}$$

$$\begin{aligned} f(\eta,T) &= 1, && T > T_U \\ f(\eta,T) &= \tanh\left[-\sqrt{3}\mu_i\eta\right], && T < T_L \\ f(\eta,T) &= \tanh\left[-\sqrt{3}\mu_i\eta\right] + \left(1-\tanh\left[-\sqrt{3}\mu_i\eta\right]\right)\left(\tfrac{T-T_L}{T_U-T_L}\right), && T_L < T < T_U \end{aligned} \tag{5}$$

where μ_i is the sensitivity parameter of the stress triaxiality and T_L is a limit temperature.

The material parameters employed in the ductile failure law are summarized in Table 3.3.

Table 3.3: Damage and failure parameters taken from Childs et al., 2018

$\varepsilon_{f,0}$	a	c	μ_i	T_{crit} (°C)	T_L (°C)	T_U (°C)
0.25	0.0012	-1.5	1	600	600	700

Finally, the sticking sliding model was selected to reproduce the friction. The friction coefficient was set to 1 ensuring the contact would be governed by the sticking region. In addition, the thermal conductivity and heat capacity of the material were taken from literature, being, at room temperature, 6.7 W/m°C and 2.3 MJ/m^3, respectively. The density was 4430 kg/m^3. The heat capacity of the tool was notably reduced from the real physical value to 0.1 MJ/m^3 in order to reduce the time needed to reach the steady state (Childs et al., 2018).

3.2 THERMOMECHANICAL ANALYSIS

In this section, the forces and the final microstructural state of the sample were analysed. These outputs reported valuable information about the material behaviour under different conditions.

First of all, the forces (normalised to the width of the sample) reached during the deformation process under the whole set of conditions tested are shown in Figure 3.5.

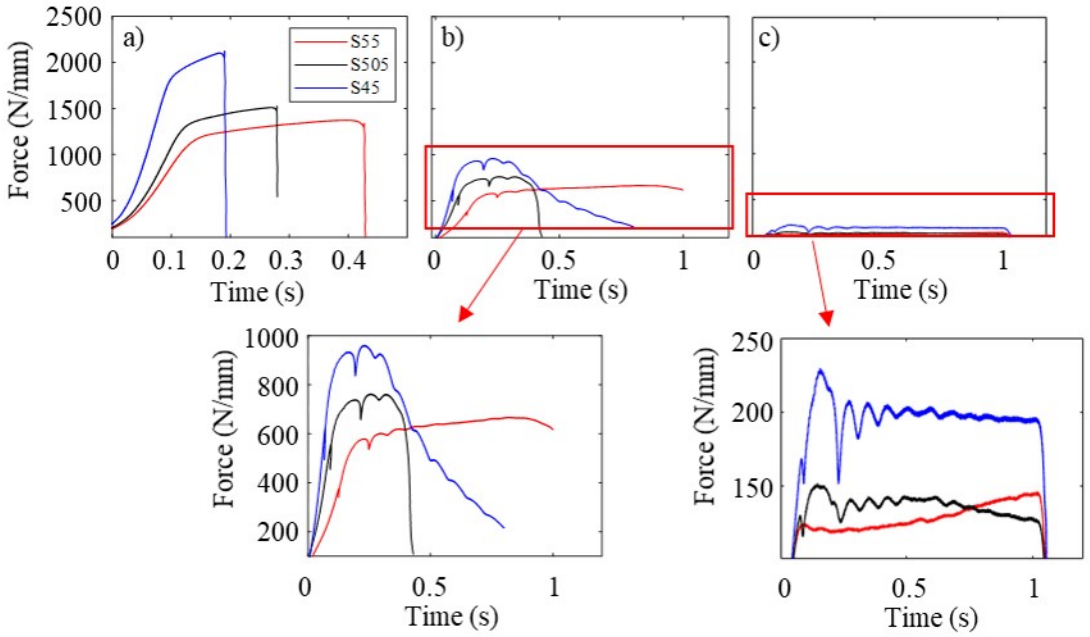

Figure 3.5: Experimental compression forces measured when deforming the Ti6Al4V samples S55, S505 and S45 (see Figure 3.2) at: a) Room temperature; b) 600°C and c) 900°C

When the test was carried out at room temperature, the flow behaviour showed the typical strain hardening up to drastic failure. In contrast, higher ductility was observed at 600°C and, for instance, no macroscopic failure seemed to take place for S55 sample. Finally, at 900°C, although the failure seemed to have started, no drastic failure was

observed in any sample. In addition, there is a notable decrease in the force when the temperature increases, due to thermal softening, as expected.

The variations in the forces between samples subjected to the same conditions could be related to the different load modes employed in the analysis because of the design of the samples. The finite element analysis showed that S55 and S505 can be assumed to be subjected to simple shear conditions (triaxiality equal to zero) whereas S45 sample is subjected to a combination of compression and shear (Bao, 2003; Bao and Wierzbicki, 2004). It is worth mentioning that triaxiality values given (see Figure 3.6) are negative, the compression being, thus, represented by positive values.

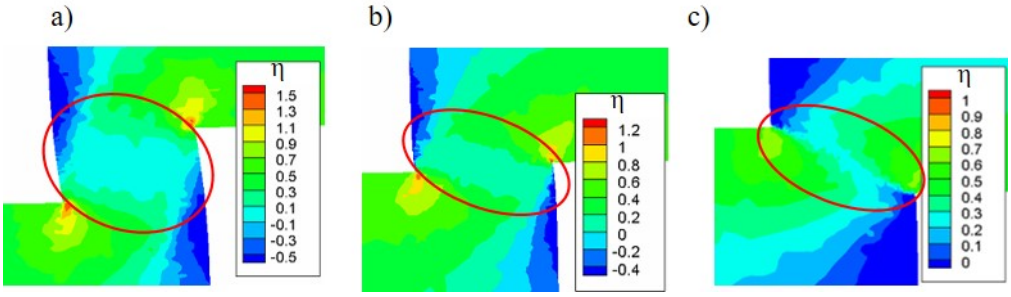

Figure 3.6: Triaxiliaty fields for: a) S55; b) S505 and c) S45

Regarding the microstructural analysis, the first geometry analysed was the S55 sample. In Figure 3.7 the microstructure evolution can be seen. No significant differences in the bulk material were found between the test at room temperature and at 600°C whereas the sample heated up to 900°C showed higher grain sizes with slight differences in the microstructure.

At room temperature, the fracture was totally brittle and shear band formation was observed. In contrast, at 600°C higher ductility was observed and, although the fracture started, there was not enough deformation to cause the drastic failure of the sample and the crack did not spread along the sample. Finally, at 900°C, the behaviour was totally different as the microstructure drastically changed, with higher grain sizes. In addition, some void formation was observed at high temperatures. Under similar conditions, similar behaviour was found by other researches such as Shahan and Taheri, 1993, Luo et al., 2015, Alabort et al., 2015 or Jiang et al., 2020.

The same analysis was carried out with the S505 sample (see Figure 3.8). Cracks were observed at the three temperatures, being the fracture especially brittle at room temperature. In addition, shear bands were observed at room temperature and 600°C, whereas no clear shear band took place at 900°C. Some void formation was also observed at the two highest temperatures. At 600°C there is a clear accumulation and grain elongation close to the shear band which can be attributed to a dynamic recovery phenomenon according to different authors (Mosecker et al., 2013; Roy and Suwas, 2013).

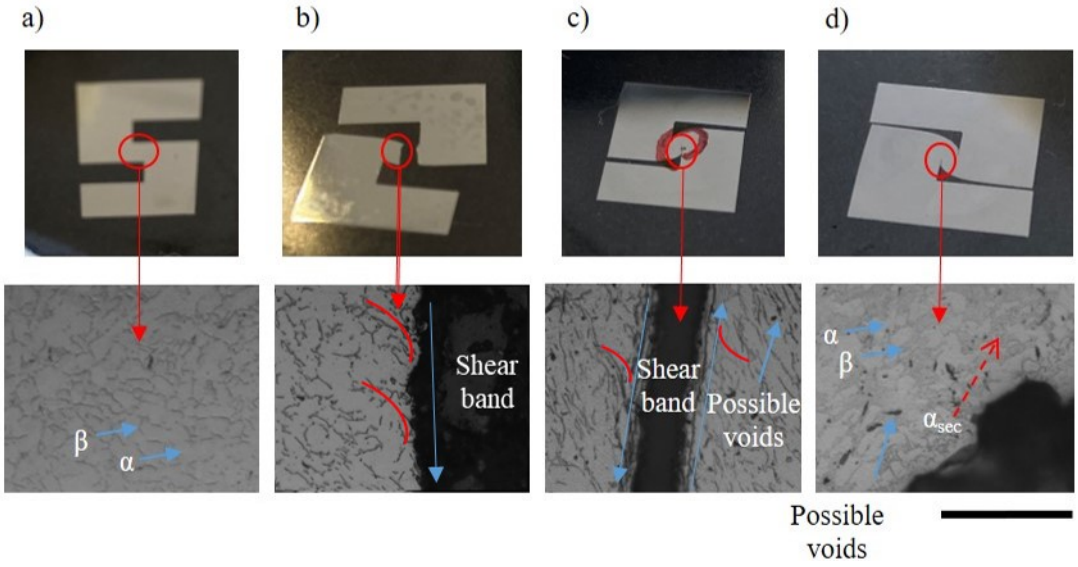

Figure 3.7: Microstructure evolution of the S55 sample: a) As received; b) Sample deformed at room temperature; c) Sample deformed at 600°C and d) Sample deformed at 900°C. Scale bar: 50 µm

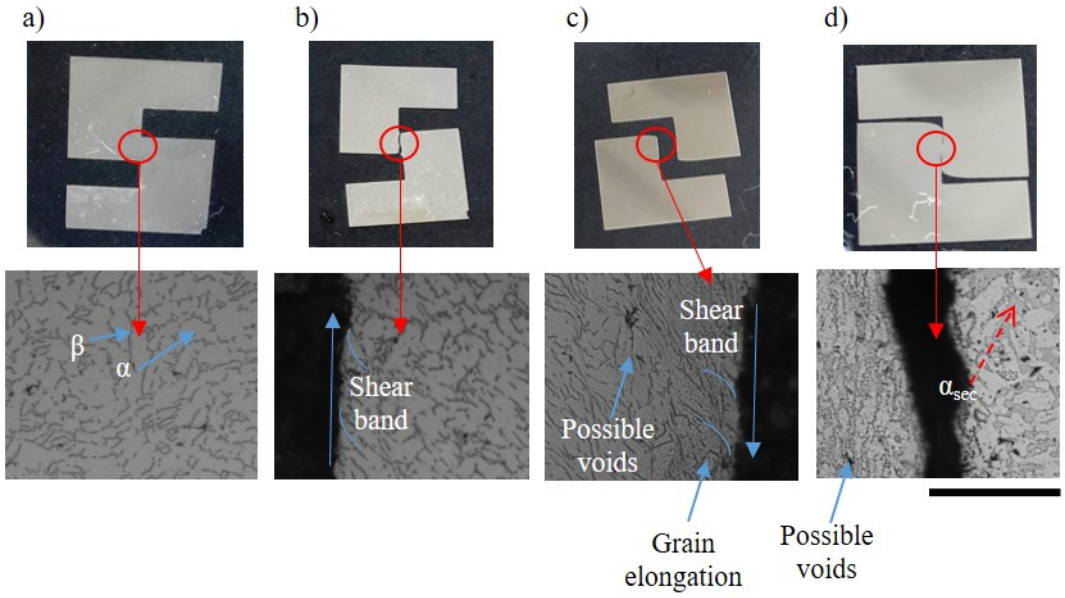

Figure 3.8: Microstructure evolution of the S505 sample: a) As received; b) Sample deformed at room temperature; c) Sample deformed at 600°C and d) Sample deformed at 900°C. Scale bar: 50 µm

Finally, the S45 sample was analysed. In this case, the crack took place with an inclination defined by sample design as Figure 3.9 shows. Similarly to previous cases, at

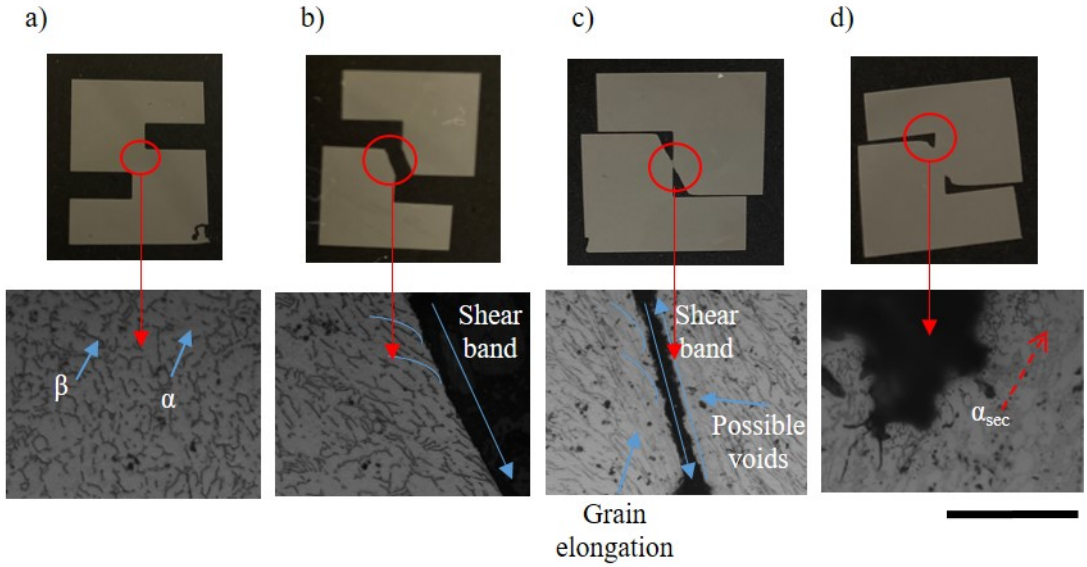

Figure 3.9: Microstructure evolution of the S45 sample: a) As received; b) Sample deformed at room temperature; c) Sample deformed at 600°C and d) Sample deformed at 900°C. Scale bar: 50 μm

room temperature a drastic brittle fracture was observed whereas the sample at 600°C showed higher ductility with grain elongation close to the shear zone. Shear bands were observed at this temperature and the sample was close to fail. Again, the microstructural changes at 900°C explained the different flow behaviour observed.

Summarizing, after the thermomechanical analysis the following conclusions can be drawn:

- Higher ductility was observed at higher temperatures when deforming Ti6Al4V regardless of the sample geometry employed and no signals of drastic failure were found at 900°C for any geometry within the range of plastic strain analysed.
- At room temperature, adiabatic shear bands were observed with the three samples as the grains were oriented in the shear direction. These shear bands also appeared when the sample was compressed at 600°C.
- No special variations in microstructure were found between room temperature and 600°C whereas at 900°C the microstructure has changed, presenting higher grain sizes. This phenomenon could explain the differences on ductility found.
- Void formation could take place during deformation of Ti6Al4V influencing the flow behaviour especially at high temperatures. In addition, grain elongation was observed in the samples deformed at 600°C which could be explained by a dynamic recovery phenomenon.

3.3 TEMPERATURE MEASUREMENTS

Thermocouples are the most reported technique to measure temperatures during thermomechanical tests. However, they report single point measurements and could influence the heat flux acting as a thermodynamic fin. In addition, thermal losses into the surroundings may be relevant, especially at high temperature, causing the temperature to be different to the set one. Therefore, thermomechanical characterization carried out based on thermocouple measurements could be inaccurate. In order to have a full field measurement of the thermal fields during a thermomechanical test, infrared cameras could be a solution. However, a proper methodology to characterize the emissivity is needed in order to report accurate values of temperature.

3.3.1 *Emissivity characterization*

Although the measurement protocol has been briefly explained in Section 3.1.1 a more detailed explanation is given here. The test temperature was controlled with a K thermocouple welded to the surface but infrared measurements were employed to determine the thermal fields and the real temperature of the material being deformed. The emissivity of the sample was calibrated in-situ for each condition taking into consideration the thermocouple measurement in the non-deformed state. A 3x3 pixel measurement point was put close to the thermocouple in order to determine the emissivity.

When capturing thermal images, the radiation is composed by the emitted, the reflected and the transmitted radiations as shown in Figure 3.10.

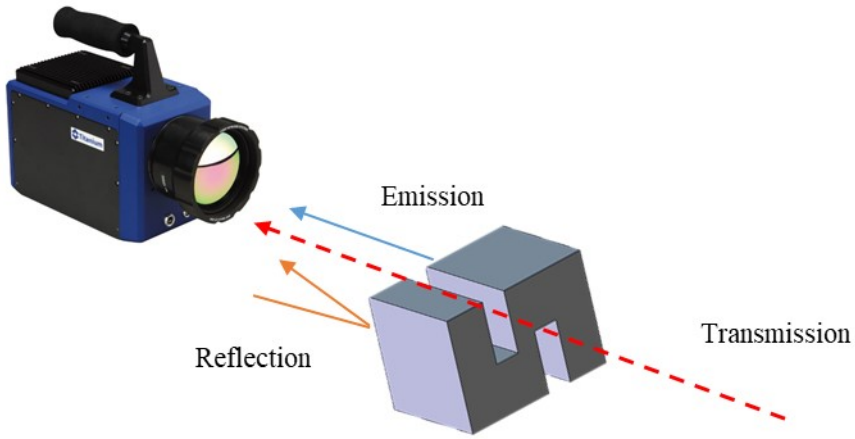

Figure 3.10: Scheme of the sources of radiation captured by the thermal camera

In metals, the transmission, that is, the capacity of being transparent to infrared radiation, could be assumed negligible. Thus, infrared signals would be mainly composed

by emissions and reflections. The radiation emitted depends on body absolute temperature and the emissivity of the material. It can be estimated according to Stefan-Boltzmann law (see equation (1) in Section 2.2.1). However, the camera not only captures emitted radiation but also the one reflected by the surface which depends on the emitted radiation by the objects located close to the body and the surroundings. Thus, reflections have influence on the radiation captured by the camera. This could cause a bad estimation of the body temperature if this phenomenon is not properly taken into account.

For the tests at high temperature, the effect of the reflection could be neglected as the reflective objects would be at much lower temperature than the region of interest (ROI), the reflected radiation being notably lower than the one related to the emission term. Thus, the emissivity could be directly estimated based on the measurement given by the thermocouple. Although thermocouples influence the heat flux, the temperature reported is assumed to be accurate. The measuring point used to estimate de emissivity was placed near the thermocouple, thus both points are assumed to be at the same temperature. In addition, temperature variations due to self-heating of the material being deformed are assumed to be small enough to produce negligible changes on the emissivity. For instance, according to Zhang et al., 2015, variations of around 0.1 in the emissivity could lead to uncertainties of 30 K.

Figure 3.11 shows the temperature evolution according to the thermocouple for a S55 sample compressed at 600°C. The cycle consisted of a heating slope during 60 seconds to the set temperature. Then, the temperature was kept constant 30 seconds to ensure the homogeneity of the heating along the ROI (shear zone). This step was employed to carry out the emissivity calibration. After that, the temperature control was switched off starting the test.

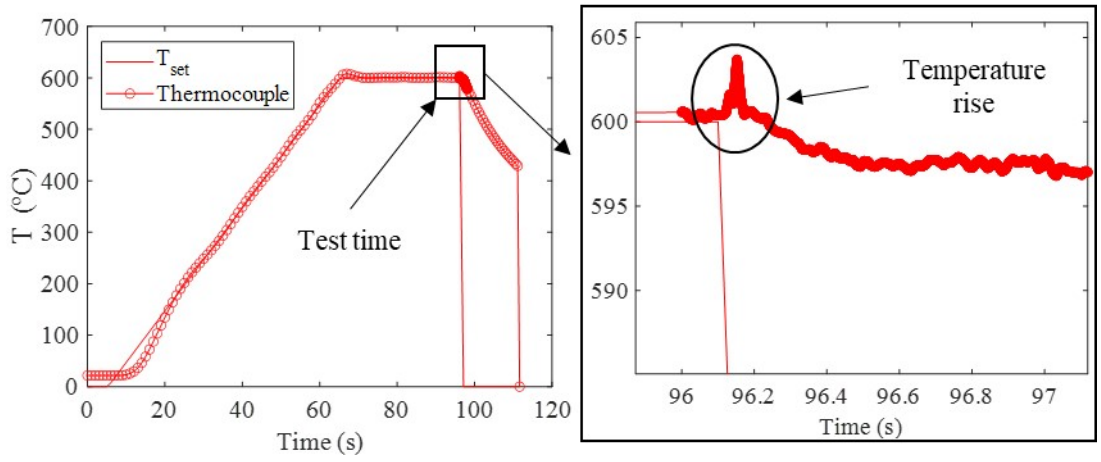

Figure 3.11: Example of the temperature evolution during a shear test with a focus on the compression test (S55 sample at 600°C)

It can be seen a slight temperature rise during the deformation due to the self heating of the material which is going to be further analysed in the following sections. This temperature rise strongly depends on the thermocouple position. An example of the thermal state obtained with the infrared camera just before the deformation process is shown in Figure 3.12.

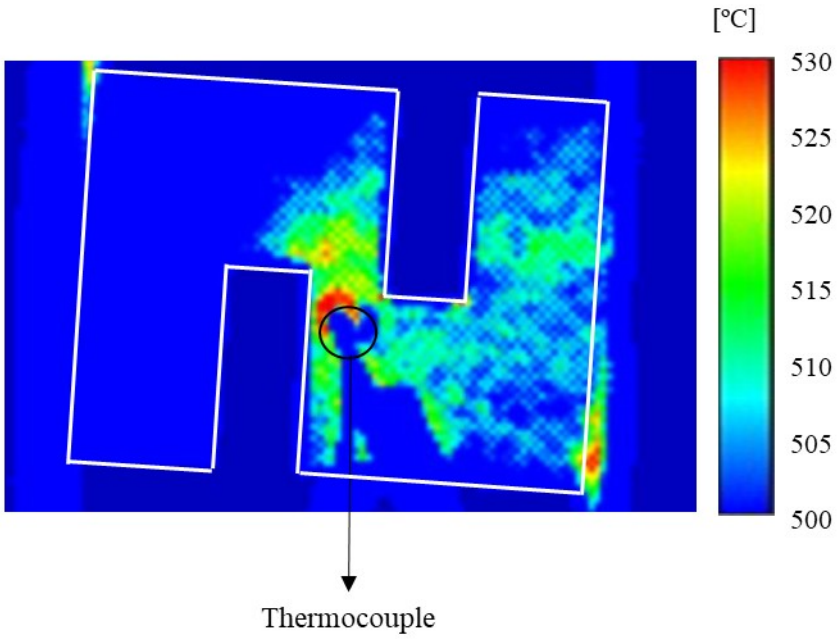

Figure 3.12: Example of the selected frame to carry out the emissivity calibration (S55 sample at 600°C). Sample contour highlighted in white and thermocouple highlighted with a black circle. Apparent temperature reported (that is, with an ε_{em} of 1)

First, it is worth mentioning that the heating is not homogeneous along the sample as the heat tends to concentrate in the zones with low section. That is why it is quite important to place the thermocouple properly in order to ensure a proper temperature distribution within the ROI as Figure 3.12 shows. The temperature reported by the thermal camera was equaled to the one measured by the thermocouple to determine the emissivity.

In contrast, the protocol for determining the emissivity at room temperature is more complex as reflections could play a relevant role. The reflected apparent temperature is the parameter employed to take into account this issue when capturing the images. To determine it, the reflector method is commonly employed as it is easy to apply and provides appropriate results. The reflector, a body whose emissivity is close to zero, is placed in the field-of-view, out of the heat source, and its temperature is measured taking into consideration an emissivity of one and a distance of zero (Usamentiaga et al., 2014), that is, the apparent temperature.

For this specific case, as the material was self heated during the test, this self heating was employed as the heat source and the temperature in the anvil was used to determine this reflected temperature. Based on this analysis, the reflected apparent temperature was set to 32°C. An example of the infrared measurement for the determination of the reflected temperature is shown in Figure 3.13.

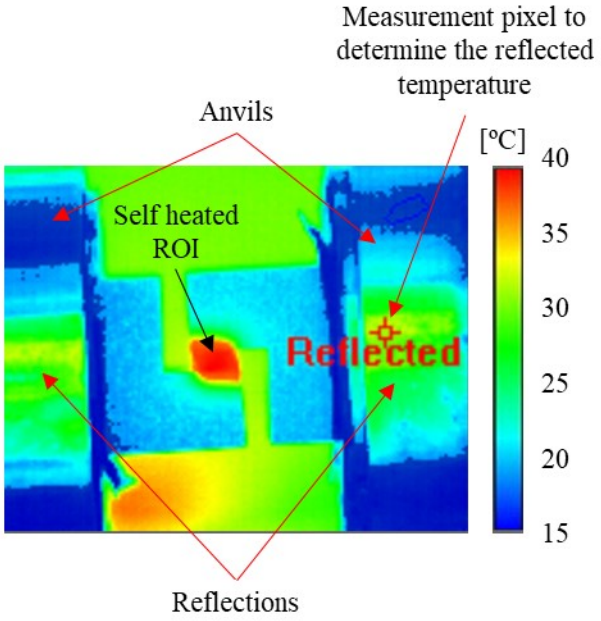

Figure 3.13: Determination of the reflected temperature. Apparent temperatures given in Celsius degrees

The values of ε_{em} obtained are shown in Figure 3.14. The emissivity was around 0.7 at room temperature and 0.65 at 600°C. Although emissivity was expected to increase with temperature, it is worth mentioning that emissivity measurement at room temperature is a big issue and other effects could be affecting this value. Nevertheless, the obtained values of temperature through infrared images can be assumed to be accurate as they were calibrated in-situ considering thermocouple measurements. Furthermore, at 900°C the emissivity increased up to 0.8 mainly because of oxidation effects. In spite of the sample being a metal, relatively high values of emissivity were obtained due to the roughness reached after the WEDM process.

In addition, the obtained emissivities varied from one sample geometry to other without any kind of trend which could be due to geometry effects. Based on the presented results, the uncertainty, u_T, on the temperature measurement taking into consideration variations of 0.1 in ε_{em} was around ± 3°C at room temperature, ± 30°C at 600°C and ± 50°C at 900°C.

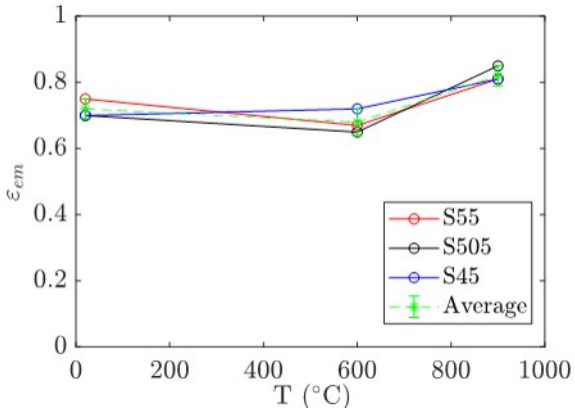

Figure 3.14: Emissivity values for the three sample geometries tested at the three temperatures analysed

3.3.2 *Temperature measurement results*

After determining the emissivity and the apparent reflected temperature of the material under all the conditions tested, the temperature evolution was measured, comparing the results reported by the thermocouple and the ones obtained with the infrared camera. For instance, the temperature evolution for a shear test with the S55 sample at 600°C measured in different ways is shown in Figure 3.15.

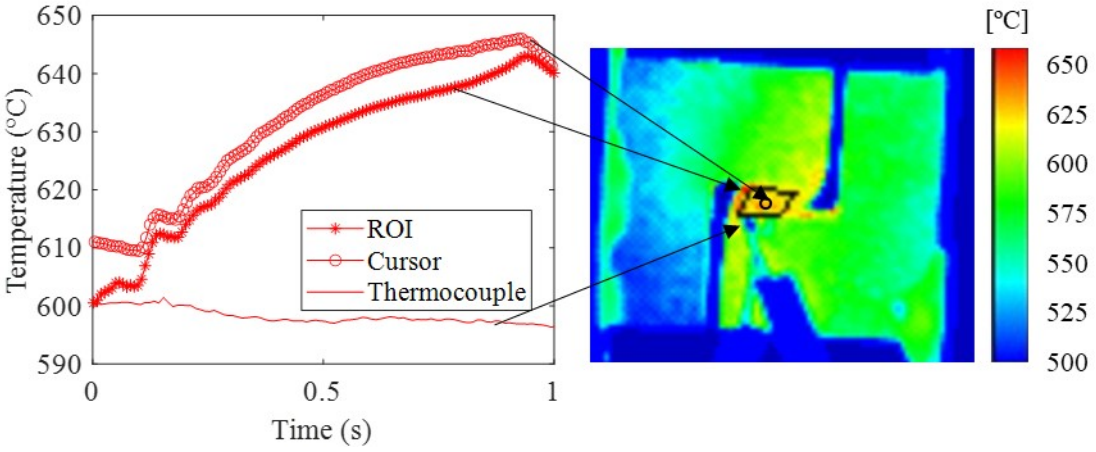

Figure 3.15: Temperature evolution during a thermomechanical test (S55 sample at 600°C). u_T = ± 30°C

First of all, it can be seen that the thermocouple was not able to measure properly the self-heating of the material. It is worth noting that ROI measurements (based on a polygon covering the shear zone) reported an average value of the temperature reached within the zone, which implied that the temperature rise suffered by the material could

be, at some points, higher than the one reported as was proved by the temperatures reported based on the 3x3 measurement cursor located in the centre of the shear zone. This aspect may be extremely important for the tests at high temperatures as, in some cases, higher temperature could induce phase transformations. The real temperature reached by the ROI was around 10% higher than the set one.

Based on previous results, the ROI measurements were used to compare the temperature evolution depending on sample geometry under the different conditions tested. The results obtained at room temperature are shown in Figure 3.16. It can be seen that the temperature progressively increased up to the point when drastic failure took place. Because of the crack, a notable temperature rise was observed. Furthermore, the heating rate was observed to be slightly higher for the S45 sample, then S505 and, finally, S55, as expected based on the force results presented in Figure 3.5. It is worth mentioning that these results follow the same trend as the one reported based on strain rate measurements that will be presented in Section 3.4. All the samples failed at a temperature close to 50°C.

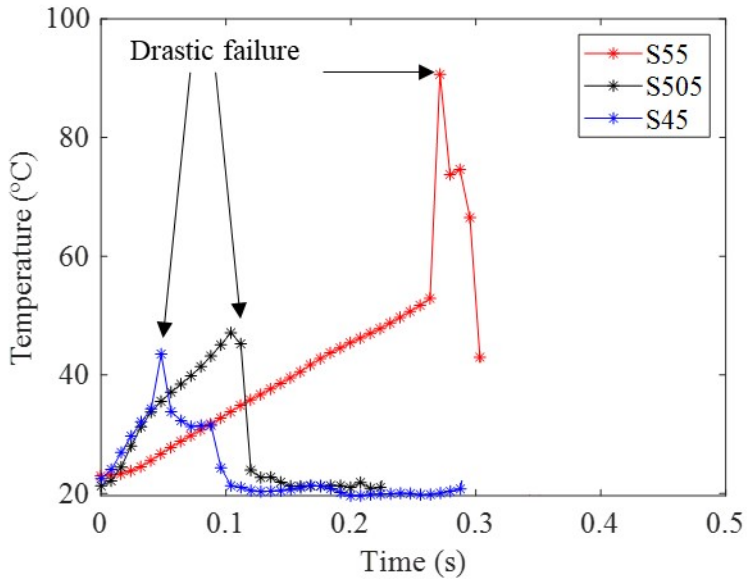

Figure 3.16: Temperature evolution during a thermomechanical test at room temperature for the three geometries analysed. Compression speed: 1.9 mm/s

The same analysis was carried at 600°C as Figure 3.17 shows. In this case, different behaviours were found. The S505 sample drastically fails suffering a notable temperature rise due to this drastic failure whereas for S45 sample the damage propagates progressively instead of causing a drastic failure. This could be due to the different load modes, as a compression component was observed for the S45 sample whereas pure shear was proved to occur for the S505 sample. In addition, S55 sample seemed not to fail as the temperature is progressively increasing during the test although the microstructural

analysis showed that the crack had been started to propagate (see Figure 3.7). The same trend was observed analysing the heating rate, being almost equal for the S45 and S505 samples, up to the drastic failure, and notably lower for the S55.

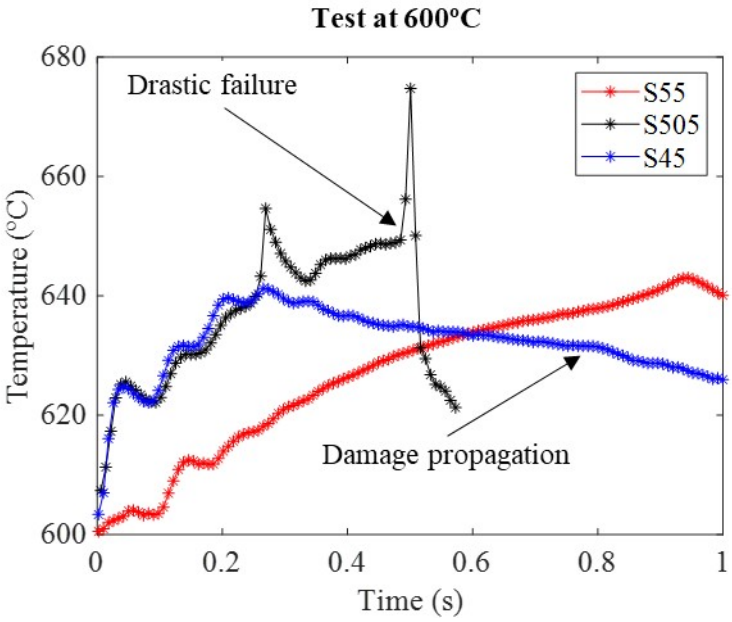

Figure 3.17: Temperature evolution during a thermomechanical test at 600°C for the three sample geometries analysed. Compression speed: 1.9 mm/s

Finally, for the tests at 900°C the results are shown in Figure 3.18. First, it should be noted that, at these high temperatures, notable heat losses took place which led to a temperature reduction of around 20°C at the beginning of the test, the real temperature being lower than the programmed one. Therefore, the temperature decreased because of heat losses as the heat generated was lower than the heat dissipated into the surroundings. Then, the temperature rise observed was due to the self-heating of the material.

It can be seen that the temperature for the S45 sample was notably higher than the other ones. This overheating may be due to geometrical effects as the temperature was controlled by a K-thermocouple located as close as possible to the region of interest as it was previously mentioned. This issue should be also taken into account as the temperature in the ROI was higher than the expected one, which could influence material properties and microstructure. This non-homogeneity during the heating can be observed in Figure 3.19.

In order to analyse the effect of initial temperature of the sample on the self heating, the evolution of the temperature rise over time was analysed as shown in Figure 3.20 (taking as reference the real temperature at the beginning of the test).

In general, at the beginning of the test no significant differences were found at room temperature and at 600°C. Then, as the test progressed, the room temperature case

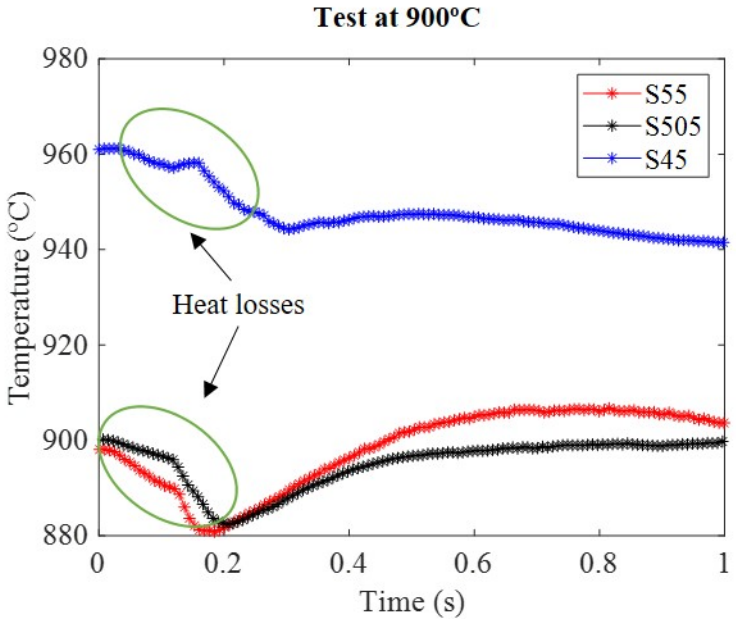

Figure 3.18: Temperature evolution during a thermomechanical test at 900°C for the three geometries analysed. Compression speed: 1.9 mm/s

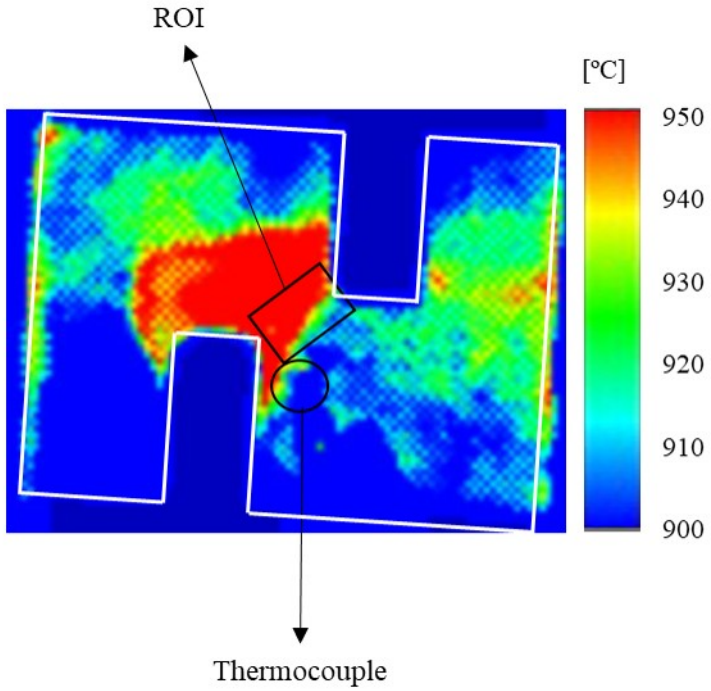

Figure 3.19: Example of the inhomogeneous heating of the S45 sample at 900°C

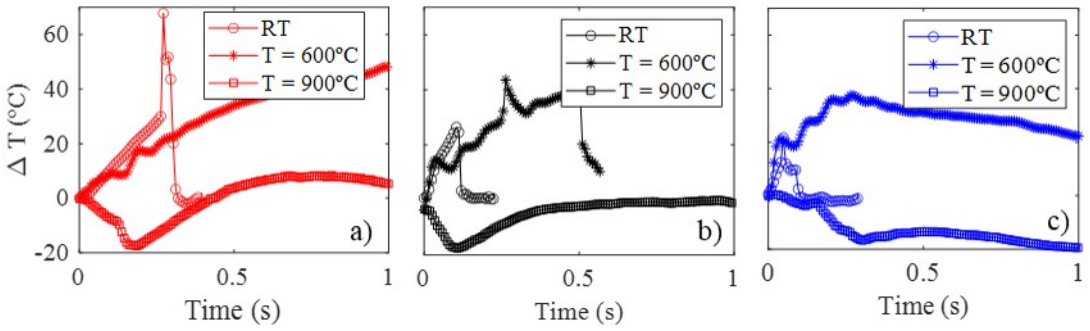

Figure 3.20: Evolution of the self-heating over time suffered for each sample at the different temperatures analysed: a) S55; b) S505 and c) S45

reached higher temperature rises in all the cases. In addition, it can be seen the importance of radiation losses at 900°C.

Summarizing, based on the results presented above, the following conclusions can be highlighted:

- The emissivity was observed to be higher at the highest temperature due to oxidation of the sample. In addition, it was observed that the effect of the geometry on the emissivity could be negligible.
- The control of the temperature based on single point thermocouple measurement for compression-shear samples was not appropriate as it could not be placed in the centre of the ROI because it would hamper the infrared filming and change the heat flux. Therefore, the temperature measured by the thermocouple and the real temperature in the region of interest were different. For instance, it was observed that the S45 sample, in the region of interest, was heated more than 60°C the set temperature. This issue could have a notable influence on material performance during the test.
- Thanks to the infrared camera, the self-heating suffered by the material during deformation was measured, leading to a non-negligible temperature rise because of the plastic work done. Thermocouples were not able to capture this phenomenon.
- At 900°C the heat losses suffered led to a temperature reduction of more than 20°C at the beginning of the test. This aspect is highly relevant and should be taken into consideration when material characterization is being carried out.

3.4 STRAIN AND STRAIN RATE MEASUREMENTS

The knowledge of plastic strain and strain rate during a mechanical process is of wide relevance to understand material behaviour and to carry out material characterization

properly. In general, plastic strain is usually determined with theoretical approaches which are limited by a high amount of assumptions. Therefore, an in-situ full-field measurement of the plastic strain would be of great interest in order to validate these approaches and to extrapolate the developed methodology to more complex processes such as orthogonal cutting experiments.

3.4.1 *Speckle pattern creation and measurement protocol*

Strain and strain rate measurements were carried out based on DIC and using high speed filming. The first step was to find a proper methodology to create the speckle pattern with good adhesion and ensuring a high density of speckles.

3.4.1.1 *Speckle pattern creation*

The method employed to create the pattern was speckle painting technique as it is widely accepted in literature to carry out DIC measurements in this kind of tests because of its simplicity and cheapness. The test at 600°C with the S55 sample was taken as reference to test the different possibilities. The aim was to find a proper technique to obtain a surface with a good speckle pattern in order to measure strain at high temperatures. Therefore, the goal was to check the capability of the technique of being employed (in terms of adhesion, brightness or paint crack) rather than create the best possible speckle pattern.

Eight different techniques were tested varying the surface finishing between polishing (etched and not), WEDM surface and sandblasting. White speckles were randomly sprayed with Molydal NB 25 which consists of small particles of boron nitride. This paint works at temperatures up to 1000°C. Some of the surfaces were previously painted black trying two different paintings, PYRO FEU matt black anti-caloric paint, resistant at high temperatures (up to 900°C) and AREMCO HiE-Coat 840-MX ceramic-based which is a black pigmented coating for metals up to 1300°C.

It is important to note that AREMCO paint needs a curing process to ensure the adhesion and resistance of the coating. For this reason, two different curing paths were analysed. The longest one which consisted of 2 hours at 200°C and 2 days at 100°C and the shortest one, consisting of 2 hours at 200°C and 1 hour at 150°C. To sum up, all the combination tested are included in Table 3.4 whereas the obtained speckle pattern with each combination is shown in Figure 3.21.

Based on Figure 3.21, without any kind of black coating (M1 to M3), good adhesion of the white paint was observed. However, these three techniques reported problems with the brightness during the test which was proved to negatively affect DIC performance. In contrast, polished and etched surface obtained following M7 method reported adhesion problems with the black coating due to the low surface roughness obtained after the polishing operation.

Table 3.4: Methods tested to create the speckle pattern: Pol. = Polished; Etched = Chemical etched with Kroll's reagent; Sandb. = Sandblasting

Method	Surface finish	Black painting	Curing	White speckles
M1	WEDM	✗	✗	✓
M2	Pol.	✗	✗	✓
M3	Pol. + Etched	✗	✗	✓
M4	WEDM	PYRO FEU	✗	✓
M5	WEDM	AREMCO	Short	✓
M6	WEDM	AREMCO	Long	✓
M7	Pol. + Etched	AREMCO	Short	✓
M8	Sandb.	AREMCO	Short	✓

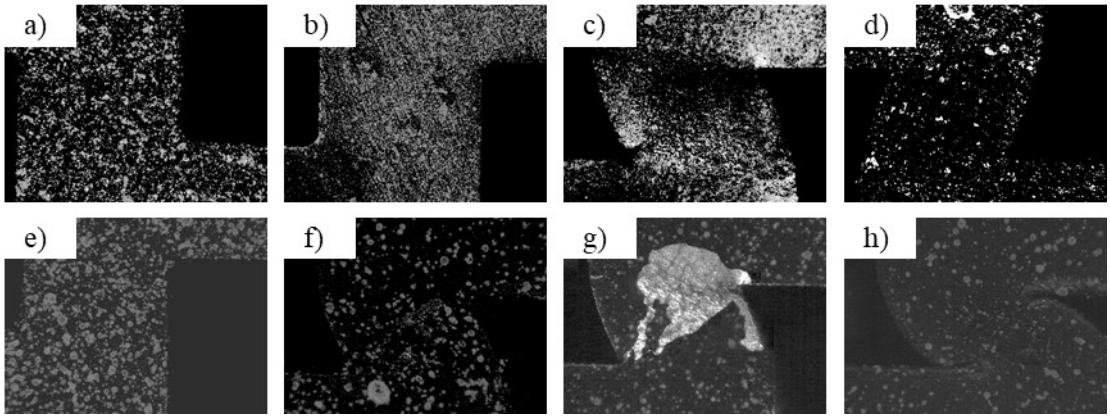

Figure 3.21: Speckle patterns generated with a) M1; b) M2; c) M3; d) M4; e) M5; f) M6; g) M7 and h) M8

To follow, when the surface was black painted with the anti-caloric PYRO FEU painting, because of the combination between high temperature and deformation, it was not matt enough during the test (M4, see Figure 3.21d). Then, the longest curing time was observed to reduce the painting plasticity causing cracking of the painting (M6). Finally, sandblasted specimen and WEDM surface with AREMCO (short curing time) showed the best results with no cracks, no problems with brightness and good adhesion (M5 and M8, see 3.21e and h).

Therefore, among all the techniques tested, at high temperature, the best technique found was M5 which consisted of: (i) the WEDM surface was directly painted in black with AREMCO HiE-Coat 840-MX; (ii) the painting was cured to ensure good adhesion; (iii) white speckles were randomly spread along the surface with Molydal NB 25. For the tests at room temperature, the procedure was similar but the AREMCO black paint was substituted by PYRO-FEU 24950-6 900°C thermal paint, making the curing process

unnecessary at this temperature. M8 method was discarded as it reported the same advantages as M5 but with the necessity of the sandblasting process.

3.4.1.2 *Strain measurement protocol*

Measurements were carried out using GOM Correlate software. After determining the best option to create the speckle pattern, the quality was analysed based on software analysis as shown in Figure 3.22. The noise error on plastic stain measurements was quantified analysing the equivalent plastic strain obtained between 100 frames with the sample fixed between the anvils without movement. The quantity determined was the equivalent plastic strain according to Von Mises criterion. The variation of plastic strain between these 100 frames were lower than 0.005 for the whole set of conditions tested.

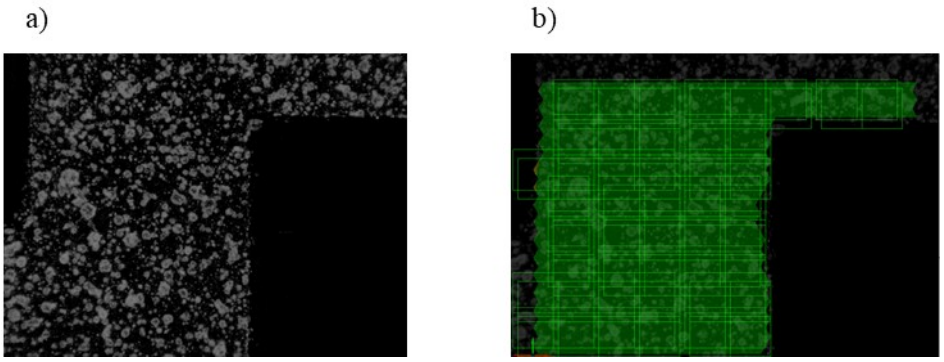

Figure 3.22: a) Example of an speckle pattern employed for DIC analysis (S55 sample at 600°C); b) Quality of the speckle pattern created according to GOM Correlate software

The speckle sizes were in the range from 0.02 to 0.12 mm. Because of the intense distortion expected (due to severe shear strain), the subset size was set to 60 pixels (which is 0.35 mm) with a step size of 20 pixels according to Society, 2018. The subset size is the width of the square to mesh the reference image. The step size is the distance between subset centres.

3.4.2 *Strain and strain rate measurements results*

In this section, the experimental strain and strain rates are presented. The strain values were reported according to the equivalent plastic strain based on Von Mises criterion. To analyse the strain evolution with time, different points were selected along the shear zone. The equivalent plastic strain evolution at two different points for the S55 sample for the three temperatures is shown in Figure 3.23. In addition, the thickness of the shear zone was determined to be 1.38 mm.

As can be seen, the strain field was similar to the strain fields showed by Bao and Wierzbicki, 2004, which is associated with a shear mode. The strain evolution was not

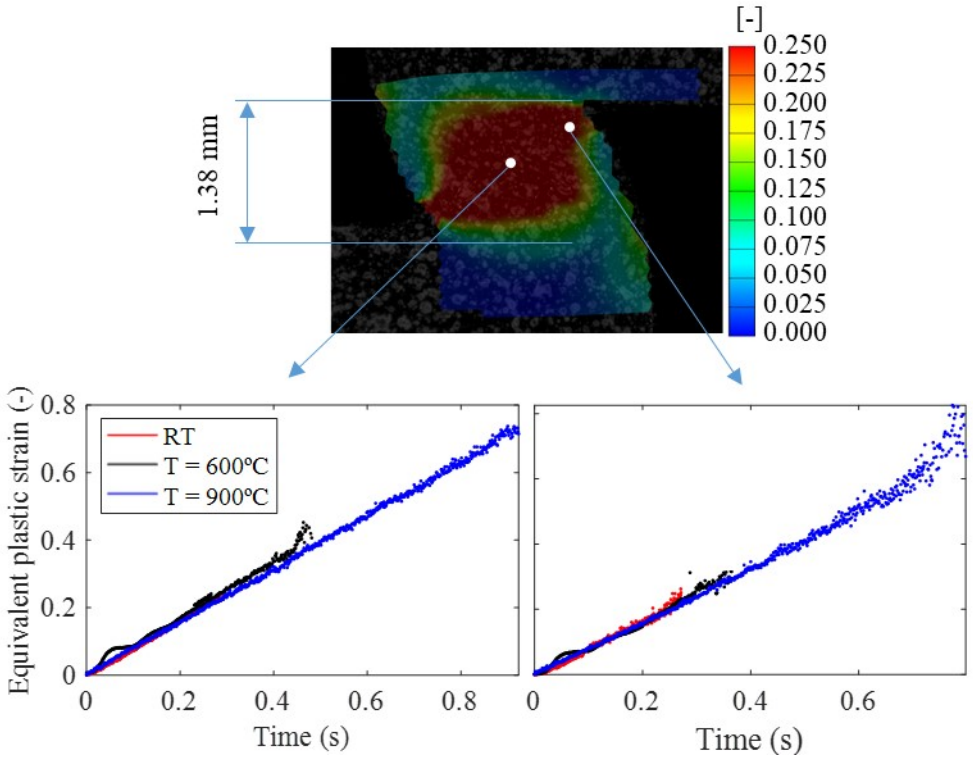

Figure 3.23: Evolution over time of the equivalent plastic during a compression test for S55 sample at two different points, one placed in the centre of the sample (left) and the other in the corner of the ROI (right)

temperature dependent, proving that strain evolution is mainly defined by the geometry and the material. In addition, when the temperature was higher the reached strain was also higher, which is associated with a higher ductility. Finally, close to the boundary, in the corner, the equivalent strain to failure was lower than in the centre of the sample, as the fracture was observed to start in the lateral and then suddenly spread to the centre, especially at room temperature. The strain rate measured for the three tests with the S55 sample was around 0.85 s^{-1} (the compression speed being 1.9 mm/s).

The same analysis was carried out with the other geometries. For instance, strain evolution for the S505 sample could be observed in Figure 3.24. First, it is worth noting that higher dispersion was observed at the end of the test, especially for the lateral positions as the crack was observed to start in the free surface and then spreads to the centre of the sample causing the drastic failure.

For this geometry, also drastic failure was observed at 600°C, which is in agreement with the force measurements shown in Figure 3.5. As in previous case, the strain field has the typical shape related to a shear deformation. In general, the effect of the temperature on strain field seemed to be negligible. However, in the case of the points located in the

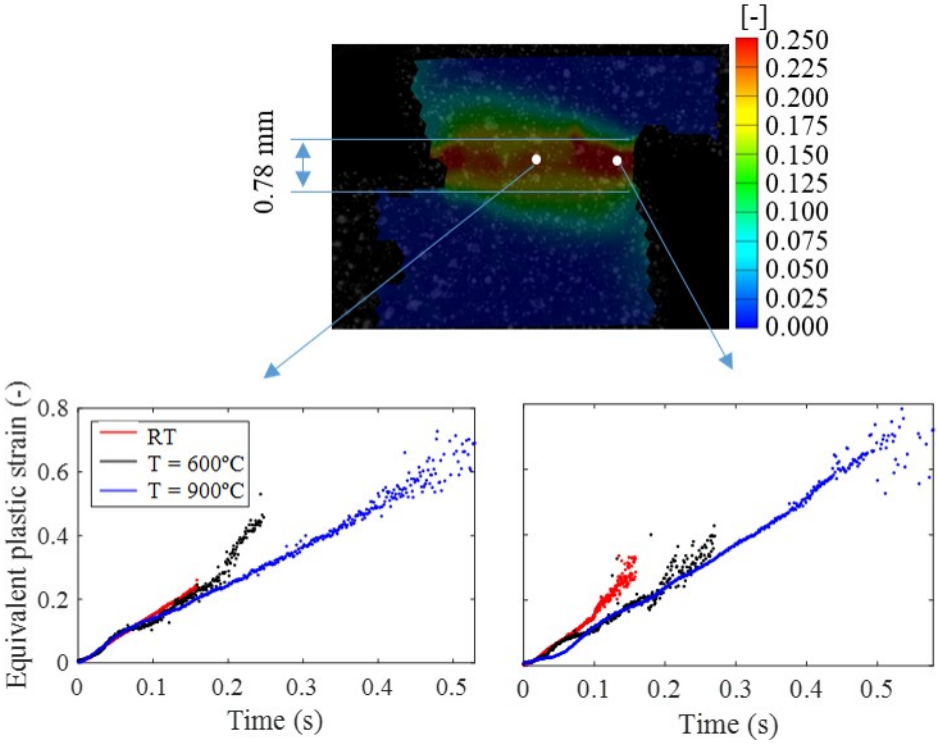

Figure 3.24: Evolution over time of the equivalent plastic during a compression test for S505 sample at two different points, one placed in the centre of the sample (left) and the other in the corner of the ROI (right)

lateral of the sample higher dispersion was observed. Within this zone, the slope slightly changes, especially at room temperature, which means higher strain rates, in this case, being around 1.5 s^{-1} for a compression speed of 1.9 mm/s.

Concerning S45 case, the evolution of plastic strain over time is shown in Figure 3.25. First, it is worth mentioning that decorrelation problems were found at 600°C so these results should be taken with care. The strain field showed the typical shape associated with a combination between compression and shear, similar to the ones shown by Dorogoy et al., 2015. In addition, between room and highest temperature cases, the strain evolution was almost equal till the failure began in the room temperature case. The calculated strain rate was around 3 s^{-1}. It should be noted that the experimental strain rates obtained are in agreement with the heating rates shown in Section 3.3.2. Furthermore, the shear zone thickness was around 0.4 mm which means that the strains are localized in a lower area which could explain why this sample began to failure before. It was not possible to obtain strain values at times higher than 0.3 s as the intense distortion suffered by the pattern caused the painting to crack and decorrelation problems.

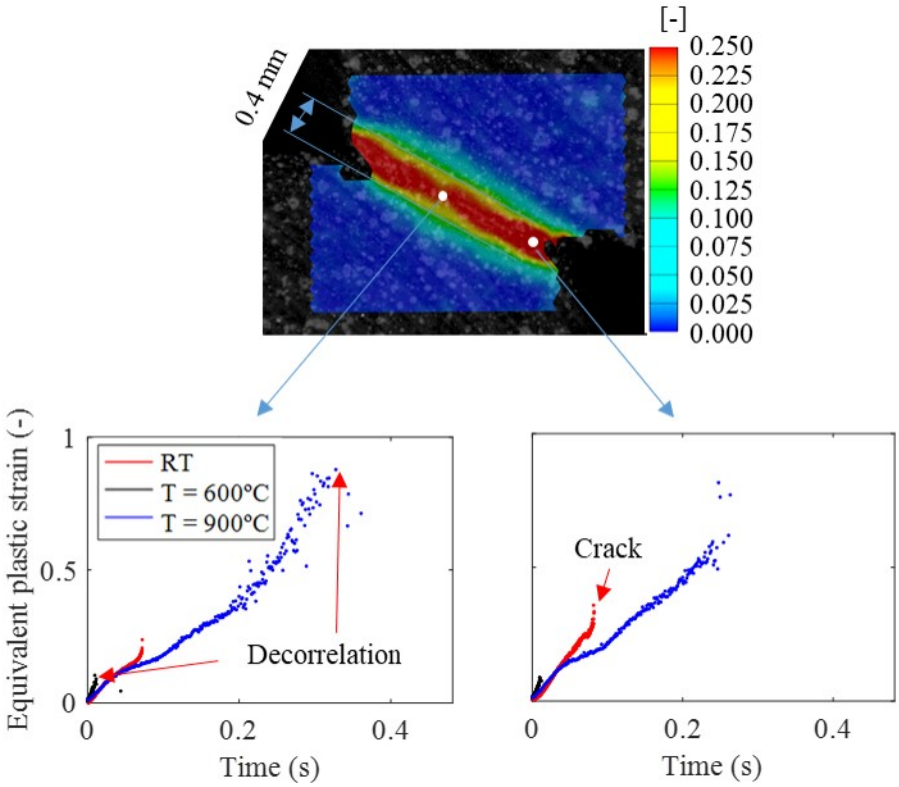

Figure 3.25: Evolution over time of the equivalent plastic during a compression test for S45 sample at two different points, one placed in the centre of the sample (left) and the other in the corner of the ROI (right)

3.4.3 *Strain and strain rate measurements validation*

The theoretical shear strain within a shear mode could be analytically determined according to equation (6). The aim of this section is to compare analytical and experimental approaches in order to prove the capability of the designed geometries to reproduce different load modes such as compression and shear. Experimental results were also compared with numerical results employing the FEM model explained in Section 3.1.2

$$\gamma_{theo} = \frac{\Delta l}{w_s} \tag{6}$$

where γ_{theo} is the theoretical shear strain, Δl is the displacement measured by the Gleeble with a longitudinal extensometer and w_s is the thickness of the shear zone, shown in Figures 3.23-3.25.

Based on this shear strain, the equivalent plastic strain could be analytically estimated taking different approaches. For instance, Shrivastava et al., 1982 proposed the following equation for a simple shear test. This approach was also taken by Hor et al., 2013a.

$$\varepsilon_{eq} = \frac{\gamma_{theo}}{\sqrt{3}} \tag{7}$$

A more complex approach was taken by Stüwe, 2003, also under simple shear assumption. The approach, shown in equation (8), reports similar values as equation (7) but could be useful to better reproduce simple shear assumption at higher shear strains.

$$\varepsilon_{eq} = \frac{1}{2} \ln \left[\frac{1 + \left(\sqrt{\frac{\gamma_{theo}^2}{4} + 1} + \frac{\gamma_{theo}}{2} \right)^2}{1 + \left(\sqrt{\frac{\gamma_{theo}^2}{4} + 1} - \frac{\gamma_{theo}}{2} \right)^2} \right] \tag{8}$$

Similarly, Polakowski and Ripling, 1966 stated that, for large shear strains, equation (7) becomes:

$$\varepsilon_{eq} = \frac{2}{\sqrt{3}} \ln \left[\frac{1}{2}\gamma_{theo} + \sqrt{\left(1 + \frac{1}{4}\gamma_{theo}^2\right)} \right] \tag{9}$$

Recently, Pardis et al., 2017 proposed different equations for large shear strains under simple shear conditions, equation (10), or under pure shear conditions, equation (11).

$$\varepsilon_{eq} = \sqrt{\frac{4}{3}\left[\ln\left(\sqrt{\gamma_{theo}^2 + 1}\right)\right]^2 + \frac{\left(\tan^{-1}\gamma_{theo}\right)^2}{3}} \tag{10}$$

$$\varepsilon_{eq} = \frac{2}{\sqrt{3}} \ln \left[\sqrt{\gamma_{theo} + \sqrt{(1 + \gamma_{theo}^2)}} \right] \tag{11}$$

Therefore, the equations (7) to (11) represent the whole set of possibilities representing shear deformation modes, reporting the average strain within the field.

The measurements shown in Section 3.4.2, for S55 and S505 samples (the ones that had a triaxiality of zero), should be in accordance with the results reported by these equations. These equations reported almost the same value at relatively low shear strains (lower than 2). Nevertheless, the difference between the resulting equivalent strain when this shear strain is higher becomes significant, conditions reached for the tests at 900°C.

For the S55 case, it can be seen that the experimental points were located in the regime defined by the equations presented above (see Figure 3.26), proving the capability of this sample to reproduce a shear mode. A similar behaviour was found with S505 sample (see Figure 3.26). Therefore, it can be seen how a slight change on sample definition could vary the experimental conditions (higher strain rates as the shear zone thickness was lower) allowing different conditions to be tested by using the same set-up disposition.

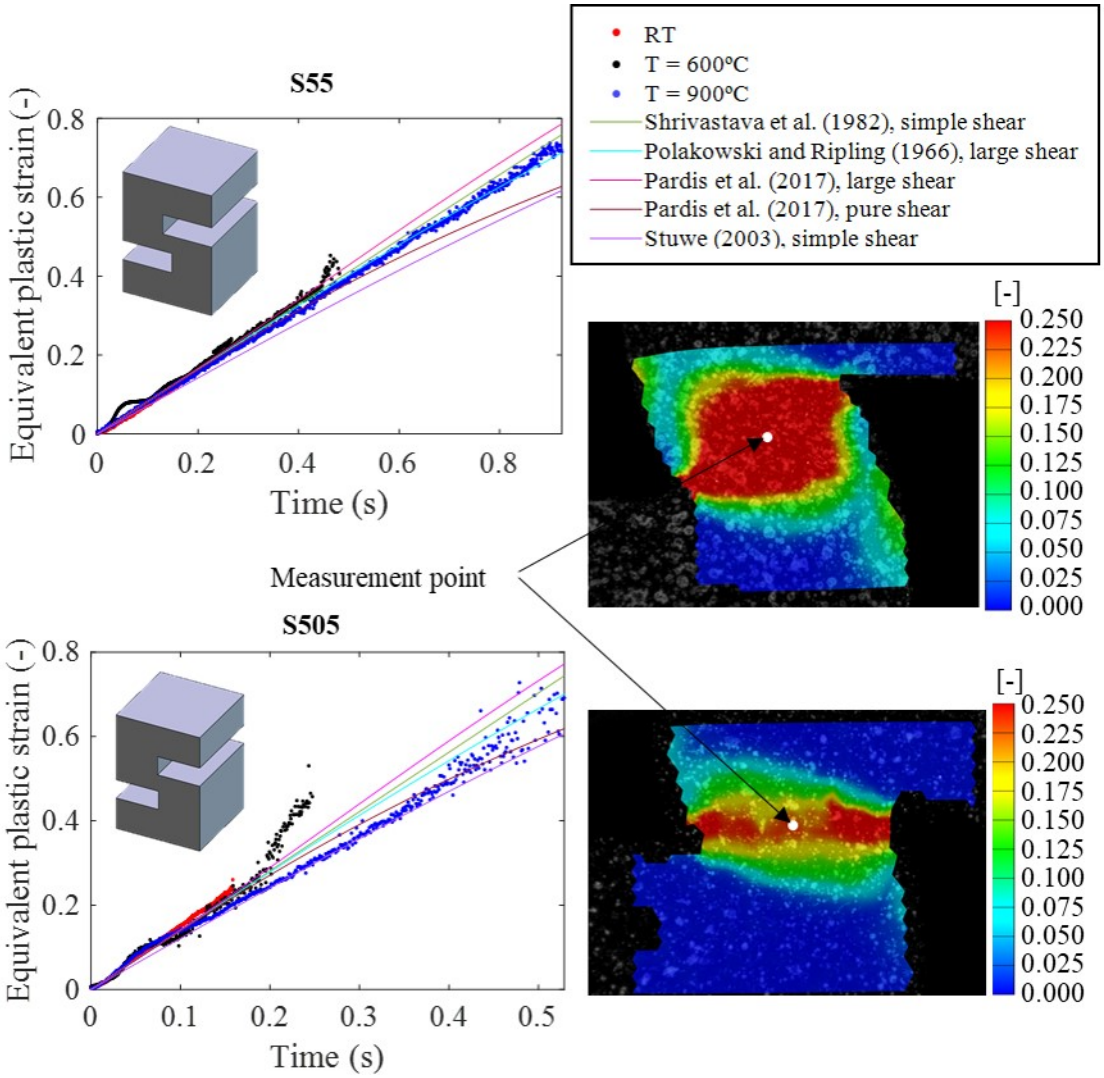

Figure 3.26: Comparison between analytical and experimental equivalent plastic strain for S55 and S505 samples at the three temperature tested

The results were also compared with those reported by the FEM model. For instance, for the S55 sample deformed at room temperature and 600°C, the results are shown in Figure 3.27 and Figure 3.28, respectively. As can be seen, the flow behaviour is well

predicted by the model at both temperatures, the strain fields reported being in agreement. However, the strain to failure predicted by the model is lower than the one measured. This suggests that the ductile failure law could be improved. As the main objective of this study is related to orthogonal cutting, this aspect will be discussed more in depth in further sections (see, for instance, Section 4.4). Similar results were obtained with the other geometries not being included here.

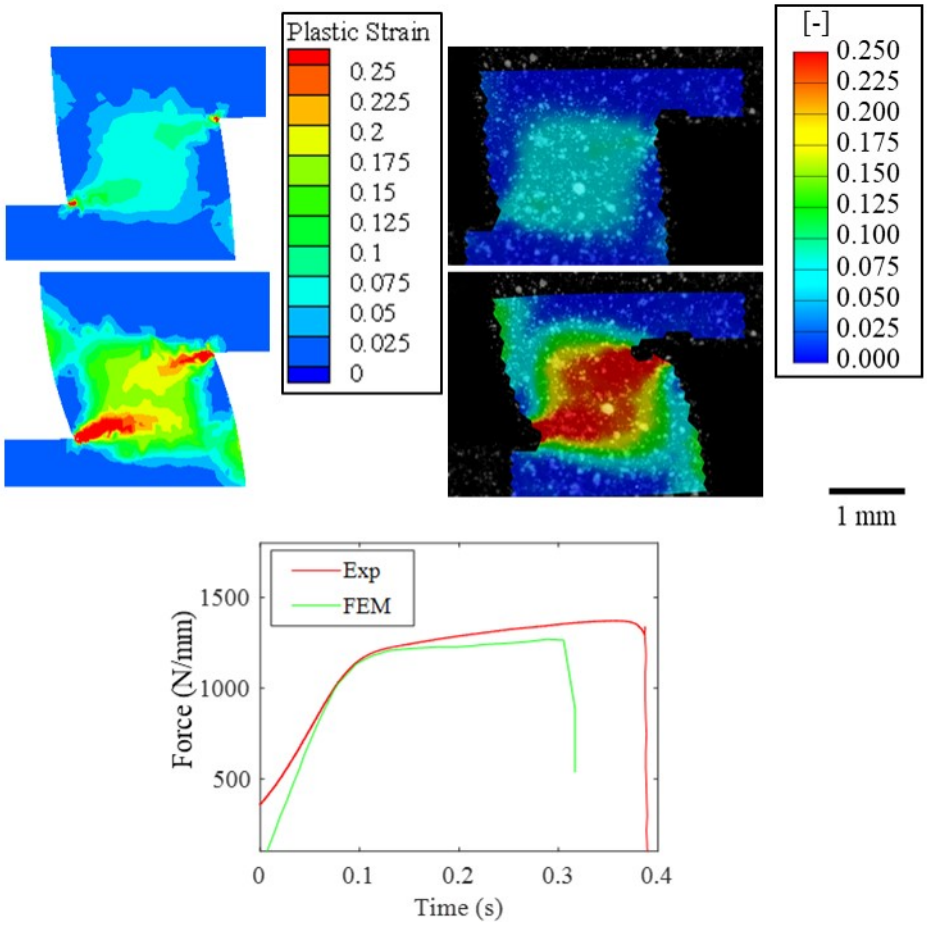

Figure 3.27: Comparison between numerical and experimental equivalent plastic strain for S55 sample at room temperature at two different times (0.1 and 0.25 s). Experimental and numerical forces are also included

Finally, with regard to the S45 sample, a combination between compression and shear would be expected (see Figure 3.6). Thus, the force applied was decomposed into two different effects, the shear action and the compression action (see Figure 3.29a) taking into consideration the sample definition shown in Figure 3.2.

The stress triaxiality was analytically estimated. For this calculus, plane stress conditions were assumed neglecting possible forces in the out of plane direction. The dimensions

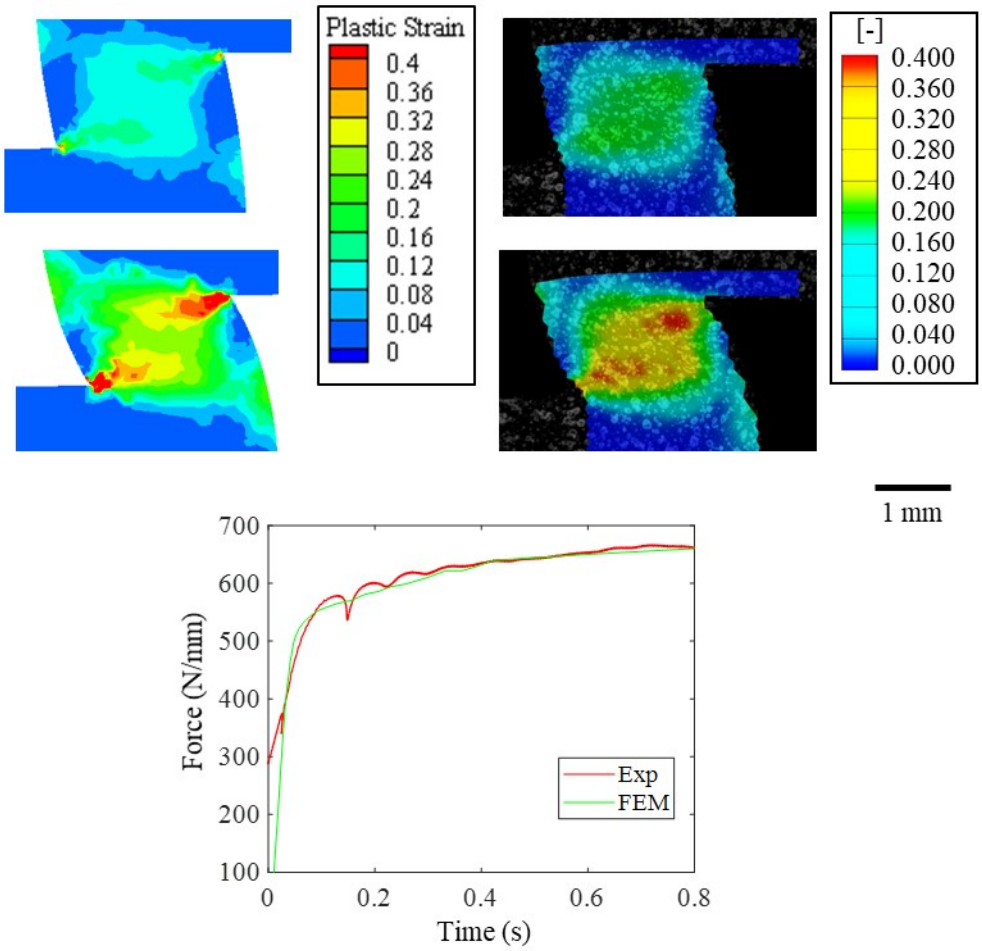

Figure 3.28: Comparison between numerical and experimental equivalent plastic strain for S55 sample at 600°C at two different times (0.1 and 0.5 s). Experimental and numerical forces are also included

of the sample in order to determine the compression and shear stresses are shown in Figure 3.2. Once these stresses were obtained, the stress triaxiality was determined for the three temperatures to be around 0.1, in agreement with the numerical results. According to different authors (Bao and Wierzbicki, 2004; Dorogoy et al., 2015), stress triaxialities between 0.02 and 0.15 represent a combination of shear and compression. Therefore, to calculate the equivalent plastic strain analytically to validate the obtained values, the effect of compression was taken into consideration. The shear strain component was calculated through equation (6) whereas the compression strain component was calculated according to equation (12).

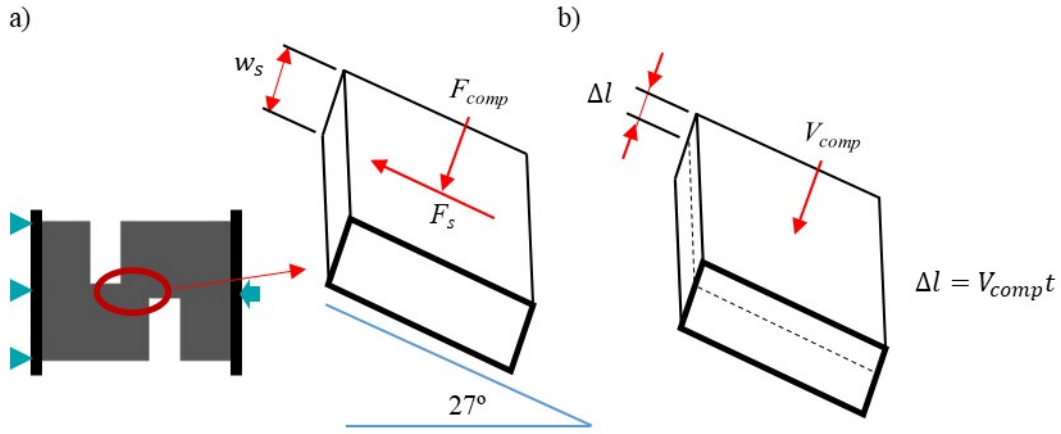

Figure 3.29: a) Force decomposition proposed for the S45 sample which combines the shear (F_s) and compressive (F_{comp}) actions; b) Representation of the compression distance to be used in equation (12)

$$\varepsilon_{comp} = \ln\left(\frac{w_s - V_{comp} \cdot t}{w_s}\right) \tag{12}$$

where V_{comp} is the compression velocity normal to the shear zone, determined employing the same decomposition shown in 3.29a. The results for the S45 case are shown in Figure 3.30.

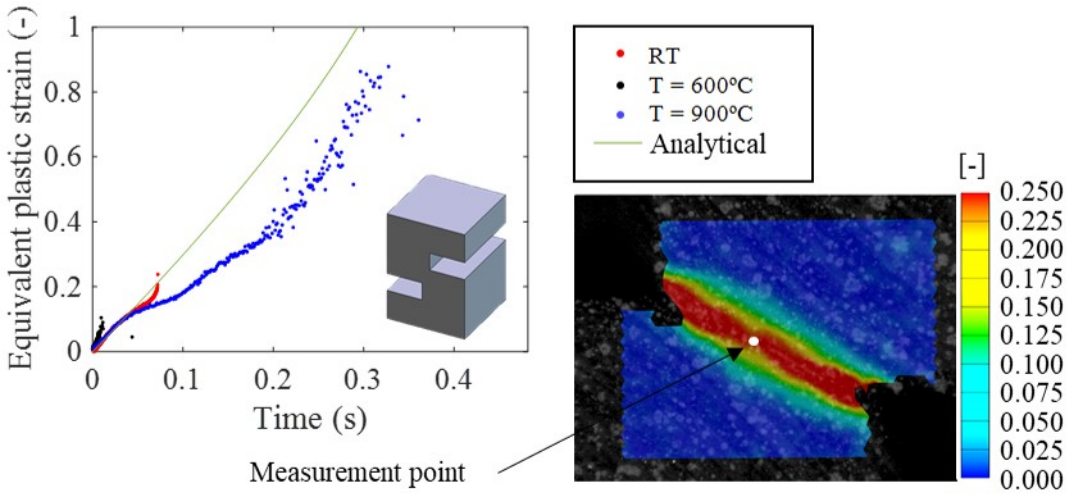

Figure 3.30: Comparison between analytical and experimental equivalent plastic strain for S45 sample at the three temperature tested

In this case, the results were in agreement only at the beginning of the test. However, at 900°C, when the reached strains are higher, there was a higher difference between the measured and the analytical strains which could indicate a change on the conditions or on the material microstructure because of the high temperature. In addition, some bending effects could take place.

Summarizing, after the strain analysis, the following conclusions can be drawn:

- Higher strain rates were obtained with the S45 geometry, enabling different conditions to be tested by only applying small changes in sample definition. These results are in agreement with the temperature measurements shown in Section 4.2.
- The design of the samples allowed the process to be filmed. This, together with the speckle painting method found, permitted the plastic strain to be measured as valuable input to validate the numerical models and to determine the plastic strain to failure.
- A proper methodology to measure equivalent plastic strain and strain rate under different conditions including high temperatures (up to 900°C) was found reporting accurate results. The plastic strain was proved to be only dependent on sample geometry not being, in general, affected by the temperature.
- S55 and S505 samples permitted the reproduction of shear conditions at different strain rates, obtaining results in agreement with analytical equations.

3.5 ADIABATIC SELF-HEATING DETERMINATION

It has been shown that the material being deformed is heated during the test because of the plastic work employed on deforming the sample. Based on infrared measurements, it has been also stated that the amount of self-heating is higher when the temperature is lower.

It has been observed in literature that different definitions are given to the self-heating which are used indistinctly. One of them, β_2, directly determines this parameter based on temperature measurements reported by infrared cameras or thermocouples, neglecting heat losses. The other definition, β_1, takes into account that the majority of the energy is converted into heat and only a small amount is absorbed by the material as stored energy in terms of dislocations and lattice defects. For this reason, very different values could be found in literature as was previously mentioned and summarized in Table 2.1.

Although both definitions are correct, it is necessary to establish a proper way to characterize the adiabatic self-heating. In addition, heat losses play an important role when the material is subjected to thermomechanical loads so they should be included in the analysis. To carry out this analysis, the S55 samples were employed as they have a higher ROI which increases the resolution of the thermal measurements to estimate the heat losses.

3.5.1 *Theoretical basis*

Mathematically, the adiabatic self-heating can be expressed as equation (13).

$$\beta = \frac{Q}{W_p} \tag{13}$$

In the present case, a shear sample was deformed. To model the heat transfer, it is not possible to assume the process as stationary. On this basis, the general heat transfer equation is given by equation (14) and the scheme of the control volume is shown in Figure 3.31. Each term in equation (14) was analysed separately.

$$W_p = Q_{\Delta T} + Q_{cond} + Q_{conv} + Q_{rad} + Q_{mt} + E_{stored} \tag{14}$$

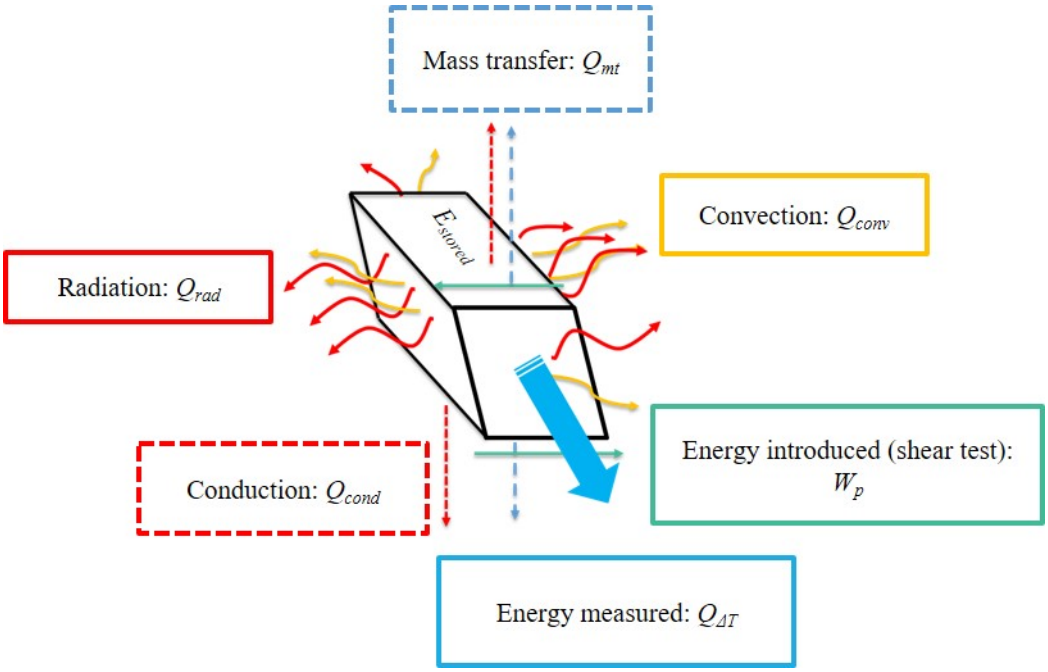

Figure 3.31: Control volume considered for the adiabatic self-heating calculus

W_p is referred to the total energy introduced by the deformation process, this means the amount of plastic work done. This term can be calculated as:

$$W_p = \int_0^{L_f} F dL \tag{15}$$

where F is the compression load and L is the displacement, that is, the area under the force curve obtained from the Gleeble tests.

$Q_{\Delta T}$ is the heat associated with the temperature rise measured with the infrared camera in the 3D control volume and can be determined according to equation (16).

$$Q_{\Delta T} = \rho c_p V \Delta T_{IR} \tag{16}$$

where ρ and c_p are the density and the specific heat capacity of the material, assumed to be constant during the test, V is the volume of the shear zone (control volume) and ΔT_{IR} is the temperature rise measured with the infrared camera. The volume of the shear zone was demonstrated to remain almost constant during the test thanks to high speed filming, with variations lower than 5%.

Several authors (Rittel et al., 2017; Härtel et al., 2018) defined the adiabatic self-heating as the ratio between the temperature rise measured and the plastic work. This has been defined as $\beta_2 = \dfrac{Q_{\Delta T}}{W_p}$ in this work.

Q_{cond} is referred to the heat exchange between the control volume and the rest of the sample by conduction (see Figure 3.31). This loss can be quantified by equation (17)

$$Q_{cond} = \rho c V d_\alpha \frac{\partial^2 T}{\partial x_i^2} = kV \frac{\partial^2 T}{\partial x_i^2} \tag{17}$$

where d_α is the thermal diffusivity of the material, T is the temperature, x_i represents the coordinate referred to the heat flux direction and k is the heat conduction. $\dfrac{\partial^2 T}{\partial x_i^2}$ was determined based on infrared measurements. Material properties were taken from literature (Li et al., 2006; Boivineau et al., 2006; Milošević and Aleksić, 2012), being the specific heat capacity 519 and 680 J/kgK and the heat conductivity 6.7 and 10 W/mK, at room temperature and at 600°C, respectively.

Q_{conv} and Q_{rad} are the heat losses of the volume control into the surroundings, representing the convection energy and the losses due to radiation, respectively. Convection losses can be calculated by equation (18).

$$Q_{conv} = A_{loss} h (T_{surf} - T_{air}) \tag{18}$$

where A_{loss} is the section of losses, this means the section in direct contact with the air, h is the heat convection coefficient of the air, which was set to 10 W/m^{2}K according to (Shitzer, 2006), T_{surf} is the average temperature of the sample measured with the infrared camera and T_{air} is the temperature of the surroundings (room temperature), both measured in K.

Likewise, the energy loss due to radiation is given by equation (19).

$$Q_{rad} = A_{loss}\varepsilon_{em}\sigma_{SB}(T_{surf}^4 - T_{air}^4) \tag{19}$$

where ε_{em} is the emissivity of the surface, measured using the infrared camera as explained in Section 3.3.1 and σ_{SB} is the Stefan-Boltzmann's constant.

Q_{mt} is related to the mass exchange between the control volume and the surroundings. This heat loss was observed, in next section, to be negligible.

Finally, E_{stored} is referred to other aspects such as restoration processes (dynamic recrystallization, recovery), the development of dislocation structures or stored lattice energy. Therefore, the adiabatic self-heating parameter, employing the definition given by Knysh and Korkolis, 2015, was defined as β_1 and can be calculated as:

$$\beta_1 = \frac{Q_{\Delta T} + (Q_{cond} + Q_{conv} + Q_{rad} + Q_{mt})}{W_p} \tag{20}$$

3.5.2 *Adiabatic self-heating results*

For the analysis, S55 sample was employed as higher shear zones were obtained, which facilitates the thermal analysis in order to calculate the heat losses. The cases analysed were at room temperature and at 600°C.

Two totally different behaviours were observed at the two temperatures as it was previously explained. When the test was carried out at room temperature, the flow behaviour shows the typical strain hardening up to drastic brittle failure when the displacement is close to 1 mm (equivalent plastic strain around 0.35). In contrast, higher ductility was observed at 600°C and no macroscopic failure seemed to take place.

Based on the DIC analysis carried out in Section 3.4, it was possible to determine the volume of the shear zone in order to define the control volume and the area of losses to be applied in equations (15)-(19). As an example, a picture of the DIC measurements is shown in Figure 3.23. As can be seen, the shear zone can be approximated by a parallelepiped, leading to a volume of 21 mm^3.

The possible heat and mass fluxes into and out of the control volume have influence on heat losses and could be relevant in the calculus of β_1. Therefore, it is necessary to determine whether some particles tend to travel out of the control volume. In order to carry out this estimation, the possible existence of velocity in Y direction would be a possible indicator. The velocity field in Y direction is shown in Figure 3.32 proving that there was no velocity in Y direction. The same result was obtained at 20°C. Thus, the heat losses due to mass transfer (Q_{mt}) were proved to be negligible.

The temperature evolution was determined by tracking a polygon ROI based on infrared measurements as was explained in Section 4.2 (see Figure 3.20). The process

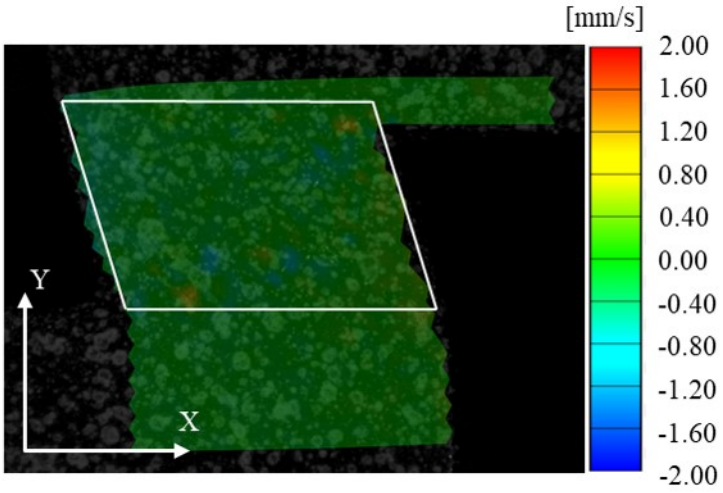

Figure 3.32: Example of the v_y field for T = 600°C

was analysed by taking measurements at different frames at both temperatures. This average temperature was used to calculate the heat losses due to convection (Q_{conv}) and radiation (Q_{rad}).

In order to estimate the heat losses due to conduction it is necessary to determine $\partial^2 T/\partial x_i^2$. Based on infrared measurements, the conduction flux along the shear zone can be reduced to a flux in Y direction as Figure 3.33 shows.

Based on Figure 3.33, it can be seen that the temperature profile along the shear zone is symmetric. Therefore, in order to numerically calculate $\partial^2 T/\partial x_i^2$ (being $x_i = Y$ in the present case) the shear zone was divided into two halves. The average value of d^2T/dY^2 was numerically calculated for each half at each analysed frame. Finally, heat conduction losses can be estimated by transforming equation (17) into (21).

$$Q_{cond} = 2k\frac{V}{2}\frac{d^2T}{dY^2} \tag{21}$$

The results obtained at 20°C are shown in Figure 3.34. The average value of β_1 during the whole test was 0.88 which is in agreement with the values reported in literature (Knysh and Korkolis, 2015). In this case, the conduction losses progressively increase with time, being close to 5% of the total energy introduced. The value of β_2 was close to 0.84. In addition, it is worth highlighting that radiation and convection losses were observed to be negligible under these conditions as they always represented less than 0.1% of the whole energy employed. The term called as "others" represents the residual in which E_{stored} is included, being around 10% in this case.

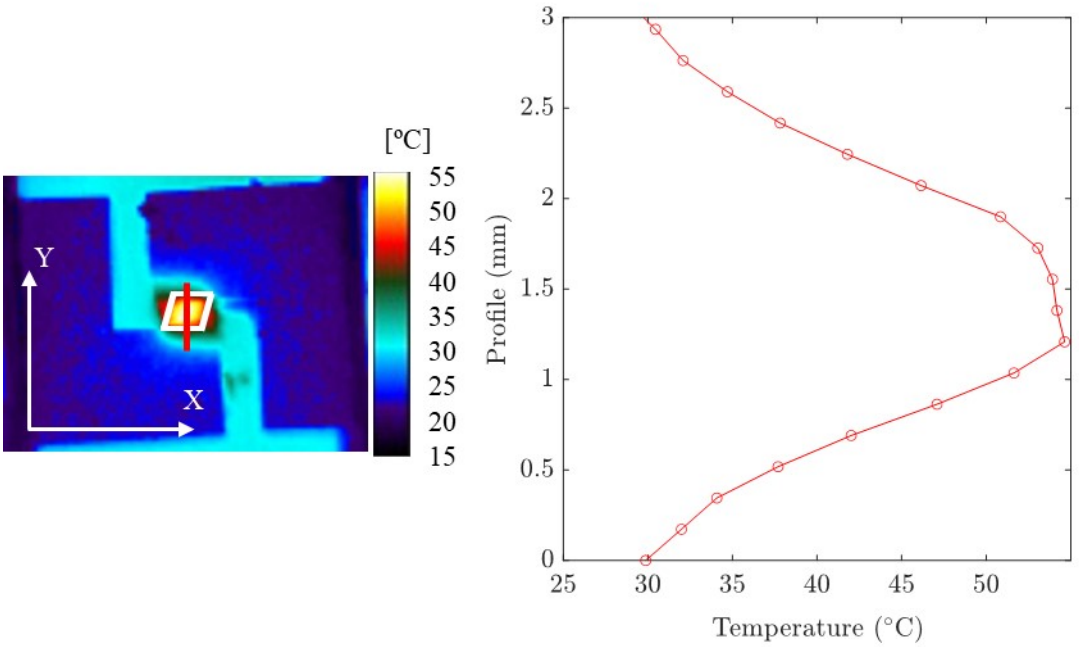

Figure 3.33: Temperature field within the shear zone at 20°C (left) and temperature profile along Y direction to determine heat losses due to conduction (right)

In this sense, according to different authors, Ti6Al4V could suffer flow instabilities at room temperature resulting in the formation of adiabatic shear bands, local melting and fracture (Kailas et al., 1994; Luo et al., 2015). In Figure 3.35 the initial and final microstructure at room temperature can be compared. It can be seen a thin affected layer where the microstructure was oriented in the fracture direction (an adiabatic shear band). This could explain the value obtained for E_{stored}.

The same analysis was carried out at 600°C as Figure 3.36 shows. Radiation represents more than 20% of all the heat losses so this term must be taken into account in the analysis to calculate β_1. Convection losses could be also relevant, representing around the 5% of the heat losses. In addition, it is worth mentioning that conduction losses increased over time, becoming more relevant at the end of the test. In contrast, convection and radiation losses remained almost constant during the test.

The average value of β_1 was 0.87, again in agreement with the values reported in literature (Knysh and Korkolis, 2015). However, the value of β_2 was 0.57 due to the high level of losses, similar to the values reported by Rittel et al., 2017. However, it is worth highlighting that the strain rates employed by Rittel et al., 2017 were much higher than in the present case.

Therefore, it can be seen that, when the heat losses were not relatively relevant (in the room temperature case radiation and convection losses are totally negligible), the values of β_1 and β_2 were quite close. These conditions are typical for tests carried out at

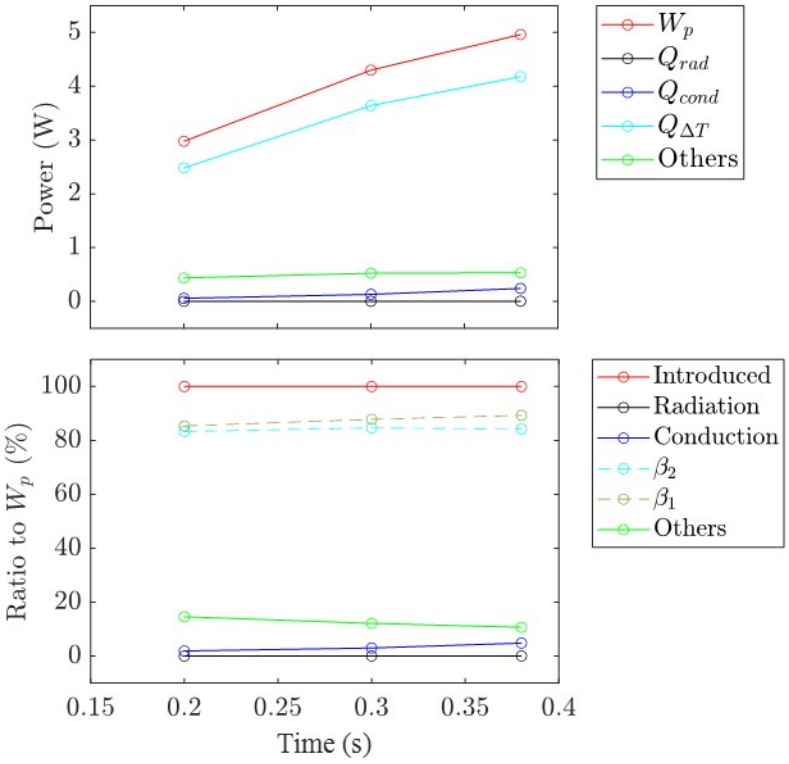

Figure 3.34: Results obtained from the test at room temperature. Calculus of power including all possible heat losses and heat losses as a percentage of W_p

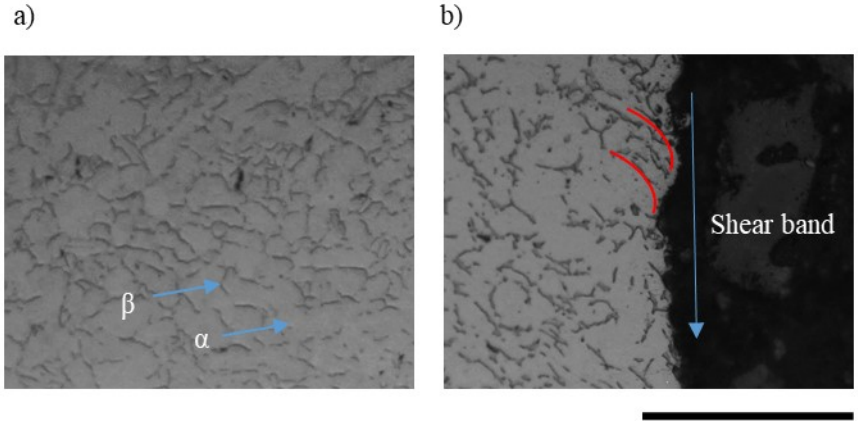

Figure 3.35: Microstructural state of the S55 sample: a) Before deformation; b) After deformation at room temperature. Example of shear band formation. Scale bar: 50 μm

high strain rates or at low temperatures, contrary to what happens at high temperatures. Finally, it was observed how the term ”others” again represented around the 10% of all

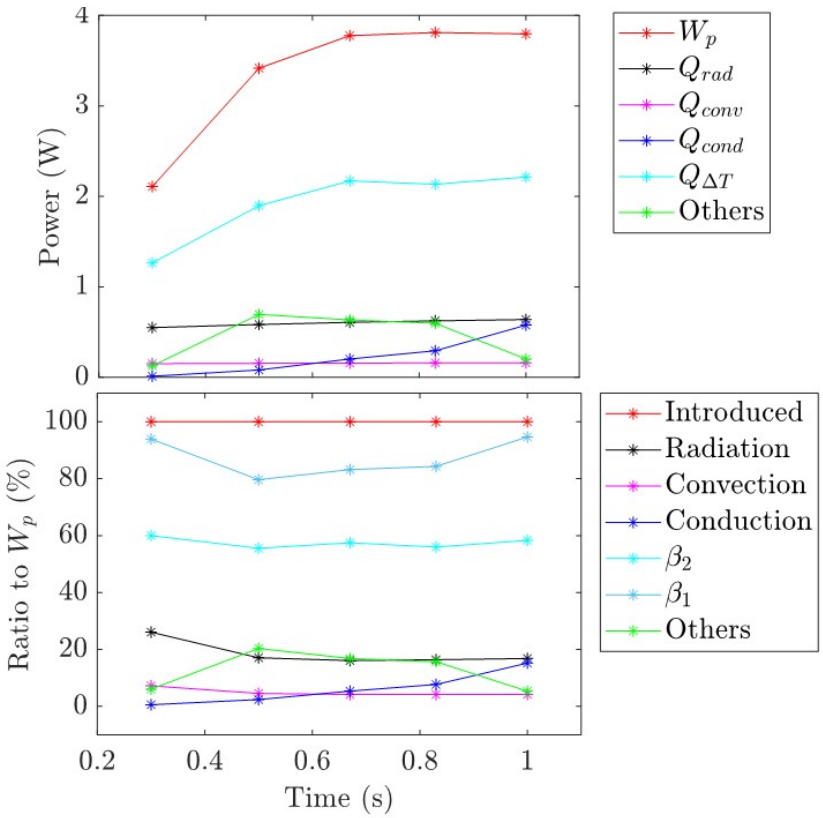

Figure 3.36: Results obtained from the test at 600°C. Calculus of power including all possible heat losses and heat losses as a percentage of W_p

energy. Under these conditions, adiabatic shear band formation is expected (Reddy et al., 2008). The microstructure before and after the deformation test is shown in Figure 3.37.

As it can be seen, the heating up to 600°C did not imply any phase change in the material. In contrast, the ductility was observed to be higher (see Figure 3.5) as the grain size was higher due to the heating, and no drastic failure was observed. Although the crack had started, there was not enough time to propagate and cause this failure. Again, shear band formation was observed. In addition, grain elongation took place close, which could be an indicator of dynamic recovery, as some authors reported (Park et al., 2002; Roy and Suwas, 2013).

The amount of energy stored was proved to be constant in the range of temperatures from 20 to 600°C, being the adiabatic self-heating coefficient (β_1) close to the widely reported 90% under both conditions. As this parameter is important in numerical simulations, if the model is able to take into account thermal losses such as radiation or convection, its value can be assumed to be 0.9 whereas if the model does not include this, which is typical for 2D models, its value should be corrected as radiation losses could represent more than 20% of all energy introduced in the system. In addition,

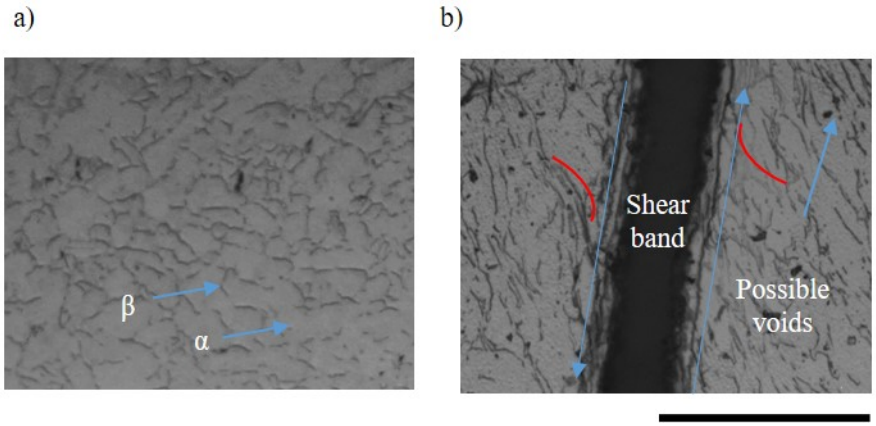

Figure 3.37: Microstructural state of the S55 sample: a) Before deformation; b) After deformation at 600°C. Example of shear band formation. Scale bar: 50 μm

this parameter is also significant in material characterization as it determines the real temperature at which the test was carried out.

To sum up, the following conclusions can be drawn:

- A technique to measure the adiabatic heating under shear conditions with a 3D control volume was proposed taking into account heat losses and the energy measured through infrared measurement proving the validity of the technique proposed at low and high temperatures.
- Different approaches were found in literature defining the adiabatic heating value. With this methodology, it was shown that, although β_1 remained almost constant at different temperatures, the value of β_2, due to the relevance of the heat losses, was notably lower when the temperature increases.
- Adiabatic self-heating parameter is of wide relevance to develop robust numerical models. If these models take into consideration the possible heat losses due to radiation, convection or conduction (typical in 3D models), this parameter could be set to the widely employed 0.9. However, when the models do not take into account these sources of losses (typical in 2D models where losses such as radiation could not be included), the value should be reduced in order to determine the real temperature of the body properly.

3.6 CONCLUSIONS

After the thermomechanical analysis, the main results that can be highlighted are:

- The new designed samples permitted the analysis of different load modes by making small changes on geometry. In addition, the design allowed also the process to be

filmed in order to measure temperatures with infrared filming and plastic strain with high speed filming.

- It was demonstrated that the temperature control through thermocouples could not be appropriate in thermomechanical testing as they could not be placed in the ROI and have influence on the heat flux, hampering the filming. The temperature measured by the thermocouple and the real temperature in the ROI could differ influencing the material performance during the test.
- The plastic strain field, measured with DIC, was demonstrated to be independent on temperature, varying depending on the employed sample. According to the numerical model, S55 and S505 samples were able to reproduce shear conditions. This was validated based on DIC measurements and analytical approaches. The numerical model was also in agreement with experimental measurements.
- Different definitions could be found for the adiabatic self-heating which are used indistinctly, this could lead to misunderstandings. Therefore, this issue has been clarified along the section. In addition, a novel methodology was developed to measure the adiabatic self-heating by using a 3D control volume instead of the 1D approaches found in literature.

4

TEMPERATURE MEASUREMENTS

The relevance of a proper temperature control during material characterization in order to develop robust and accurate models has been demonstrated. Regarding the orthogonal cutting process, temperature measurement in the shear zone is still a challenge. Workpiece temperature could be a valuable input to validate and optimize numerical models. In this sense, the use of this variable to validate numerical models is not widely found in literature and just few attempts can be identified, as is summarized in Table 2.3.

Thermocouples could be used to estimate tool temperature but they can not be employed to measure workpiece temperature in the shear zone as they would be removed during the test. In addition, they only allow single point measurements to be made, influencing the heat flux.

For this reason, infrared measurements are gaining importance as they could overcome these difficulties. Some examples could be found aiming to measure tool thermal fields during orthogonal cutting (Davies et al., 2007; Dinc et al., 2008). However, a lack of knowledge about workpiece temperature in cutting was found, perhaps due to the difficulties in determining characteristics such as the emissivity under the severe conditions reached in the shear zone.

The chapter is organized as follows. First, the experimental set-up employed was explained. Then, an in depth analysis of workpiece temperature measurements in the shear zone was carried out. To follow, the model was validated, including the validation of the ductile failure law. Finally, the infrared method was used to measure the oscillation frequency and to optimize the ductile failure law by using inverse simulation.

4.1 EXPERIMENTAL SET-UP OF ORTHOGONAL CUTTING TESTS

The set-up employed consisted of a Lagun CNC Milling centre (CNC 8070) which provides high precision and stiffness up to 30 m/min of cutting speed. During the tests, cutting forces were measured using a Kistler 9129AA dynamometer with a sampling frequency of 5000 Hz. The tool holder was set in the spindle, while the workpiece was fixed to the dynamometer clamped to the table. The set-up is shown in Figure 4.1. Thermal fields were captured through the Flir Titanium 550M infrared camera located at 30 mm of the shear zone, equipped with a macroscopic lens giving a spatial resolution of 1 pixel = 10 μm^2, with a sampling frequency of 1000 fps. The workpiece consisted of a L shape specimen. In addition, chip thickness and chip morphology were measured by mounting the chips on resin and they were polished up to mirror finishing. The cutting conditions

analysed are summarized in Table 4.1. Each condition was repeated three times to ensure the robustness of the results.

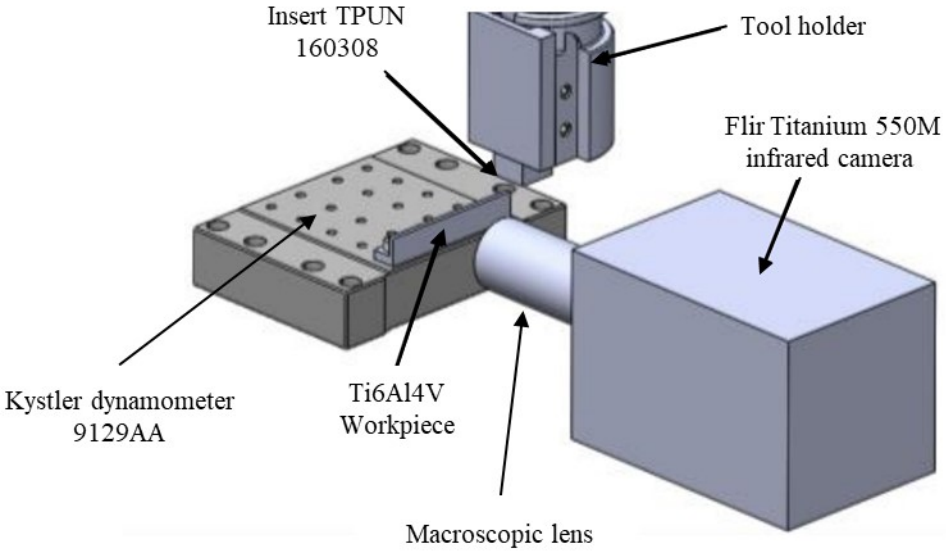

Figure 4.1: Scheme of the CNC cutting set-up

Table 4.1: Experimental conditions tested in the shear zone thermal analysis

Tool	Reference	TPUN 160308
	Rake angle, γ [°]	6
	Clearance angle, α [°]	5
	Edge radius, r_e [µm]	24
	Coating	Uncoated
Cutting conditions	Cutting speed, v_c [m/min]	2.5; 7.5; 10; 20; 30
	Feed f (uncut chip thickness) [mm]	0.1; 0.2; 0.4
	Width [mm]	4
	Lubrication	Dry

The experimental results were also compared with those reported employing the FEM model explained in Section 3.1.2. For this specific case, workpiece and tool are shown in Figure 4.2 in which the boundary conditions were also included. Remeshing ensures a proper mesh along the shear zone in order to report accurate results. The minimum element size was set to 2 µm to achieve accurate results. The residual stress analysis was activated in order to ensure also a good mesh along the machined surface. The cutting

conditions, tool geometry and tool material are summarized in Table 4.1, the width of cut being 1 mm.

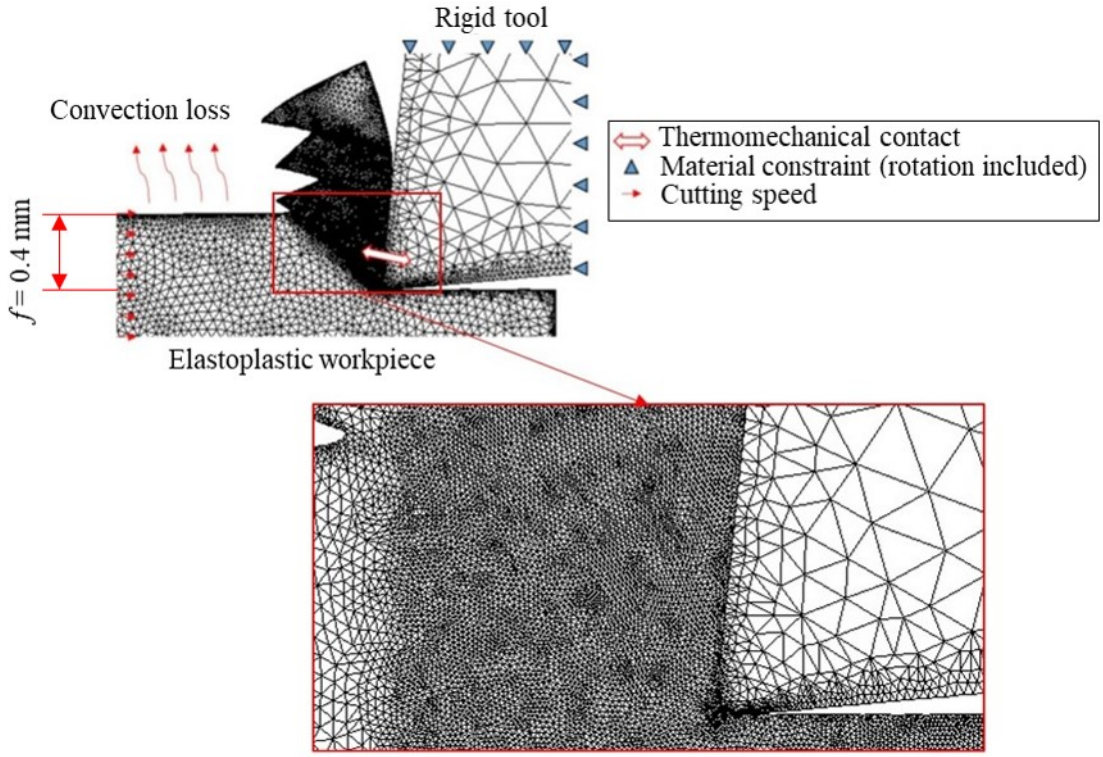

Figure 4.2: Mesh example for the orthogonal cutting case with special focus on the shear zone

4.2 SHEAR ZONE TEMPERATURE MEASUREMENTS

This section aims to carry out an in-depth analysis of the temperature in the shear zone, studying the effect of cutting conditions on it. Temperature results were combined with other important outcomes such as cutting forces, chip morphology and segmentation frequency.

The temperature in the shear zone was obtained through different measurement points (3x3 pixel^2) located at different positions and different cutting times in order to obtain a representative average of the temperature in the shear zone, as shown in Figure 4.3. Although in Section 3.3 the emissivity of Ti6Al4V was determined for dissimilar sample geometries, in this case, the surface to be filmed was previously painted black as it was not possible to put a thermocouple close to the region of interest. The aim was to ensure the highest possible emissivity as material surface emissivity is expected to vary during the test because of the high thermomechanical loads (high strain and temperatures) applied. A emissivity value of 0.8 was set to determine the temperature values. Nevertheless, it

was observed that variations lower than ± 20°C were expected by varying the emissivity between 0.6 and 1, which is in agreement with Zhang et al., 2015.

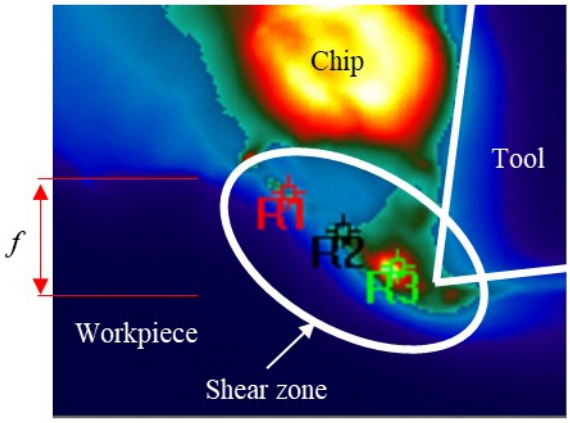

Figure 4.3: Example of a thermogram. R1, R2 and R3 represent 3x3 measurement points located along the shear zone. Cutting conditions: $v_c = 7.5$ m/min and $f = 0.4$ mm

Infrared measurements allow chip segmentation mechanisms to be studied. Chip segmentation makes the model of the machining process much more complicated as it is necessary to include a ductile failure law.

During orthogonal cutting of Ti6Al4V, at low cutting speeds, the crack, because of the lack of ductility of the material, is generated close to the tool and it suddenly propagates to the rest of the shear zone, causing the drastic failure. In terms of temperature, this phenomenon could be observed as a concentration of heat, which is due to a coupling between severe strain and cracking close to the tool. This heat then suddenly spreads to the rest of the shear zone as Figure 4.4 shows.

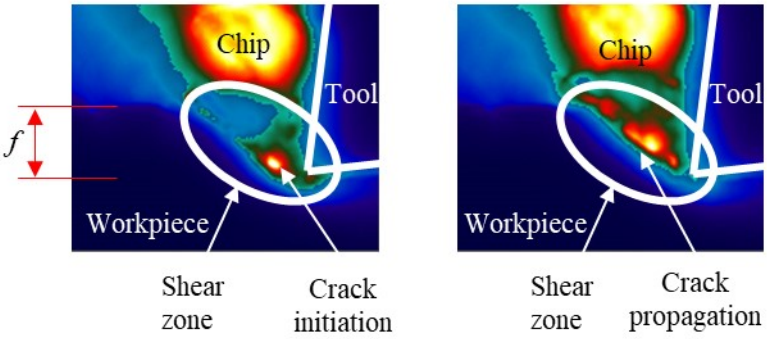

Figure 4.4: Thermal fields during orthogonal cutting of Ti6Al4V at different cutting times. Left side represents crack initiation and right side rack propagation. The time between both frames was 1 ms. Cutting conditions: $v_c = 7.5$ m/min and $f = 0.4$ mm

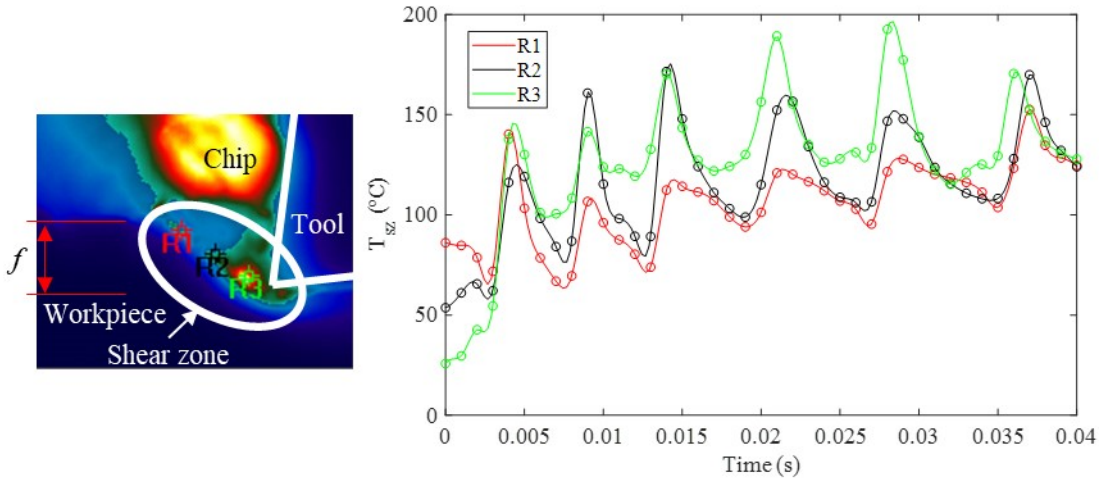

Figure 4.5: Temperature evolution on the visible surface during orthogonal cutting of Ti6Al4V at different points of the shear zone. Cutting conditions: $v_c = 7.5$ m/min and $f = 0.4$ mm. R1, R2 and R3 represent 3x3 measurement points located along the shear zone

Taking into consideration that the sampling frequency of the thermal camera, 1000 Hz, was not able to capture the sudden increase in the temperature of the shear zone it is clear that this behaviour was due to a crack propagation (mechanical phenomenon) rather than a heat propagation by conduction along the shear zone.

Because of this phenomenon, temperature notably varies along the shear zone. Although temperature is notably variable, temperature frequency associated with chip segmentation along the shear zone was observed to be independent on the selected point as Figure 4.5 shows.

It was measured that when the cutting force reached a minimum value, the workpiece temperature in the shear zone was at a maximum. This phenomenon could be observed in Figure 4.6. The increase on the cutting force yields to higher strains within the shear zone, then, when this plastic strain reaches a critical value (damage equal to 1) the crack starts, causing a notable reduction on the cutting force. The plastic work is converted into heat, implying a localized and fast temperature rise in the shear zone. Moreover, it was experimentally observed that cutting force and temperature are in counter-phase, both signals having the same frequency.

As this is a very fast phenomenon, the sampling frequency limited the analysis of chip segmentation through infrared measurements to cutting speeds up to 7.5 m/min. In addition, in order to have enough measurement resolution, high feed values (0.2 and 0.4 mm) were chosen.

Finally, the effect of cutting conditions (feed and cutting speed) on shear zone temperature was analysed based on average values obtained taking into account different times and positions along the shear zone (as shown in Figure 4.5) for the whole set of cutting conditions shown in Table 4.1. Figure 4.7 shows these effects.

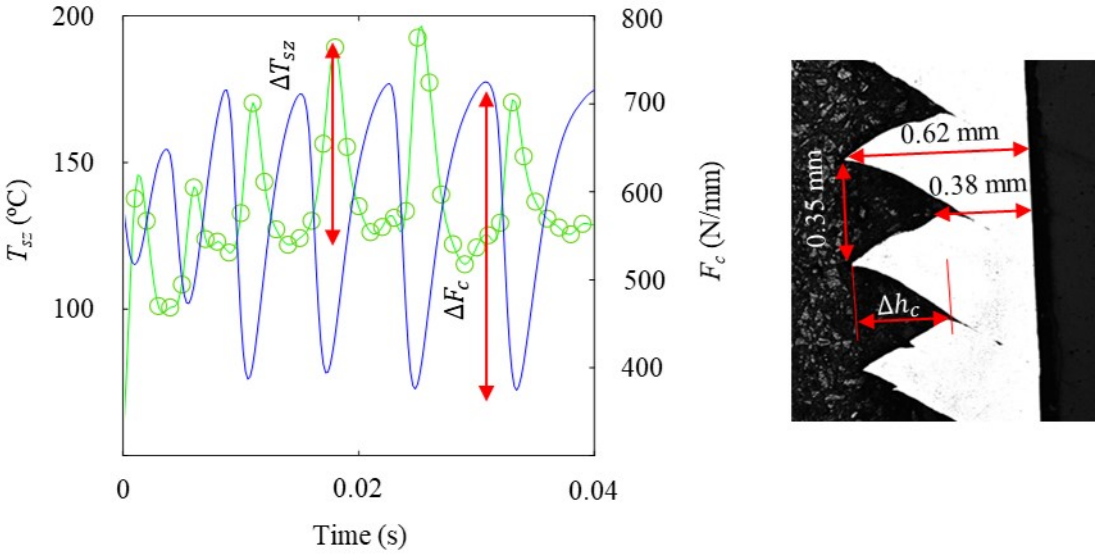

Figure 4.6: Temperature (green) and force (blue) evolution during orthogonal cutting of Ti6Al4V. Cutting conditions: $v_c = 7.5$ m/min and $f = 0.4$ mm. Cutting force and temperature shear zone signals are in counter-phase. Chip morphology also represented to show the chip segmentation. ΔT_{sz}, ΔF_c and Δh_c represent the amplitudes of the oscillations

As can be observed in Figure 4.7, the temperature in the shear zone slightly increases when the feed and the cutting speed increase. It can be clearly observed that the influence of the cutting speed is much more relevant. At low cutting speeds, up to 10 m/min, the increase of the temperature in the shear zone with cutting speed is more noticeable although it continues increasing above this speed.

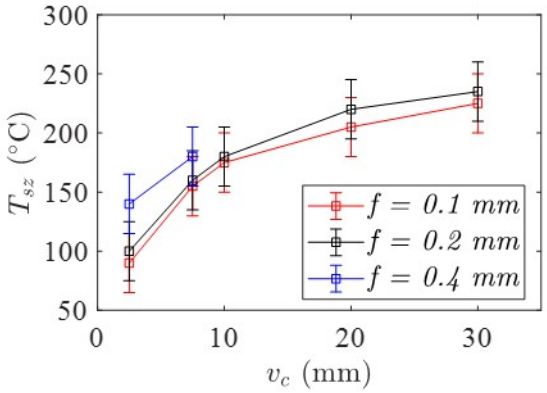

Figure 4.7: Effect of cutting seed on shear zone temperature during orthogonal cutting of Ti6Al4V at different cutting speeds

A more detailed analysis of the results including forces and chip morphology was developed to analyse chip segmentation up to 7.5 m/min. Temperature oscillation frequency also increases with cutting speed but decreases with feed as Figure 4.8 shows. Furthermore, although the temperature in the shear zone was observed to increase with the cutting speed as mentioned above, higher oscillations were measured at high feeds.

As expected, the cutting force increased with the feed and no remarkable effect of the cutting speed was found. This is assumed to be due to the fact that under these cutting conditions, at low cutting speeds, thermal effects may not be activated, causing the reduction on the cutting force due to thermal softening (Zhang et al., 2018). Regarding the amplitude of the cutting force, ΔF_c, it was higher at the highest feed.

Finally, chip morphology in terms of pitch value (distance peak to peak in a chip) and chip thickness (average and oscillation amplitude) was experimentally determined (an example could be found in Figure 4.6). It can be seen that the pitch value increases with the cutting speed and the feed. In addition, it is worth noting that, the higher the oscillation amplitude of the cutting forces, the higher the pitch values that were observed, which means higher segmentation. In this sense, higher pitch values are related to lower segmentation frequencies. Concerning chip thickness, a notable increase was found with the feed, as expected. In addition, no remarkable variation when the cutting speed is modified was found, which is in agreement with cutting force measurement.

Therefore, the following results could be highlighted:

- The temperature in the shear zone was measured through infrared measurements and emissivity variations are expected to be low, being the temperature variation around $\pm$ 20°C thanks to the black coating employed.
- The temperature in the shear zone increases with cutting speed and, slightly, with feed. This temperature rise is highly remarkable especially at cutting speeds lower than 10 m/min.
- Chip segmentation produced during machining of Ti6Al4V leads to the oscillation of relevant outcomes such as cutting forces, chip thickness and workpiece temperature. Infrared technique was employed to measure the oscillation frequency during orthogonal cutting of Ti6Al4V under different cutting conditions, proving that cutting forces and workpiece temperature in the shear zone were in counter-phase.
- It was observed that at low cutting speeds, the crack starts close to the tool and then suddenly spreads to the rest of the shear zone causing drastic failure, proving the lack of ductility of the material. This plastic work is transformed into heat observable by the thermal infrared camera.

Workpiece temperature could be a valuable input to optimize the material constitutive laws under realistic machining conditions. However, the temperature measured through infrared techniques is not representative of the orthogonal process. For this reason, in the

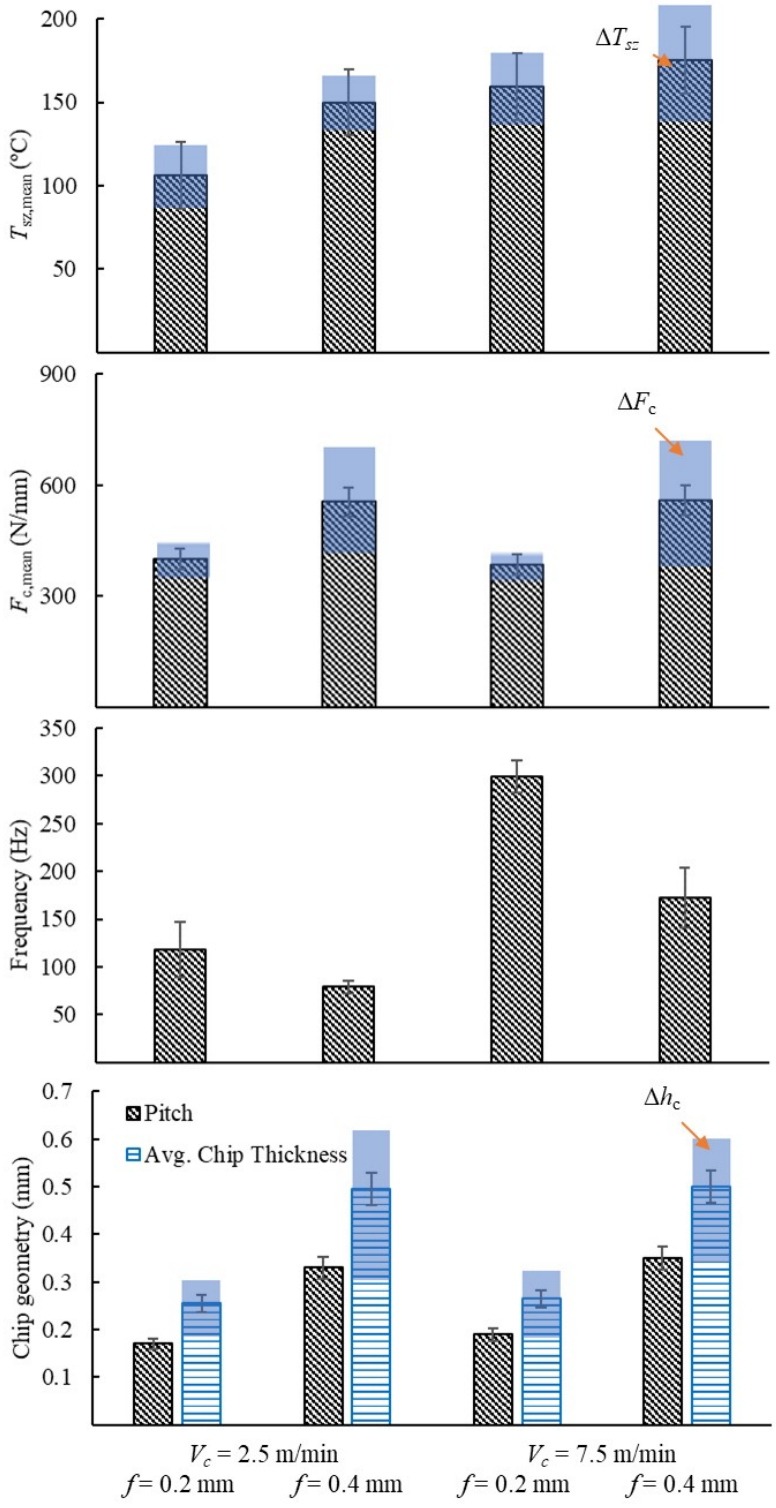

Figure 4.8: Summary of the effect of cutting conditions on different outcomes such as oscillation frequency, cutting temperature, cutting force and chip geometry. The average temperature oscillation (ΔT_{sz}), force oscillation (ΔF_c) and chip thickness oscillation (Δh_c) were also included

future, it would be necessary to obtain an analytical equation in order to calculate the workpiece temperature based on the temperature measured in the visible surface based on a thermodynamic analysis similar to the one shown in Section 3.5. Something similar has been previously applied, for instance, by Saez de Buruaga et al., 2018 to determine the temperature profile along the tool edge.

4.3 DUCTILE FAILURE MODEL VALIDATION

The experimental results presented above were compared with analytical equations and FEM results employing the model explained in Section 3.1.2. The aim of this section is to prove the validity of the ductile failure model included in the FEM based on infrared and cutting force measurements.

4.3.1 *Model validation results*

The difficulties on measuring workpiece temperature has led to different analytical equations to estimate it. One of the most successful and employed laws was proposed by Loewen and Shaw, 1954.

In short, the model assumes that the 90% of the plastic work is transformed into heat as it has been widely discussed in Section 3.5. On this basis, equation (22) was proposed.

$$T_{sz} = \frac{0.9}{1 + 1.328\sqrt{\frac{d_\alpha \gamma_{theo}}{v_c f}}} \frac{\tau \gamma_{theo}}{\rho c} + T_0 \tag{22}$$

where d_α is the thermal diffusivity of the material, taken from Milošević and Aleksić, 2012, τ is the shear stress, γ_{theo} is the equivalent shear strain and T_0 is the room temperature.

According to Bai et al., 2017, unequal division shear zone model could be employed to compute the equivalent shear strain. First, the maximum equivalent strain rate on the shear zone for Ti6Al4V alloy can be calculated with equation (23).

$$\dot{\varepsilon}_{eq,max} = \frac{(q+1) v_c \cos(\gamma)}{\sqrt{3} t_{sz} \cos(\phi - \gamma)} \tag{23}$$

where q refers to the non-uniform power law distribution of velocity in the primary shear zone and can be assumed to be 3 for Ti6Al4V under these cutting conditions, t_{sz} is the thickness of the shear zone and ϕ is the shear angle.

Then, the equivalent shear strain on the shear zone can be calculated with equation (24).

$$\gamma_{theo} = -\frac{\sqrt{3}\dot{\varepsilon}_{eq,max} K t_{sz}}{(q+1)v_c \sin(\phi)} + \frac{\cos(\gamma)}{\cos(\phi-\gamma)\sin(\phi)} \tag{24}$$

where K is given by equation (25).

$$K = \frac{\sin(\phi)\sin(\phi-\gamma)}{\cos(\gamma)} \tag{25}$$

Boothroyd, 1963 proposed another easy model decomposing the shearing heat flux depending on the thermal number (Peclet number), $Pe = fv_c/d_\alpha$. Thus, the temperature in the shear zone can be calculated according to equation (26).

$$T_{sz} = \frac{1-\chi}{\rho c}\frac{\tau\cos(\gamma)}{\cos(\phi-\gamma)\sin\phi} + T_0 \tag{26}$$

where χ is the proportion of the shearing flux that flows into the workpiece, defined by equation (27).

$$\begin{aligned} \chi &= 0.5 - 0.35\log_{10}(Pe\tan(\phi)); \text{ if } 0.004 \leq Pe\tan(\phi) \leq 10 \\ \chi &= 0.3 - 0.15\log_{10}(Pe\tan(\phi)); \text{ otherwise} \end{aligned} \tag{27}$$

The shear angle (ϕ) for each cutting condition was experimentally estimated based on infrared images. Furthermore, the shear stress (τ) was taken from the FEM simulations and it was around 650 MPa for each cutting condition, which is in agreement with literature results (Budak et al., 1996).

In order to compare with numerical simulations, first, it was demonstrated that the model was able to reproduce the thermal aspects concerning orthogonal cutting. This is shown in Figure 4.9.

As can be seen, the temperature along the shear zone in both numerical and experimental results varies along the shear zone. Therefore, an average value was taken from the numerical simulations by calculating the average value of the temperature along the shear zone at different cutting positions as made in the experimental case.

The temperature values obtained were plotted against the cutting severity. This is, the product $v_c f$, in $\mathrm{m^3 min^{-1}}$, and qualitatively represents the amount of energy introduced in the system. The obtained results are shown in Figure 4.10. As can be observed, predicted values, regardless of numerical or analytical, were higher than the ones measured with the infrared camera. First, it is worth mentioning that the measurements were made based on the visible surface, that is, under plane stress measurements whereas both numerical and analytical approaches were based on plane strain assumption. Therefore, thermal

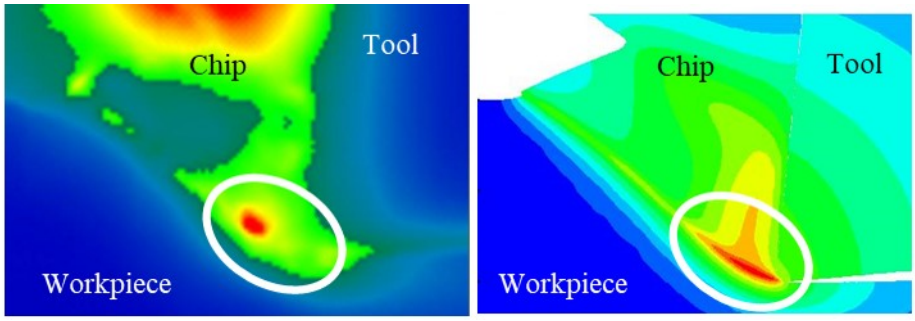

Figure 4.9: Experimental (left) and simulated (right) thermal fields during orthogonal cutting of Ti6Al4V. Cutting conditions: $v_c = 7.5$ m/min and $f = 0.4$ mm

losses could play a relevant role and the temperature inside the workpiece (plane strain) could be notably higher than the one measured. This was stated, for instance, by Soler et al., 2018, observing a gap higher than 100°C between the visible face and the centre of the tool.

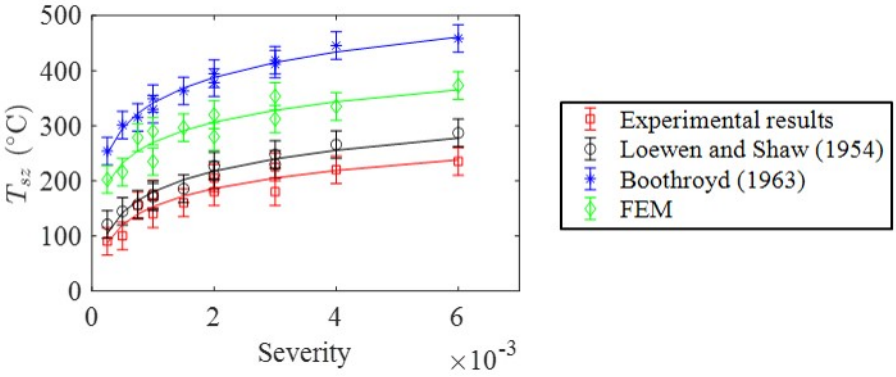

Figure 4.10: Shear zone temperature as a function of cutting severity. Analytical, experimental and FEM results

Nevertheless, it should be noted that analytical and numerical approaches are able to reproduce the trends and even the values reported with the approach proposed by Loewen and Shaw, 1954 are in agreement with the experimental ones.

4.3.2 *Ductile failure model validation*

First of all, the model, widely explained in Section 3.1.2, was proved to be capable of reproducing chip segmentation. Taking into consideration the chip morphology, an example of the accuracy of the predictions is shown in Figure 4.11. As can be seen, the chip segmentation is well reproduced by the numerical model thanks to the implementation of

the ductile failure model. However, the pitch (which is associated with the segmentation frequency) is underpredicted.

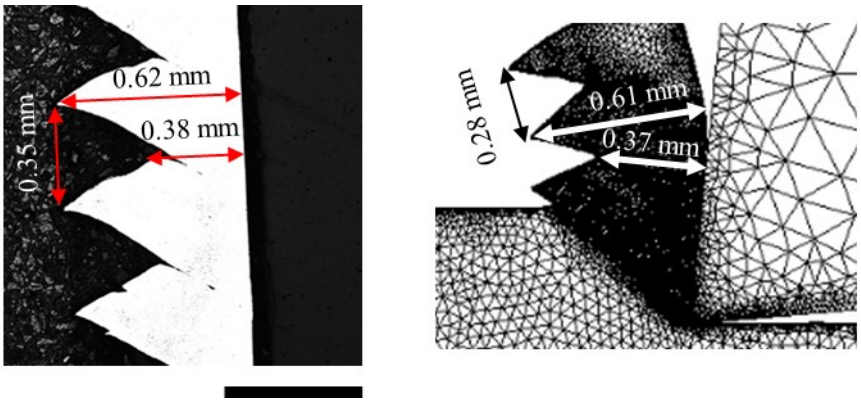

Figure 4.11: Experimental (left) and simulated (right) chip morphology. Cutting conditions: v_c = 7.5 m/min and f = 0.4 mm. Experimental and FEM results at the same scale. Scale bar: 0.5 mm

As stated in Section 4.2, when the cutting force reached a minimum value, the workpiece temperature along the shear zone was maximum. This phenomenon, showed in Figure 4.6, was reproduced by the numerical model as shown in Figure 4.12 (the temperature showed in the plot was taken from a point located close to the tool).

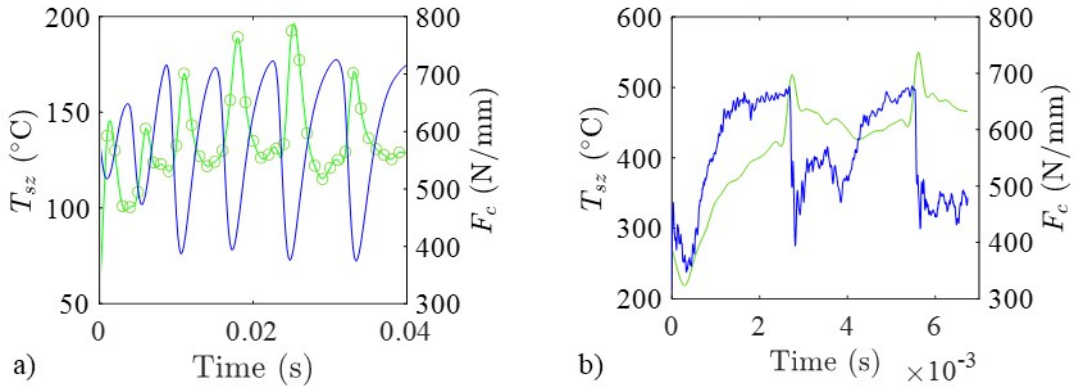

Figure 4.12: Temperature (green) and force (blue) evolution during orthogonal cutting of Ti6Al4V (a) Experimental results; b) FEM model). Cutting conditions: v_c = 7.5 m/min and f = 0.4 mm. Note that the time scale is not the same in both pictures

Therefore, it was proved that the proposed ductile failure model describes the different physical phenomena occurring during the cutting process properly, as FEM predictions were reproduced by experimental measurements. Experimental results were also compared with those from the FEM as Figure 4.13 shows.

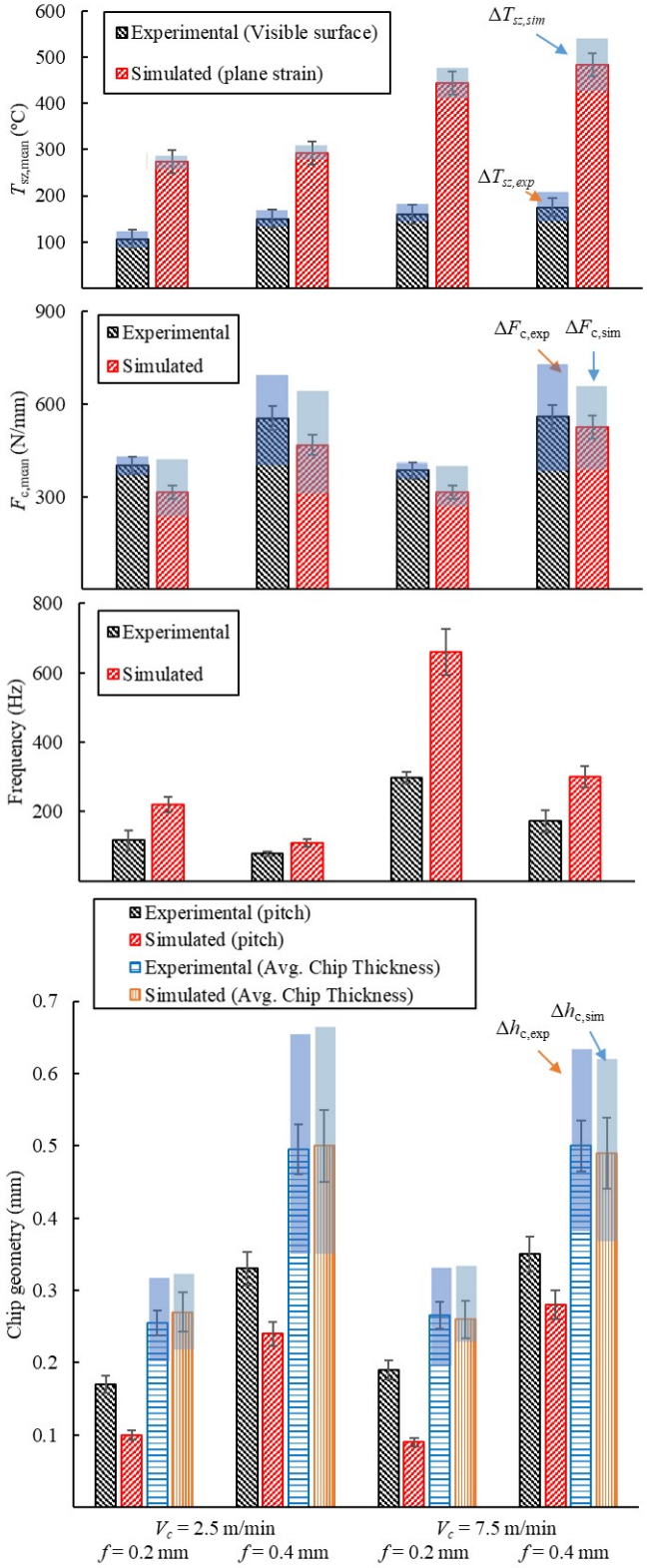

Figure 4.13: Effect of cutting conditions on oscillation frequency, cutting temperature, cutting force and chip geometry. Comparison between experimental and FEM results

It can be seen that the simulated segmentation frequencies were notably higher than the ones measured, being, in some cases ($v_c = 7.5$ m/min and $f = 0.2$ mm), more than 100% higher. This aspect is in agreement with the lower pitch values reported by the numerical model and shown, as for example, in Figure 4.11. These discrepancies were more noticeable at 7.5 m/min. Nevertheless, it is worth mentioning that the trends were well predicted by the numerical model.

Cutting forces were also well predicted with average prediction errors lower than 20% taking into consideration the whole set of cutting conditions, being the trends also reproduced comparing experimental and numerical average temperatures in the shear zone.

Finally, prediction error, concerning chip geometry (chip thickness and Δh_c), was lower than 6%, whereas the pitch values were underpredicted for the whole set of cutting conditions, with prediction error up to 100% in low feed cases.

Based on the presented results, the following conclusions can be drawn:

- The numerical model presented in Section 3.1.2 was able to reproduce the thermal fields associated with the machining process accurately. However, the temperature values reported by the numerical model were higher than the ones measured experimentally. This issue is assumed to be due to the different load modes between numerical simulation and experimental set-up and the presence of heat losses.
- Early analytical models proposed by Loewen and Shaw, 1954 and Boothroyd, 1963 perfectly reproduced the measured trends. Again, the obtained values were higher than the measured ones, especially when Boothroyd's approach was employed.
- It was observed that at low cutting speeds, the crack starts close to the tool and then suddenly spreads to the rest of the shear zone causing drastic failure, this phenomenon was reproduced by the numerical model.
- The numerical model employed was able to reproduce chip segmentation and to simulate thermal fields. To be more specific, the ductile failure model implemented reproduced the physical phenomena occurring during cutting as cutting force and temperature signals reported by the model were also in counter-phase.

4.4 DUCTILE FAILURE MODEL OPTIMIZATION

Material constitutive models (flow stress and ductile failure law) are usually obtained through thermomechanical tests under conditions far different from those reached in machining. Therefore, the determination of an inverse method to optimize the ductile failure law under real machining conditions would be of great interest as this input is of considerable relevance to reproduce chip segmentation.

Inverse approaches found in literature are usually focused on improving the constitutive law rather than optimize the ductile failure law as could be seen in Table 2.3.

Therefore, in this section, an inverse approach is shown based on infrared and force measurements aiming to optimize the ductile failure law in order to improve machining predictions.

4.4.1 *Inverse approach*

Based on a previous analysis (Ortiz de Zarate et al., 2019), the effect of the flow stress law on the pitch (and, thus, on the segmentation frequency) was observed to be negligible. However, notable influence was found by modifying parameters of the ductile failure law, especially when $\varepsilon_{f,0}$ (failure initiation parameter) was modified (Ortiz de Zarate et al., 2020). Thereby making this outcome a useful input to optimize the material model implemented.

Therefore, an inverse approach was taken to improve the accuracy of the predictions based on segmentation frequency. First, different simulations were launched (see Table 4.2), employing the model explained in Section 3.1.2, varying the value of $\varepsilon_{f,0}$ between 0.25 (the reference value given by Childs et al., 2018) and 0.5 (Hammer, 2012; Liu et al., 2014; Allahverdizadeh et al., 2015; Simha and Williams, 2016) under the condition of v_c = 7.5 m/min and f = 0.2 mm as it corresponded to the worst condition predicted.

Table 4.2: Conditions launched during the inverse analysis

Cutting conditions		Parameter analysed
v_c (m/min)	f (mm)	$\varepsilon_{f,0}$
2.5	0.2	0.25
7.5	0.2	0.25
2.5	0.4	0.25
7.5	0.4	0.25
7.5	0.2	0.35
7.5	0.2	0.45
7.5	0.2	0.50
7.5	0.2	0.41
7.5	0.4	0.41
2.5	0.2	0.41
2.5	0.4	0.41

According to Ortiz de Zarate et al., 2020, the increase of this parameter led to higher pitches and, thus, lower frequencies. This behaviour is shown in Figure 4.14.

The effect of this parameter over cutting forces, cutting temperature and chip thickness was analysed. It was observed that this parameter has no remarkable effect on force and

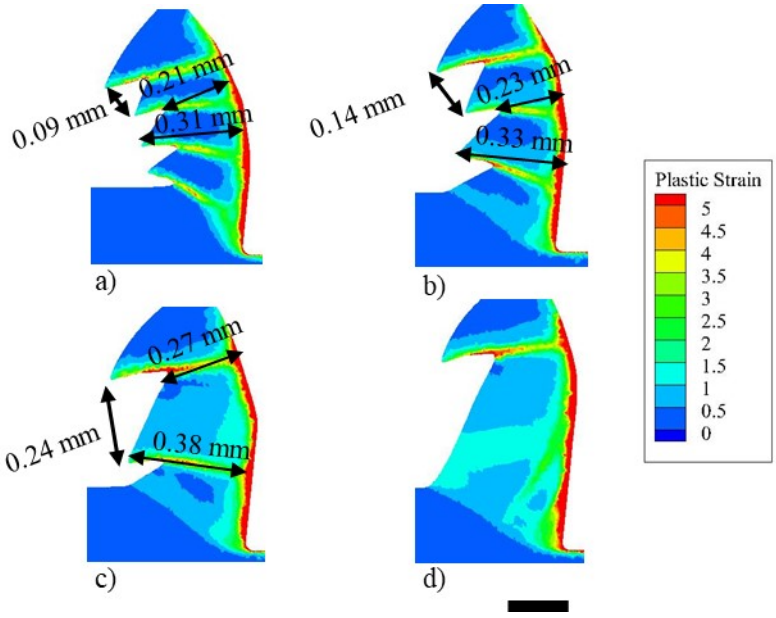

Figure 4.14: Variation of chip geometry by varying the $\varepsilon_{f,0}$ parameter: a) $\varepsilon_{f,0} = 0.25$; b) $\varepsilon_{f,0} = 0.35$; c) $\varepsilon_{f,0} = 0.45$ and d) $\varepsilon_{f,0} = 0.5$. Cutting conditions: $v_c = 7.5$ m/min and $f = 0.2$ mm. Scale bar: 0.2 mm

cutting temperature predictions, taking into consideration either the average value or the amplitudes of the oscillations (see Figure 4.15).

In addition, by increasing this parameter a slight increase on the average chip thickness was obtained, not affecting the magnitude of the chip thickness amplitude. However, this variation did not have any influence on the accuracy of the predictions. It is worth mentioning that chip shape and curvature was slightly modified by increasing $\varepsilon_{f,0}$.

A linear relationship was found, however, between the parameter $\varepsilon_{f,0}$ the segmentation frequency and the pitch value as Figure 4.16 shows. It is worth mentioning that with $\varepsilon_{f,0} = 0.5$ no segmentation was observed. Based on the linear regression, the optimum $\varepsilon_{f,0}$ for a segmentation frequency of 300 Hz (experimental value obtained) was 0.41.

Therefore, based on this optimization, the analysed cutting conditions were launched again. Table 4.2 summarizes the simulations launched before and after the optimization process.

After performing the optimization, it can be seen that the errors on frequency and pitch predictions were notably reduced not only in the condition employed to optimize the law but also in the rest of the cutting conditions analysed (see Figure 4.17).

For instance, for $v_c = 7.5$ m/min and $f = 0.2$ mm, the error in frequency and pitch prediction was reduced from more than 100% to less than 10%, whereas for $v_c = 2.5$ m/min and $f = 0.4$ mm the prediction error was reduced from 30% to 7%. The average prediction error was 9%.

Thus, the following conclusions can be summarized:

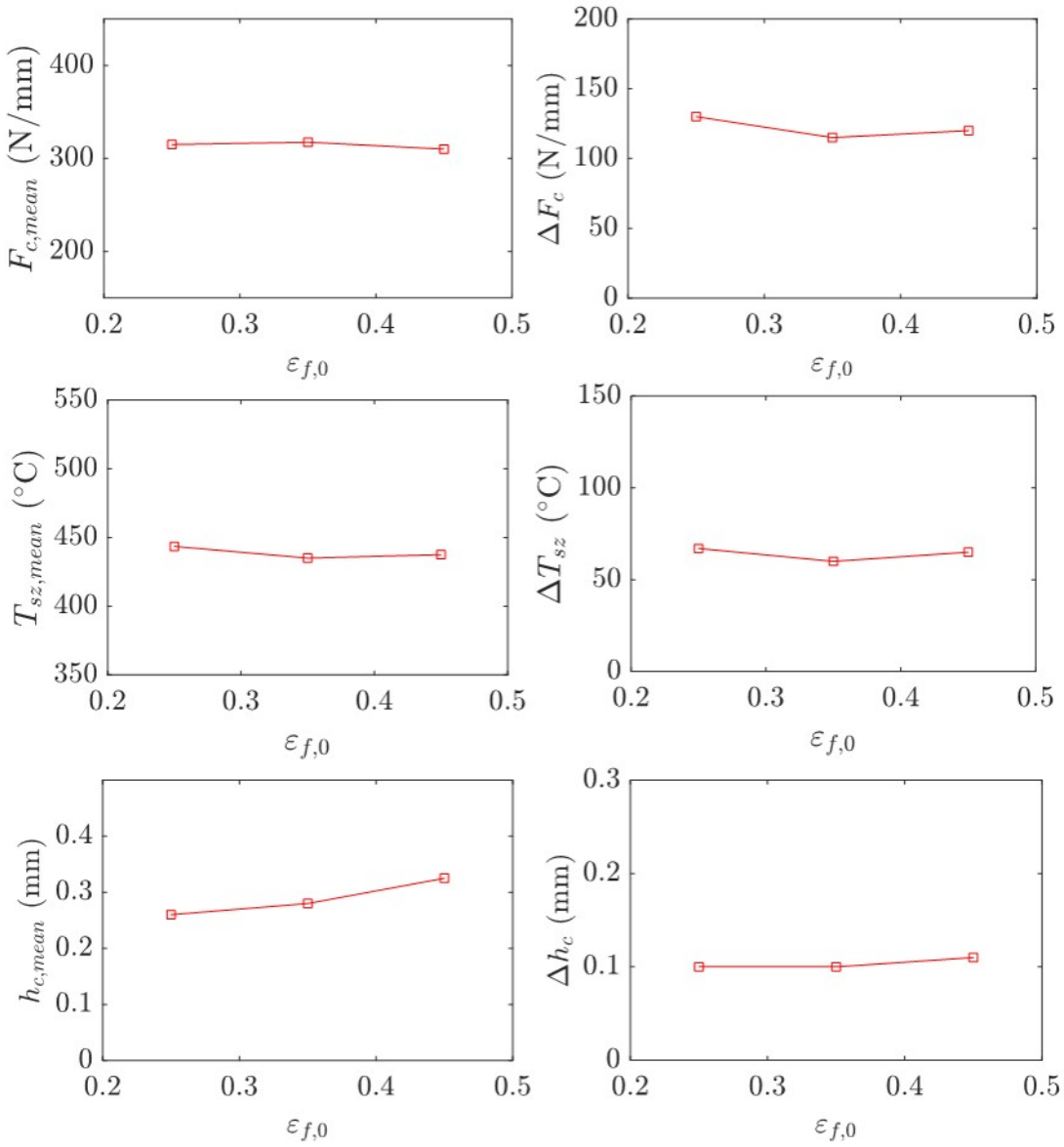

Figure 4.15: Effects of $\varepsilon_{f,0}$ on cutting forces, cutting temperature and chip morphology. Cutting conditions: $v_c = 7.5$ m/min and $f = 0.2$ mm

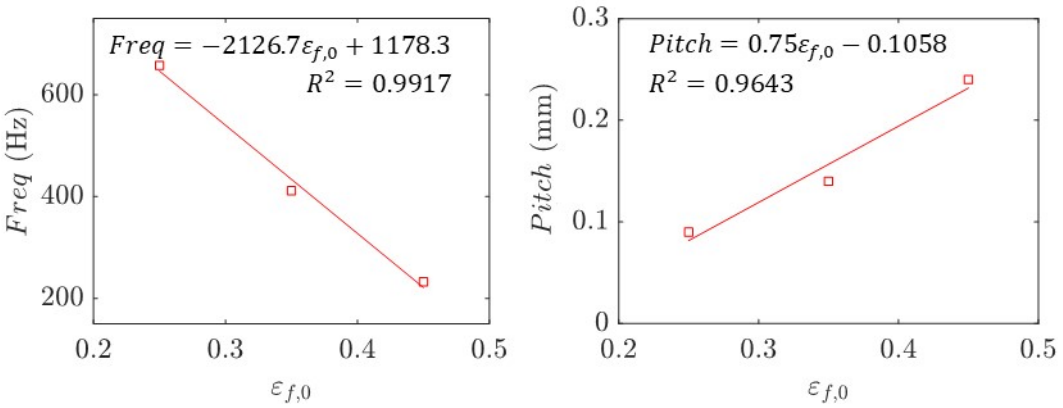

Figure 4.16: Variation of segmentation frequency and pith with $\varepsilon_{f,0}$. Cutting conditions: $v_c = 7.5$ m/min and $f = 0.2$ mm

- Chip segmentation frequency was identified as an interesting input to be considered so as to optimize the numerical model, as the trends were well reproduced. The ductile failure law was optimized by using inverse methodology by optimizing the parameter $\varepsilon_{f,0}$.
- The prediction error was reduced from more than 100% to less than 10% in the worst case, keeping the accuracy in the rest of the predictions.
- The modification of $\varepsilon_{f,0}$ led to higher segmentation frequencies not affecting the rest of the variables analysed. With $\varepsilon_{f,0}$ higher than 0.5 it was observed that continuous chip would be obtained.

4.5 CONCLUSIONS

After the thermal analysis of the orthogonal cutting process, the following conclusions can be drawn:

- The temperature in the shear zone showed an increasing trend with cutting speed, the influence being higher at low cutting speeds. The effect of feed was proved to be almost negligible compared to this effect. Numerical and analytical predictions reproduced the same trend, proving the accuracy of the numerical model to accurately reproduce thermal fields during the orthogonal cutting process.
- Chip segmentation produced during machining of Ti6Al4V causes the oscillation of important variables such as cutting forces, chip thickness and workpiece temperature. This oscillation frequency, measured by using force measurements and infrared filming, was identified as a valuable input to optimize the ductile failure model.

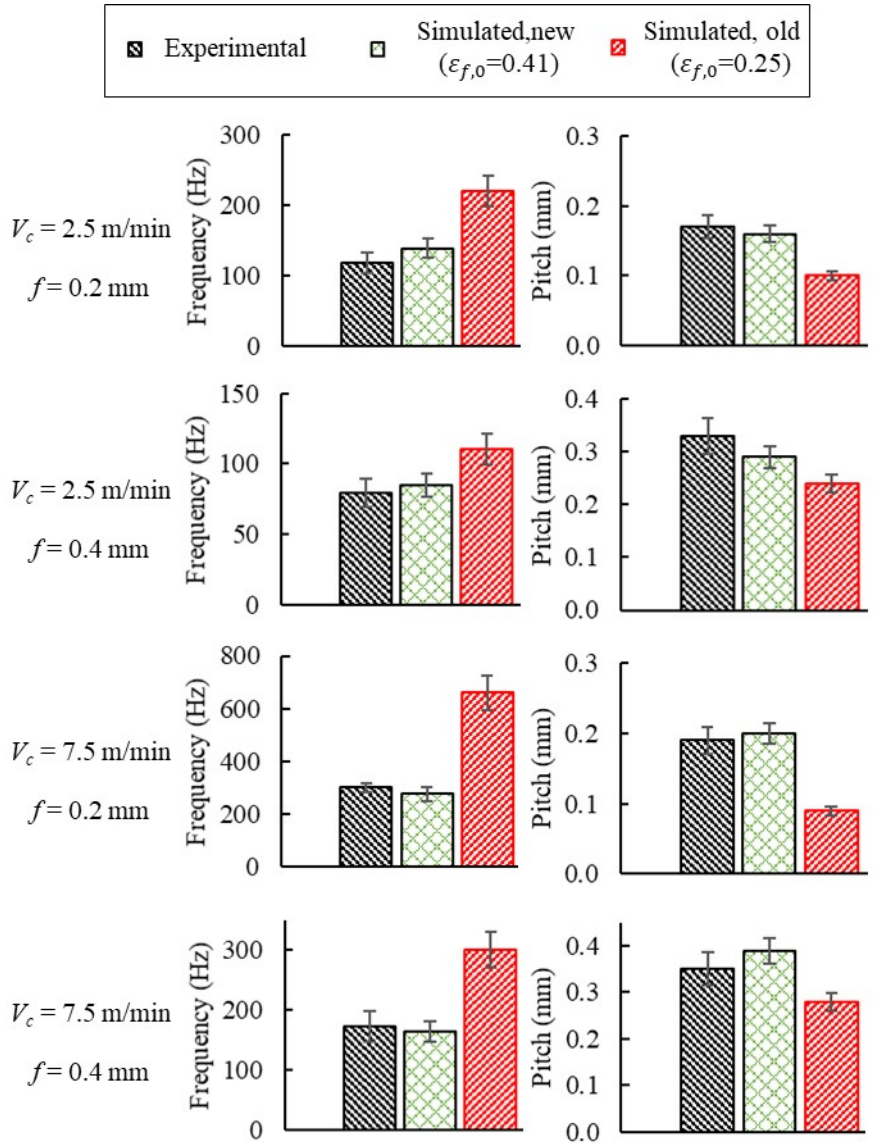

Figure 4.17: Frequency and pitch predictions, comparing the reference and the optimized law

- It was experimentally observed and in the FEM that, at low cutting speeds, the crack starts close to the tool and then suddenly spreads to the rest of the shear zone causing drastic failure. This issue demonstrates the lack of ductility of the material under these conditions. In addition, cutting forces and temperatures were proved to be in counter-phase. This was also reproduced by the numerical model, validating the ductile failure model implemented.

- It is worth highlighting that the temperatures reported by the numerical model were higher than the ones measured. Nevertheless, this is assumed to be due to the different load modes, as the experimental measurement was carried out under plane stress conditions whereas the numerical model assumed plane strain conditions representative of the orthogonal cutting process. This is in agreement, for instance, with the tool thermal fields measured by Soler et al., 2018.

- Inverse simulation was employed aiming to optimize the ductile failure law, by varying $\varepsilon_{f,0}$. After the optimization, the error in the frequency prediction was reduced from more than 100% to less than 10% in the worst case, without influencing the accuracy in the rest of the predictions.

5 STRAIN AND STRAIN RATE MEASUREMENTS

In spite of the several attempts to measure plastic strain in machining that could be found in literature, there is a clear lack of knowledge with regard to materials which tend to create segmented chips, summarized in Table 2.4. Moreover, many of these attempts are based on the visible surface which is not subjected to plane strain conditions representative of the orthogonal cutting process. Thus, the measurements of the plastic strain may not be accurate enough.

To reproduce plane strain conditions reached during orthogonal cutting, an specific set-up has been designed, based on quick stop tests. The grid distortion method was employed to determine plastic strain and strain rate and a new methodology was developed taking into consideration one single image in the analysis, avoiding decorrelation problems.

Therefore, in this chapter the use of DIC to measure plastic strain when cutting Ti6Al4V and a self-designed grid technique to measure plastic strain and strain rate under plain strain conditions were presented.

5.1 DIGITAL IMAGE CORRELATION

The use of DIC (mechanical patterns, microstructure or speckle painting technique) to measure plastic strain during machining has been tested by different authors. However, it needs further investigation in order to be applied under realistic conditions when cutting Ti6Al4V.

Based on the analysis shown in Section 3.4, the M5 method (see Table 3.4) was taken as the best option aiming to create a robust speckle pattern to measure strain and strain rates during orthogonal cutting. In short, it consists of speckle painting with AREMCO HiE-coat black coating and Molydal NB 25 to spray white random speckles along a WEDM surface.

The tests were carried out at low cutting speeds (2.5 and 7.5 m/min) and high feeds (0.4 mm) in order to have high spatial resolution to facilitate DIC performance. These cutting speeds are representative of the broaching process, a widely used finishing process in machining. The tests were recorded with Photron FASTCAM APX-RS 250K at 9000 frames per second (fps), employing the same set-up explained in Section 4.1, positioning the camera in the same place as the Flir Titanium 550 m shown in Figure 4.1. The Kistler dynamometer was synchronized with the high speed camera the sampling frequency being 9000 Hz.

Preliminary trials were carried out aiming just to study the adhesion and the possibility of the paint to be peeled off during the cutting process, regardless of the pattern quality.

Examples of the preliminary pattern created are shown in Figure 5.1. As can be seen, the density of speckles was low and the speckle size was high which would result in a poor speckle quality. Three different repetitions were carried out under each condition. Figure 5.1 shows for each condition an example of the speckle performance.

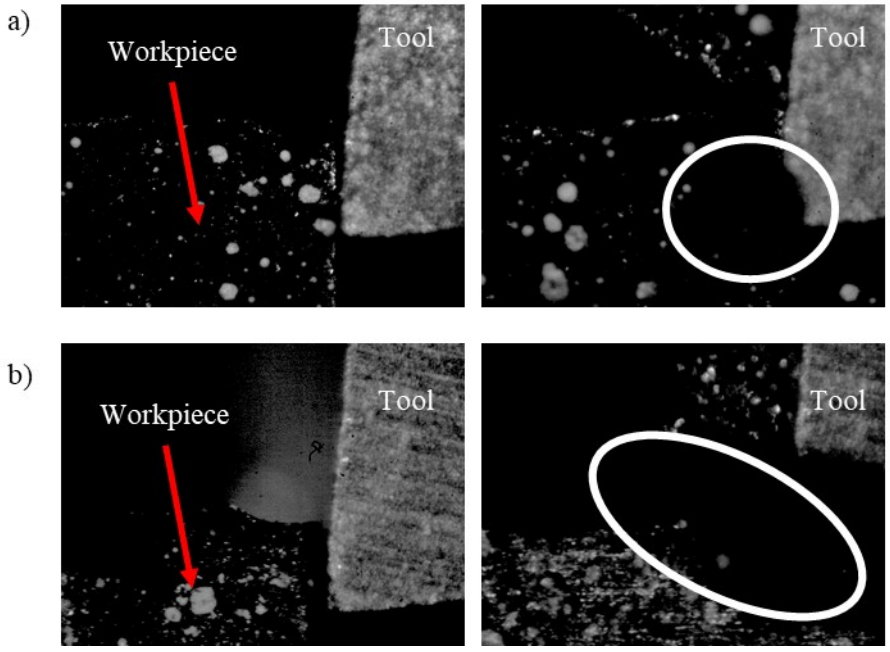

Figure 5.1: Example of a speckle performance during orthogonal cutting: a) Cutting speed of 2.5 m/min; b) Cutting speed of 7.5 m/min. Speckle appearance before cutting (left) and picture taken during the process (right)

It can be observed, based on the highlighted areas in Figure 5.1 that the adhesion of the speckle was not consistent during the test and it peeled off due to the high thermomechanical loads. Previous analyses with acrylic paints reported the same results. Therefore, the use of speckle painting seems to be inappropriate for DIC analysis of a machining process under industrial conditions although accurate results were reported for thermomechanical compression tests.

Aiming to overcome this drawback, DIC analysis was also carried out with a mechanical grid, as mechanical patterns were tested successfully by different authors such as Zhang et al., 2019 or Meurer et al., 2020.

5.1.1 *Grid creation*

To perform the grid a Kern Evo Machine with a microball end mill with HARDMAX coating and a nominal radius of 50 µm (HSB 2001-0010) were used. To ensure a good microgrid quality it is important to guarantee a good surface finish of the sample face

where the grid is to be built. For this reason, before performing the grid, the surface was face-milled obtaining a *Ra* of 1.4 µm measured with a Mitutoyo roughness tester.

The created microgrid was formed by orthogonal straight paths (each one with a width (a_e) of 30 µm) placed every 60 µm (distance between two straight paths, a_v), as shown in Figure 5.2. To determine the depth of cut a_p, equation (28) was used.

$$a_p = r - \frac{1}{2}\sqrt{4r^2 - a_e^2} \tag{28}$$

where r is the radius of the ball end mill, obtaining a theoretical value of 2.3 µm. However, it is worth noting that a_v is very sensitive to a_p (especially at very low depths of cut) so this parameter must be notably controlled.

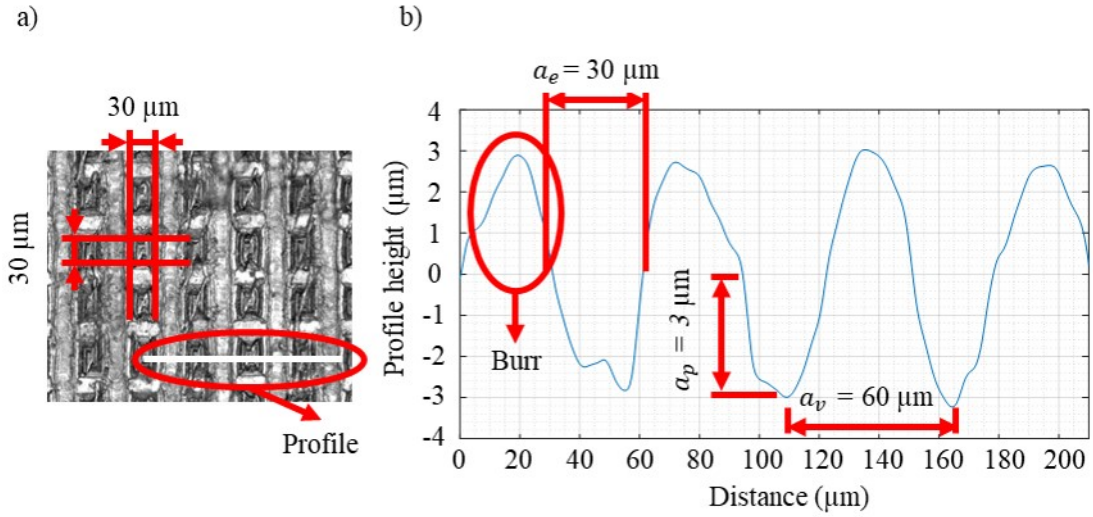

Figure 5.2: a) Undeformed grid measured using Alicona profilometer IFG4 with a magnification of 50X; b) Roughness profile from Alicona profilometer IFG4

The depth of cut, a_p, was set to 2.5 µm, the real depth of cut being between 2 and 3 µm, taking into consideration thermal expansion, vibrations and machine tolerances (Gandarias et al., 2006). Therefore, according to equation (28), values of a_e between 28 and 35 µm would be obtained.

Nevertheless, as could be seen in Figure 5.2b, the peak to valley height was about 6 µm because of burring effects. However, this issue was not relevant as the aim was to create a mechanical grid to be tracked. A set of 20 grids were created and measured using the Alicona profilometer. Based on these measurements, the dimensions of the grid were 30x30 μm^2 (see Figure 5.2) with a standard deviation of ± 2 µm.

5.1.2 *Digital Image Correlation results*

Because of the intense distortion expected, different subset sizes were tested to generate the most accurate mesh with a step size between 1/2 and 1/3 of the subset based on Society, 2018 in order to achieve the best correlation. As it was explained in Section 3.4, the subset size defines the width of the square to mesh the reference image and the step size is the distance between subsets. Therefore, the following relationships between subset and step sizes were tested: 21/10, 30/12, 15/7, 21/7, 40/16 and 50/20 pixels, which are 61/29, 88/35, 44/20, 61/20, 117/47 and 146/59 µm, respectively.

The values of the plastic strain obtained with different sizes did not suffer variations (see Figure 5.3). However, because of the extreme conditions (high strain and strain rate), notable decorrelation problems were observed, especially with low subset sizes. These low subsets were not able to capture the intense distortion suffered by the pattern.

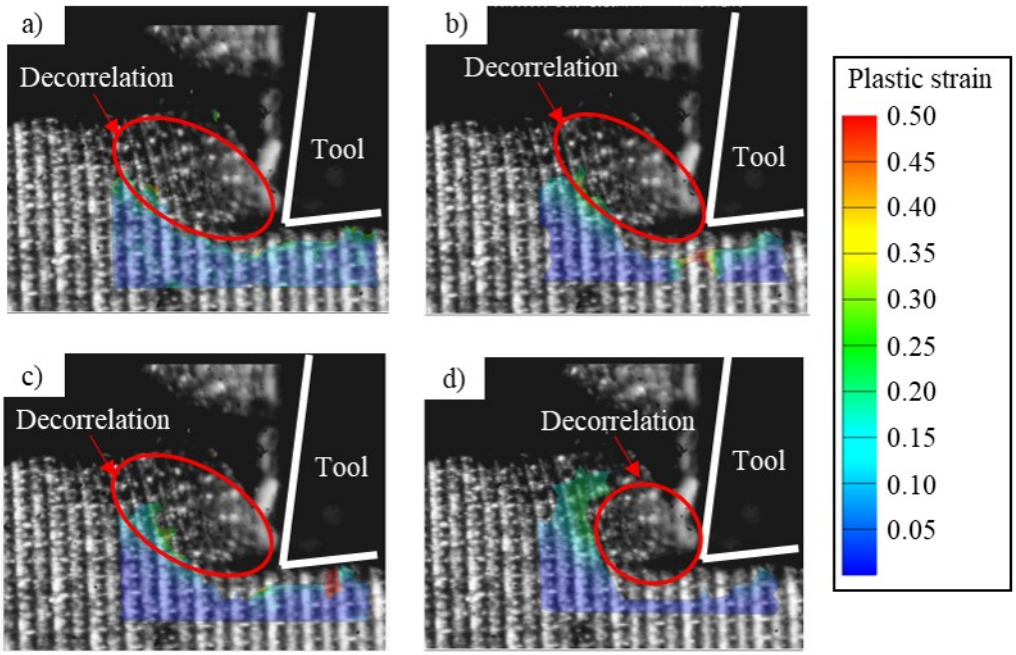

Figure 5.3: Equivalent plastic strain with different subset and step sizes (in pixels): a) 15/7; b) 40/16; c) 30/12 and d) 50/20. Cutting conditions: $v_c = 7.5$ m/min; $f = 0.4$ mm. Decorrelation problems in the shear zone, mainly close to the tool (highlighted in red)

In spite of the decorrelation problems observed, the plastic strain and strain rate in the upper zone of the shear zone can be estimated as Figure 5.4 shows. The plastic strain rate was calculated numerically differentiating the equivalent plastic strain. The plastic strain reached values close to 0.3 whereas the strain rate was around 400 s^{-1}.

The method was not able to track the selected zone after close to 3 ms of cutting. In this point, the cutting force was close to the maximum and the segmentation was about

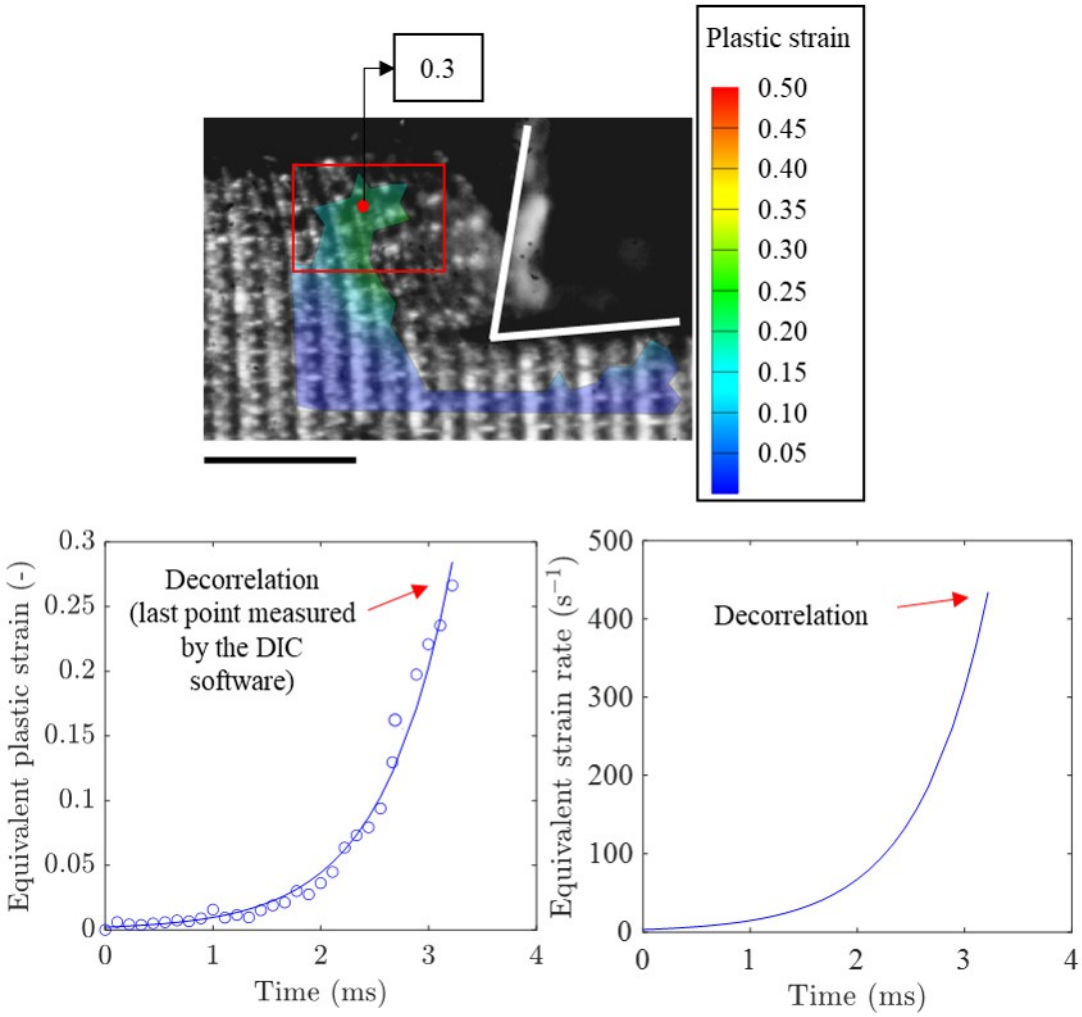

Figure 5.4: Experimental plastic strain and strain rate measured in the upper zone of the shear zone including evolution with time. Scale bar: 0.4 mm

to occur because of the drastic failure. This behaviour can be observed in Figure 5.5. The same behaviour was found at the cutting speed of 2.5 m/min.

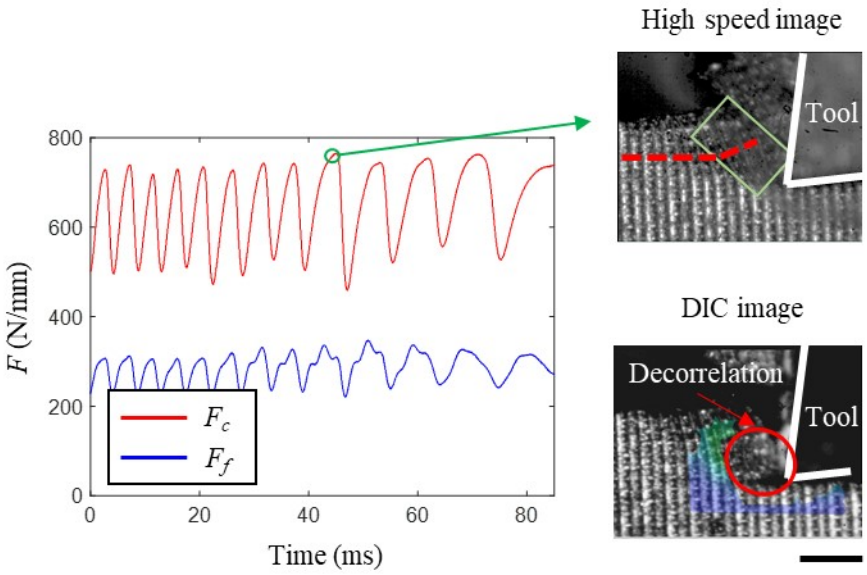

Figure 5.5: Experimental representation of the cutting force evolution with time for $v_c = 7.5$ m/min and $f = 0.4$ mm, representing chip segmentation and the exact point at which the DIC analysis fails in Figure 5.4. Scale bar: 0.4 mm

One of the main problems on employing this kind of techniques is the lack of experimental data available to validate the measurements. Therefore, in order to, at least, estimate the accuracy or robustness of the measurement presented above, the experimental strain and strain rates were compared with the numerical ones obtained according to the model explained in section 3.1.2. This model had been previously validated and optimized in Section 4.4 taking into consideration cutting forces, chip geometry, segmentation frequency and thermal fields.

In Figure 5.6, the comparison between experimental and numerical equivalent plastic strain is shown. It can be observed that, in the upper zone of the shear zone, the equivalent plastic strain reported by the DIC analysis was slightly lower than that obtained from the FEM (0.3 for DIC analysis and 0.5 for the FEM). As mentioned above, the visible face in which DIC analysis was carried out is not subjected to pure orthogonal cutting conditions (plane strain) and side flow could occur, which could result in lower plastic strains.

Something similar happened with the strain rate (see Figure 5.7). The experimental value was around 400 s^{-1} whereas the numerical one reported was 700 s^{-1}. Similar conclusions would be obtained at 2.5 m/min.

The experimental results were also compared with the analytical model proposed by Bai et al., 2017. This model was explained in Section 4.3.1 and is based on the

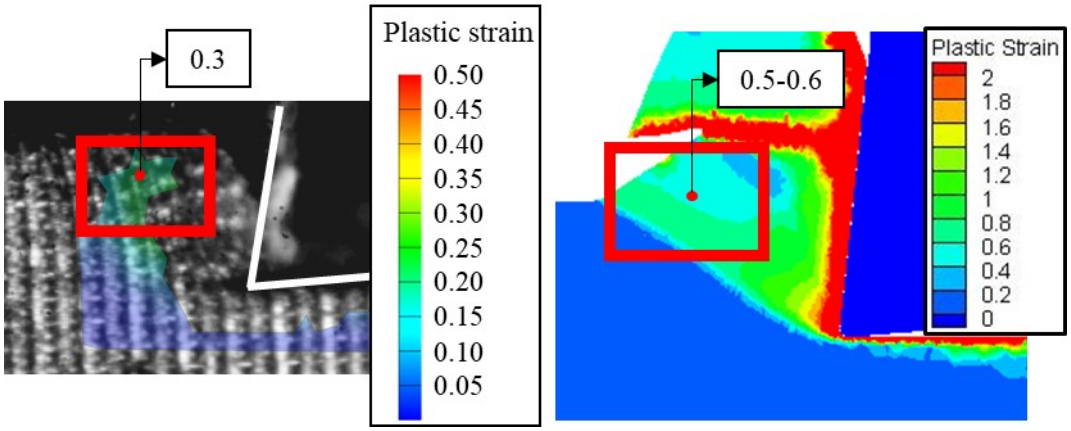

Figure 5.6: Comparison between experimental equivalent strain (through DIC measurements) and FEM results

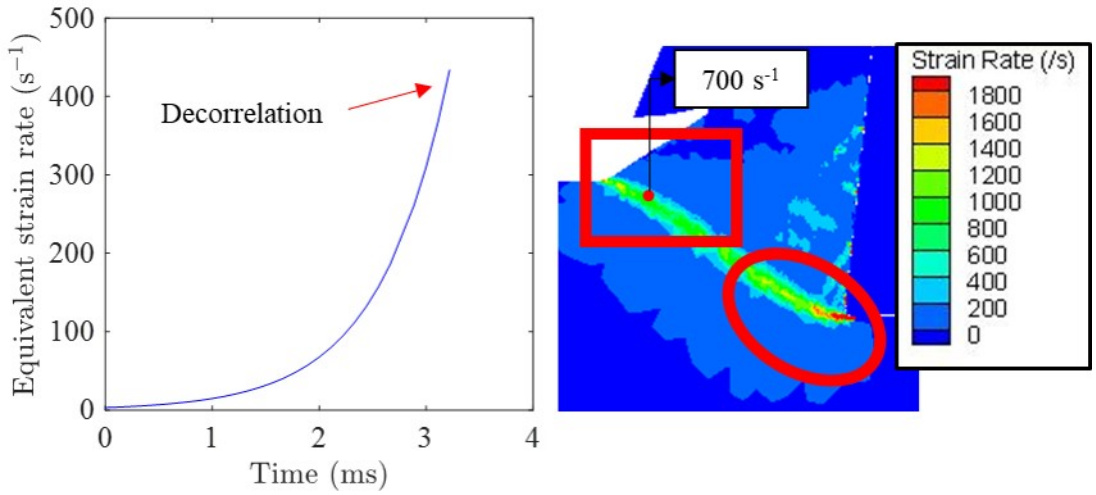

Figure 5.7: Comparison between experimental strain rate (through DIC measurements) and FEM results

unequal division shear zone model. The thickness of the shear zone and the shear angle were measured for each cutting condition based on recorded images, being the thickness around 0.15 mm for each condition and the shear angle 40 and 36° at 2.5 and 7.5 m/min, respectively.

Therefore, the maximum strain rate for each cutting condition calculated analytically (according to equation (23)) were 753 and 2230 s^{-1} for the cutting speed of 2.5 and 7.5 m/min, respectively. This implies that the trend reported by this analytical model matches with the experimental trend. However, the values obtained by the analytical

model were higher than the measured ones, as the maximum strain could be located close to the tool, where DIC could not be performed because of decorrelation.

Similarly, the equivalent strain on the shear zone can be calculated according to equation (24). Under both conditions, the calculated equivalent strain was around 0.7, notably higher than the measured one. The model was based on the shear angle and the thickness of the shear zone. These parameters remained almost constant during the chip formation process, especially at the lowest cutting speed. The model was not able to properly reproduce the variations on the variables because of chip segmentation. Nevertheless, it is a good tool to obtain a first notion about the order of magnitude expected in the results.

To sum up, the following results could be highlighted:

- Speckle patterns generated by spray painting were not valid for strain measurements in orthogonal cutting because of decorrelation problems and peeling off due to the extreme thermomechanical loads.
- Mechanical patterns could be a good option to overcome the limitations associated with spray painting as peeling off problems are avoided. It was possible to measure the equivalent plastic strain and strain rate evolution during orthogonal cutting of Ti6Al4V in the upper zone of the shear zone whereas close to the tool decorrelation problems occurred.
- Discrepancies were found between numerical and experimental values which could be related to the differences in the load modes (plane strain vs planes stress). Nevertheless, the order of magnitude reported is in agreement. This proved the capability of mechanical patterns to be used as random pattern for DIC analysis. The analytical results reported the same trend but the values were notably higher as the experimental method was not able to measure close to the tool.

5.2 GRID DISTORTION ANALYSIS

Based on previous DIC analysis, it has been observed that traditional DIC methods were not capable of measuring strain and strain rates under plane strain conditions typical of the orthogonal cutting process.

Apart from this, although decohesion problems were avoided by using mechanical patterns, decorrelation problems still took place, probably due to the side flow (out of plane displacements). Therefore, within this section, a methodology to address these limitations was proposed by measuring the plastic strain and strain rate based on a single image of a deformed grid.

5.2.1 *Theoretical basis*

To compute equivalent strain rates from a picture of a deformed grid a steady flow was assumed. Steady flow assumption was supported by high speed filming and it was proved that vertical displacements of the points on the non-deformed region were negligible, thus the horizontal grid lines represent streamlines (see Figure 5.8). Therefore, using the coordinates of the grid points, the length and the angle of each segment can be computed.

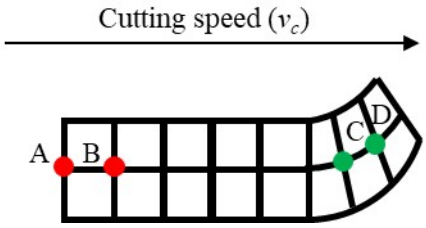

Figure 5.8: Schematic view of the grid distortion. AD curve represents a streamline based on the steady flow assumption

Steady flow ensures that the time spent by the workpiece on travelling from A to B (an undeformed segment), was the same as for going from C to D (any deformed segment). A straightforward calculation allows the computation of the speed of the deformed segment CD (V_{CD}) by equation (29).

$$V_{CD} = V_{AB}\left(\frac{L_{CD}}{L_{AB}}\right) \tag{29}$$

where V_{CD} is the speed of the deformed segment, V_{AB} is the speed of the undeformed segment, L_{CD} is the length of the deformed segment and L_{AB} is the length of the undeformed segment.

Taking into account that AB segment was chosen far enough from the shear zone it can be assumed that the undeformed segment travels at the cutting speed, i.e. $V_{AB} = v_c$. The real speed was validated through high speed imaging. Using the inclination angle of each deformed segment, the velocity of each grid point could be decomposed (V_x, V_y). A biharmonic interpolation was then used to estimate velocity fields (Gáspár, 1999), and those were used to perform numerical derivatives of V_x and V_y.

Assuming small displacement hypothesis, the strain rate components can be calculated by equations (30) to (32).

$$\dot{\varepsilon}_{xx} = \frac{dV_x}{dx} \tag{30}$$

$$\dot{\varepsilon}_{yy} = \frac{dV_y}{dy} \tag{31}$$

$$\dot{\gamma}_{xy} = \frac{dV_x}{dy} + \frac{dV_y}{dx} \tag{32}$$

where $\dot{\varepsilon}_{xx}$ represents the strain rate at the end of the segment in horizontal direction, $\dot{\varepsilon}_{yy}$ the strain rate at the end of the segment in vertical direction and $\dot{\gamma}_{xy}$ is the shear strain rate. With these components, the equivalent strain rate was calculated by equation (33), according to Von Mises criterion.

$$\dot{\varepsilon}_{eq} = \sqrt{\frac{4}{9}\left(\frac{1}{2}\left[(\dot{\varepsilon}_{xx} - \dot{\varepsilon}_{yy})^2 + \dot{\varepsilon}_{xx}^2 + \dot{\varepsilon}_{yy}^2\right] + \frac{3}{4}\dot{\gamma}_{xy}^2\right)} \tag{33}$$

Once the strain rate was obtained, the equivalent plastic strain was calculated by integrating the strain rate along each streamline according to equation (34).

$$\varepsilon_{eq} = \left[\oint \dot{\varepsilon}_{eq} dt\right]_{streamline} \tag{34}$$

5.2.1.1 *Uncertainty estimation of measurements using Monte Carlo simulation*

The uncertainty of the measurements was given in accordance with GUM (ISO, 2008), using in all cases a coverage factor of 2. The measurement method depends on the length L_0 of an undeformed segment of the grid (L_{AB} in Figure 5.8). This length, taking into consideration equipment resolution and statistical methods, was around 60.56 µm with a standard uncertainty of $u_{L_0} = 0.05$ µm (see Figure 5.2).

The measurement method is strongly conditioned by the grid coordinates of the ROI used to calculate the length of the deformed segments of the grid. At the present time, this set of coordinates was selected by a researcher by clicking on a picture of a deformed grid obtained with the Alicona profilometer IFG4.

In order to evaluate measurement uncertainty, the points selected by the researcher were disturbed using a two Gaussian distribution with a standard deviation of $\sigma_x = 1.2$ µm and $\sigma_y = 1.4$ µm in X and Y axis, respectively. These standard deviations were determined after taking the standard deviations of a sample of more than 10 repeated measurements into consideration. The new set of coordinates was then used to recalculate physical parameters explained above. Therefore, the equivalent plastic strain and equivalent strain rate fields reported corresponded to the most probable maximum strain rate in the ROI, after performing more than 50000 iterations of Monte Carlo simulation of the grid points.

The extended uncertainty is computed based on the variation of the maximum value of each field at each iteration, reporting an uncertainty of 15%.

The inclination angle of the horizontal line of the undeformed grid with respect to the X axis, which was 0.020 ± 0.002 rad, could be taken as an extra source of uncertainty. However, its influence on equivalent strain and strain rate uncertainty was proved to be negligible.

5.2.2 *Plane strain set-up*

Within the literature review, the methodologies employed to measure plastic strain for a machining test are often based on the visible part of the surface (see Table 2.4). However, this approach could underestimate the plastic strain measured due to out of plane displacements (side flow). This side flow could also cause decorrelation. Therefore, plane strain restrictions are not fulfilled and the measurements are not carried out under pure orthogonal cutting conditions.

To overcome this issue a self-designed set-up was employed to measure plastic strain and strain rate. A grid was created, through micromilling (according to the methodology explained in Section 5.1.1), on both sides of a workpiece (see Figure 5.9). This workpiece was clamped to a second workpiece (L-shape), of the same material and same width (in the present case, 2 mm). This L-shape workpiece was then clamped to the dynamometer with the help of two screws as shown in Figure 5.9a. Both workpieces were subjected to the machining process, being the total width of cut 4 mm. The clamping device shown in Figure 5.9a kept both workpieces clamped together during the cutting test.

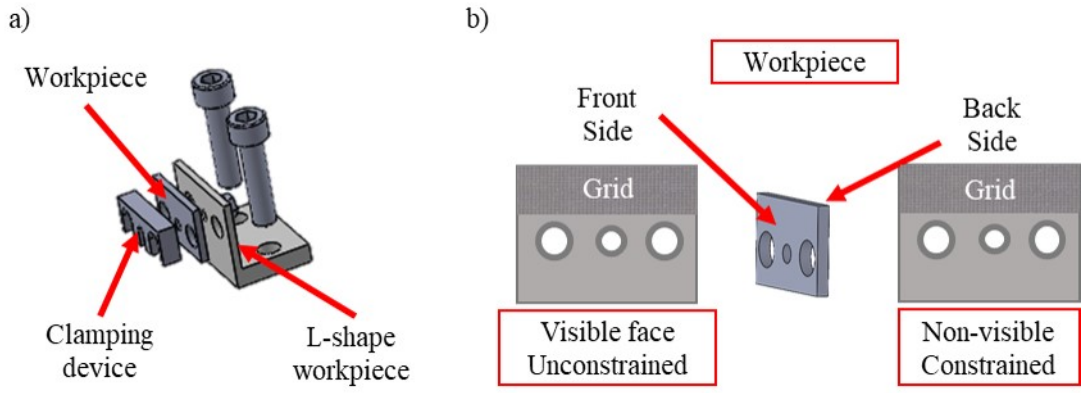

Figure 5.9: Scheme of the self-designed set-up to obtain plane strain conditions. a) Clamping device, workpiece and second (L-shape) workpiece; b) Focus on the workpiece with the grids created in both sides

The validity of the set-up proposed to avoid side flow was verified after the cutting test by observing the lateral expansion (profile height) using profilometer Alicona IFG4. The lateral expansion was lower than 5 µm in the constrained face whereas in the

non-constrained one this expansion was higher than 20 µm (see Figure 5.10). In Figure 5.10 profile height represents the lateral expansion.

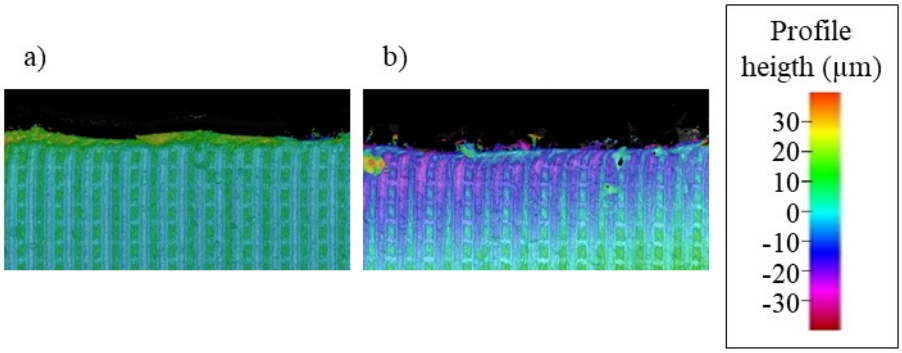

Figure 5.10: Profile height measurements for a cutting speed of 7.5 m/min and feed of 0.4 mm. a) Constrained face (plane strain conditions); b) Non-constrained face (plane stress conditions)

In order to obtain images of the deformed grid subjected to plane strain (see Figure 5.11), as the grid was constrained between two workpieces, the machining process was stopped suddenly during cutting. The workpiece was then unclamped enabling a picture of the grid to be obtained using the Alicona profilometer IFG4. High speed images were taken from the grid located on the front side (external grid) in order to determine the state of the cut when the cutting process was stopped. This was extremely important as Ti6Al4V tends to create segmented chips, causing notable variations on different variables. At these cutting speeds, the influence of the deceleration could be assumed to be negligible.

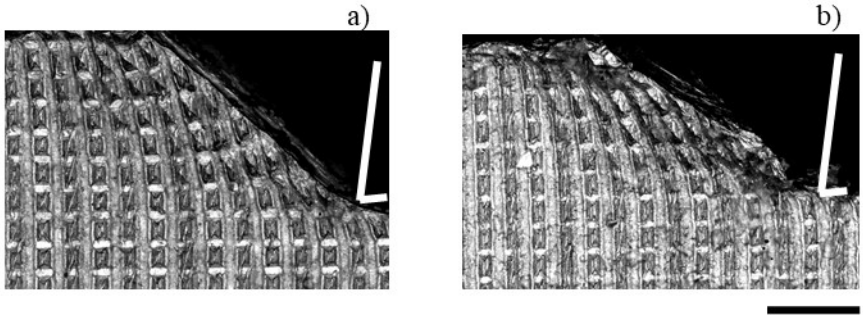

Figure 5.11: State of the deformed grid after carrying out the cutting test (f = 0.4 mm): a) Cutting speed of 2.5 m/min; b) Cutting speed of 7.5 m/min. Scale bar: 200 µm

5.2.3 *Grid distortion results*

Figure 5.12 shows cutting and feed forces under the cutting conditions analysed. Experimental forces showed a periodic behaviour due to chip segmentation, in both cutting and feed forces. When a new cut started, the force was minimum reaching then a maximum value just before cracking as it was deeply analysed in Section 4.2.

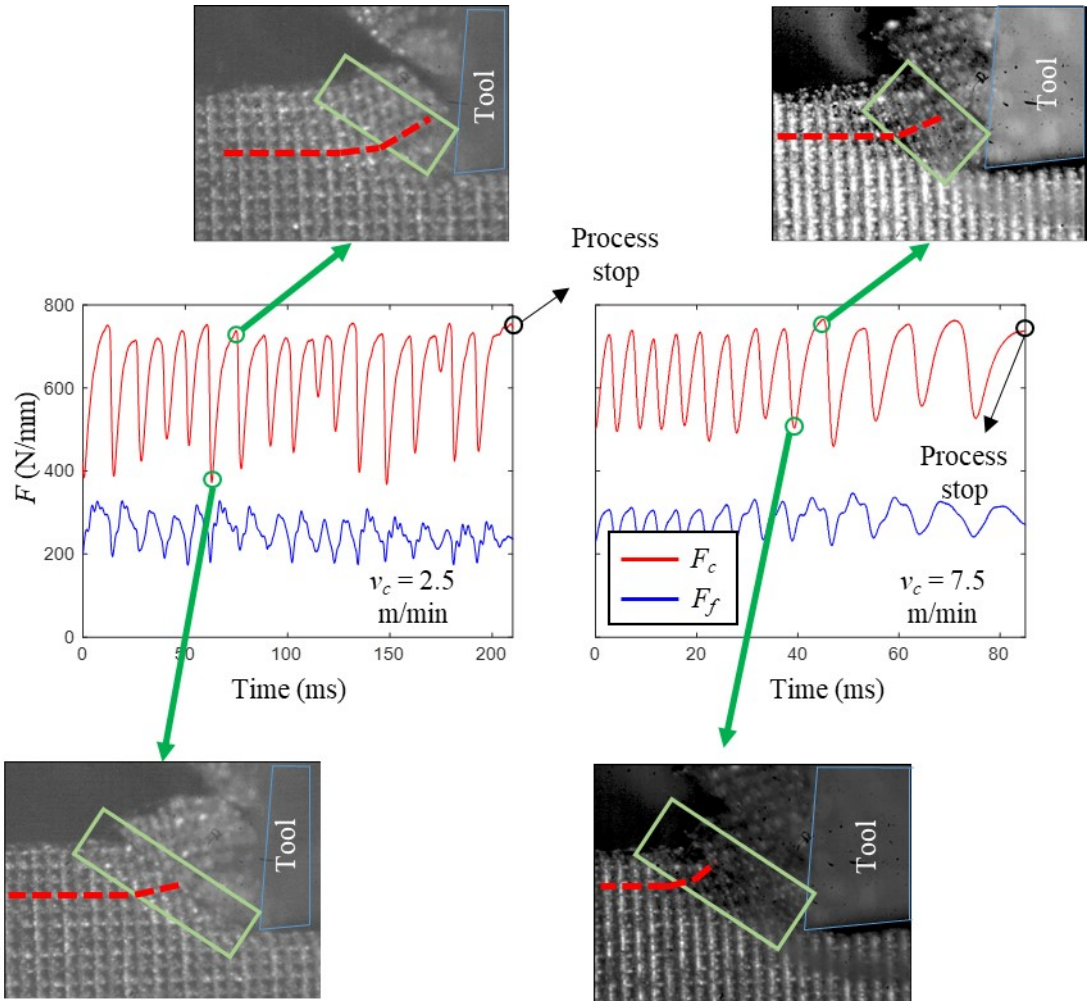

Figure 5.12: Experimental cutting and feed forces under the cutting conditions analysed

With regard to Figure 5.12, it is possible to see that under both conditions the cutting was stopped when the cutting forces were at a maximum. Plastic strain and strain rate were not uniform along the shear zone. This could be qualitatively observed taking into consideration the grid state as can be seen based on the dashed lines shown in Figure 5.12. Green rectangles were included to highlight this variation focusing on the shear zone at different steps of the cutting process. Thus, as explained in Section 5.2.1, strain

rate and plastic strain were computed at 2.5 and 7.5 m/min based on the distorted grids shown in Figure 5.11. Figure 5.13 shows the obtained results.

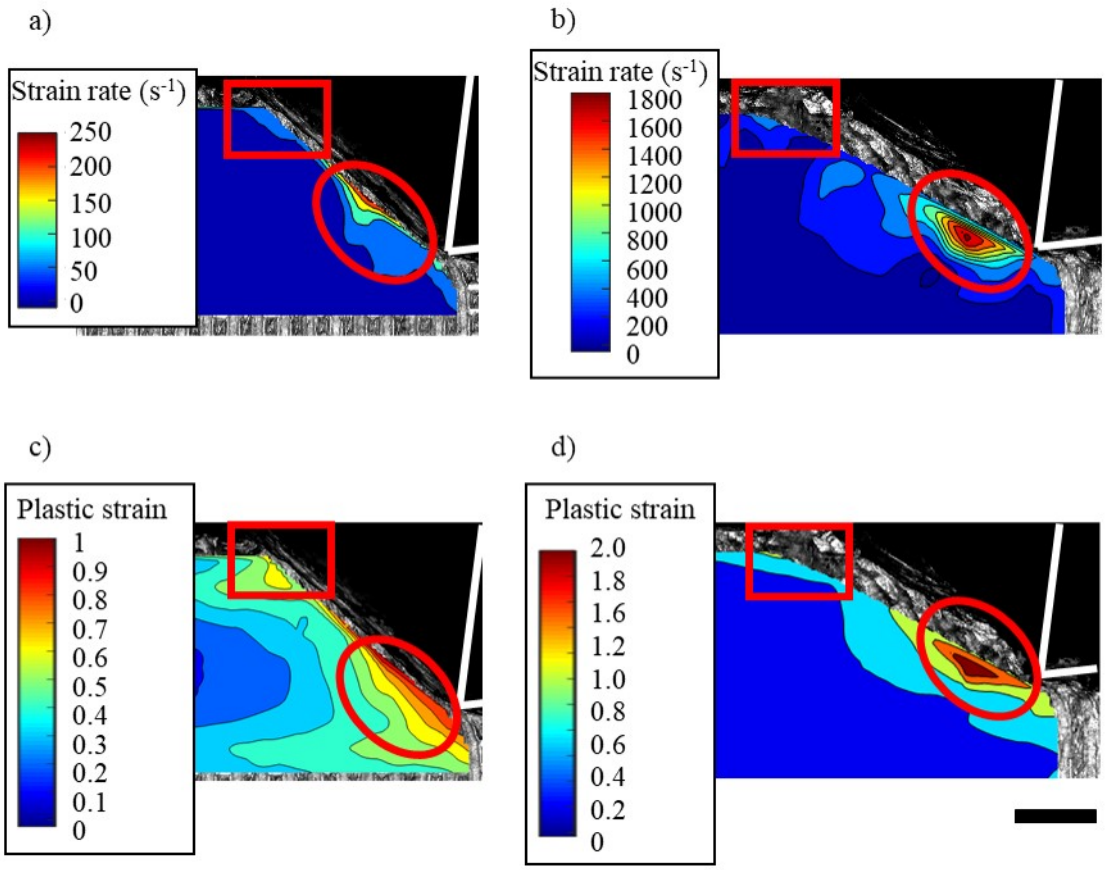

Figure 5.13: Experimental strain rate (a and b) and plastic strain fields (c and d) at the cutting speeds analysed ($f = 0.4$ mm): a) $v_c = 2.5$ m/min; b) $v_c = 7.5$ m/min; c) $v_c = 2.5$ m/min; d) $v_c = 7.5$ m/min. Tool contour is represented in white. Scale bar: 200 µm

The experimental strain rate fields, which can be seen in the Figure 5.13a and b, showed the typical shape expected in machining: a thin layer with significantly high values of equivalent strain rate in the primary shear zone. In the case of $v_c = 7.5$ m/min, the plastic strain rate varied between values around 200, in the upper zone (red squares in Figure 5.13), and 2000 s^{-1}, close to the tool (red circles). In the case of $v_c = 2.5$ m/min this variation was between 0 and 250 s^{-1}. The uncertainty was calculated according to the Monte Carlo method explained in section 5.2.1, obtaining a value of 15%. The highest values were observed close to the cutting edge, especially when v_c was 7.5 m/min. In addition, a notable influence of cutting speed was observed as the strain rate measured for 2.5 m/min was around 7 times lower. As can be observed, proposed method was able to measure strain rates close to 2000 s^{-1}, which was, for instance, 10 times higher

than the normal one reached in a compression test on a Gleeble machine (Harzallah et al., 2017). It is worth mentioning that such strain rates could be obtained in a SPHB test. However, using SPHB machine, the obtained strain and heat rate would not be representative of machining and, also, the load mode could be totally different (Field et al., 2004).

According to equation (34), equivalent plastic strain fields could be computed from equivalent strain rate field by integrating this variable along each streamline. Results are shown in Figure 5.13c and d. Machining is a very aggressive mechanical process in which the equivalent plastic strain could reach values between 1 and 2 in the primary shear zone. A thin layer of high plastic strain concentration was obtained but more spread into the workpiece compared to the thin layer observed in the equivalent strain rate fields. The highest values were reached close to the tool, being around 2 at 7.5 m/min and 1 at 2.5 m/min. In the upper zone, the equivalent plastic strain was around 0.5 under both conditions.

5.2.4 *Grid distortion validation*

In order to validate the applied technique, obtained results were compared with other different techniques including the experimental (DIC) technique explained in Section 5.1, the analytical approach proposed by Bai et al., 2017 and employed in Section 4.2 and Section 5.1, literature and numerical results obtained with the FEM model explained in Section 3.1.2.

5.2.4.1 *DIC measurements*

In Figure 5.14, plastic strain results using DIC and grid method proposed are shown and compared. Both methods can be only compared in the upper zone of the shear zone, where GOM Correlate was able to carry out the calculus as was explained in previous section. In this specific zone, the values reported by DIC method were slightly lower than the ones observed with the grid method, being around 0.3 and 0.5, respectively. Something similar happened with the strain rate, where DIC reported around 400 s^{-1} and grid method 500 s^{-1}. Similar results were obtained at 2.5 m/min.

As mentioned above, DIC measurements were made under conditions close to plane stress in which strains in the direction out of the shear plane were not constrained and side flow was proved to occur. Contrary, with the grid method proposed, the measurement zone was subjected to plane strain conditions, reducing out of plane displacements. Therefore, the technique proposed was shown to be able to measure plastic strain and strain rate fields under real machining conditions overcoming typical DIC technical difficulties. The proposed method was able to capture the equivalent plastic strain close to the tool, where higher values were obtained. High speed filming allow both images to be compared as it was possible to establish the time when the process was stopped (see Figure 5.12).

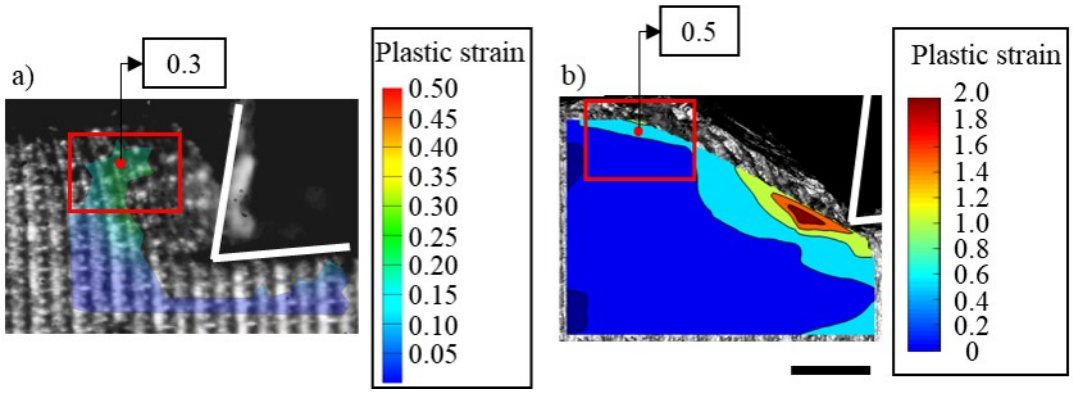

Figure 5.14: Equivalent plastic strain fields: a) DIC results; b) Grid results. Cutting conditions: $v_c = 7.5$ m/min; $f = 0.4$ mm. Note that the scale of the colour bars is different. Scale bar: 200 µm

5.2.4.2 *Literature results*

Although equivalent plastic strain and strain rate measurements under real machining conditions are still under research, a recent attempt was found in the literature aiming to measure them in Ti6Al4V. Harzallah et al., 2020 proposed the use of the microstructure of the material as a random speckle pattern to develop DIC measurements as it is summarized in Table 2.4.

The cutting conditions analysed differed from the ones proposed here. The cutting speeds were 3 and 15 m/min, for a feed of 0.25 mm. In addition, the tool geometry was also different and two different rake angles were employed being 0 and 15°. Although the proposed technique overcame the difficulties found when DIC was employed (decorrelation, loss of focus), it is worth noting that it was not able to measure under plane strain conditions, representative of the orthogonal cutting process.

Under these cutting conditions, different strain rate fields were obtained depending on the cutting state. At the highest cutting speed, the maximum strain rate, close to the tool, was around 5000 s^{-1} for the highest rake angle, being lower for the 0 rake angle. In the upper zone these values were notably lower, similar to the results shown in Figure 5.13. As the cutting speed employed was twice the highest one analysed in this study, the order of magnitude obtained was in agreement with the experimental technique proposed. Similar results were observed for the lowest cutting speed.

Analytical models could also report a first notion about the order of magnitude to validate the experimental results obtained. The analytical model was explained in Section 4.2 and the results obtained concerning equivalent plastic strain and strain rate were presented in Section 5.1. The maximum strain rate for each cutting condition calculated analytically were 753 and 2230 s^{-1}, which are higher than the measured ones (especially at 2.5 m/min) but the trend was in agreement with the reported one. It is worth mentioning that the model was not able to represent the non uniformities along the shear zone in

the strain rate fields. Similarly, under both conditions, the calculated average equivalent plastic strain was around 0.7. This is the same order of magnitude measured, although the model was not able to reproduce the effect of cutting speed on equivalent plastic strain.

5.2.4.3 *Finite Element Modelling results*

Realistic values of strain and strain rate would be expected employing the numerical model shown in Section 3.1.2 and optimized in Section 4.4 as it has been proved to be able to reproduce chip segmentation accurately, reporting also accurate values of cutting forces and chip morphology (see Figure 5.15). Therefore, the experimental strain and strain rates obtained based on the deformed grid shown in Figure 5.11 were compared with the numerical values for the different cutting conditions.

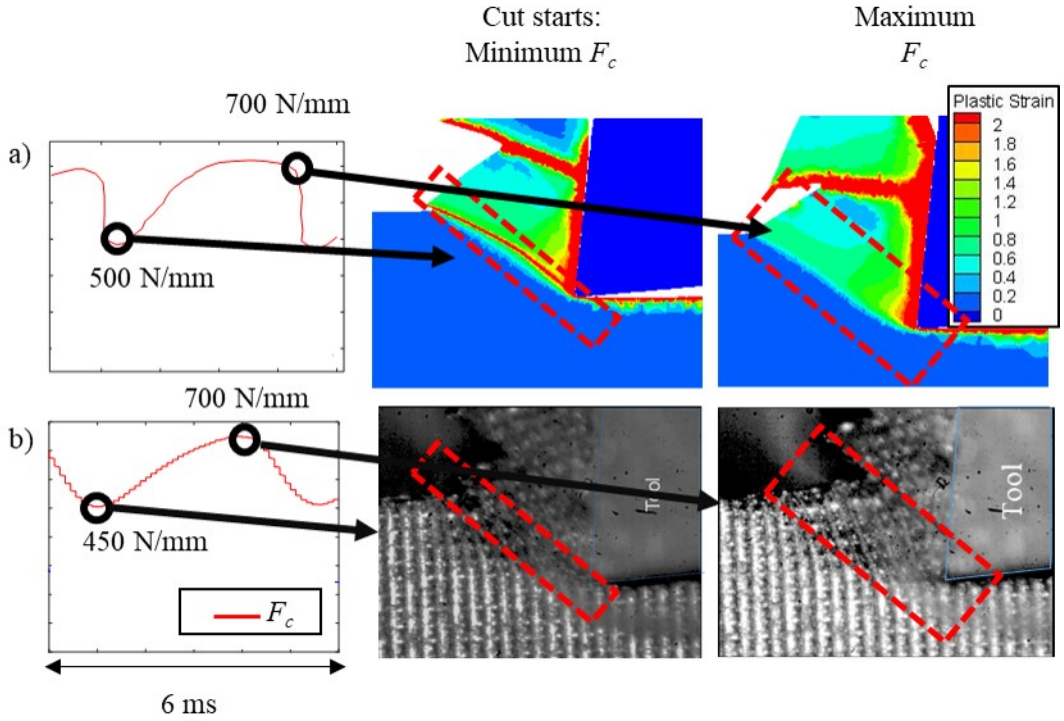

Figure 5.15: Plastic strain evolution on the shear zone at two different moments of the cutting process obtained with the FEM model compared with experimental grids. Cut starts (minimum cutting force, left) and maximum cutting force (right). Cutting conditions: $v_c = 7.5$ m/min and $f = 0.4$ mm. a) Finite element modelling results; b) Experimental results

The corresponding frame in the numerical simulations was chosen (for each condition), taking the frame at which the cutting force was maximum, in order to compare numerical and experimental results. Figure 5.16 shows the obtained results. The red squares represent

the upper zone of the shear zone whereas the red circles represent the zone named as close to the tool.

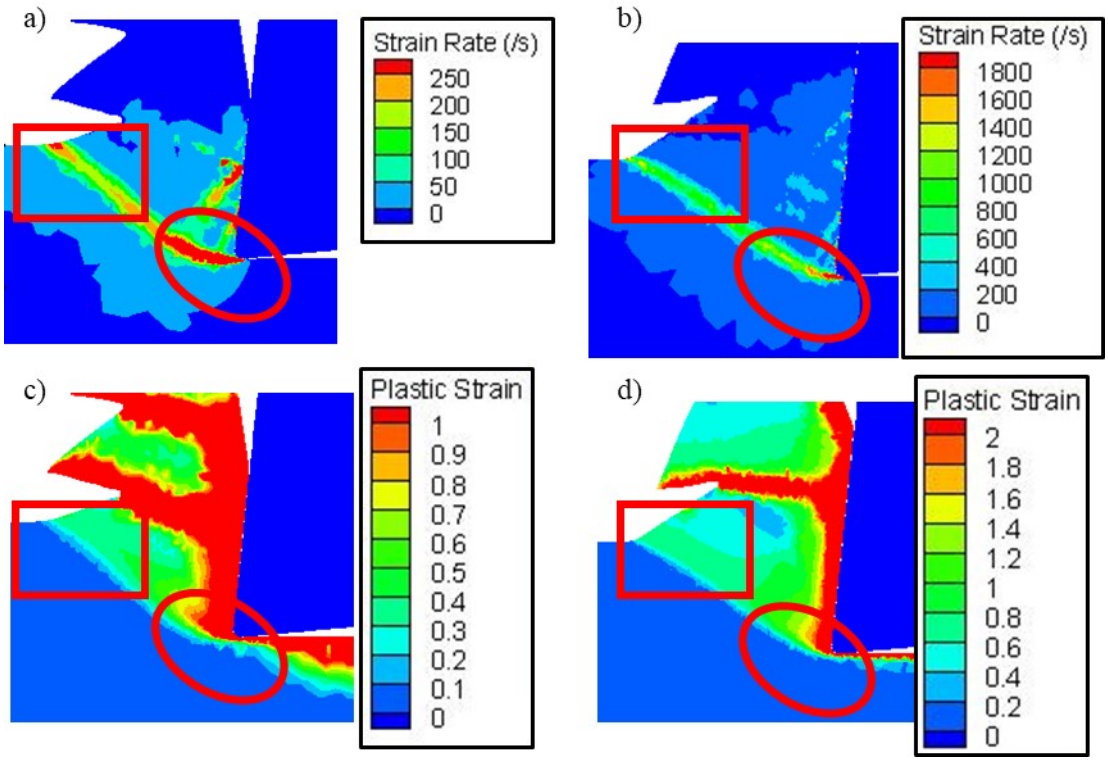

Figure 5.16: Numerical strain rate (a and b) and plastic strain fields (c and d) under the cutting speeds analysed: a) $v_c = 2.5$ m/min; b) $v_c = 7.5$ m/min; c) $v_c = 2.5$ m/min; d) $v_c = 7.5$ m/min

The numerical strain rate fields also showed the typical shape expected in machining and observed by the experimental technique. In the case of $v_c = 7.5$ m/min, the plastic strain rate oscillated between 500 s^{-1} in the upper zone and a maximum value close to the tool around 1800 s^{-1}. In the case of $v_c = 2.5$ m/min, as in the experimental case, this variation was between 0 and 250 s^{-1}. In general, the highest values were observed close to the cutting edge for both cutting speeds. The same trend with the cutting speed was reported by the numerical model. Experimental and numerical results reported the same order of magnitude. In addition, a thin layer of high plastic strain concentration was obtained with the highest values located close to the tool. At 2.5 m/min the highest plastic strain was around 1 whereas at 7.5 m/min was around 2, in agreement with the equivalent plastic strains measured. Under both conditions, in the upper zone, an equivalent plastic strain between 0.3 and 0.5 was obtained.

Summarizing, the following conclusions can be highlighted:

- The methodology was employed to measure plastic strain and strain rate during orthogonal cutting under realistic broaching conditions using a unique image, avoiding decorrelation problems typical of DIC based methodologies and under plane strain conditions.
- With the methodology presented, equivalent strain rates of more than 1800 s^{-1} and equivalent plastic strains of 2 were measured in the shear zone with a standard deviation of 15% when cutting Ti6Al4V at 7.5 m/min with a feed of 0.4 mm.
- It was experimentally observed that the strain rate notably decreases when cutting speed decreases. Also equivalent plastic strain measured was lower for the lowest cutting speed.
- Experimental strain and strain rates were compared with analytical results and the observed trends matched well. Experimental results were also compared with results presented in literature, observing the agreement between the literature results and those obtained with the proposed grid method. Finally, FEM results also showed agreement with the experimental ones.

The methodology is expected to be employed at higher cutting speeds using images obtained by high speed filming, because i) at such conditions the stop methodology is not applicable, and ii) the digital image correlation software was observed to fail under these conditions. Moreover, the use of high speed images will permit the analysis of the variation of strain and strain rate as the cutting progresses, taking into account the measurement will be carried out under plane stress conditions. Finally, an important issue to be implemented is the use of some kind of artificial intelligence able to select grid points to apply the method.

5.3 CONCLUSIONS

Having made the equivalent plastic strain measurements of the orthogonal cutting process, the main results are summarized here:

- It was shown that patterns generated by spray painting, typically employed in thermomechanical tests, were not valid to carry out plastic strain measurements during orthogonal cutting because of decorrelation and decohesion problems due to the extreme thermomechanical loads and side flow. Therefore, mechanical patterns were tested and proved to be a possible technique to overcome these limitations. However, these techniques could not measure the plastic strain under plane strain conditions representative of the orthogonal cutting process.
- Slight discrepancies found between the experimental values obtained with DIC and FEM were assumed to be due to the different load modes applied. The development of a 3D model would be needed to study this issue.

- In order to overcome these limitations, a set-up was designed to fulfil plane strain conditions. The new technique enabled plastic strain and strain rates to be measured using a single image, avoiding decorrelation problems.
- With the methodology presented, equivalent strain rates close to 2000 s^{-1} and equivalent plastic strains of 2 were measured. The value of strain rate is, for instance, around 10 times higher than the typical ones reached with a Gleeble thermomechanical simulator. The standard deviation was quantified to be 15% by a Monte Carlo simulation.
- The proposed technique was validated based on analytical results employing the unequal division shear zone model, experimental results from literature and FEM results, observing good agreement between the reported trends.

6 SUBSURFACE DAMAGE MEASUREMENTS

The knowledge of subsurface state after a mechanical process is of great interest as it could directly influence the mechanical properties of the final part. Due to the high thermomechanical loads at which the material is exposed during the machining process, the material suffers microstructural alterations to a shallow depth from the surface that may have different thermomechanical behaviour compared to the bulk material. Therefore, one of the most widely employed techniques to characterize the surface state is the microstructural analysis.

However, the main drawback of this technique lies in the fact that it might not be possible to wholly measure the defects leading to some subjectivity in the measurements. To address this, different methods appear in literature as possible solutions as summarized in Section 2.5.

In this sense, microhardness and grid distortion methodologies could be a solution. Although microhardness analysis might be less qualitative, the resolution may not be enough, depending on the hardness of the bulk material and the applied load. Small loads generate lower traces which could be affected by microstructural issues (phases, particles) whereas the traces generated by big loads are higher, reducing the resolution. Grid distortion was thus employed aiming to overcome these limitations. These methodologies were also used to analyse the effect of machining inputs such as workpiece material, tool geometry and tool material.

Therefore, this chapter is organized as follows. First the experimental set-up employed was briefly explained. Then, different methods tested to quantify subsurface damage including microstructural method, microhardness and grid distortion were analysed and discussed. They were also compared to FEM results. To follow, the effect of material initial microstructure on subsurface damage was studied. Finally, the effect of cutting edge radius and tool coating was analysed proving the importance of selecting a proper tool to carry out the experimental tests.

6.1 EXPERIMENTAL SET-UP FOR SUBSURFACE DAMAGE ANALYSIS

The tests were carried out with an orthogonal linear cutting device which allows higher cutting speeds than the ones reached with the set-up explained in Section 4.1 (up to 70 m/min). Forces were measured with a Kistler dynamometer 9257 implemented in the linear device with a sampling rate of 5000 Hz. Photron FASTCAM APX-RS 250K and FLIR Titanium 550M were able to record the process at the same time, as Figure 6.1 shows. The sampling rate for the infrared camera was 1000 Hz whereas different

frame rates were used with the high speed camera depending on the cutting speed. A magnification lens of 10X was added to the Navitar 12X to achieve higher magnifications. The ROI was illuminated during the test with a coaxial light and with HMI HSL 250 cool light at the same time. The high speed filming was carried out to determine the real feed of the test as the stiffness was lower than in the CNC case explained in Section 4.1.

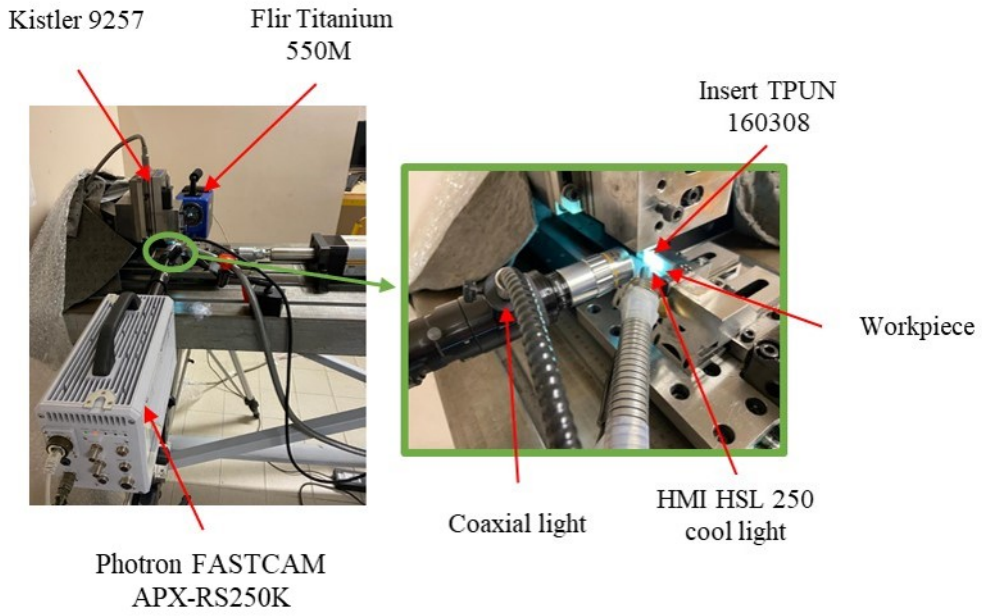

Figure 6.1: Linear cutting set-up to carry out subsurface damage analysis

For the microstructural observations, the workpiece was mounted on resin and polished up to mirror finishing. Then, the sample was etched with Kroll's reagent and observed through an optical microscope with 500X magnification, although some images were taken with 1000X so as to have higher resolution.

Concerning microhardness analysis, a Vickers indenter was employed in the etched sample with a load of 50 g. Finally, a self-made grid through micromilling, like the one in Section 5.1.1, was employed for the grid analysis. The width of the grid paths was 30 μm.

The samples employed consisted of flat specimens of 50x40 mm^2. The samples were obtained from a rolled bar along the longitudinal direction (Z axis, rolling direction, in Figure 6.2). In addition, it can be seen that the grains were mainly oriented in the rolling direction. The experimental conditions analysed are summarized in Table 6.1. Experimental results were also compared with those obtained employing the model explained in Section 3.1.2. The highest feed was varied between 0.3 and 0.4 due to the accuracy of the positioning system and the necessity of avoiding high mechanical impacts which could affect the clamping system.

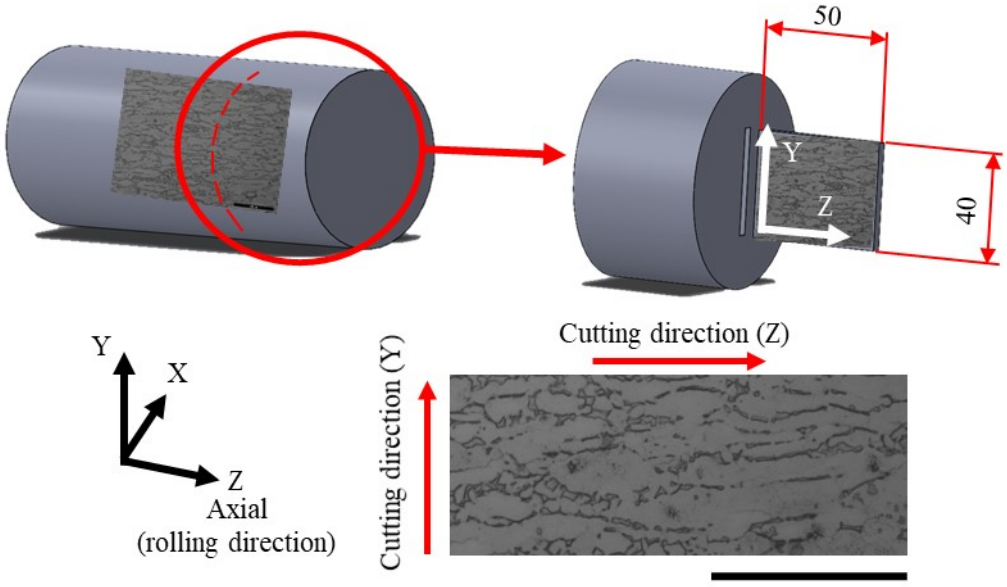

Figure 6.2: Rolled bar from which linear samples are taken and microstructure orientation. Scale bar: 50 µm

Table 6.1: Experimental conditions of the orthogonal cutting tests carried out to develop subsurface damage analysis

Tool	Reference	TPUN 160308
	Rake angle, γ [°]	6
	Clearance angle, α [°]	5
	Edge radius, r_e [µm]	8-24
	Coating	Uncoated-TiN (4 µm)
Material	Reference	Ti6Al4V
	Microstructural orientation	Z (rolling direction)-Y
Cutting conditions	Cutting speed, v_c [m/min]	2.5; 7.5; 30; 50; 70
	Feed f [mm]	0.07; 0.2; 0.3-0.4
	Width [mm]	4
	Lubrication	Dry

It is worth mentioning that, firstly, so as to ensure the robustness of the results, the possible variation of the subsurface damage along the width of cut was analysed based on the metallographic etching analysis. Therefore, this was carried out employing the

set-up shown in Figure 4.1 in order to ensure high stiffness, at low cutting speeds (the width of the sample was 2 mm).

In addition, the effect of tool edge radius, tool coating and material microstructure was analysed at the lowest feed and at different cutting speeds, as these conditions are representative of the finishing processes in machining. Feed forces and the temperature in the machined surface were measured under these conditions, as these outputs are assumed to be important to define the surface state.

The surface filmed with the infrared camera was painted black to ensure high emissivity which was set to 0.8. The resolution (0.18 pixel/mm) was lower than in the previous case shown in Section 4.1 as the set-up did not permit the location of the camera so close to the workpiece. A measurement point was taken to measure the temperature reached on the surface after the cutting process as shown in Figure 6.3.

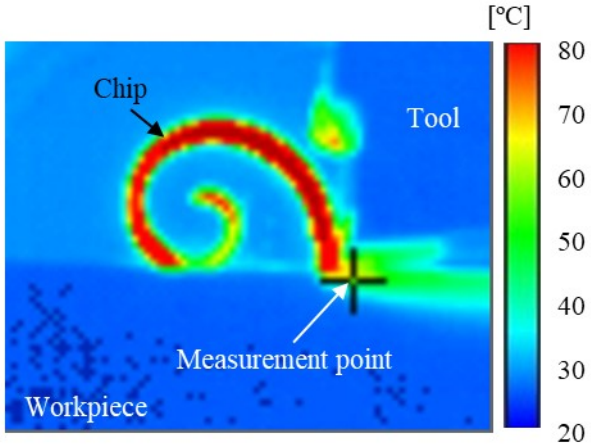

Figure 6.3: Example of the surface temperature measurement for the subsurface damage analysis. Cutting conditions: $v_c = 2.5$ m/min and $f = 0.07$ mm, $r_e = 24$ µm, uncoated tool

For the analysis of the effect of the initial microstructure on subsurface damage, it was measured employing the three techniques presented above, in order to see whether the proposed technique was sensitive to microstructural effects or not.

6.2 SUBSURFACE DAMAGE MEASUREMENTS

This section aims to compare the use of grid distortion with methods traditionally employed to measure subsurface damage (microstructural observations and microhardness). The measurements were also compared with subsurface damage values obtained from the FEM model explained in Section 3.1.2

Apart from the subjectivity and uncertainties related to these measurements, subsurface damage may vary depending on the workpiece width. In general, it is widely accepted that subsurface damage does not vary along the width of cut in orthogonal

cutting and the measurements are usually carried out in the centre of the sample where plane strain conditions could be assumed. However, no studies were found analysing the validity of this hypothesis.

Therefore, the potential variation of subsurface damage along the width of cut was tested at different widths aiming to validate this assumption. To perform the analysis, microstructure based measurements were performed along the width of the sample under different cutting conditions (cutting speed of 2.5 and 7.5 m/min and feed of 0.1 and 0.2 mm).

An example is shown in Figure 6.4. Four different measurements were carried out along the width (0.12, 0.32, 0.62 and 1 mm). As can be seen, no remarkable variations were found along the width of cut, the subsurface damage being between 7.2 and 7.5 µm.

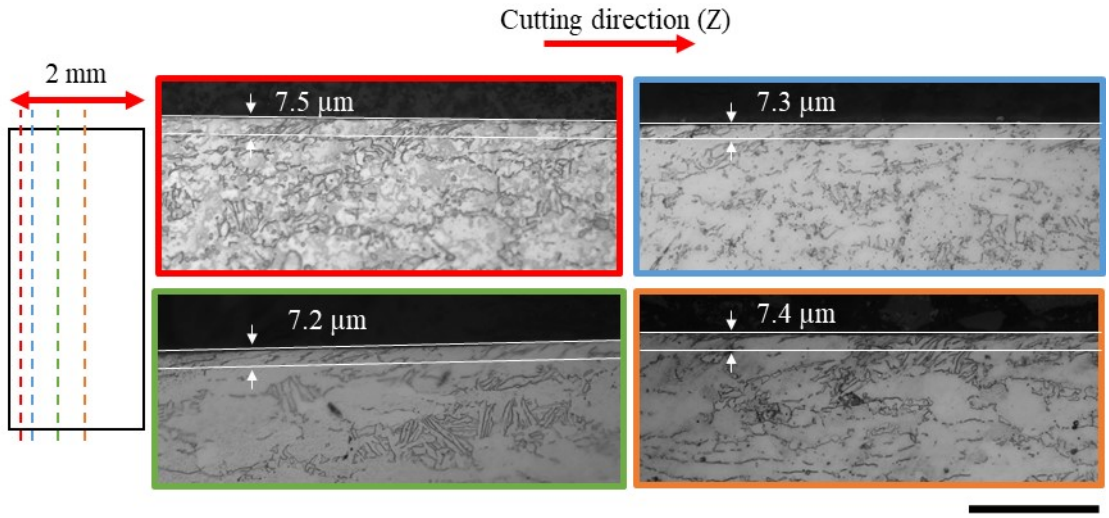

Figure 6.4: Variation of the subsurface damage along the width of cut. Red: 0.12 mm of depth; blue: 0.32 mm of depth; green: 0.62 mm of depth; orange: centre of the sample. Cutting conditions: $v_c = 2.5$ m/min; $f = 0.07$ mm. Scale bar: 50 µm. Standard deviation: 10%

The same behaviour was found with the other cutting conditions. Therefore, it can be assumed that the obtained results of subsurface damage would be representative of the surface integrity state regardless of the width position. This is of considerable relevance as microgrid based measurements were carried out with the grid located in the external face where side flow could take place. This analysis permitted the comparison of different methodologies regardless of the width position.

Microhardness is another widely employed technique and an example of a microhardness measurement is shown in Figure 6.5. As can be seen, the microhardness traces were around 15 µm for an applied load of 50 g. Therefore, the subsurface damage must be greater in order to measure it with this technique.

In order to have higher resolution (lower traces), smaller loads were tested, up to 10 g. However, the traces were too low and any microstructural issue could influence the

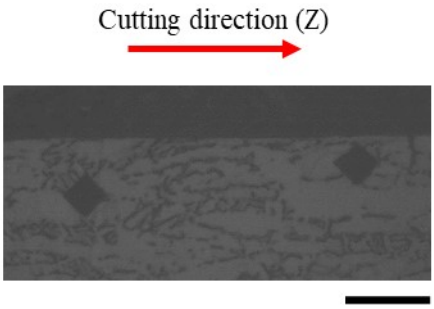

Figure 6.5: Example of different microhardness measurements at different depths. Cutting conditions: $v_c = 50$ m/min and $f = 0.07$ mm. Scale bar: 30 µm

measurement causing notable variations in the measurements making it impossible to determine the subsurface damage. Thus, all the measurements were carried out with 50 g of load.

In Figure 6.6 the variation of the material microhardness over the depth of the workpiece is shown for a cutting speed of 50 m/min and a feed of 0.07 mm. It can be seen that the bulk microhardness was around 340 $HV_{0.05}$ whereas the workpiece was hardened up to 480 $HV_{0.05}$ close to the machined surface. The hardened layer was observed up to around 24 µm.

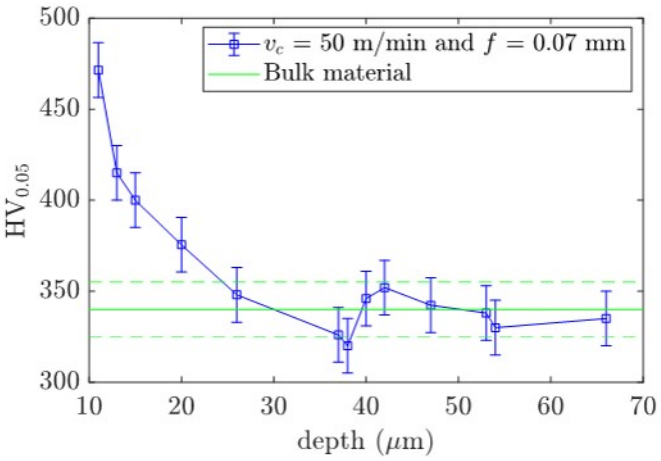

Figure 6.6: Microhardness evolution over depth in comparison to the bulk material. Cutting conditions: $v_c = 50$ m/min and $f = 0.07$ mm. Cutting conducted in the rolling direction (Z)

Subsurface damage was also measured through grid distortion. A deformed microgrid after the machining process is shown in Figure 6.7. As can be seen, the deformed layer was easily measured. At this moment, the measurements were taken by a researcher based on the deformed grid. This could lead to some degree of subjectivity which is not

comparable to that employing other methods. In the future, these measurements are expected to be made by some kind of artificial intelligence, reducing as much as possible this subjectivity.

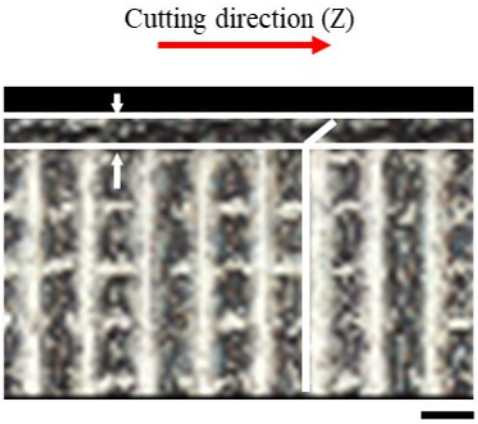

Figure 6.7: Example of grid distortion measurement to determine the subsurface damage. Cutting conditions: $v_c = 50$ m/min and $f = 0.07$ mm. Scale bar: 50 µm

Finally, the measurements were also compared with the results reported by the numerical model explained in Section 3.1.2. In order to obtain comparable results, the subsurface damage from FEM results was measured based on plastic strain field, assuming 0.02 of strain as the threshold value (Ghadbeigi et al., 2012). An example is shown in Figure 6.8.

6.2.1 *Subsurface damage measurements results*

Figure 6.9 shows the results obtained employing the techniques presented above under different cutting conditions.

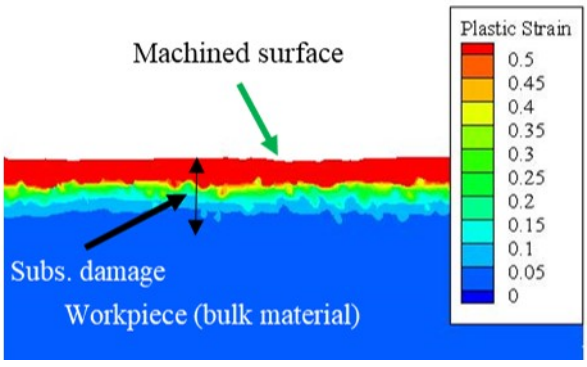

Figure 6.8: Example of FEM subsurface damage measurements. Cutting conditions: $v_c = 50$ m/min and $f = 0.07$ mm. Subsurface damage: 17 µm

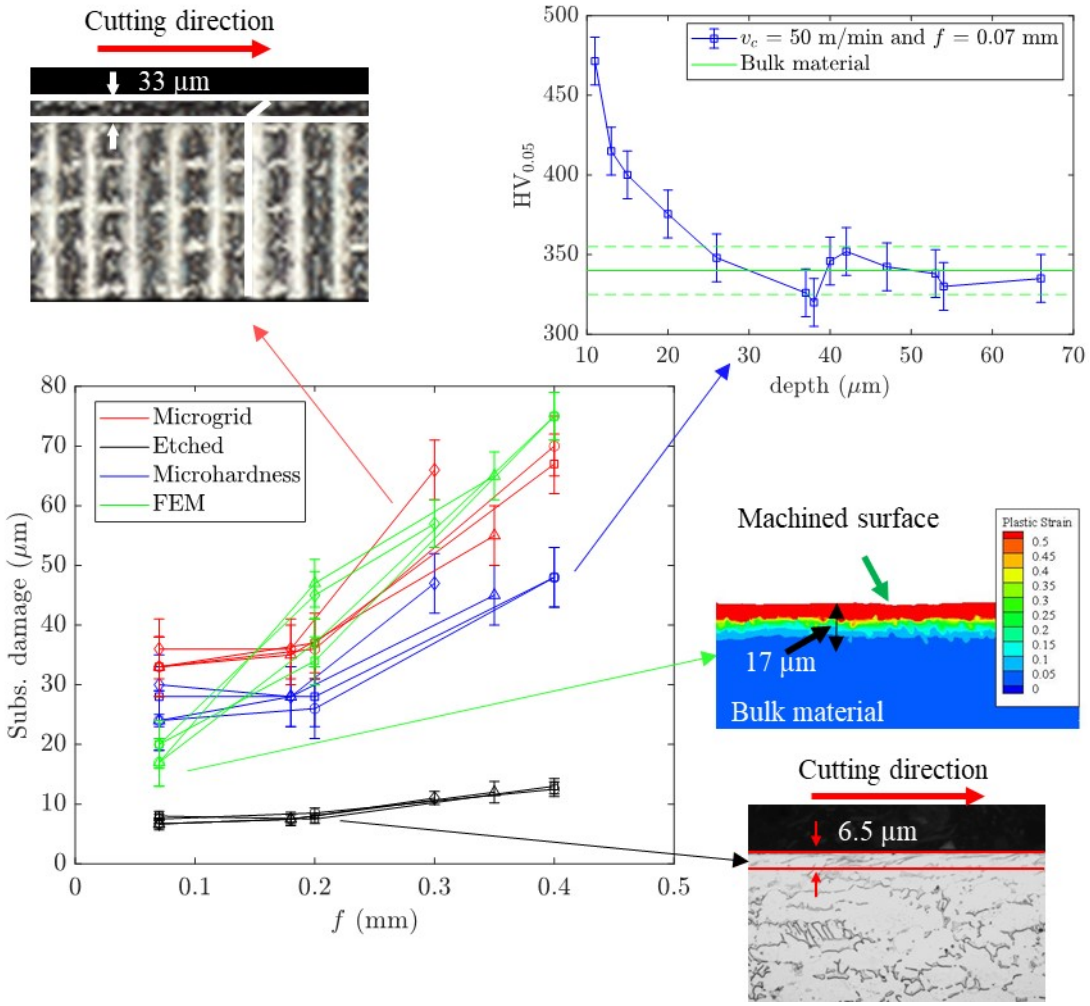

Figure 6.9: Subsurface damage measurements. Each marker represent a different cutting speed: circles, 2.5 m/min; squares: 7.5 m/min; triangles: 50 m/min; diamonds: 70 m/min. Examples of the measurements: v_c = 50 m/min and f = 0.07 mm for the four methodologies tested. Cutting conducted in the rolling direction (Z)

As can be seen, in general, the increase in the feed resulted in an increase of the subsurface damage regardless of the measurement technique employed. Nevertheless, it is worth noting that this effect was more prominent at high feeds, whereas at low feeds (between 0.07 and 0.2 mm) the effect was less noticeable. This could be due to the edge effect, as higher edge radii would result in higher ploughing and rubbing actions. FEM model was not able to reproduce this properly, showing a progressive increase of the subsurface damage with the feed. The edge radius employed in the tests was 24 µm. In addition, the surface state at the lowest feed is of considerable relevance as finishing operations are usually done at low feeds, aiming to ensure an appropriate surface integrity.

The three experimental techniques reported the same trend. This proves the robustness of the proposed technique to measure subsurface damage as microhardness and etched measurements are widely accepted in literature.

Focusing on the effect of cutting speed, the results with all the techniques presented were compared in Figure 6.10 at the lowest feed. It can be seen that all the techniques tested reported the same trend with no remarkable effect of cutting speed. The values reported with the microgrid technique were always higher, even compared to FEM measurements.

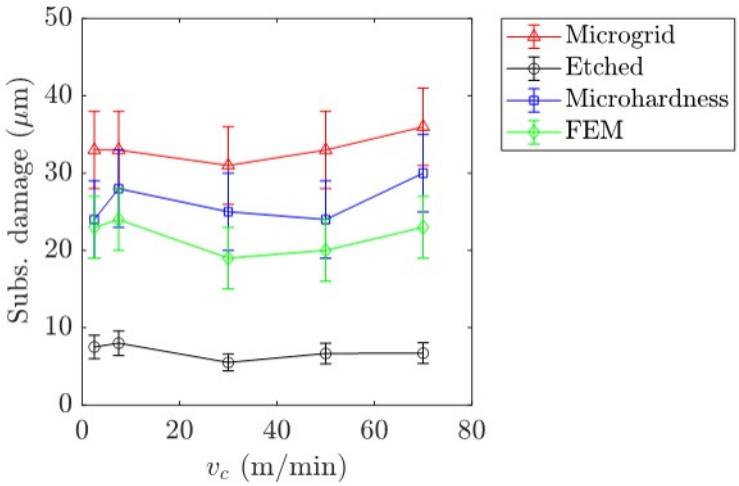

Figure 6.10: Effect of cutting speed on subsurface damage. Comparison among different measurement techniques ($f = 0.07$ mm). Cutting conducted in the rolling direction (Z)

This suggests that the microgrid based method is more sensitive to material deformation than the traditional ones based on microstructure and microhardness measurements. In addition, FEM model was able to reproduce material behaviour in terms of subsurface damage, as the reported trend was coherent with the experimental results.

Therefore, the use of microgrid to measure subsurface damage could report a valuable input to optimize material law by using inverse simulation in order to develop numerical models able to accurately report industrial outcomes.

To sum up, based on the presented results, the following conclusions can be drawn:

- The subsurface damage was observed to increase with feed specially at high feeds. At low feeds the value remains almost constant which is assumed to be due to the edge effect.
- The effect of cutting speed on subsurface damage was proved to be negligible as all the measurement techniques reported the same trend between 2.5 and 70 m/min.
- The microgrid technique is more sensitive to material deformation as the values reported were higher than the ones reported by microhardness and etched based

measurements. In addition, the proposed technique reduces the subjectivity associated with optical based measurements and could be improved by employing artificial intelligence.

6.3 EFFECT OF MACHINING INPUTS: WORKPIECE MATERIAL AND TOOL

It is widely accepted that sharp tools provide better surface integrity as the force in feed direction is reduced. Another significant aspect with regard to cutting tool is the coating. For difficult-to-cut alloys, coating is often used to preserve the tool from wear as it could lead to a decrease on cutting forces as it improves the tribological conditions during the cutting process. However, the effect of coating on surface integrity, is not widely analysed in literature.

The microstructure of the material being cut is also an important aspect to be taken into consideration. The majority of the studies however are focused on shear band formation or subsurface microstructure without analysing the effect of material microstructure on different machining outcomes such as machinability or surface integrity. Therefore, in spite of the few references widely discussed in Section 2.5, further research is needed concerning tool edge radius, tool coating and material microstructure. In addition, the majority of these studies are focused on high cutting speeds whereas the broaching regime, of wide relevance in finishing operations, is usually not taken into consideration in the analysis.

The first parameter analysed was the material microstructure. Figure 6.11 shows the surface state of the machined part subjected to the same cutting conditions (v_c = 70 m/min and f = 0.07 mm) employing both microstructural orientations.

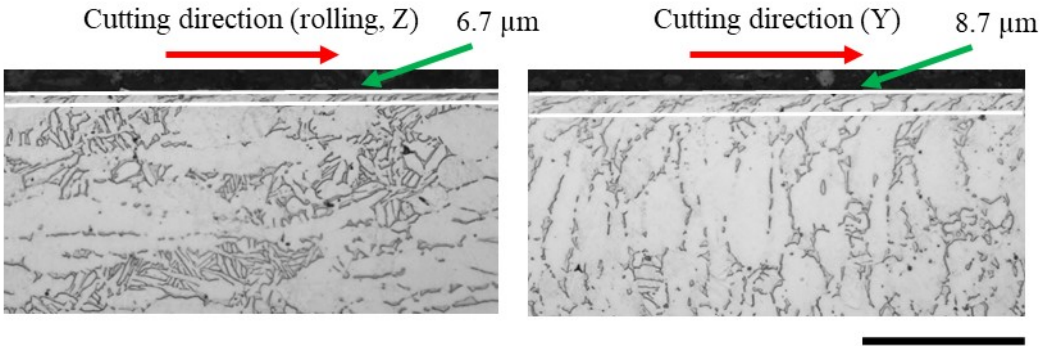

Figure 6.11: State of the machined surface (subsurface damage) with different microstructural orientations (see Figure 6.2). Rolling direction (Z, left) and Y direction (right). Cutting conditions: v_c = 70 m/min and f = 0.07 mm. Scale bar: 50 µm

As can be seen, the surface state varied depending on the microstructural orientation, being the subsurface damage higher when the material was cut in the Y direction. However, Y orientation made the measurement easier as the grains were mainly oriented

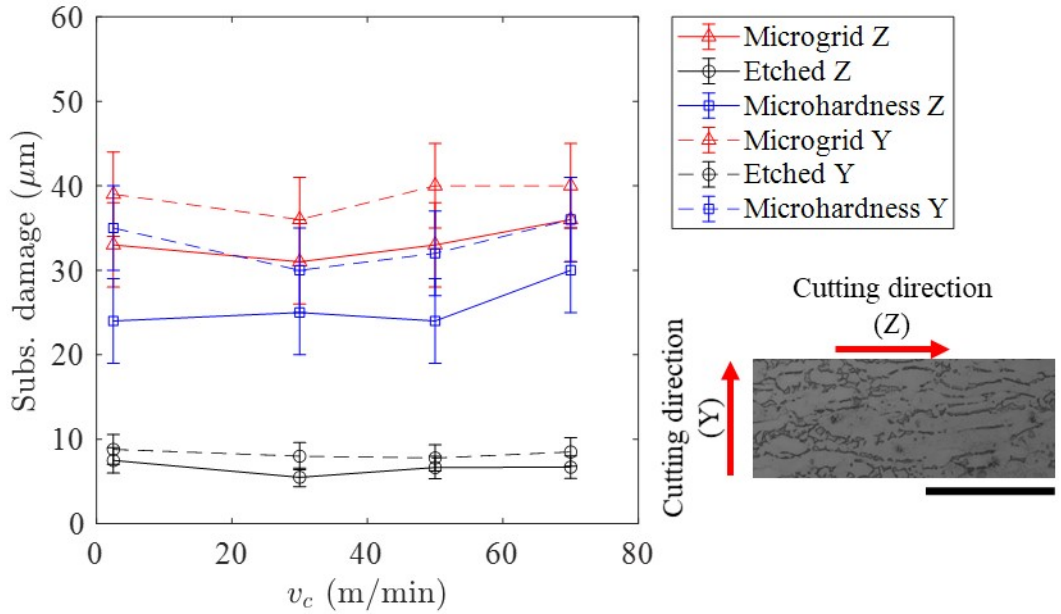

Figure 6.12: Effect of microstructure orientation on subsurface damage at different cutting speeds. Comparison of different measurement techniques (f = 0.07 mm). Scale bar: 50 μm

perpendicular to cutting direction. Therefore, it is difficult to establish whether this variation on subsurface damage was due to microstructure effect or it could be affected by the subjectivity on the measurement. To overcome this, subsurface damage was also measured with microhardness and microgrid methods. The results under different cutting conditions are shown in Figure 6.12.

It can be observed that regardless of the method employed that the subsurface damage was always around 17% (in average) higher in the Y direction. This means that the surface integrity state obtained after orthogonal cutting would be worse when cutting the material oriented in Y direction.

It is also clear that, as in previous section, microgrid based method was more sensitive than the other ones, all of them reporting the same trend. Therefore, hereafter only etched and microgrid based methods were employed.

With regard to the effect of the edge radius, the results employing two different edge radii (8 and 24 μm) are shown in Figure 6.13.

The effect of the edge radius on surface integrity in terms of subsurface damage seems clear. With both microstructural orientations, the subsurface damage was reduced around 40% regardless of the measurement method employed. This could be expected as lower rubbing and ploughing actions (edge effects) would be obtained with lower edge radii (Wyen and Wegener, 2010).

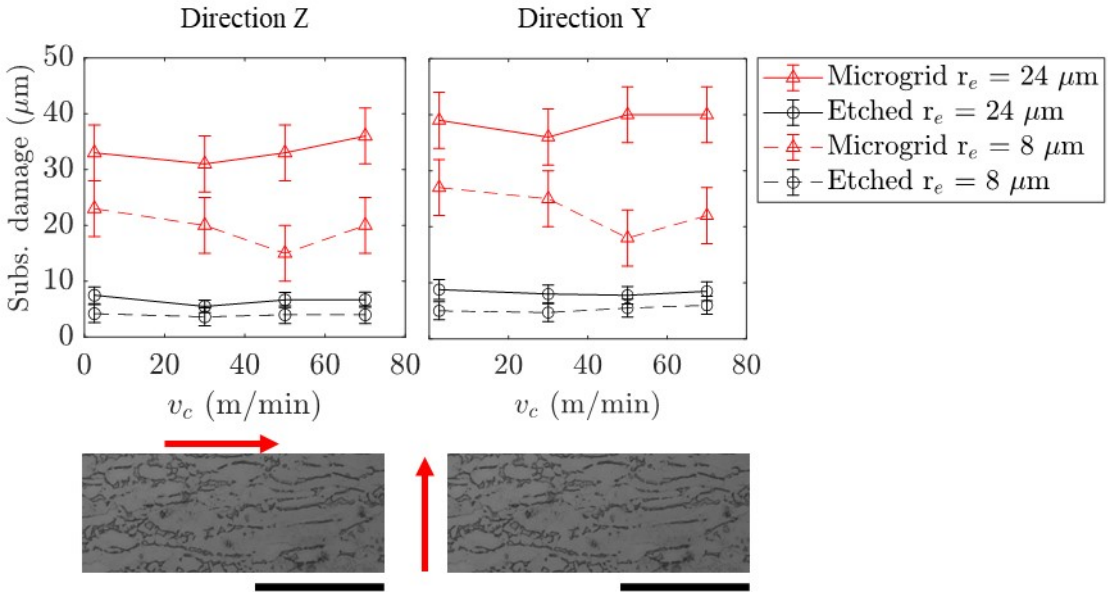

Figure 6.13: Effect of edge radius on subsurface damage at different cutting speeds. Comparison of different measurement techniques with the two microstructural orientations (f = 0.07 mm)

Finally, the effect of coating was analysed. The coating layer was around 4 µm and no significant influence was found in the cutting edge radius. The edge radii were measured with Alicona profilometer IFG4 with 10X magnification and three different inserts were measured in order to ensure the robustness of the results. The obtained tool profiles are shown in Figure 6.14. It is worth mentioning that the nominal rake and clearance angle of the insert were 0 and 11°, respectively. The angles shown in Table 6.1 were achieved once the tool was positioned in the tool-holder. Therefore, it can be assumed that any effect of tool coating was not affected by the edge radius.

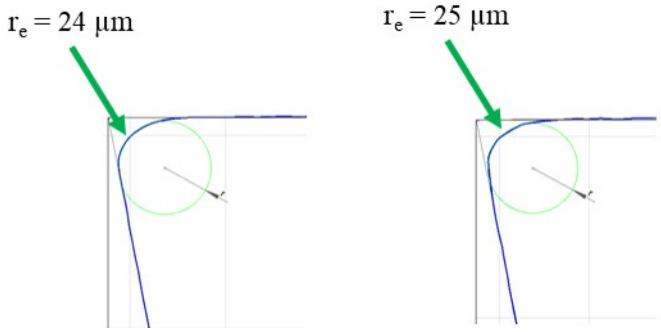

Figure 6.14: Profile of the edge radius for the uncoated case (left) and coated case (right) measured with Alicona IFG4. Standard deviation: 2 µm

The effect of tool coating on subsurface damage is shown in Figure 6.15. This effect was lower compared to edge radius although it seems to be a slight decrease in the subsurface damage, especially at high cutting speeds. At 2.5 m/min no differences were found using both coated and uncoated tools.

At high cutting speeds, higher than 30 m/min, the reduction using coated tools was around the 12% taking into consideration microgrid based measurements. It is worth mentioning that this trend was not reported by traditional etched measurements, thus the microstructure seems not to have enough sensitivity to detect the influence of the coating.

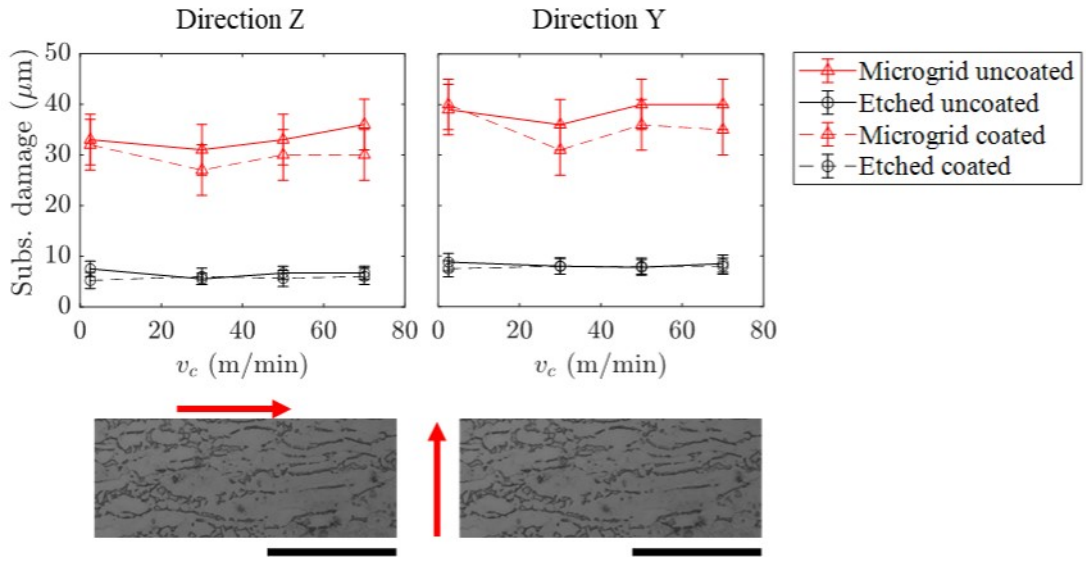

Figure 6.15: Effect of tool coating on subsurface damage at different cutting speeds. Comparison of different measurement techniques with the two microstructural orientations (f = 0.07 mm)

In order to analyse more in depth these results, cutting forces and workpiece temperature in the surface were measured as explained in Section 6.1. The force to be used in the analysis was the feed force as it is known to have higher influence on surface integrity than cutting force. The variation of feed force due to edge or coating effect is shown in Figure 6.16.

Based on Figure 6.16, the effect of tool coating seems negligible on cutting forces whereas the feed force reduction was noticeable with the lowest edge radius. The reduction on the feed force was around 36%. This could explain the reduction of the subsurface damage observed in Figure 6.13. However, the effect of tool coating is still unclear. For this reason, the surface temperature was measured. The results are shown in Figure 6.17.

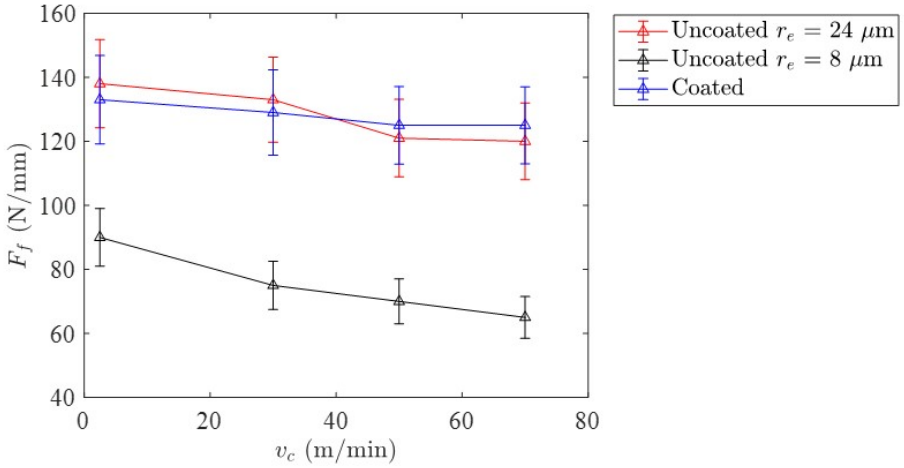

Figure 6.16: Effect of edge radius and tool coating on feed force at different cutting speeds (f = 0.07 mm, rolling direction)

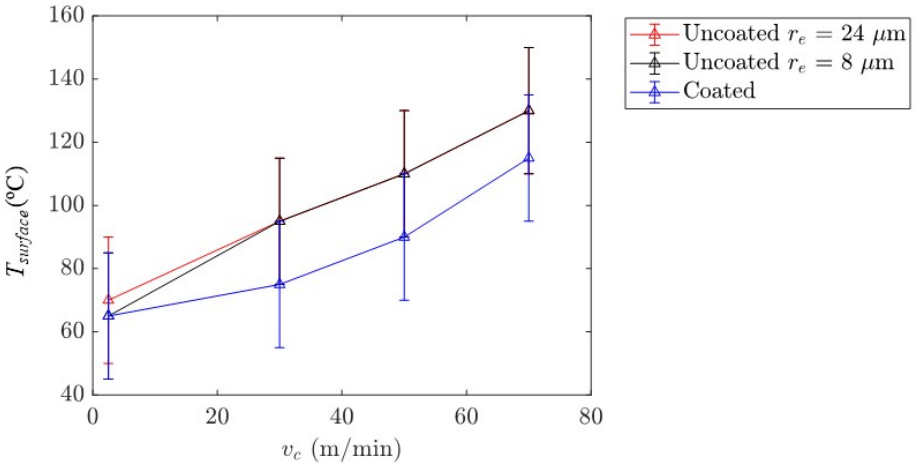

Figure 6.17: Effect of edge radius and tool coating on surface temperature at different cutting speeds (f = 0.07 mm, rolling direction)

It can be seen that surface temperature was slightly lower in the coated case whereas no influence was found with the edge radius. The coating changes the tribological behaviour. Thus, the lower temperatures obtained in the coated case could lead to a better surface integrity as heat could become a relevant source of damage when machining titanium alloys, especially under dry conditions as stated by Ginting and Nouari, 2009.

Summarizing, based on the presented results, the following conclusions can be highlighted:

- The microstructure of the workpiece material plays a relevant role in terms of surface integrity. Two different microstructural orientations were analysed and worse surface integrity states were obtained when cutting in the Y direction, with subsurface damages 15% higher than in the rolling direction. The same trend was reported with the three measurement techniques employed.
- As expected, the sharpest tool reported the best results in terms of subsurface damage. The subsurface damage was 40% higher when the cut was carried out with the tool with an edge radius of 24 µm. The reduction of the cutting edge radius led to a notable reduction on the feed force which could explain this improvement.
- The effect of tool coating seems negligible on surface integrity based on etched measurements. However, it was found a slight decrease (around 12%) on subsurface damage at high cutting speeds employing microgrid technique when the coated tool was used. The coating caused the surface to become less warm based on infrared measurements.

6.4 CONCLUSIONS

After the comprehensive subsurface analysis was carried out, the following conclusions can be drawn:

- No clear agreement was found between researchers when reporting subsurface damage results. Therefore, a novel microgrid technique was proposed in order to measure it while reducing the subjectivity associated with the other tested methodologies.
- The microgrid technique was more sensitive to material deformation as the values were higher than the ones reported by the other methods. A clear increase of the subsurface damage with the feed was observed, whereas the cutting speed effect seemed negligible.
- A relevant input briefly studied in literature is the initial microstructure. Two different microstructural orientations were analysed and it was demonstrated that worse surface integrity was obtained when cutting the material in the Y direction, the subsurface damage being 15% lower in the rolling direction.

- The sharpest tool reported the best results, the subsurface damage being 40% lower. This reduction could be explained based on the reduction observed in the feed force.
- Microstructure based measurements were not sensitive enough to detect the effect of tool coating on subsurface damage. However, a reduction of 12% was measured based on microgrid measurements when employing the coated tool. These results are in accordance with the temperature measurements.

7

CONCLUSIONS AND FUTURE LINES

7.1 CONCLUSIONS

The analysis of the orthogonal cutting process elucidates the necessity of reliable experimental data to develop robust numerical models. However, there is a clear lack of knowledge regarding experimental outcomes such as workpiece temperature, equivalent plastic strain or strain rate. In the present study, as a first step, a thermomechanical analysis of the Ti6Al4V alloy has been done. Then, a novel methodology to measure plastic strain in the shear zone and subsurface damage has been presented together with a methodology to characterize the ductile failure law by inverse simulation. This methodology considers chip segmentation measurements to carry out the optimization. All the proposed methodologies were validated theoretically and compared with numerical results, and the following conclusions can be drawn:

Thermomechanical characterization of the workpiece material

- New samples were designed aiming to reproduce the complex tensional state reached during real machining processes. The new sample design enabled different load conditions to be tested with slight changes in geometry. The process could also be filmed, which allowed infrared measurements to be made and plastic strain to be measured based on DIC.
- A proper speckle pattern technique was found to measure equivalent plastic strain at temperatures up to 900°C. Based on thermal measurements, it was observed that the sample was self-heated because of the intense strain reached during the deformation process. This parameter is critical for the development of robust numerical models. However, different definitions can be found in literature, with the potential for misunderstandings, and this aspect was clarified in the present work.
- A technique to measure the adiabatic self-heating under shear conditions taking into consideration a 3D control volume was also proposed. The technique considers heat loss and energy captured with infrared measurement, demonstrating its validity at high temperatures.

Orthogonal cutting

- Through the use of infrared measurements in the shear zone, it was observed that there was a significant increase in temperature with cutting speed, especially at cutting speeds lower than 10 m/min. Chip segmentation produced during machining of Ti6Al4V led to the oscillation of outcomes such as cutting forces, chip thickness and workpiece temperature. The oscillation frequency was proved to be a valuable input to optimize the ductile failure law by using inverse methodology, reducing the error in the frequency prediction from more than 100% to less than 10%, and maintaining the accuracy in the rest of the predictions.

- Speckle patterns generated by spray painting were not valid for strain measurements in orthogonal cutting because the extreme thermomechanical loads caused the paint to peel off, resulting in decorrelation problems. Therefore, a new method to measure plastic strain based on grid distortion was proposed. The uncertainty in the measurement was determined to be 15% through a Monte Carlo simulation. This technique measures plastic strain and strain rates using a single image. The use of a customized set-up prevented decorrelation problems typical of DIC based methodologies allowing the test to be made under plane strain conditions (orthogonal cutting). This technique was validated with the experimental results from DIC measurements, analytical results, FEM results, and experimental values reported in the literature, with good agreement.

- The grid distortion technique was also employed to measure surface integrity (subsurface damage). The subsurface damage was found to increase with feed, particularly at high feeds. In contrast, the effect of cutting speed, at least at low feeds, was negligible. The microgrid technique is more sensitive reporting higher values than microhardness or etched based techniques, which reduces subjectivity in the measurements. The microstructure of the workpiece material also plays an important role as subsurface damages were 15% higher when the material was cut in the Y direction. In addition, a slight decrease was found (around 12%) on subsurface damage when employing the coated tool and a considerable decrease (around 40%) when employing the sharpest tool.

7.2 FUTURE LINES

A number of new research questions have arisen in the development of this work, and further research in the following lines could usefully advance understanding of the modelling of the machining process:

- Knowledge of the temperature in the shear zone during cutting is a valuable input which facilitates understanding of material behaviour under realistic machining

conditions. Nevertheless, the temperature reported through infrared measurements is based on the visible surface, and is not representative of the orthogonal cutting process as the load mode is plane stress rather than plane strain conditions. For this reason, an analytical equation, similar to that presented in Section 3.5 to determine adiabatic self-heating, should be developed to determine the workpiece temperature in the centre based on infrared measurements. This would allow comparison with numerical 2D models. Similar analyses have been conducted previously, for instance, by Saez de Buruaga et al., 2018 to determine the temperature profile along the tool edge.

- The inverse analysis carried out in the present study should be taken as a first step. Although the predictions, especially those concerning chip segmentation frequency, were notably improved with this optimization, chip shape and curvature could be better predicted. Therefore, the use of other inputs measured under real machining conditions, such as workpiece temperature or equivalent plastic strain and strain rate, to optimize material laws (constitutive law, ductile failure law or friction) would be invaluable for the development of more robust models.

- The grid method developed to measure plastic strain will be employed at higher cutting speeds using images obtained by high speed filming. Under these conditions, the stop methodology is not applicable and failure of the DIC software was observed. High speed images will therefore enable the analysis of the variation of strain and strain rate as the cutting progresses. It should be noted that these measurements will be carried out under plane stress conditions, assuming that slight discrepancies will be found when comparing them with numerical 2D orthogonal models. Therefore, a orthogonal 3D model should be developed. To improve the grid method, the use of artificial intelligence to select the grid points would be helpful to limit sources of error associated with the manual selection of points as much as possible.

- The use of the grid method to measure subsurface damage after machining proved to be accurate, less subjective, and more sensitive than other traditional methods such as microstructural or microhardness based techniques. Nevertheless, using artificial intelligence to automate the measurement process would further reduce the subjectivity and improve the robustness of the results.

- EBSD measurement is also becoming widely used to quantify subsurface damage, however it has the disadvantage of being expensive and time consuming. It would be interesting to compare EBSD results with those obtained through the grid distortion method.

- The amount of residual plastic strain along the machined surface is also critical as it could lead to crack initiation, and affect fatigue life. The grid method, as employed in Section 5.2.1, could be used to determine this plastic strain. Analysis of both

residual plastic strain and subsurface damage could be used to estimate the residual stresses on the machined workpiece

8

CONTRIBUTIONS

During the development of this PhD the following scientific contributions can be summarized:

Articles in peer-reviewed journals:

Sela, A., Ortiz-de-Zarate, G., Soler, D., Germain, G., Aristimuño, P., Arrazola, P. J. (2021). *Measurement of plastic strain and plastic strain rate during orthogonal cutting for Ti-6Al-4V.* International Journal of Mechanical Sciences (Q1).

Sela, A., Soler, D., Ortiz-De-Zarate, G., Germain, G., Docubu, F., Arrazola, P. J. (Under review) *Inverse simulation for predicting chip segmentation during orthogonal cutting of Ti6Al4V at low cutting speeds: optimization of the ductile failure law.* Journal of Materials Processing Technology (Q1).

Ortiz-de-Zarate, G., Sela, A., Saez-de-Buruaga, M., Cuesta, M., Madariaga, A., Garay, A., Arrazola, P. J. (2019). *Methodology to establish a hybrid model for prediction of cutting forces and chip thickness in orthogonal cutting condition close to broaching.* The International Journal of Advanced Manufacturing Technology, 101(5), 1357-1374 (Q2).

Medina-Clavijo, B., Ortiz-de-Zarate, G., Sela, A., Arrieta, I. M., Fedorets, A., Arrazola, P. J., Chuvilin, A. (2021). *In-SEM micro-machining reveals the origins of the size effect in the cutting energy.* Scientific Reports, 11(1), 1-18 (Q1).

International conferences:

Sela, A., Ortiz-de-Zarate, G., Arrieta, I., Soriano, D., Aristimuño, P., Medina-Clavijo, B., Arrazola, P. J. (2019). *A mechanistic model to predict cutting force on orthogonal machining of Aluminum 7475-T7351 considering the edge radius.* Procedia CIRP, 82, 32-36 (presenting author).

Sela, A., Ortiz-de-Zarate, G., Soriano, D., Cuesta, M., Arrieta, I., Arrazola, P. J. (2019). *Towards inverse simulation: Effect of material parameters on machining predictions.* AIP Conference Proceedings 2113-1, 21-27 (presenting author).

Sela, A., Ortiz-De-Zarate, G., Soler, D., Aristimuño, P., Soriano, D., Germain, G.,

Docubu, F., Arrazola, P. J. (2020). *Surface drag analysis after Ti-6Al-4V orthogonal cutting using grid distortion.* Procedia CIRP, 87, 372-377 (presenting author).

Aristimuño, P., Lazcano, X., Sela, A., Basagoiti, R., Arrazola, P. J. (2018). *An optimization methodology for material databases to improve cutting force predictions when milling martensitic stainless steel JETHETE-M152.* Procedia CIRP, 77, 287-290.

Ortiz-de-Zarate, G., Sela, A., Ducobu, F., Saez-de-Buruaga, M., Soler, D., Childs, T. H. C., Arrazola, P. J. (2019). *Evaluation of different flow stress laws coupled with a physical based ductile failure criterion for the modelling of the chip formation process of Ti-6Al-4V under broaching conditions.* Procedia CIRP, 82, 65-70.

Ortiz-de-Zarate, G., Sela, A., Soriano, D., Soler, D., Aristimuño, P., Arrazola, P. J. (2019). *Influence of chip segmentation of Ti64 on the topography of the machined surface.* AIP Conference Proceedings 2113-1, 27-33.

Ortiz-de-Zarate, G., Sela, A., Madariaga, A., Childs, T. H. C., Arrazola, P. J. (2020). *Sensitivity analysis of the input parameters of a physical based ductile failure model of Ti-6Al-4V for the prediction of surface integrity.* Procedia CIRP, 87, 533-538.

BIBLIOGRAPHY

Agmell, Mathias et al. (2014). "Identification of plasticity constants from orthogonal cutting and inverse analysis." In: *Mechanics of Materials* 77, pp. 43–51.

Al Huda, M. et al. (2002). "Investigation of temperature at tool-chip interface in turning using two-color pyrometer." In: *Journal of manufacturing science and engineering* 124.2, pp. 200–207.

Alabort, E et al. (2015). "Superplasticity in Ti–6Al–4V: Characterisation, modelling and applications." In: *Acta Materialia* 95, pp. 428–442.

Allahverdizadeh, Nima et al. (2015). "An experimental and numerical study for the damage characterization of a Ti–6AL–4V titanium alloy." In: *International Journal of Mechanical Sciences* 93, pp. 32–47.

Arrazola, P.J. et al. (2004). "Material flow stress sensitivity analysis in numerical cutting modeling." In: *AIP Conference Proceedings*. Vol. 712. 1. AIP, pp. 1408–1413.

Arrazola, P.J. et al. (2013). "Recent advances in modelling of metal machining processes." In: *CIRP Annals* 62.2, pp. 695–718.

Arulkirubakaran, D and V Senthilkumar (2017). "Performance of TiN and TiAlN coated micro-grooved tools during machining of Ti-6Al-4V alloy." In: *International Journal of Refractory Metals and Hard Materials* 62, pp. 47–57.

Bai, Wei et al. (2017). "Improved analytical prediction of chip formation in orthogonal cutting of titanium alloy Ti6Al4V." In: *International Journal of Mechanical Sciences* 133, pp. 357–367.

Bailey, J.A. and S. Jeelani (1976). "Determination of subsurface plastic strain in machining using an embossed grid." In: *Wear* 36.2, pp. 199–206.

Baizeau, T. et al. (2016). "Prediction of surface integrity using Flamant–Boussinesq analytical model." In: *CIRP Annals* 65.1, pp. 81–84.

Baizeau, Thomas et al. (2017). "Kinematic Field Measurements During Orthogonal Cutting Tests via DIC with Double-frame Camera and Pulsed Laser Lighting." In: *Experimental Mechanics* 57.4, pp. 581–591.

Bao, Y. (2003). "Prediction of ductile crack formation in uncracked bodies." PhD thesis. Massachusetts Institute of Technology.

Bao, Yingbin and Tomasz Wierzbicki (2004). "On fracture locus in the equivalent strain and stress triaxiality space." In: *International Journal of Mechanical Sciences* 46.1, pp. 81–98.

Bennett, CJ et al. (2010). "A critical analysis of plastic flow behaviour in axisymmetric isothermal and Gleeble compression testing." In: *Computational materials science* 50.1, pp. 125–137.

Bertolini, R et al. (2019). "Improving surface integrity and corrosion resistance of additive manufactured Ti6Al4V alloy by cryogenic machining." In: *The International Journal of Advanced Manufacturing Technology* 104.5, pp. 2839–2850.

Boivineau, M et al. (2006). "Thermophysical properties of solid and liquid Ti-6Al-4V (TA6V) alloy." In: *International journal of thermophysics* 27.2, pp. 507–529.

Bonk, Christian et al. (2016). "An Experimental-Numerical Method to Determine the Plastic Work Converted into Heat Applied on AHSS." In: *Advanced Materials Research*. Vol. 1140. Trans Tech Publ, pp. 51–58.

Boothroyd, G (1963). "Temperatures in orthogonal metal cutting." In: *Proceedings of the Institution of Mechanical Engineers* 177.1, pp. 789–810.

Bordin, Alberto et al. (2014). "Comparison between wrought and EBM Ti6Al4V machinability characteristics." In: *Key Engineering Materials*. Vol. 611. Trans Tech Publ, pp. 1186–1193.

Bossuyt, S. (2013). "Optimized patterns for digital image correlation." In: *Imaging Methods for Novel Materials and Challenging Applications, Volume 3*. Springer, pp. 239–248.

Brinksmeier, E. et al. (1982). "Residual stresses: measurement and causes in machining processes." In: *CIRP Annals* 31.2, pp. 491–510.

Bruschi, S et al. (2004). "Workability of Ti–6Al–4V alloy at high temperatures and strain rates." In: *Materials Letters* 58.27-28, pp. 3622–3629.

Budak, E et al. (1996). "Prediction of milling force coefficients from orthogonal cutting data." In: *Journal of Manufacturing Science and Engineering*.

Calistes, R et al. (2009). "Controlling gradation of surface strains and nanostructuring by large-strain machining." In: *Scripta Materialia* 60.1, pp. 17–20.

Cao, G et al. (2011). "In situ measurements of spectral emissivity of materials for very high temperature reactors." In: *Nuclear technology* 175.2, pp. 460–467.

Chen, Guang et al. (2019). "Effect of cutting edge radius and cooling strategies on surface integrity in orthogonal machining of Ti-6Al-4V alloy." In: *Procedia CIRP* 82, pp. 148–153.

Childs, T.H.C. et al. (2018). "Ti6Al4V metal cutting chip formation experiments and modelling over a wide range of cutting speeds." In: *Journal of Materials Processing Technology* 255, pp. 898–913.

Chrysochoos, A et al. (1989). "Plastic and dissipated work and stored energy." In: *Nuclear Engineering and Design* 114.3, pp. 323–333.

Cotterell, M et al. (2013). "Temperature and Strain Measurement during Chip Formation in Orthogonal Cutting Conditions Applied to Ti-6Al-4 V." In: *Procedia Engineering* 63, pp. 922–930.

da Silva, M.B. and J. Wallbank (1999). "Cutting temperature: prediction and measurement methods: a review." In: *Journal of materials processing technology* 88.1-3, pp. 195–202.

Daoud, M. et al. (2015a). "A machining-based methodology to identify material constitutive law for finite element simulation." In: *The International Journal of Advanced Manufacturing Technology* 77.9-12, pp. 2019–2033.

Daoud, M. et al. (2015b). "Effect of rake angle on Johnson-Cook material constants and their impact on cutting process parameters of Al2024-T3 alloy machining simulation." In: *The International Journal of Advanced Manufacturing Technology* 81.9-12, pp. 1987–1997.

Davies, MA et al. (2007). "On the measurement of temperature in material removal processes." In: *CIRP annals* 56.2, pp. 581–604.

Davim, J.P. et al. (2009). "Surface roughness aspects in milling MDF (medium density fibreboard)." In: *The International Journal of Advanced Manufacturing Technology* 40.1-2, pp. 49–55.

Dearnley, P.A. (1986). "A preliminary investigation of the effect of tool geometry on tool temperatures when turning steel at high speed." In: *International Journal of Machine Tool Design and Research* 26.1, pp. 15–20.

Dewes, R.C. et al. (1999). "Temperature measurement when high speed machining hardened mould/die steel." In: *Journal of Materials Processing Technology* 92, pp. 293–301.

Dinc, C. et al. (2008). "Analysis of thermal fields in orthogonal machining with infrared imaging." In: *Journal of materials processing technology* 198.1-3, pp. 147–154.

Dogu, Y. et al. (2006). "A numerical model to determine temperature distribution in orthogonal metal cutting." In: *Journal of Materials Processing Technology* 171.1, pp. 1–9.

Dorogoy, A et al. (2015). "Modification of the shear-compression specimen for large strain testing." In: *Experimental mechanics* 55.9, pp. 1627–1639.

Drozd, Kamil et al. (2011). "Study of development of strain in plane strain compression test." In: *International Conference on Metallurgy and Materials METAL*.

Dumoulin, Stéphane et al. (2010). "Heat sources, energy storage and dissipation in high-strength steels: Experiments and modelling." In: *European Journal of Mechanics-A/Solids* 29.3, pp. 461–474.

Edkins, Kyle D et al. (2014). "Evaluating the subsurface microstructure of machined Ti-6Al-4V." In: *Procedia Cirp* 13, pp. 270–275.

Elbestawi, MA et al. (1996). "A model for chip formation during machining of hardened steel." In: *CIRP annals* 45.1, pp. 71–76.

Evans, RW and PJ Scharning (2001). "Axisymmetric compression test and hot working properties of alloys." In: *Materials science and technology* 17.8, pp. 995–1004.

Ezugwu, EO (2005). "Key improvements in the machining of difficult-to-cut aerospace superalloys." In: *International Journal of Machine Tools and Manufacture* 45.12-13, pp. 1353–1367.

Ezugwu, EO and ZM Wang (1997). "Titanium alloys and their machinability—a review." In: *Journal of materials processing technology* 68.3, pp. 262–274.

Feng, Fei et al. (2014). "Experimental study on tensile property of AZ31B magnesium alloy at different high strain rates and temperatures." In: *Materials & Design* 57, pp. 10–20.

Field, J.E. et al. (2004). "Review of experimental techniques for high rate deformation and shock studies." In: *International journal of impact engineering* 30.7, pp. 725–775.

Franchi, R. et al. (2017). "Inverse analysis procedure to determine flow stress and friction data for finite element modeling of machining." In: *International Journal of Material Forming* 10.5, pp. 685–695.

Gandarias, E et al. (2006). "Deteccion de rotura de herramientas en el microfresado mediante nuevos sistemas de monitorizado." In: *INVEMA, Fundación de Investigación de la Máquina-Herramienta*.

Gáspár, C (1999). "Multigrid technique for biharmonic interpolation with application to dual and multiple reciprocity method." In: *Numerical Algorithms* 21.1-4, pp. 165–183.

Germain, Guénaël et al. (2013). "Identification of material constitutive laws representative of machining conditions for two titanium alloys: Ti6Al4V and Ti555-3." In: *Journal of Engineering Materials and Technology* 135.3, p. 031002.

Ghadbeigi, H. et al. (2008). "Determination of micro-scale plastic strain caused by orthogonal cutting." In: *International Journal of Machine Tools and Manufacture* 48.2, pp. 228–235.

Ghadbeigi, H. et al. (2010). "Local plastic strain evolution in a high strength dual-phase steel." In: *Materials Science and Engineering: A* 527.18-19, pp. 5026–5032.

Ghadbeigi, H et al. (2012). "Quantitative strain analysis of the large deformation at the scale of microstructure: comparison between digital image correlation and microgrid techniques." In: *Experimental mechanics* 52.9, pp. 1483–1492.

Ginting, A and M Nouari (2009). "Surface integrity of dry machined titanium alloys." In: *International Journal of Machine Tools and Manufacture* 49.3-4, pp. 325–332.

Gnanamanickam, E.P. et al. (2009). "Direct measurement of large-strain deformation fields by particle tracking." In: *Measurement Science and Technology* 20.9, pp. 095710–1–15.

Goetz, RL and SL Semiatin (2001). "The adiabatic correction factor for deformation heating during the uniaxial compression test." In: *Journal of materials engineering and performance* 10.6, pp. 710–717.

Güler, Baran and Mert Efe (2018). "Forming and fracture limits of sheet metals deforming without a local neck." In: *Journal of Materials Processing Technology* 252, pp. 477–484.

Guo, Y. et al. (2011). "Controlling deformation and microstructure on machined surfaces." In: *Acta materialia* 59.11, pp. 4538–4547.

Guo, Y. et al. (2015). "In situ analysis of flow dynamics and deformation fields in cutting and sliding of metals." In: *Proc. R. Soc. A* 471.2178, pp. 20150194–1–15.

Haddadi, H. and S. Belhabib (2008). "Use of rigid-body motion for the investigation and estimation of the measurement errors related to digital image correlation technique." In: *Optics and Lasers in Engineering* 46.2, pp. 185–196.

Hammer, Jeremiah Thomas (2012). "Plastic deformation and ductile fracture of Ti-6Al-4V under various loading conditions." PhD thesis. The Ohio State University.

Hardt, M et al. (2021). "Investigations on the Application of the Downhill-Simplex-Algorithm to the Inverse Determination of Material Model Parameters for FE-Machining Simulations." In: *Simulation Modelling Practice and Theory* 107, p. 102214.

Härtel, Sebastian et al. (2018). "Novel Approach for the Determination of the Taylor-Quinney Coefficient." In: *Materials Science Forum*. Vol. 918. Trans Tech Publ, pp. 103–109.

Harzallah, Mahmoud (2018). "Caractérisation in-situ et modélisation des mécanismes et couplages thermomécaniques en usinage: application à l'alliage de titane Ti-6Al-4V." PhD thesis. Ecole des Mines d'Albi-Carmaux.

Harzallah, Mahmoud et al. (2017). "Numerical and experimental investigations of Ti-6Al-4V chip generation and thermo-mechanical couplings in orthogonal cutting." In: *International Journal of Mechanical Sciences* 134, pp. 189–202.

Harzallah, Mahmoud et al. (2020). "Thermomechanical coupling investigation in Ti-6Al-4V orthogonal cutting: Experimental and numerical confrontation." In: *International Journal of Mechanical Sciences* 169, p. 105322.

Herbert, C. et al. (2012). "Investigation into the characteristics of white layers produced in a nickel-based superalloy from drilling operations." In: *Machining Science and Technology* 16.1, pp. 40–52.

Hong, S.Y. and Y. Ding (2001). "Cooling approaches and cutting temperatures in cryogenic machining of Ti-6Al-4V." In: *International Journal of Machine Tools and Manufacture* 41.10, pp. 1417–1437.

Hor, Anis et al. (2013a). "An experimental investigation of the behaviour of steels over large temperature and strain rate ranges." In: *International Journal of Mechanical Sciences* 67, pp. 108–122.

— (2013b). "Modelling, identification and application of phenomenological constitutive laws over a large strain rate and temperature range." In: *Mechanics of Materials* 64, pp. 91–110.

Hosford, W.F. (2010). *Mechanical behavior of materials*. Cambridge University Press.

Hou, Guanming et al. (2018). "Effect of cutting parameters on surface quality in multi-step turning of Ti-6Al-4V titanium alloy." In: *The International Journal of Advanced Manufacturing Technology* 98.5, pp. 1355–1365.

Hoyne, A.C. et al. (2013). "Cutting Temperature Measurement During Titanium Machining With an Atomization–Based Cutting Fluid (ACF) Spray System." In: *ASME 2013 International Mechanical Engineering Congress and Exposition*. American Society of Mechanical Engineers, pp. 1–10.

Islam, Md Aquidul (2012). "Determination of the Deformation State of a Ti-6Al-4V Alloy Subjected to Orthogonal Cutting Using Experimental and Numerical Methods." PhD thesis.

ISO, IEC (2008). "Guide 98-3 Uncertainty of measurement—Part 3: guide to the expression of uncertainty in measurement (GUM: 1995)." In: *International Organization for Standardization, Geneva*.

Jawahir, IS et al. (2011). "Surface integrity in material removal processes: Recent advances." In: *CIRP annals* 60.2, pp. 603–626.

Jeelani, S. and K. Ramakrishnan (1982). "Subsurface plastic deformation in machining annealed 18% Ni maraging steel." In: *Wear* 81.2, pp. 263–273.

Jiang, Yu-Qiang et al. (2020). "Hot tensile properties, microstructure evolution and fracture mechanisms of Ti-6Al-4V alloy with initial coarse equiaxed phases." In: *Materials Characterization* 163, p. 110272.

Joshi, Shashikant et al. (2015). "Microstructural characterization of chip segmentation under different machining environments in orthogonal machining of Ti6Al4V." In: *Journal of Engineering Materials and Technology* 137.1.

Kailas, Satish V et al. (1994). "Flow instabilities and fracture in Ti-6Al-4V deformed in compression at 298 K to 673 K." In: *Metallurgical and materials transactions a* 25.10, pp. 2173–2179.

Kapoor, Rajeev and Sia Nemat-Nasser (1998). "Determination of temperature rise during high strain rate deformation." In: *Mechanics of materials* 27.1, pp. 1–12.

Kardoulaki, Erofili et al. (2014). "Investigation of the effects of thermal gradients present in Gleeble high-temperature tensile tests on the strain state for free cutting steel." In: *The Journal of Strain Analysis for Engineering Design* 49.7, pp. 521–532.

Karimi, A. (1984). "Plastic flow study using the microgrid technique." In: *Materials Science and Engineering* 63.2, pp. 267–276.

Kato, T. and H. Fujii (1996). "PVD film method for measuring the temperature distribution in cutting tools." In: *Journal of engineering for industry* 118.1, pp. 117–122.

Khoo, S-W et al. (2016). "A review of surface deformation and strain measurement using two-dimensional digital image correlation." In: *Metrology and Measurement Systems* 23.3.

Kishawy, Hossam A and Ali Hosseini (2019). "Machining difficult-to-cut materials." In: *Mater. Form. Mach. Tribol.*

Klocke, F. et al. (2013). "Inverse identification of the constitutive equation of Inconel 718 and AISI 1045 from FE machining simulations." In: *Procedia Cirp* 8, pp. 212–217.

Knysh, Paul and Yannis P Korkolis (2015). "Determination of the fraction of plastic work converted into heat in metals." In: *Mechanics of materials* 86, pp. 71–80.

Kolsky, H. (1949). "An investigation of the mechanical properties of materials at very high rates of loading." In: *Proceedings of the physical society. Section B* 62.11, pp. 1–10.

Komanduri, R and ZB Hou (2001). "A review of the experimental techniques for the measurement of heat and temperatures generated in some manufacturing processes and tribology." In: *Tribology International* 34.10, pp. 653–682.

Koohbor, Behrad et al. (2016). "Thermo-mechanical properties of metals at elevated temperatures." In: *Advancement of Optical Methods in Experimental Mechanics, Volume 3*. Springer, pp. 117–123.

Kröning, Hans-Jürgen et al. (2016). "High temperature Gleeble microtensile testing of metallic micro specimens." In: *Materials Testing* 58.10, pp. 826–832.

Lecompte, D. et al. (2006). "Quality assessment of speckle patterns for digital image correlation." In: *Optics and lasers in Engineering* 44.11, pp. 1132–1145.

Lee, D. (1984). "The nature of chip formation in orthogonal machining." In: *Journal of Engineering Materials and Technology* 106.1, pp. 9–15.

Lee, S. et al. (2006). "Large strain deformation field in machining." In: *Metallurgical and Materials Transactions A* 37.5, pp. 1633–1643.

Li, Guojian et al. (2016). "Low adhesion effect of TaO functional composite coating on the titanium cutting performance of coated cemented carbide insert." In: *Materials & Design* 110, pp. 105–111.

Li, John JZ et al. (2006). "Thermal expansion of liquid Ti–6Al–4V measured by electrostatic levitation." In: *Applied physics letters* 89.11, p. 111913.

Liang, Xiaoliang and Zhanqiang Liu (2017). "Experimental investigations on effects of tool flank wear on surface integrity during orthogonal dry cutting of Ti-6Al-4V." In: *The International Journal of Advanced Manufacturing Technology* 93.5-8, pp. 1617–1626.

Liang, Xiaoliang et al. (2019). "State-of-the-art of surface integrity induced by tool wear effects in machining process of titanium and nickel alloys: a review." In: *Measurement* 132, pp. 150–181.

Liu, Jiajia et al. (2019). "Effects of rotary ultrasonic elliptical machining for side milling on the surface integrity of Ti-6Al-4V." In: *The International Journal of Advanced Manufacturing Technology* 101.5, pp. 1451–1465.

Liu, Jian et al. (2014). "Evaluation of ductile fracture models in finite element simulation of metal cutting processes." In: *Journal of Manufacturing Science and Engineering* 136.1.

Lizzul, Lucia et al. (2020a). "Effect of AM-induced Anisotropy on the Surface Integrity of Laser Powder Bed Fused Ti6Al4V Machined Parts." In: *Procedia Manufacturing* 47, pp. 505–510.

Lizzul, Lucia et al. (2020b). "Influence of additive manufacturing-induced anisotropy on tool wear in end milling of Ti6Al4V." In: *Tribology International* 146, p. 106200.

Loewen, E.G. and M.C. Shaw (1954). "On the analysis of cutting-tool temperatures." In: *Tras. ASME* 76, p. 217.

Longbottom, J.M. and J.D. Lanham (2005). "Cutting temperature measurement while machining–a review." In: *Aircraft Engineering and Aerospace Technology* 77.2, pp. 122–130.

Luo, Yu-Meng et al. (2015). "Adiabatic shear banding of hot-rolling Ti–6Al–4V alloy subjected to dynamic shearing and uniaxial dynamic compression." In: *Rare Metals* 34.9, pp. 632–637.

Macdougall, DAS and J Harding (1998). "The measurement of specimen surface temperature in high-speed tension and torsion tests." In: *International journal of impact engineering* 21.6, pp. 473–488.

Malakizadi, Amir et al. (2016). "Inverse identification of flow stress in metal cutting process using Response Surface Methodology." In: *Simulation Modelling Practice and Theory* 60, pp. 40–53.

Martínez-Donaire, AJ et al. (2014). "New approaches to detect the onset of localised necking in sheets under through-thickness strain gradients." In: *Materials & Design* 57, pp. 135–145.

Mason, JJ et al. (1994). "On the strain and strain rate dependence of the fraction of plastic work converted to heat: an experimental study using high speed infrared detectors and the Kolsky bar." In: *Mechanics of Materials* 17.2-3, pp. 135–145.

Mataya, MC and VE Sackschewsky (1994). "Effect of internal heating during hot compression on the stress-strain behavior of alloy 304L." In: *Metallurgical and Materials Transactions A* 25.12, p. 2737.

Medina-Clavijo, Bentejui et al. (2018). "Microstructural aspects of the transition between two regimes in orthogonal cutting of AISI 1045 steel." In: *Journal of Materials Processing Technology* 260, pp. 87–96.

Melkote, S.N. et al. (2017). "Advances in material and friction data for modelling of metal machining." In: *CIRP Annals* 66.2, pp. 731–754.

Merchant, M.E. (1945). "Mechanics of the metal cutting process. II. Plasticity conditions in orthogonal cutting." In: *Journal of applied physics* 16.6, pp. 318–324.

Meurer, Markus et al. (2020). "Development of a methodology for strain field analysis during orthogonal cutting." In: *Procedia CIRP* 87, pp. 444–449.

Milošević, Nenad and Ivana Aleksić (2012). "Thermophysical properties of solid phase Ti-6Al-4V alloy over a wide temperature range." In: *International journal of materials research* 103.6, pp. 707–714.

Mosecker, Linda et al. (2013). "Deformation mechanisms of Ti6Al4V sheet material during the incremental sheet forming with laser heating." In: *Key Engineering Materials*. Vol. 549. Trans Tech Publ, pp. 372–380.

M'Saoubi, R. et al. (2015). "High performance cutting of advanced aerospace alloys and composite materials." In: *CIRP Annals* 64.2, pp. 557–580.

M'Saoubi, Rachid et al. (2012). "Surface integrity analysis of machined Inconel 718 over multiple length scales." In: *CIRP annals* 61.1, pp. 99–102.

M'Saoubi, Rachid et al. (2014). "Surface integrity of nickel-based alloys subjected to severe plastic deformation by abusive drilling." In: *CIRP Annals* 63.1, pp. 61–64.

Narutaki, Norihiko et al. (1983). "Study on machining of titanium alloys." In: *CIRP Annals* 32.1, pp. 65–69.

Nespor, Dennis et al. (2015). "Differences and similarities between the induced residual stresses after ball end milling and orthogonal cutting of Ti–6Al–4V." In: *Journal of Materials Processing Technology* 226, pp. 15–24.

Novak, Mark D and Frank W Zok (2011). "High-temperature materials testing with full-field strain measurement: experimental design and practice." In: *Review of scientific instruments* 82.11, p. 115101.

Novovic, D. et al. (2004). "The effect of machined topography and integrity on fatigue life." In: *International Journal of Machine Tools and Manufacture* 44.2-3, pp. 125–134.

Oh, SI et al. (1992). "An analysis of the isothermal hot compression test." In: *Metallurgical transactions A* 23.3, pp. 963–975.

Ortiz de Zarate, G et al. (2018). "Experimental and FEM analysis of surface integrity when broaching Ti64." In: *Procedia Cirp* 71, pp. 466–471.

Ortiz de Zarate, G et al. (2019). "Evaluation of different flow stress laws coupled with a physical based ductile failure criterion for the modelling of the chip formation process of Ti-6Al-4V under broaching conditions." In: *Procedia CIRP* 82, pp. 65–70.

Ortiz de Zarate, G et al. (2020). "Sensitivity analysis of the input parameters of a physical based ductile failure model of Ti-6Al-4V for the prediction of surface integrity." In: *Procedia CIRP* 87, pp. 533–538.

Ortiz de Zarate, G et al. (2021). "A novel methodology to characterize tool-chip contact in metal cutting using partially restricted contact length tools." In: *CIRP Annals*.

O'sullivan, D. and M. Cotterell (2001). "Temperature measurement in single point turning." In: *Journal of Materials Processing Technology* 118.1-3, pp. 301–308.

Outeiro, J.C. et al. (2015). "Experimental and numerical assessment of subsurface plastic deformation induced by OFHC copper machining." In: *CIRP Annals* 64.1, pp. 53–56.

Oxley, P.L.B. (1989). *The Mechanics of Machining: An Analytical Approach to Assesing Machinability*. Ellis Horwood.

Oyelola, Olusola et al. (2018). "On the machinability of directed energy deposited Ti6Al4V." In: *Additive Manufacturing* 19, pp. 39–50.

Pardis, Nima et al. (2017). "Equivalent strain at large shear deformation: Theoretical, numerical and finite element analysis." In: *Journal of Applied Research and Technology* 15.5, pp. 442 –448. ISSN: 1665-6423.

Park, Nho-Kwang et al. (2002). "Characterization of deformation stability in hot forging of conventional Ti–6Al–4V using processing maps." In: *Journal of Materials Processing Technology* 130, pp. 540–545.

Pawade, R.S. et al. (2008). "Effect of machining parameters and cutting edge geometry on surface integrity of high-speed turned Inconel 718." In: *International Journal of Machine Tools and Manufacture* 48.1, pp. 15–28.

Polakowski, Natalis Horace and Edward Joseph Ripling (1966). "Strength and structure of engineering materials." In: *Englewood Cliffs*.

Pottier, T. et al. (2014). "Sub-millimeter measurement of finite strains at cutting tool tip vicinity." In: *Experimental Mechanics* 54.6, pp. 1031–1042.

Puerta Velásquez, JD et al. (2010). "Sub-surface and surface analysis of high speed machined Ti–6Al–4V alloy." In: *Materials Science and Engineering: A* 527.10-11, pp. 2572–2578.

Pujana, J. et al. (2007). "Analysis of the inverse identification of constitutive equations applied in orthogonal cutting process." In: *International Journal of Machine Tools and Manufacture* 47.14, pp. 2153–2161.

Pujana, J et al. (2008). "In-process high-speed photography applied to orthogonal turning." In: *Journal of materials processing technology* 202.1-3, pp. 475–485.

Quan, Guo-Zheng et al. (2016). "Phase transformation and recrystallization kinetics in space–time domain during isothermal compressions for Ti–6Al–4V analyzed by multi-field and multi-scale coupling FEM." In: *Materials & Design* 94, pp. 523–535.

Rahman, Mustafizur et al. (2003). "Machinability of titanium alloys." In: *JSME International Journal Series C Mechanical Systems, Machine Elements and Manufacturing* 46.1, pp. 107–115.

Razanica, S et al. (2020). "FE modeling and simulation of machining Alloy 718 based on ductile continuum damage." In: *International Journal of Mechanical Sciences* 171, p. 105375.

Reddy, NS et al. (2008). "High temperature deformation behavior of Ti- 6Al- 4V alloy with and equiaxed microstructure: a neural networks analysis." In: *Metals and materials International* 14.2, p. 213.

Rittel, D and ZG Wang (2008). "Thermo-mechanical aspects of adiabatic shear failure of AM50 and Ti6Al4V alloys." In: *Engineering Systems Design and Analysis*. Vol. 48357, pp. 529–550.

Rittel, D et al. (2017). "The dependence of the Taylor–Quinney coefficient on the dynamic loading mode." In: *Journal of the Mechanics and Physics of Solids* 107, pp. 96–114.

Rooyen, Melody van and Thorsten Hermann Becker (2018). "High-temperature tensile property measurements using digital image correlation over a non-uniform temperature field." In: *The Journal of Strain Analysis for Engineering Design* 53.3, pp. 117–129.

Rotella, G et al. (2014). "The effects of cooling conditions on surface integrity in machining of Ti6Al4V alloy." In: *The International Journal of Advanced Manufacturing Technology* 71.1-4, pp. 47–55.

Rotella, Giovanna et al. (2018). "Surface integrity of machined additively manufactured Ti alloys." In: *Journal of Materials Processing Technology* 259, pp. 180–185.

Roy, Shibayan and Satyam Suwas (2013). "The influence of temperature and strain rate on the deformation response and microstructural evolution during hot compression of a titanium alloy Ti–6Al–4V–0.1 B." In: *Journal of Alloys and Compounds* 548, pp. 110–125.

Saez de Buruaga, M. et al. (2018). "Determining tool/chip temperatures from thermography measurements in metal cutting." In: *Applied Thermal Engineering* 145, pp. 305–314.

Safari, H et al. (2015). "Surface integrity characterization in high-speed dry end milling of Ti-6Al-4V titanium alloy." In: *The International Journal of Advanced Manufacturing Technology* 78.1-4, pp. 651–657.

Sakanashi, Y et al. (2017). "Measurement of creep deformation across welds in 316H stainless steel using digital image correlation." In: *Experimental Mechanics* 57.2, pp. 231–244.

Sartkulvanich, P. et al. (2004). "Determination of flow stress for metal cutting simulation: a progress report." In: *Journal of Materials Processing Technology* 146.1, pp. 61–71.

Schnur, D.S. and D. Lee (1984). "Determination of strain distributions in machined chips." In: *Metallurgical Transactions A* 15.9, pp. 1777–1779.

Semiatin, SL et al. (2017). "The radial temperature gradient in the Gleeble® hot-torsion test and its effect on the interpretation of plastic-flow behavior." In: *Metallurgical and Materials Transactions A* 48.11, pp. 5357–5367.

Shahan, AR and A Karimi Taheri (1993). "Adiabatic shear bands in titanium and titanium alloys: a critical review." In: *Materials & Design* 14.4, pp. 243–250.

Shao, Z et al. (2016). "Development of a new biaxial testing system for generating forming limit diagrams for sheet metals under hot stamping conditions." In: *Experimental Mechanics* 56.9, pp. 1489–1500.

Shao, Zhutao et al. (2018). "Strain measurement and error analysis in thermo-mechanical tensile tests of sheet metals for hot stamping applications." In: *Proceedings of the Institution of Mechanical Engineers, Part C: Journal of Mechanical Engineering Science* 232.11, pp. 1994–2008.

Shi, Y. et al. (2018). "The setup and application of the multi-scale in-situ test system for fatigue damage analysis." In: *MATEC Web of Conferences*. Vol. 165. EDP Sciences, pp. 04005–1–5.

Shitzer, Avraham (2006). "Wind-chill-equivalent temperatures: regarding the impact due to the variability of the environmental convective heat transfer coefficient." In: *International journal of biometeorology* 50.4, pp. 224–232.

Shrivastava, SC et al. (1982). "Equivalent strain in large deformation torsion testing: theoretical and practical considerations." In: *Journal of the Mechanics and Physics of Solids* 30.1-2, pp. 75–90.

Shrot, A. and M. Bäker (2010). "Is it possible to identify Johnson-Cook law parameters from machining simulations?" In: *International Journal of Material Forming* 3.1, pp. 443–446.

— (2011). "Inverse identification of Johnson-Cook material parameters from machining simulations." In: *Advanced Materials Research*. Vol. 223. Trans Tech Publ, pp. 277–285.

— (2012). "Determination of Johnson–Cook parameters from machining simulations." In: *Computational Materials Science* 52.1, pp. 298–304.

Shyha, Islam et al. (2018). "Analysis of Microstructure and Chip Formation When Machining Ti-6Al-4V." In: *Metals* 8.3, p. 185.

Simha, C Hari Manoj and Bruce W Williams (2016). "Modeling failure of Ti-6Al-4V using damage mechanics incorporating effects of anisotropy, rate and temperature on strength." In: *International Journal of Fracture* 198.1-2, pp. 101–115.

Smart, E.F. and E.M. Trent (1975). "Temperature distribution in tools used for cutting iron, titanium and nickel." In: *The International Journal of Production Research* 13.3, pp. 265–290.

Smith, Jarrod L et al. (2019). "Full-Field Determination of the Taylor-Quinney Coefficient in Tension Tests of Ti-6Al-4V at Strain Rates up to 7000 s^{-1}." In: *Advancement of Optical Methods & Digital Image Correlation in Experimental Mechanics, Volume 3*. Springer, pp. 133–139.

Society, International Digital Image Correlation (2018). *A good practices guide for digital image correlation*.

Soler, D. et al. (2015). "Uncertainty of temperature measurements in dry orthogonal cutting of titanium alloys." In: *Infrared Physics & Technology* 71, pp. 208–216.

Soler, D. et al. (2018). "New calibration method to measure rake face temperature of the tool during dry orthogonal cutting using thermography." In: *Applied Thermal Engineering* 137, pp. 74–82.

Stevenson, MG and PLB Oxley (1969). "An experimental investigation of the influence of speed and scale on the strain-rate in a zone of intense plastic deformation." In: *Proceedings of the Institution of Mechanical Engineers* 184.1, pp. 561–576.

Stüwe, Hein Peter (2003). "Equivalent strains in severe plastic deformation." In: *Advanced Engineering Materials* 5.5, pp. 291–295.

Tapetado, A. et al. (2016). "Two-color pyrometer for process temperature measurement during machining." In: *Journal of Lightwave Technology* 34.4, pp. 1380–1386.

Tarigopula, Venkat et al. (2008). "A study of large plastic deformations in dual phase steel using digital image correlation and FE analysis." In: *Experimental Mechanics* 48.2, pp. 181–196.

Taylor, Geoffrey Ingram and H Quinney (1934). "The latent energy remaining in a metal after cold working." In: *Proceedings of the Royal Society of London. Series A, Containing Papers of a Mathematical and Physical Character* 143.849, pp. 307–326.

Tekçe, Neslihan et al. (2018). "The effect of glazing and aging on the surface properties of CAD/CAM resin blocks." In: *The journal of advanced prosthodontics* 10.1, p. 50.

Telrandhe, Sagar V et al. (2017). "Effect of microstructure and cutting speed on machining behavior of Ti6Al4V alloy." In: *Journal of Mechanical Science and Technology* 31.5, pp. 2177–2184.

Thimm, B et al. (2019). "Using Digital Image Correlation Measurements for the Inverse Identification of Constitutive Material Parameters applied in Metal Cutting Simulations." In: *Procedia CIRP* 82, pp. 95–100.

Touazine, Heithem et al. (2019). "Characterization of subsurface microstructural alterations induced by hard turning of Inconel 718." In: *Journal of Materials Engineering and Performance* 28.11, pp. 7016–7024.

Trent, E.M. and P.K. Wright (2000). *Metal cutting*. Butterworth-Heinemann.

Ulutan, D. and T. Özel (2013). "Determination of constitutive material model parameters in FE-based machining simulations of Ti-6Al-4V and IN-100 alloys: an inverse methodology." In: *Proceedings of NAMRI/SME* 41.

Ulutan, Durul and Tugrul Ozel (2011). "Machining induced surface integrity in titanium and nickel alloys: A review." In: *International Journal of Machine Tools and Manufacture* 51.3, pp. 250–280.

Usamentiaga, Rubén et al. (2014). "Infrared thermography for temperature measurement and non-destructive testing." In: *Sensors* 14.7, pp. 12305–12348.

Wang, Bing and Zhanqiang Liu (2016). "Evaluation on fracture locus of serrated chip generation with stress triaxiality in high speed machining of Ti6Al4V." In: *Materials & Design* 98, pp. 68–78.

— (2018). "Influences of tool structure, tool material and tool wear on machined surface integrity during turning and milling of titanium and nickel alloys: a review." In: *The International Journal of Advanced Manufacturing Technology* 98.5, pp. 1925–1975.

Wang, Fuzeng et al. (2014). "Experimental study on cutting forces and surface integrity in high-speed side milling of Ti-6Al-4V titanium alloy." In: *Machining Science and Technology* 18.3, pp. 448–463.

Wyen, C-F and Konrad Wegener (2010). "Influence of cutting edge radius on cutting forces in machining titanium." In: *CIRP annals* 59.1, pp. 93–96.

Wyen, Carl-Frederik et al. (2013). "Influence of cutting edge radius on surface integrity and burr formation in milling titanium." In: *The International Journal of Advanced Manufacturing Technology* 67.1-4, pp. 589–599.

Xiao, H et al. (2021). "Flow stress correction for hot compression of titanium alloys considering temperature gradient induced heterogeneous deformation." In: *Journal of Materials Processing Technology* 288, p. 116868.

Yaich, Mariem et al. (2020). "A 2D finite element analysis of the effect of numerical parameters on the reliability of Ti6Al4V machining modeling." In: *Machining Science and Technology* 24.4, pp. 509–543.

Yang, D. and Z. Liu (2015). "Surface topography analysis and cutting parameters optimization for peripheral milling titanium alloy Ti–6Al–4V." In: *International Journal of Refractory Metals and Hard Materials* 51, pp. 192–200.

Yang, D and Z Liu (2018). "Surface integrity generated with peripheral milling and the effect on low-cycle fatigue performance of aeronautic titanium alloy Ti-6Al-4V." In: *The Aeronautical Journal* 122.1248, p. 316.

Ye, GG et al. (2018). "On the instability of chip flow in high-speed machining." In: *Mechanics of Materials* 116, pp. 104–119.

Zhang, D. et al. (2017). "Stress field analysis in orthogonal cutting process using digital image correlation technique." In: *Journal of Manufacturing Science and Engineering* 139.3, pp. 031001–1–6.

Zhang, D. et al. (2018). "Inverse identification of material plastic constitutive parameters based on the DIC determined workpiece deformation fields in orthogonal cutting." In: *Procedia CIRP* 71, pp. 134–139.

Zhang, Feng et al. (2015). "An emissivity measurement apparatus for near infrared spectrum." In: *Infrared Physics & Technology* 73, pp. 275–280.

Zhang, R et al. (2020). "Measurement and Analysis of Heterogeneous Strain Fields in Uniaxial Tensile Tests for Boron Steel Under Hot Stamping Conditions." In: *Experimental Mechanics* 60.9, pp. 1289–1300.

Zhang, Xiao-Ming et al. (2019). "New In Situ Imaging-Based Methodology to Identify the Material Constitutive Model Coefficients in Metal Cutting Process." In: *Journal of Manufacturing Science and Engineering* 141.10.

Zhao, Dan (1993). "Temperature correction in compression tests." In: *Journal of materials processing technology* 36.4, pp. 467–471.

Zhou, J.M. et al. (2012). "An investigation of surface damage in the high speed turning of Inconel 718 with use of whisker reinforced ceramic tools." In: *Journal of Materials Processing Technology* 212.2, pp. 372–384.

Zubelewicz, Aleksander (2019). "Century-long Taylor-Quinney interpretation of plasticity-induced heating reexamined." In: *Scientific Reports* 9.1, pp. 1–7.